sid.inpe.br/mtc-m21d/2022/06.10.12.02-TDI

LINEAR TIME-INVARIANT AND BAYESIAN FILTERS FOR MONITORING AND MITIGATION OF IONOSPHERIC SCINTILLATION IN GNSS RECEIVERS

Rafael Anderson Martins Lopes

Doctorate Thesis of the Graduate Course in Engineering and Space Technology/Spatial Mechanics and Control, guided by Drs. Hélio Koiti Kuga, and Felix Dieter Antreich, approved in June 02, 2022.

URL of the original document:
<http://urlib.net/8JMKD3MGP3W34T/473TT4E>

INPE

São José dos Campos

2022

LINEAR TIME-INVARIANT AND BAYESIAN FILTERS FOR MONITORING AND MITIGATION OF IONOSPHERIC SCINTILLATION IN GNSS RECEIVERS

Rafael Anderson Martins Lopes

Doctorate Thesis of the Graduate Course in Engineering and Space Technology/Spatial Mechanics and Control, guided by Drs. Hélio Koiti Kuga, and Felix Dieter Antreich, approved in June 02, 2022.

URL of the original document:
<http://urlib.net/8JMKD3MGP3W34T/473TT4E>

INPE

São José dos Campos

2022

INSTITUTO NACIONAL DE PESQUISAS ESPACIAIS

Serviço de Pós-Graduação - SEPGR

DEFESA FINAL DE TESE RAFAEL ANDERSON MARTINS LOPES
BANCA Nº 085/2022, REG 133205/2016.

No dia 02 de junho de 2022, as 09h00min, por teleconferência, o(a) aluno(a) mencionado(a) acima defendeu seu trabalho final (apresentação oral seguida de arguição) perante uma Banca Examinadora, cujos membros estão listados abaixo. O(A) aluno(a) foi APROVADO(A) pela Banca Examinadora, por unanimidade, em cumprimento ao requisito exigido para obtenção do Título de Doutor em Engenharia e Tecnologia Espaciais/Mecânica Espacial e Controle. O trabalho precisa da incorporação das correções sugeridas pela Banca e revisão final pelo(s) orientador(es).

Título Novo: "LINEAR TIME-INVARIANT AND BAYESIAN FILTERS FOR MONITORING AND MITIGATION OF IONOSPHERIC SCINTILLATION IN GNSS RECEIVERS'

Membros da Banca:

Dr. Mario César Ricci – Presidente – INPE
Dr. Hélio Koiti Kuga – Orientador – INPE
Dr. Felix Dieter Antreich – Orientador – ITA
Dr. Eurico Rodrigues de Paula – Membro Interno – INPE
Dr. Marcelo Gomes da Silva Bruno – Membro Externo – ITA
Dra. Roberta Veloso Garcia – Membro Externo - USP/Ciências Básicas e Ambientais.

Declaração de aprovação do membro estrangeiro Dr. Felix Dieter Antreich anexa ao processo.(10033455)

Documento assinado eletronicamente por **Helio Koiti Kuga (E)**, **Usuário Externo**, em 14/06/2022, às 13:25 (horário oficial de Brasília), com fundamento no § 3º do art. 4º do Decreto nº 10.543, de 13 de novembro de 2020.

Documento assinado eletronicamente por **Roberta Veloso Garcia (E)**, **Usuário Externo**, em 14/06/2022, às 13:51 (horário oficial de Brasília), com fundamento no § 3º do art. 4º do Decreto nº 10.543, de 13 de novembro de 2020.

Documento assinado eletronicamente por **MaRCELO GOMES DA SILVA BRUNO (E)**, **Usuário Externo**, em 14/06/2022, às 14:27 (horário oficial de Brasília), com fundamento no § 3º do art. 4º do Decreto nº 10.543, de 13 de novembro de 2020.

Documento assinado eletronicamente por **Mario Cesar Ricci**, **Tecnologista**, em 20/06/2022, às 15:29 (horário oficial de Brasília), com fundamento no § 3º do art. 4º do Decreto nº 10.543, de 13 de novembro de 2020.

Documento assinado eletronicamente por **Eurico Rodrigues de Paula**, **Pesquisador**, em 21/06/2022, às 11:45 (horário oficial de Brasília), com fundamento no § 3º do art. 4º do Decreto nº 10.543, de 13 de novembro de 2020.

A autenticidade deste documento pode ser conferida no site http://sei.mctic.gov.br/verifica.html, informando o código verificador **10012702** e o código CRC **CB1D2751**.

Referência: Processo nº 01340.002573/2022-01   SEI nº 10012702

ACKNOWLEDGEMENTS

ABSTRACT

The propagating radio signals emitted by the satellites forming the constellation of Global Navigation Satellite Systems (GNSS) interact with the electron content inside the ionosphere, resulting in scintillation. The ionospheric scintillation can have significant impact on the availability, accuracy, continuity, and integrity of the positioning for users of such systems. It is a source of disturbances impairing the signal processing implemented in the GNSS receivers, where the effects are more pronounced in their carrier tracking loops, with the induced amplitude and phase scintillation added to the input signals. The detection, monitoring, and mitigation of the scintillation effects are challenging from the signal processing perspective, and constitute relevant topics of research related to GNSS. This work presents contributions to the scintillation monitoring and the scintillation mitigation in GNSS receivers. Regarding scintillation monitoring, we propose an algorithm composed of linear time-invariant (LTI) filtering of observables available or easily derived in traditional or Kalman filter-based carrier tracking loop structures, exploiting their complementary frequency content, to provide real-time scintillation phase estimates for monitoring purposes. This algorithm is developed for receivers with traditional and Kalman frequency locked loops (FLL), but can be adapted to receivers with traditional and Kalman phase locked loops (PLL). The performance of the algorithm is evaluated via Monte Carlo simulations with synthetic severe scintillation data, showing its capability to provide the scintillation phase estimates. In addition, the algorithm is evaluated with real data presenting equatorial scintillation, collected by a professional GNSS receiver, where the scintillation phase standard deviation computed from the estimates provided by the real-time algorithm is compared to the standard deviation derived by state-of-the-art post-processing procedure, showing good agreement. Regarding scintillation mitigation, we propose two adaptive Kalman PLL structures employing radial basis function (RBF) networks to model the scintillation induced effects. In the first structure, the Kalman filter innovations are computed by the phase discriminator, and the scintillation phase estimates are provided, in addition to the robust carrier synchronization performed. In the second structure, the Kalman filter measurements are taken from the prompt correlator outputs, and a state feedback controller is designed to drive the carrier replica generation for robust synchronization. In this structure, the Kalman filter also estimates the scintillation amplitude. In both adaptive Kalman PLL structures, the weights of the RBF networks are estimated in real-time by recursive sliding window least squares, and the process and measurement noise covariance matrices of the Kalman filters are also updated in real-time. Monte Carlo simulations with synthetic severe scintillation data show the capability of the proposed Kalman PLLs to improve robustness to scintillation effects in carrier synchronization, presenting performance similar to the corresponding state-of-the-art structures employing the autoregressive (AR) scintillation models, with a slight advantage to the proposed structures with the RBF networks. The RBF networks allow to capture eventual nonlinear dynamics induced in the receiver by the ionospheric scintillation, an advantage in relation to

the linear AR models, at the expense of a more complex structure. Simulations with real scintillation data collected by a professional receiver highlight the learning and generalization capability of the RBF networks to cope with residual effects related to the receiver present in the data and evolving scintillation characteristics over time, with possibly nonlinear effects, with the Kalman PLL structures employing the RBF networks presenting reduced error when compared to the structures employing AR models.

Keywords: GNSS receivers. Carrier tracking loops. Ionospheric scintillation real-time monitoring. LTI filtering. Ionospheric scintillation mitigation. Bayesian filtering.

FILTROS LINEAR INVARIANTE NO TEMPO E BAYESIANO PARA MONITORAMENTO E MITIGAÇÃO DE CINTILAÇÃO IONOSFÉRICA EM RECEPTORES GNSS

RESUMO

Os sinais de rádio emitidos pelos satélites que formam a constelação de Sistemas Globais de Navegação por Satélite (GNSS) em propagação interagem com o conteúdo de elétrons da ionosfera, resultando em cintilação. A cintilação ionosférica pode ter impacto significativo na disponibilidade, acurácia, continuidade, e integridade do posicionamento de usuários de tais sistemas. É uma fonte de distúrbios que prejudicam o processamento de sinais implementado nos receptores GNSS, sendo que os efeitos são mais pronunciados em suas malhas de rastreio de portadora, com as cintilações induzidas de amplitude e fase adicionadas aos sinais de entrada. A detecção, o monitoramento, e a mitigação dos efeitos da cintilação são desafiadores do ponto de vista do processamento de sinais e constituem tópicos relevantes de pesquisa relacionada a GNSS. Este trabalho apresenta contribuições para o monitoramento e para a mitigação de cintilação em receptores GNSS. Em relação ao monitoramento de cintilação, propomos um algoritmo composto de filtragem linear invariante no tempo (LTI) de observáveis disponíveis ou facilmente calculadas em estruturas de malha de rastreio de portadora tradicionais ou baseadas em filtro de Kalman, explorando seu conteúdo complementar de frequência, para fornecer estimativas de fase de cintilação em tempo-real para fins de monitoramento. Este algoritmo é desenvolvido para receptores com malhas de captura de frequência (FLL) tradicionais e de Kalman, mas pode ser adaptado a receptores com malhas de captura de fase (PLL) tradicionais e de Kalman. O desempenho do algoritmo é avaliado através de simulações de Monte Carlo com dados sintéticos de cintilação severa, mostrando sua capacidade de fornecer as estimativas da fase de cintilação. Além disso, o algoritmo é avaliado com dados reais apresentando cintilação equatorial, coletados por um receptor GNSS profissional, onde o desvio padrão da fase de cintilação calculado a partir das estimativas fornecidas pelo algoritmo de tempo-real é comparado ao desvio padrão calculado pelo procedimento de pós-processamento de estado-da-arte, mostrando boa concordância. Em relação à mitigação de cintilação, propomos duas estruturas adaptativas de Kalman PLL empregando redes de funções de base radial (RBF) para modelar os efeitos induzidos por cintilação. Na primeira estrutura, as inovações do filtro de Kalman são computadas pelo discriminador de fase, e as estimativas de fase de cintilação são fornecidas, além da sincronização robusta de portadora realizada. Na segunda estrutura, as medidas do filtro de Kalman são tomadas a partir das saídas do correlacionador alinhado no tempo, e um controlador de realimentação de estados é projetado para conduzir a geração de réplica da portadora para sincronização robusta. Nesta estrutura, o filtro de Kalman também estima a amplitude de cintilação. Em ambas as estruturas adaptativas Kalman PLL, os pesos das redes RBF são estimados em tempo-real por mínimos quadrados recursivos com janela deslizante, e as matrizes de covariância de ruídos de processo e medida dos filtros de Kalman também são atualizadas em tempo-real. Simulações de Monte Carlo com dados sintéticos de cintilação severa mostram a capacidade das Kalman PLLs propostas para melhorar a robustez aos efeitos de cintilação na

sincronização de portadora, apresentando desempenho semelhante ao das estruturas de estado-da-arte correspondentes que empregam modelos autorregressivos (AR) de cintilação, com um ligeira vantagem para as estruturas propostas com as redes RBF. As redes RBF permitem capturar eventuais dinâmicas não-lineares induzidas no receptor pela cintilação ionosférica, uma vantagem em relação aos modelos AR lineares, à custa de uma estrutura mais complexa. Simulações com dados reais de cintilação coletados pelo receptor profissional destacam a capacidade de aprendizado e generalização das redes RBF para lidar com efeitos residuais relacionados ao receptor presentes nos dados e com a evolução das características da cintilação ao longo do tempo, com efeitos possivelmente não-lineares, com as estruturas Kalman PLL empregando as redes RBF apresentando erro reduzido quando comparadas às estruturas empregando modelos AR.

Palavras-chave: Receptores GNSS. Malhas de rastreio de portadora. Monitoramento em tempo-real de cintilação ionosférica. Filtragem LTI. Mitigação de cintilação ionosférica. Filtragem Bayesiana.

LIST OF FIGURES

LIST OF TABLES

LIST OF ABBREVIATIONS

ADC   – Analog-to-digital converter
AGC   – Automatic gain control
AIC   – Akaike Information Criterion
AR   – Autoregressive
ARMA   – Autoregressive moving average
BB   – Baseband
BIC   – Bayesian Information criterion
BOC   – Binary offset carrier
BPSK   – Binary phase shift keying
C/A   – Coarse/aquisition
CDMA   – Code division multiple access
COTS   – Commercial off-the-shelf
CSM   – Cornell Scintillation Model
CT   – Continuous time
D-GNSS   – Differential GNSS
DLL   – Delay locked loop
DLR   – German Aerospace Center
DS-CDMA   – Direct Sequence Code Division Multiple Access
DSP   – Digital signal processing
DSSS   – Direct sequence spread spectrum
DT   – Discrete time
ERR   – Error Reduction Ratio
FDMA   – Frequency division multiple access
FLL   – Frequency locked loop
GISM   – Global Ionospheric Scintillation Model
GNSS   – Global Navigation Satellite Systems
GPS   – Global Positioning System
I&D   – Integrate and dump
IF   – Intermediate frequency
INPE   – Brazilian Institute for Space Research
I/Q   – In-phase/quadrature
LNA   – Low noise amplifier
LO   – Local oscillator
LOS   – Line-of-sight
LS   – Least squares
LTI   – Linear time-invariant
MA   – Multiple access
MAP   – Maximum *a posteriori*
MMSE   – Minimum mean square error
NAV   – Navigation solution algorithm

NCO	–	Numerically controlled oscillator
OS	–	Open service
PAF	–	Partial autocorrelation function
PLL	–	Phase locked loop
PPP	–	Precise point positioning
PR	–	Pseudo-random
PRN	–	Pseudo-random noise
PVT	–	Position, velocity and timing
QPSK	–	Quadrature phase shift keying
RBF	–	Radial basis function
RF	–	Radio frequency
RMSE	–	Root mean square error
RMSS	–	Root mean of sum of squares
RTK	–	Real-time kinematics
SDR	–	Software-defined radio
SW	–	Software
TDMA	–	Time division multiple access
UFC	–	Universidade Federal do Ceará
UHF	–	Ultra High Frequency
WBMOD	–	WideBand Model
WSCS	–	Wide-sense cyclostationary

CONTENTS

1 INTRODUCTION

In Global Navigation Satellite Systems (GNSS), the position of a user is determined by measurements of the ranges from satellites emitting signals via radio waves to the user's receiver. The processing of the signals emitted by the different in-view satellites forming the GNSS constellation in a GNSS receiver allows the computation of the ranges, and by knowing the ranges to a sufficient number of satellites and also their position, the user position can be obtained.

The basic idea behind the estimation of the range to each satellite is to compute the time taken by a signal emitted by a satellite to be detected by the receiver, considering the signal is traveling at the speed of light. If the receiver clock would be synchronized with the system time, then the knowledge of the ranges to three different satellites would be sufficient to determine the position of a receiver being on the surface of the Earth. However, the offset between the system time and the receiver clock must also be accounted for, requiring the estimation of the range to a fourth satellite to remove the influence of this clock bias from the positioning, if we assume that the satellite clocks are all perfectly synchronized with the system time.

Basically, the receiver is performing the task of signal synchronization prior to the positioning. The synchronization involves the acquisition and tracking of the signals emitted by the satellites in the so-called receiver processing channels. In acquisition, the visible satellites are identified and coarse estimates of Doppler frequency shift and code delay are provided to initialize the carrier and code tracking, respectively. Carrier and code tracking are traditionally performed in closed loop by, respectively, phase locked loop (PLL) and delay locked loop (DLL), furnishing the internal observables employed in the range estimation and positioning. Alternatively, a frequency locked loop (FLL) can be used for carrier tracking or to provide an augmentation signal to a PLL (KAPLAN; HEGARTY, 2017).

Many sources of error can contribute to increase the error of the positioning solution, such as atmospheric propagation errors in the signals emitted by the satellites of the GNSS constellation, errors in the knowledge of the ephemerides of the satellites, multipath of the signals incoming to the receiver, and others.

Regarding the atmospheric propagation errors, the ionosphere is a dispersive medium for radio waves, where the refractive index is a function of the frequency. It is a region of the atmosphere that extends from about 50 km to 1000 km of altitude where the solar activity, especially, contributes to the existence of free electrons that affect the

propagation of radio waves (TEUNISSEN; MONTENBRUCK, 2017).

The interaction of transient fluctuations of electron content inside the ionosphere with the propagating radio waves via refraction and diffraction results in scintillation of radio signals. These fluctuations depend on factors such as solar activity, geomagnetic activity, location, daytime (MORAES et al., 2012). They are generated by different physical processes depending on these factors, such as plasma dynamics, electron density gradients, ionization and recombination process induced by the daily solar activity (ALFONSI et al., 2011),(TEUNISSEN; MONTENBRUCK, 2017). For GNSS in particular, ionospheric scintillation can have a significant impact on the availability, accuracy, continuity, and integrity of the positioning with such systems.

Regarding the carrier of the GNSS signals, ionospheric irregularities are one source of amplitude and phase scintillations adding up to the line-of-sight (LOS) dynamics, which is the dynamics of the movement of the line-of-sight vector from a receiver to a GNSS satellite, reflected in the phase evolution related to the Doppler effect in the carrier tracking loops of the receiver. The scintillation introduces disturbances to the GNSS tracking algorithms in the receiver that in many cases cause a reduction of precision in the positioning and eventually the loss of lock of the satellite signals. Such disturbances are more prominent in high-latitude and equatorial regions of the Earth, mainly associated with the magnetic poles and the equatorial magnetic anomaly, respectively, and manifest in different ways. While at high latitudes the effect is in general milder and more frequently observed in the phase (JIAO et al., 2013a), the equatorial region experiences the most significant activity including rapid amplitude and phase scintillations with deep amplitude fades for short periods of time (VILÁ-VALLS et al., 2020). The ionospheric scintillation effects are generally observed after the sunset.

The detection, monitoring and mitigation of ionospheric scintillation effects in receivers are relevant topics of research related to GNSS. They constitute challenging problems in GNSS receivers from the signal processing point of view (VILÁ-VALLS et al., 2020). Ionospheric scintillation monitoring contributes to the scientific research of the ionosphere, where networks of spatially distributed monitoring stations provide data to support the study of the dynamics of the related physical processes. Monitoring stations are deployed for other purposes also, such as for space weather research (XU et al., 2015a), as part of the infrastructure for aircraft instrument landing systems (MAYER et al., 2009), or any other GNSS application where ionospheric scintillation poses a major threat, performing forecast and broadcast of information

used by the target application. In the monitoring stations, usually a reliable and precise receiver in a known position provides estimates of the LOS dynamics using additional accurate information, so the scintillation induced effects can be isolated from the LOS dynamics tracked by the receivers (LEE et al., 2017), (DIERENDONCK et al., 1993). We further discuss about scintillation monitoring in Chapter 4.

In the ionospheric scintillation mitigation problem, the intent is to increase the receiver robustness to the scintillation induced effects in the carrier tracking loops, improving the availability, continuity and the accuracy of the estimates provided by the carrier tracking loop. High availability, continuity and accuracy in the carrier tracking is vital for modern receivers applying carrier-based positioning techniques, such as real-time kinematics (RTK) and precise point positioning (PPP) (JACOBSEN; ANDALSVIK, 2016), (BANVILLE; LANGLEY, 2013). Originally, the traditional PLLs and FLLs have fixed parameters adjusted for LOS-only tracking, not directly handling the disturbance of the scintillation induced effects. A first attempt to improve robustness in these structures is to tune their parameters such as noise bandwidth in PLLs (LEGRAND et al., 2000) or use a PLL assisted by an augmentation signal of a FLL (XU et al., 2015b). However, the Kalman filter has been successfully employed in the carrier tracking loop with the intent of scintillation mitigation, from the early applications with static Kalman gains obtained by the solution of the steady-state Riccati equation (STATMAN; HURD, 1990), to the state-of-the-art extended Kalman PLLs which explicitly account for the scintillation induced effects, along with the LOS dynamics, with phase and amplitude scintillation modeled as autoregressive (AR) processes and adaptive update of model parameters and process and measurement noise covariance matrices (VILÁ-VALLS et al., 2018). We further discuss about state-of-the-art scintillation mitigation in Chapter 5.

In this work we propose algorithms for scintillation monitoring and for scintillation mitigation. Regarding ionospheric scintillation monitoring, the typical approach found in the literature consists of the batch post-processing of data collected by a GNSS receiver, where scintillation amplitude and phase metrics are computed from phase and amplitude estimates obtained after post-processing of the stored data (DIERENDONCK et al., 1993), (FREMOUW et al., 1978), (ZHANG et al., 2010), (FORTE, 2007), (O'HANLON et al., 2011), (NIU et al., 2012). Our approach is to explore a linear approximation of a traditional FLL, evaluating its frequency content characteristics, to recover the complementary information in the frequency domain based on its sensitivity and complementary sensitivity transfer functions from internal observables, to design a real-time scintillation monitoring algorithm based on linear

time-invariant (LTI) filtering. The algorithm provides estimates of the scintillation phase, from which the scintillation phase metrics can be computed also in real-time. The parameters of the filters can be adjusted to delimit the frequency band of interest, as is also typically done in the batch post-processing with Butterworth filters, as well. The approach is extended to LOS-only Kalman FLLs by analogy with the traditional FLL, and then to LOS-only traditional and Kalman PLLs. The performance of the algorithm is evaluated by numerical simulations with synthetic scintillation data and real scintillation data collected by a commercial off-the-shelf (COTS) professional GNSS receiver located close to the magnetic equator in Fortaleza, Brazil.

Regarding the problem of ionospheric scintillation mitigation, we propose two Kalman filter PLL structures employing radial basis functions (RBF) networks (POWELL, 1985), (HARDY, 1971), (BROOMHEAD; LOWE, 1988) to model scintillation dynamics, for carrier synchronization with increased robustness to scintillation induced effects. We call these structures discriminator-based Kalman PLL and correlator-based Kalman PLL. In the discriminator-based Kalman PLL, the residuals are taken from the phase discriminator, and the scintillation phase model is added to the LOS dynamics model. In the correlator-based Kalman PLL, the observations are obtained from the in-phase/quadrature (I/Q) prompt correlators and both the scintillation phase and amplitude models are added to the LOS dynamics model. We propose to use RBF networks to model scintillation phase and amplitude dynamics, instead of the AR models, as suggested in the literature. The nonlinear radial basis functions provide more flexibility to capture nonlinear dynamics eventually present in the phase and amplitude scintillation. The performances of the proposed Kalman PLLs are evaluated by numerical simulations with synthetic scintillation data and real scintillation data collected by a commercial GNSS receiver.

Thesis outline

This thesis consists of six chapters. After presenting above the motivations and the proposed contributions of the work in this introductory **Chapter 1**, in **Chapter 2** we present the basic signal model of the GNSS receiver used in the subsequent chapters, describing the structure of the GNSS signal emitted by the satellites employing Direct Sequence Code Division Multiple Access (DS-CDMA) technique to the transmission channel access, and specializing to the Global Positioning System (GPS) signal, which will be used throughout the thesis. The baseband (BB) signal model in the receiver is then presented for the GPS at L1 frequency coarse/acquisition (C/A) code, including the terms related to the ionospheric scintillation induced effects. We

also present the model of the LOS dynamics, related to the Doppler dynamics, of GPS satellites with respect to a static receiver positioned on ground, and the metrics largely accepted to evaluate the severity of the scintillation activity.

In **Chapter 3**, we present a review of the stochastic processes and Itô stochastic differential equations, and the AR and the kinematic process models, used to model scintillation and LOS dynamics, respectively, in the state-of-the-art Kalman filters. Then, the derivation of the Bayesian nonlinear filter is presented, which is specialized to the Kalman filter in the following.

In **Chapter 4** we present the first contribution of the work, a real-time monitoring algorithm. Firstly, we present the linear approximation of a traditional FLL, which is compared to the nonlinear traditional FLL via numeric simulations considering the response to initial conditions and the response to sinusoidal inputs. Then, we explore the frequency domain characteristics of the linear model, especially the characteristics of the sensitivity and complementary sensitivity of the closed loop, to design the filters that compose the real-time monitoring algorithm. The monitoring algorithm is extended to Kalman FLLs, traditional PLLs and Kalman PLLs. Its performance is evaluated via Monte Carlo simulations including synthetic severe scintillation variations and via simulations with real scintillation data collected by a commercial GNSS receiver.

In **Chapter 5** we present the second contribution of the work, two Kalman PLL structures for scintillation mitigation employing RBF networks to model the amplitude and phase scintillation. The modeling of the mitigation problem for both the discriminator-based and correlator-based Kalman PLLs is presented, first considering the AR models to represent scintillation dynamics, and then substituting them by the RBF networks. The Kalman PLLs employing the RBF networks are evaluated via Monte Carlo simulations with synthetic severe scintillation data and via simulation with real scintillation data. Their performance is compared to the performance of the state-of-the-art Kalman PLLs with scintillation modeled by AR processes. In **Chapter 6**, a summary and the conclusions of the work are presented.

2 MODELING IONOSPHERIC SCINTILLATION EFFECTS ON GNSS RECEIVERS

This chapter presents the signal model employed throughout the work. This model considers typical characteristics of a GNSS signal received by a GNSS receiver, the typical signal processing implemented in the tracking loops of a GNSS receiver, the Doppler effect and the ionospheric scintillation induced effects. The derived signal model is employed in the design and analysis of the ionospheric scintillation monitoring and mitigation algorithms, which are presented in Chapter 4 and Chapter 5, respectively.

First, the overall GNSS signal and GNSS receiver structures are presented. In this work, we consider only the GPS L1 C/A code signal by taking into account the analog operations of the front-end up to the signal quantization. The digital signal processing implemented in a receiver is presented, and also the signal model including the ionospheric scintillation induced effects. We discuss the Doppler effect based on the LOS dynamics of GPS satellites to a static receiver positioned on ground. Then, the characteristics of the ionospheric scintillation induced effects are presented, relevant to the signal processing implemented in the receiver, describing the typical parameters and indexes largely accepted to evaluate scintillation activity. Lastly, we describe the adopted model to generate the synthetic scintillation data used in the numerical simulations throughout this work.

2.1 GNSS signal model

The positioning in a GNSS receiver is obtained by range measurements from the receiver to different in-view satellites from the GNSS constellation. If the system time scale, the receiver clock and also all satellite clocks are synchronized to the system time scale, and the ephemerides of the satellites are known, then the range estimates based on the signals emitted by three satellites of the constellation allows to determine the receiver position in three dimensions with the ambiguity of two points: the intersection of two satellite-centered spheres is a circle, and the intersection of this circle with a sphere centered at the third satellite is a set with two points. Ambiguity would be resolved with the introduction of an additional ranging signal from a fourth satellite. In fact, the receiver clock is not perfectly synchronized to the system time scale, and this timing bias must be determined as well, requiring the measurement of a ranging signal emitted by a fifth satellite. For a receiver positioned on ground, Earth can act as one of the spheres, so only four satellites can be used in the computation of the positioning solution. Individual ranging er-

rors to each satellite due to several sources, such as atmospheric propagation errors and ephemeris errors, contribute to delimit a region of uncertainty around the true receiver position.

The ranging signals emitted by the GNSS satellites share a common transmission medium or channel. Different multiple access (MA) techniques can be employed to share the transmission medium or channel. The basic techniques employed are: frequency division multiple access (FDMA), time division multiple access (TDMA) and code division multiple access (CDMA) (HAYKIN, 2014). In FDMA, multiple carrier frequencies are used to transmit multiple signals. In TDMA, each signal is transmitted in its respective time slot. Finally, in CDMA, different spreading codes are used to allow the sharing of a common carrier frequency (KAPLAN; HEGARTY, 2017). A combination of these techniques can also be employed. Most existing GNSS use direct sequence spread spectrum (DSSS) CDMA, or DS-CDMA (LEE; MILLER, 1998), where each satellite uses a different code sequence for transmitting its signal, and most existing systems use different carrier frequencies allocated in L-band, but S-band is also used (KAPLAN; HEGARTY, 2017).

Employing the spreading symbols in the direct sequence enables precise ranging due to the frequent phase inversions in the signals. It also enables multiple satellites to transmit signals simultaneously and at the same carrier frequency, and further provides significant rejection of narrow band interference (KAPLAN; HEGARTY, 2017). Pseudo-random (PR) or pseudo-random noise (PRN) binary sequences (SIMON et al., 1994), which are periodic and can be assumed to be zero mean wide-sense cyclostationary (WSCS) (PAPOULIS; PILLAI, 2002), are typically employed as code or spreading sequences. They can be described by

$$c(t) = \sum_{i=-\infty}^{\infty} d_i \sqrt{T_c} \delta(t - iT_c) * p(t), \qquad (2.1)$$

where $\{d_i\} \in \{-1, 1\}$ is a PR sequence, T_c is the chip period, $\delta(t)$ is the Dirac delta, $*$ is the convolution symbol, and $p(t)$ is the chip pulse shape. The periodic direct sequence $c(t)$ is composed of N_d chips, with period $T = N_d T_c$, considering it is employed in an open service (OS) signal (KAPLAN; HEGARTY, 2017). Restricted-use signals use ranging codes that are encrypted and thus are aperiodic (KAPLAN; HEGARTY, 2017). For example, in baseline (nonmodernized) GPS satellites, two direct PR sequences are generated with rectangular chip pulse shapes: the C/A code and the precision P(Y) code. The C/A sequence is a Gold sequence (GOLD, 1967) with $N_d = 1023$ chips and period $T = 1$ ms, so the chipping rate is 1.023×10^6

chips per second. The P(Y) is generated with a period of several days, but reset each week, with a chipping rate of 10.23×10^6 chips per second. The chip pulse shape is not constrained to specific shapes, although the rectangular pulse $p_R(t)$ is the more commonly employed chip pulse shape. It can be described by

$$p_R(t) = \frac{1}{\sqrt{T_c}} \left[U \left(t + \frac{T_c}{2} \right) - U \left(t - \frac{T_c}{2} \right) \right],$$

(2.2)

where $U(t)$ is the unit step or Heaviside's unit step function, with

$$U(t) = \begin{cases} 0, t < 0 \\ 1, t \geq 0 \end{cases}.$$

(2.3)

The binary offset carrier (BOC) became standard in GNSS signals design (BETZ, 2002), (REBEYROL, 2007), (HEGARTY et al., 2004), and their chip pulse shapes are generated by a multiplication of a rectangular pulse and a square wave subcarrier. A $BOC(n_S, n_C)$ signal is parametrized by the n_S subcarrier rate and the n_C chip rate. If the cosine function is used to generate the square wave, instead of the sine function, the direct sequence is represented by $BOC_{cos}(n_S, n_C)$. Composite signals can also be formed by linear combination of BOC signals (TEUNISSEN; MONTENBRUCK, 2017).

The GNSS ranging signals emitted by the satellites are bandpass signals composed of the modulation of a radio frequency (RF) carrier with the direct sequence in the case of DS-CDMA. The carrier frequency will be allocated in the L band for most GNSS signals. Navigation data can also be included in the modulation, although in more modern GNSS signals, as Galileo OS, the total power is split into two components, the data and the pilot. In this case, the pilot component is not modulated by the navigation data, but both are modulated by a spreading signal. Modulation with the navigation data is a digital modulation, generated by binary phase shift keying (BPSK), with 180° phase shifts in navigation bit transitions (SIMON et al., 1994). Two binary DS signals can be combined at the same frequency using quadrature phase shift keying (QPSK), where two carriers with a phase difference of 90° are used in the modulation of the two DS signals and then added together. Other multiplexing techniques can be employed as well to accommodate more than two signals on one carrier while in most cases achieving a constant-envelope signal (SPILKER JUNIOR, 1977), (BUTMAN; TIMOR, 1972), (TIMOR, 1972), (DAFESH et al., 1999).

This work deals with the ionospheric scintillation induced effects on the GNSS receivers in baseband. Henceforth, we consider the GPS C/A code signal transmitted

on the L1 carrier frequency $f_{L1} = 1575.42$ MHz in the remainder of the work, so that in the following only the ranging signal emitted by GPS satellites is described to obtain the BB signal processed by a GNSS receiver, without loss of generality.

A simplified block diagram of a GNSS receiver is shown in Figure 2.1. In the front-end side of the receiver, the antenna is the first element in the received signal path. Characteristics of the antennas used in GNSS receivers can be found in antenna theory textbooks, such as (STRAW, 2003), (BALANIS, 1996), (TSUI, 2000). The signal is amplified in a first stage by the low noise amplifier (LNA), then is mixed with the signal generated by the local oscillator (LO) to downconvert the carrier frequency to an intermediate frequency (IF), which could be zero if the received signal is to be translated to baseband. Downstream, the signal is low pass and/or band-pass filtered and then sampled by the analog-to-digital converter (ADC). In the software (SW) based side of the receiver or in a software-defined radio (SDR) receiver, the discrete I/Q samples at IF or BB frequencies from the front-end ADC are the input signals to be processed by the implemented digital signal processing (DSP) algorithms to track the ranging signals and compute the observables needed by the navigation solution algorithm (NAV) to compute the position, velocity and timing (PVT) information. In the diagram of Figure 2.1 we solely considered a SDR receiver since the scope of the work is the digital signal processing employing estimation algorithms including Bayesian estimation.

Figure 2.1 - Simplified schematic of a GNSS receiver.
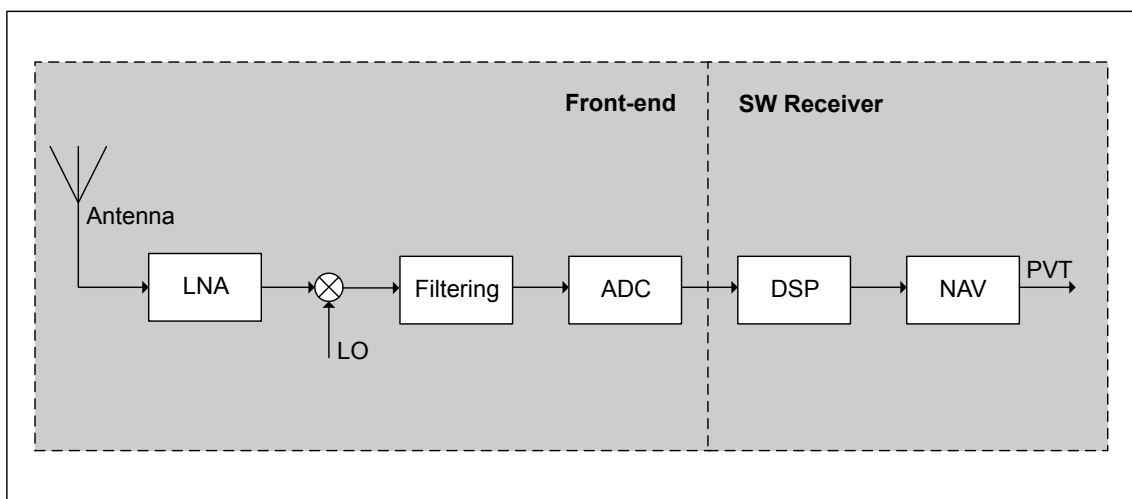
SOURCE: Author's production.

Considering a narrow band-pass filter around the C/A code frequency in the front-end, the P(Y) code content is distorted (BORRE et al., 2007). After downconversion to an intermediate frequency in the front-end and disregarding this P(Y) code content and noise component, the GPS L1 C/A code signal from one satellite can be given as the real signal

$$s_{IF}(t) = A(t)g(t - \tau(t))c(t - \tau(t))\cos[2\pi f_{IF}t + \phi_T(t)], \qquad (2.4)$$

where $A(t)$ is the signal amplitude, $g(t - \tau)$ and $c(t - \tau)$ are, respectively, the navigation data and the C/A code delayed by $\tau(t)$, f_{IF} is the intermediate frequency (IF) in Hz, and $\phi_T(t)$ is the total carrier phase, including Doppler, reference oscillator offset, and other sources of phase variations, such as ionospheric scintillation. This IF signal downconverted to baseband and filtered by a low pass filter with single-sided bandwidth B in the front-end, prior to the quantization, has the following complex I/Q components

$$\begin{cases} I(t) = A(t)g(t - \tau(t))c(t - \tau(t))\cos(\phi_T(t)) + n_I(t) \\ \quad = A(t)g(t - \tau(t))c(t - \tau(t))\cos(\phi_D(t) + \phi(t)) + n_I(t) \\ Q(t) = A(t)g(t - \tau(t))c(t - \tau(t))\sin(\phi_T(t)) + n_Q(t) \\ \quad = A(t)g(t - \tau(t))c(t - \tau(t))\sin(\phi_D(t) + \phi(t)) + n_Q(t), \end{cases} \qquad (2.5)$$

where $\phi_D(t)$ is the phase component related to the Doppler frequency shift due to the relative velocity between the GPS satellite and the receiver, and $\phi(t)$ is the phase component that includes all other sources of phase variations. Therefore, the complex BB signal is

$$s(t) = I(t) + jQ(t), \qquad (2.6)$$

and $n_I(t) \in \mathbb{R}$ and $n_Q(t) \in \mathbb{R}$ are the independent noise processes of the complex Gaussian white noise

$$n(t) = n_I(t) + jn_Q(t), \qquad (2.7)$$

each with power spectral density with value $N_0/2$.

Disregarding the navigation message $g(t - \tau(t))$, the I/Q components can be given by

$$\begin{cases} I(t) = A(t)c(t - \tau(t))\cos(\phi_T(t)) + n_I(t) \\ Q(t) = A(t)c(t - \tau(t))\sin(\phi_T(t)) + n_Q(t). \end{cases} \qquad (2.8)$$

Considering only a scintillation induced term as a source of disturbance, multiplica-

11

tive in amplitude and additive in phase $\rho(t)e^{j\phi(t)}$, the signal amplitude can be written as

$$A(t) = A_0(t)\rho(t), \tag{2.9}$$

where $A_0(t)$ is the undisturbed amplitude, and the signal total phase can be written as

$$\phi_T(t) = \phi_D(t) + \phi(t), \tag{2.10}$$

disregarding other sources of phase variations in $\phi(t)$. The phase $\phi_D(t)$ is the integral of the angular Doppler frequency $f_D(t)$

$$\phi_D(t) = \int_{t_0}^{t} f_D(\tilde{t}) \, d\tilde{t}, \tag{2.11}$$

which can be approximated by a Taylor series in a sufficiently short period of time in relation to the LOS dynamics. Truncation of the series after the second order term can represent constant Doppler frequency drift in the LOS signal, and yields

$$\phi_D(t) = \phi_D(t_0) + f_D(t_0)(t - t_0) + (1/2)a_D(t_0)(t - t_0)^2, \tag{2.12}$$

where $a_D(t)$ is the Doppler frequency drift. The complex BB signal (2.6) sampled with sampling frequency $f_s = \frac{1}{T_s} = 2B$, $n = 0, \ldots, N-1$, and $k = 0, 1, 2, \ldots, \in \mathbb{Z}^+$ can be given as

$$\begin{aligned} s((kN + n)T_s) =& A((kN + n)T_s) \, c((kN + n)T_s - \tau((kN + n)T_s)) \\ & e^{j\phi_T((kN+n)T_s)} + n((kN + n)T_s), \end{aligned} \tag{2.13}$$

where $N = f_s T_I$ samples are collected for the kth coherent integration period of duration T_I. The fast functions of the receiver, such as carrier and code wipe-off, are performed at f_S. Assuming that $A(t)$, $\phi(t)$, $f_D(t)$, and $\tau(t)$ are approximately constant over one coherent integration period, the discrete input sequence can be written in vector form as

$$\mathbf{s}[k] = A[k]e^{j\phi[k]}(\mathbf{c}[k; \tau[k]] \odot \mathbf{d}[k; f_D[k]]) + \mathbf{n}[k], \tag{2.14}$$

where

$$\mathbf{s}[k] = [s(kNT_s), \ldots, s((kN + N - 1)T_s)]^{\mathrm{T}}, \tag{2.15}$$

$$\mathbf{n}[k] = [n(kNT_s), \ldots, n((kN + N - 1)T_s)]^{\mathrm{T}}, \tag{2.16}$$

$$\mathbf{c}[k; \tau[k]] = [c(kNT_s - \tau[k]),$$
$$\ldots, c((kN + N - 1)T_s - \tau[k])]^{\mathrm{T}}, \tag{2.17}$$

$$\mathbf{d}[k; f_D[k]] = \left[e^{j\phi_D[k]}, \ldots, e^{j(f_D[k](N-1)T_s + \phi_D[k])}\right]^{\mathrm{T}}, \tag{2.18}$$

and $\odot$ denotes element-by-element multiplication of two vectors (Hadamard-Schur product).

Before the despreading, all operations have to be performed on the data with a rate of f_S. After correlation or despreading, all operations can be performed with a significantly smaller rate. The coherent integration time T_I defines this rate of operations and the tracking loops.

The result of the prompt correlation with the code $\mathbf{c}[k; \hat{\tau}[k]]$ generated by an estimate of the time-delay $\hat{\tau}[k]$ after mixing with the carrier $\mathbf{d}[k; \hat{f}_D[k]]$ generated by Doppler phase $\hat{\phi}_D[k]$ and frequency $\hat{f}_D[k]$ estimates can be given by

$$y[k] = \frac{1}{N}(\mathbf{c}[k; \hat{\tau}[k]] \odot \mathbf{d}[k; \hat{f}_D[k]])^{\mathrm{H}}\mathbf{s}[k], \tag{2.19}$$

where $^{\mathrm{H}}$ denotes Hermitian of a matrix or vector. Other algorithms can be used for the signal mixing with the carrier replica generated by the receiver (KAPLAN; HEGARTY, 2017).

Considering that $\tau[k] \approx \hat{\tau}[k]$ we get

$$y[k] = \frac{A[k]}{N} e^{j(\phi[k] + \phi_D[k] - \hat{\phi}_D[k])} \sum_{n=0}^{N-1} e^{j(f_D[k] - \hat{f}_D[k])nT_s} + \eta_D[k]. \tag{2.20}$$

The zero-mean complex white Gaussian noise sequence $\eta_D[k]$ has variance $\sigma_{\eta_D}^2 = \sigma_n^2/N$, where $\sigma_n^2 = 2BN_0$ is the variance of $n((kN + n)T_s)$. With $\delta\phi_D[k] = \phi_D[k] - \hat{\phi}_D[k]$ and $\delta f_D[k] = f_D[k] - \hat{f}_D[k]$ we get [1]

$$y[k] = \frac{A[k]}{N}\frac{\sin(N\delta f_D[k]T_s/2)}{\sin(\delta f_D[k]T_s/2)}e^{j(\phi[k] + \delta\phi_D[k])} \tag{2.21}$$

$$e^{j[(N-1)T_s/2]\delta f_D[k]} + \eta_D[k].$$

---

[1] $\sum_{n=0}^{N-1} e^{jnz} = \frac{\sin(Nz/2)}{\sin(z/2)}e^{j(N-1)z/2}$, with $z = \delta f_D[k]T_s$.

Substituting $T_s = T_I/N \approx T_I/(N-1)$ yields

$$y[k] = \frac{A[k]}{N} \frac{\sin(\delta f_D[k]T_I/2)}{\sin(\delta f_D[k]T_I/2N)} e^{j(\phi[k]+\delta\phi_D[k])} \tag{2.22}$$

$$e^{j(T_I/2)\delta f_D[k]} + \eta_D[k].$$

Assuming that $\delta f_D[k]T_I/2N$ is sufficiently close to zero, $\sin(\delta f_D[k]T_I/2N) \approx \delta f_D[k]T_I/2N$, and we can derive an approximate expression for the prompt correlator output after mixing with the carrier generated by the receiver as [2]

$$y[k] = A[k]\mathrm{sinc}\left(\frac{\delta f_D[k]T_I}{2\pi}\right) e^{j(\phi[k]+\delta\phi_D[k])} \tag{2.23}$$

$$e^{j(T_I/2)\delta f_D[k]} + \eta_D[k].$$

If $|\delta f_D[k]T_I| \ll 1$, $\mathrm{sinc}\left(\frac{\delta f_D[k]T_I}{2\pi}\right) \approx 1$. For an unitary amplitude of the carrier undisturbed by scintillation, $A[k] = \rho[k]$. Thus, we can write the I/Q components of $y[k] = y_I[k] + jy_Q[k]$ as

$$\begin{cases} y_I[k] = \rho[k]\cos\left(\phi[k] + \delta\phi_D[k] + \dfrac{T_I}{2}\delta f_D[k]\right) \\ \qquad + \eta_{D_I}[k] \\ y_Q[k] = \rho[k]\sin\left(\phi[k] + \delta\phi_D[k] + \dfrac{T_I}{2}\delta f_D[k]\right) \\ \qquad + \eta_{D_Q}[k], \end{cases} \tag{2.24}$$

with $\sigma_{\eta_{D_I}}^2 = \sigma_{\eta_{D_Q}}^2 = \sigma_{\eta_D}^2/2$. Further simplifying, by disregarding the term in $\delta f_D[k]$, we get

$$\begin{cases} y_I[k] = \rho[k]\cos\left(\phi[k] + \delta\phi_D[k]\right) + \eta_{D_I}[k] \\ y_Q[k] = \rho[k]\sin\left(\phi[k] + \delta\phi_D[k]\right) + \eta_{D_Q}[k]. \end{cases} \tag{2.25}$$

Application of the four quadrant arctangent $\varepsilon_P[k] = \mathrm{atan2}[y_Q[k], y_I[k]]$ yields

$$\varepsilon_P[k] = \phi[k] + \delta\phi_D[k] + \eta_A[k], \tag{2.26}$$

where $\eta_A[k]$ is the noise at the output of the four quadrant arctangent. Its variance $\sigma_{\eta_A}^2$ can be computed by the approximate expression (PARKINSON; SPILKER JR., 1996), (LUO et al., 2017)

$$\sigma_{\eta_A}^2 = \frac{1}{2c/n_0 T_I}\left(1 + \frac{1}{2c/n_0 T_I}\right), \tag{2.27}$$

---

[2]$\mathrm{sinc}(t) = \sin(\pi t)/(\pi t)$.

where c/n_0 is defined as the carrier-to-noise density ratio in Hz, obtained from C/N$_0$, which is defined as the carrier-to-noise density ratio in dB-Hz, as $c/n_0 = 10^{C/N_0/10}$. An estimation of the rate of $\varepsilon_P[k]$ can be obtained by the frequency discriminator (TEUNISSEN; MONTENBRUCK, 2017)

$$\varepsilon_D[k] = \frac{\text{atan2}\,[cross, dot]}{T_I} = \frac{\varepsilon_P[k] - \varepsilon_P[k-1]}{T_I} \quad (2.28)$$

where $cross = y_Q[k]y_I[k-1] - y_Q[k-1]y_I[k]$ and $dot = y_I[k]y_I[k-1] + y_Q[k]y_Q[k-1]$. The noise variance of the frequency discriminator $\sigma^2_{\eta_B}$ can be obtained from the above expression, as (LUO et al., 2017)

$$\sigma^2_{\eta_B} = \frac{\sigma^2_{\eta_A} + \sigma^2_{\eta_A}}{T_I^2} = \frac{1}{c/n_0 T_I^3}\left(1 + \frac{1}{2c/n_0 T_I}\right). \quad (2.29)$$

2.2 Doppler geometry

Considering a Keplerian orbit with null eccentricity for one GPS satellite with height $h = 20184$ km, its velocity magnitude is, approximately

$$v = \sqrt{\frac{\mu_E}{h + R_E}} \approx 3.87 \text{ km/s}, \quad (2.30)$$

where $\mu_E = 3.986 \times 10^5$ km^3/s^2 is the Earth's standard gravitational parameter and $R_E = 6378$ km is the mean radius of the Earth. The satellite orbital period is

$$T = 2\pi\sqrt{\frac{(h + R_E)^3}{\mu_E}} \approx 43083 \text{ s.} \quad (2.31)$$

Considering a minimum elevation angle of 5° of the satellites with respect to user's position on Earth, the angle of the cone of visibility is 71.2° (PARKINSON; SPILKER JR., 1996).

Defining an Earth-centered-Earth-fixed (ECEF) coordinate system such that axes x and z are in the orbit plane of one GPS satellite, with z coincident with the satellite visibility center, and axes x and y are in the equator plane of the Earth, then the satellite radius vector $\mathbf{r}$ and velocity vector $\mathbf{v}$, the user position vector on Earth $\mathbf{r}_u$ and the line-of-sight vector from user position to the satellite $\mathbf{l}_u$ are defined as shown in Figure 2.2. Also shown in Figure 2.2 is the visibility cone in green, the user position vector rotated to the orbit plane $\mathbf{r}_p$ by the user east-longitude φ_u and at same co-latitude θ_u, and the position vector from this point to the satellite $\mathbf{l}_p$. All

vectors in black are in the orbit plane and Earth is considered a sphere.

Figure 2.2 - User-satellite geometry for Doppler shift computation.
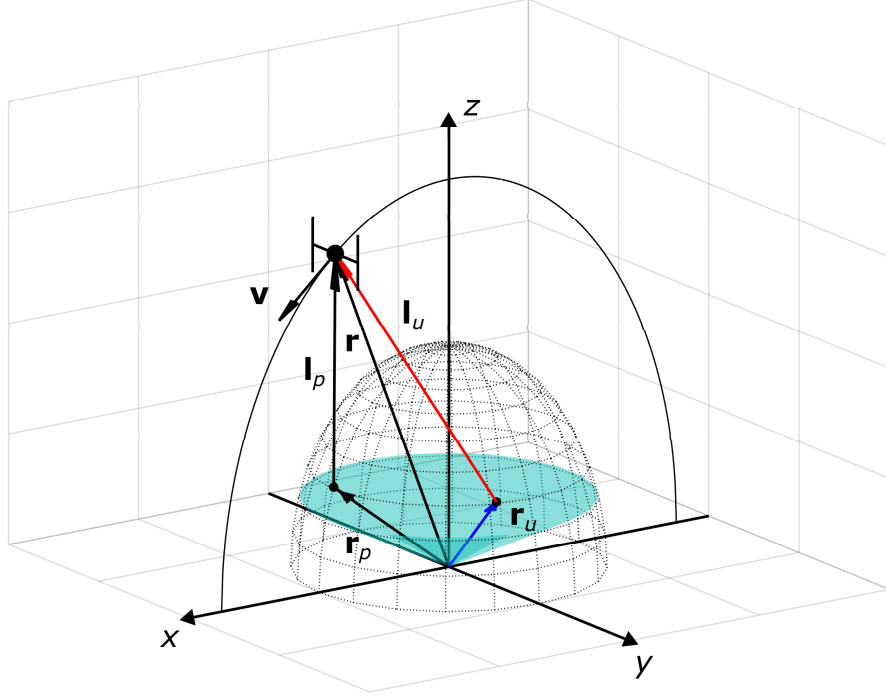
For the hemisphere containing the visibility cone, the radius $\mathbf{r}$, velocity $\mathbf{v}$ and acceleration $\mathbf{a}$ vectors of the satellite can be given, in spherical coordinates, by

$$\mathbf{r} = r \begin{bmatrix} \sin\theta\cos\varphi \\ 0 \\ \cos\theta \end{bmatrix}, \ \mathbf{v} = r\dot{\theta} \begin{bmatrix} \cos\theta \\ 0 \\ -\sin\theta \end{bmatrix}, \ \mathbf{a} = -r\dot{\theta}^2 \begin{bmatrix} \sin\theta\cos\varphi \\ 0 \\ \cos\theta \end{bmatrix}, \quad (2.32)$$

where θ is the satellite co-latitude, $\dot{\theta} = 2\pi/T$, $r = \|\mathbf{r}\|$ and φ is the satellite east-longitude, which is π over negative x axis and 0 over positive x axis. The user

position, and user position rotated to orbit plane are, respectively

$$\mathbf{r}_u = R_E \begin{bmatrix} \sin\theta_u \cos\varphi_u \\ \sin\theta_u \sin\varphi_u \\ \cos\theta_u \end{bmatrix}, \; \mathbf{r}_p = R_E \begin{bmatrix} \sin\theta_u \text{sign}[\cos\varphi_u] \\ 0 \\ \cos\theta_u \end{bmatrix}. \tag{2.33}$$

From the geometry in Figure 2.2, $\mathbf{l}_p = \mathbf{r} - \mathbf{r}_p$ and $\mathbf{l}_u = \mathbf{l}_p + \mathbf{r}_p - \mathbf{r}_u = \mathbf{l}_p + \Delta\mathbf{r}$, where $\Delta\mathbf{r}$ is a constant vector. The Doppler shift for GPS L1 frequency is

$$f_D = -\left(\frac{\mathbf{v} - \mathbf{v}_u}{c} \cdot \frac{\mathbf{l}_u}{l_u}\right) f_{L1} = -\frac{f_{L1}}{c}\frac{\mathbf{v} \cdot \mathbf{l}_u}{l_u}, \tag{2.34}$$

where $\mathbf{v}_u$ is the user velocity, which was considered zero, $l_u = \|\mathbf{l}_u\|$, $f_{L1} = 1575.42$ MHz is the GPS L1 frequency, and $c = 3 \times 10^8$ m/s is the speed of light. Taking the derivative of the equation above, we get

$$\dot{f}_D = -\frac{f_{L1}}{c}\frac{l_u d(\mathbf{v} \cdot \mathbf{l}_u)/dt - \dot{l}_u(\mathbf{v} \cdot \mathbf{l}_u)}{l_u^2}, \tag{2.35}$$

with

$$\dot{l}_u = \frac{\mathbf{v} \cdot \mathbf{l}_u}{l_u}, \tag{2.36}$$

and

$$\frac{d}{dt}(\mathbf{v} \cdot \mathbf{l}_u) = \mathbf{a} \cdot \mathbf{l}_u + \mathbf{v} \cdot \frac{d}{dt}(\mathbf{l}_u) = \mathbf{a} \cdot \mathbf{l}_u + \mathbf{v} \cdot \mathbf{v}, \tag{2.37}$$

taking into account that $d\mathbf{l}_u/dt = d\mathbf{l}_p/dt = d\mathbf{r}/dt = \mathbf{v}$. Therefore, (2.35) relates the Doppler shift f_D dynamics with the dynamics of the LOS $\mathbf{l}_u$.

One passage of a GPS satellite over the visibility cone for different user positions on Earth was simulated, with the formulation described above, and the Doppler shift, the Doppler drift, and the Doppler drift rate were computed. The results are shown in Figures 2.3, 2.4, and 2.5, respectively. The red lines show f_D, df_D/dt, and d^2f_D/dt^2 for user positions in the orbit plane, for different co-latitudes. The blue lines show f_D, df_D/dt, and d^2f_D/dt^2 for user positions out of the orbit plane, on the positive y axis side, for different east-longitudes. A symmetric result is expected for user positions on the negative y axis side. The grid for the simulations was formed by 7 points equally spaced from $0°$ to $71.2°$ for co-latitudes and by 7 points equally spaced from $0°$ to $180°$ for east-longitudes. From Figures 2.3, 2.4, and 2.5, the approximate maximum absolute values of Doppler shift, Doppler drift, and Doppler drift rate are, respectively, 4866 Hz, 0.94 Hz/s, and 1.35×10^{-4} Hz/s^2.

Figure 2.3 - Doppler shift. Red lines are relative to user positions in the orbit plane and blue lines are relative to user positions out of the orbit plane.
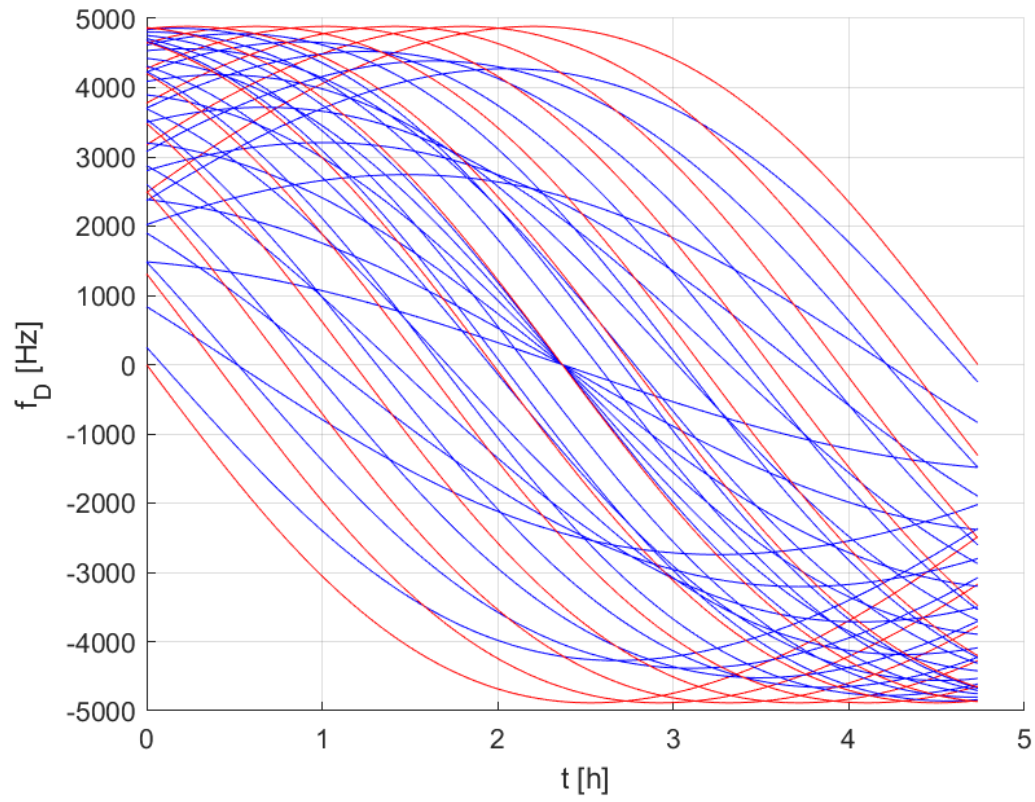
SOURCE: Author's production.

Figure 2.4 - Doppler drift. Red lines are relative to user positions in the orbit plane and blue lines are relative to user positions out of the orbit plane.
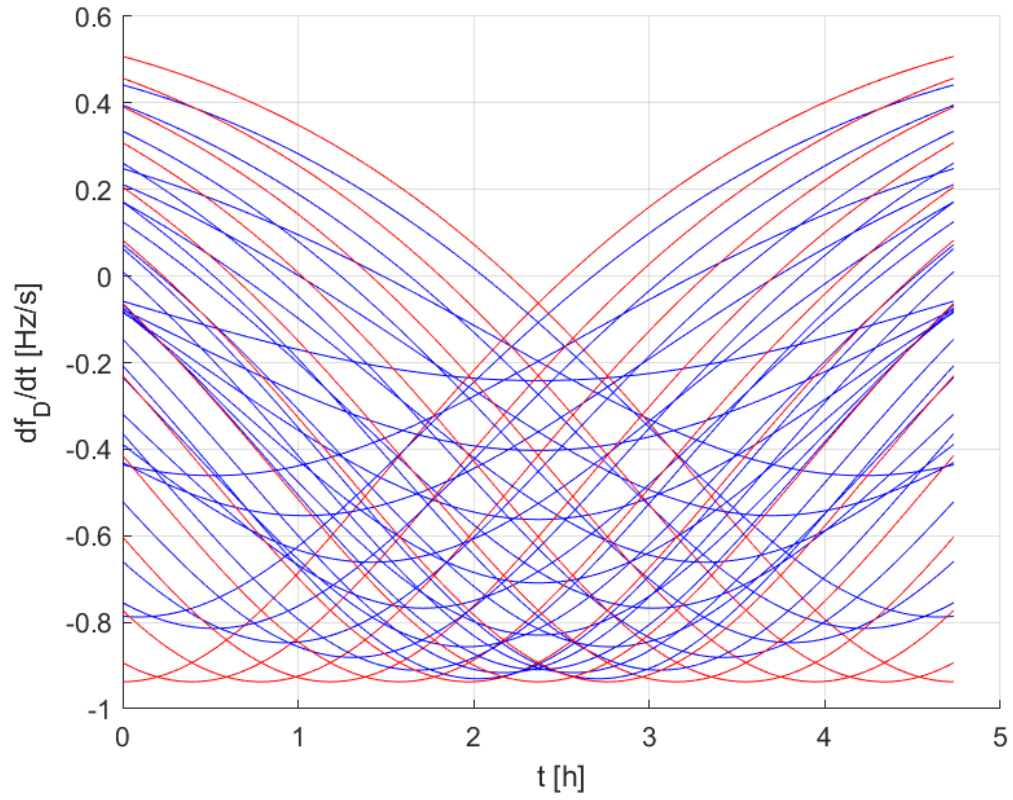
Figure 2.5 - Doppler drift rate. Red lines are relative to user positions in the orbit plane and blue lines are relative to user positions out of the orbit plane.
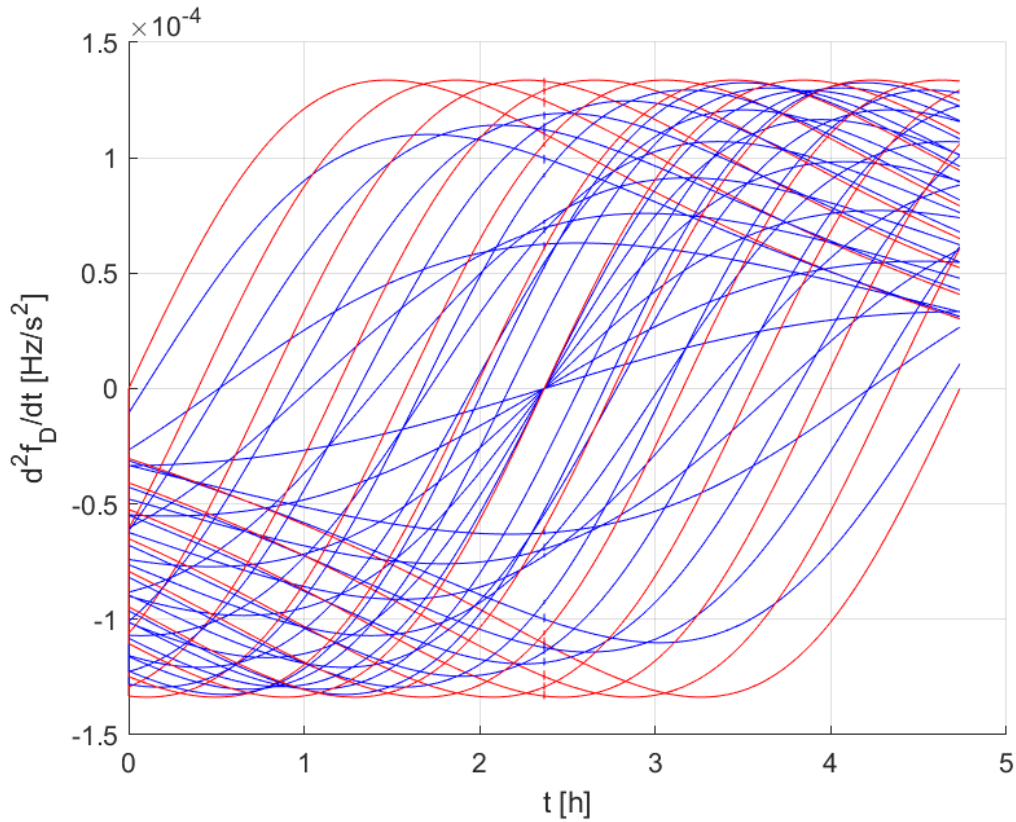
2.3 Scintillation induced effects on GNSS receivers

The ionosphere is an ionized region of the atmosphere between 50 km to 1000 km of altitude with free electrons generated especially by ionization processes related to the solar activity. The ionosphere is a dispersive medium for radio propagation, with the refractive index being a function of the frequency, and mainly characterized by the electrons density (TEUNISSEN; MONTENBRUCK, 2017). The interaction of transient fluctuations of electron content inside ionosphere with the propagating radio waves via refraction and diffraction results in amplitude and phase scintillation of the radio signal.

The ionospheric behavior is very dynamic and irregular, with the motion of electrons

controlled by the geomagnetic field and plasma instabilities related to vertical drift mechanisms. The plasma vertical drift is more common in the equatorial region, generally downwards after sunset due to the plasma cooling, but upwards during equinoxes and summer solstice of the south hemisphere, with a pre-reversion peak in the vertical drift just after sunset, in general, and intensification upwards from 18:00 to 21:00 local time. An eastward directed electric field contributes to the upwards drift. Increased scintillation activity is more pronounced in the equatorial region from sunset to midnight, and can also be observed along strong ionization gradients related to ionization and a recombination process induced by the daily solar activity (ALFONSI et al., 2011),(TEUNISSEN; MONTENBRUCK, 2017). The occurrence probability of equatorial scintillation depends on solar activity and the season, being more probable around the equinoxes over African region and around the solstices over American region (NISHIOKA et al., 2008). At high latitudes, irregularities on the solar wind may create chaotic plasma structures that can also result in scintillation, which is not limited to post sunset hours (SMITH et al., 2008),(JIAO et al., 2013a). Thus, scintillation are more frequently observed at equatorial and high latitude regions, and, in general, the electron fluctuations depend on factors such as solar activity, geomagnetic activity, location, and daytime (MORAES et al., 2012).

While large scale irregularities are more associated to signal refraction resulting in lower frequency variations in the code and carrier of the signal, smaller scale irregularities of approximately 400 m are more associated to signal diffraction, where the primary ray is scattered into many different rays at terrestrial receiver level. The constructive and destructive interactions of these diffracted rays result in stronger and more rapid variations in both amplitude and phase of the carrier (TEUNISSEN; MONTENBRUCK, 2017).

At high latitudes, the scintillation effects on a GNSS receiver can be observed for many hours, they are normally milder and more associated with phase variations when compared to the equatorial scintillation effects, where severe scintillation with signal intensity fading depth up to 25 dB can be observed (BASU et al., 1988). The deep power fades in signal intensity are typically associated to abrupt phase variations, and the rapidity of scintillation is measured by the decorrelation time τ_0, where values smaller than 0.5 s implies in effects changing rapidly with time (TEUNISSEN; MONTENBRUCK, 2017). The consequence of scintillation to a receiver is a degradation of the precision of the estimates provided by the tracking loops, eventually leading to a loss of lock of a satellite in the respective processing channel (MYER et al., 2017). The abrupt variations in strong equatorial scintillations, with the large

power fades and half-cycle phase jumps, can induce cycle slips in the carrier tracking loops (KINTNER et al., 2009b), which is particularly relevant for carrier-based positioning techniques such as RTK and PPP. Signal intensity effects are measured by the S_4 index, which is a variational coefficient of the intensity standard deviation over its mean. Phase variation effects are typically measured by the phase standard deviation σ_ϕ.

2.3.1 Scintillation effect quantification - signal intensity index

The metric commonly used in scintillation monitoring to quantify the strength of amplitude scintillation is the S_4 index

$$S_4 = \sqrt{\frac{E[S^2] - E[S]^2}{E[S]^2}}, \tag{2.38}$$

which is the ratio of the standard deviation of the signal intensity S to the absolute value of its mean. Therefore, the S_4 index is a positive and normalized measure. Referring to the continuous-time BB signal amplitude (2.9), we can write

$$S(t) = A^2(t), \tag{2.39}$$

and after signal sampling and despreading, the discrete sequence of the signal intensity must be estimated. The standard algorithm for the signal intensity estimation is based on the narrow and wide band powers (DIERENDONCK et al., 1993) of the prompt correlator outputs (2.24). They are computed by, respectively

$$NBP[i] = \left(\sum_{k=iK}^{(i+1)K-1} y_I[k] \right)^2 + \left(\sum_{k=iK}^{(i+1)K-1} y_Q[k] \right)^2, \tag{2.40}$$

and

$$WBP[i] = \sum_{k=iK}^{(i+1)K-1} \left(y_I^2[k] + y_Q^2[k] \right), \tag{2.41}$$

where the last K samples of the discrete sequences $y_I[k]$ and $y_Q[k]$, the I/Q outputs of the prompt correlators (2.24), respectively, are used to compute the narrow band power $NBP[i]$ and the wide band power $WBP[i]$ sequences. As the index k represents the kth integration period T_I, the index i represents an update period of KT_I. To avoid the computation over navigation bit transitions, which occurs with a 20 ms period, $K = 20$ is chosen for a coherent integration time of 1 ms. Therefore, in this case, $NBP[i]$ and $WBP[i]$ are computed every 20 ms, or at a 50 Hz sampling fre-

quency. The signal intensity can be estimated by the difference between the narrow and wide band powers

$$\hat{S}[i] = NBP[i] - WBP[i]. \tag{2.42}$$

If the receiver gain is constant, this difference is proportional to the received signal power. An enabled automatic gain control (AGC) may introduce errors in this computation (DIERENDONCK et al., 1993). For a practical computation of the S_4 index, a temporal averaging is employed to approach the expectations of S in (2.38), and the index can be computed as

$$S_4[i] = \sqrt{\frac{\langle \hat{S}^2 \rangle_M - \langle \hat{S} \rangle_M^2}{\langle \hat{S} \rangle_M^2}}, \tag{2.43}$$

where the symbol $\langle \cdot \rangle_M$ denotes the temporal mean in a time window of M samples. For a GNSS receiver statically positioned on Earth, the means are typically computed over a 60 s time window (DIERENDONCK et al., 1993), (NIU et al., 2012). Once the index i is increased in a 50 Hz rate, $M = 3000$ for a 60 s time window.

Fluctuations in the received signal power can occur due to fluctuations in signal generation, antenna patterns, and multipath, and because of this, $\hat{S}$ is typically detrended dividing its raw value by its low pass filtered value (DIERENDONCK et al., 1993), (FREMOUW et al., 1978). The filtering is performed by up to three cascaded digital second order filters sampled at 50 Hz, and typically Butterwoth filters are employed (DIERENDONCK et al., 1993), (ZHANG et al., 2010). The idea is to remove spurious low-frequency content present in the input signal. Typically, the cutoff frequency of the filters is chosen to be 0.1 Hz (FREMOUW et al., 1978), but adjustments may be needed to better characterize the scintillation phenomenon (FORTE, 2007). Calling the low pass filtered signal intensity by $\hat{S}_F$, the detrended signal intensity $\hat{S}_D$ is

$$\hat{S}_D[i] = \frac{\hat{S}[i]}{\hat{S}_F[i]}, \tag{2.44}$$

and the filtered signal intensity is represented in the z-domain as

$$\hat{S}_F(z) = H_{LP}(z)\hat{S}(z), \tag{2.45}$$

where $H_{LP}(z)$ represents the cascaded low pass filters.

The computed value of S_4 can be overrated due to the ambient noise. The formula

to compute the noise contribution is (DIERENDONCK et al., 1993)

$$S_{4_N} = \sqrt{\frac{2}{KT_I c/n_0}\left(1 + \frac{1}{2\left(K-1\right)T_I c/n_0}\right)}, \tag{2.46}$$

where c/n_0 is the carrier-to-noise density ratio in Hz. For a coherent integration time of $T_I = 1 \times 10^{-3}$ s, $K = 20$ and an estimated carrier-to-noise density ratio discrete sequence $\frac{\hat{c}}{n_0}[i]$, the noise component in the S$_4$ index is

$$S_{4_N}[i] = \sqrt{\frac{100}{\frac{\hat{c}}{n_0}[i]}\left(1 + \frac{500}{19\frac{\hat{c}}{n_0}[i]}\right)}. \tag{2.47}$$

Hence, the S$_4$ index corrected of ambient noise is

$$S_{4_C}[i] = \sqrt{S_4^2[i] - S_{4_N}^2[i]} = \sqrt{\frac{\langle\hat{S}_D^2\rangle_M - \langle\hat{S}_D\rangle_M^2}{\langle\hat{S}_D\rangle_M^2} - \frac{100}{\frac{\hat{c}}{n_0}[i]}\left(1 + \frac{500}{19\frac{\hat{c}}{n_0}[i]}\right)}. \tag{2.48}$$

Since the noise contribution is removed, in the case of absence of ionospheric scintillation, the value computed inside the square root will fluctuate around 0. This is an indication that the noise contribution is being correctly removed, and a protection against the computation of negative numbers inside the square root must be inserted in the algorithm (DIERENDONCK et al., 1993).

2.3.2 Scintillation effect quantification - phase standard deviation

The metric generally accepted to quantify phase scintillation is the phase standard deviation σ_ϕ. A detrending procedure is also necessary to minimize the influence of undesired effects in the index computation. In addition to the phases related to the LOS dynamics and scintillation considered in the total phase (2.10), a phase term induced by the receiver clock needs also to be considered. Thus, for the receiver channel i, discarding the noise term, we have

$$\phi_{T_i}[k] = \phi_{D_i}[k] + \phi_i[k] + \phi_R[k], \tag{2.49}$$

where $\phi_R[k]$ is the clock induced phase, $\phi_{D_i}[k]$ is the phase related to the LOS dynamics and $\phi_i[k]$ is the scintillation induced phase, for the index k representing each coherent integration period. The clock induced phase variation is considered to be common for all channels. Therefore, one possibility to remove its effect is to choose one non-scintillating channel r as reference, with $\phi_{T_r}[k] = \phi_{D_r}[k] + \phi_R[k]$,

and subtract its phase from channel i (O'HANLON et al., 2011), yielding

$$\Delta\phi_{T_{ir}}[k] = \phi_{T_i}[k] - \phi_{T_r}[k] \qquad (2.50)$$
$$= \phi_{D_i}[k] - \phi_{D_r}[k] + \phi_i[k]$$
$$= \Delta\phi_{D_{ir}}[k] + \phi_i[k].$$

This procedure can remove a common mode clock induced phase. However, if this effect is very small, the fluctuating tracking error of the reference channel carrier tracking loop can slightly increase the phase variance of the ith channel.

A 3rd order polynomial is considered to fit the LOS dynamics or the difference LOS dynamics $\Delta\phi_{D_{ir}}$ (NIU et al., 2012). A procedure to remove the LOS dynamics applied in data post-processing is to fit the polynomial to a time-moving data window of typically 60 s (NIU et al., 2012) and subtract this estimated LOS dynamics $\Delta\hat{\phi}_{D_{ir}}[k]$ from $\Delta\phi_{T_{ir}}[k]$. A 4th order polynomial with time-moving data window of 100 s can also be employed (ZHANG et al., 2010). The resulting detrended phase is

$$\Delta\tilde{\phi}_{T_{ir}} = \Delta\phi_{T_{ir}}[k] - \Delta\hat{\phi}_{D_{ir}}[k] \approx \phi_i[k]. \qquad (2.51)$$

In order to detrend the phase, removing low frequency components, three cascaded 2nd order Butterworth high pass filters represented by $H_{HP}(z)$ with cut-off frequency of 0.1 Hz are generally applied (NIU et al., 2012), resulting in

$$\Delta\phi_{F_{ir}}(z) = H_{HP}(z)\Delta\tilde{\phi}_{T_{ir}}(z). \qquad (2.52)$$

The phase standard deviation is then computed, where the mean is computed over a period of typically 60 s for a static receiver on-ground. Thus, the standard deviation of the carrier phase can be given as

$$\sigma_\phi = \sqrt{\langle\Delta\phi_{F_{ir}}^2\rangle - \langle\Delta\phi_{F_{ir}}\rangle^2}. \qquad (2.53)$$

2.3.3 Scintillation effect quantification - severity classification

As the scintillation effects at high latitudes can be observed for longer periods, are normally milder and more associated with phase variations, at equatorial latitudes, more severe effects can be observed with signal fading and associated rapid phase variations, so that the classification of scintillation severity based on S_4 index and σ_ϕ can take different approaches.

At high latitudes, in order to consider that a tracked satellite signal is under scintillation, separating the observed effect from multipath in the data analysis, a threshold of $S_4 > 0.12$ and $\sigma_\phi > 0.1$ rad to eliminate multipath false alarms was employed in (TAYLOR et al., 2012). In (JIAO et al., 2013b), mild scintillation events are considered if $S_4 > 0.15$ and $\sigma_\phi > 0.26$ rad, and the same threshold of (TAYLOR et al., 2012) for low scintillation events was used. In (JIAO et al., 2013a) the same threshold of (TAYLOR et al., 2012) was chosen, to not exclude weak scintillation events. Others consider $\sigma_\phi > 0.25$ rad as the threshold for moderate scintillation activity (DUBEY et al., 2006), (LINTY et al., 2018).

Concerning equatorial scintillation, some works consider moderate scintillation activity if $0.2 < S_4 \leq 0.5$ and strong scintillation activity if $S_4 > 0.5$ (JIAO; MORTON, 2015), (JIAO, 2013). Others consider $S_4 > 0.4$ as threshold for significant scintillation activity (DUBEI et al., 2005). In (HUMPHREYS et al., 2009), amplitude scintillation strength is considered weak if $S_4 \leq 0.4$, moderate if $0.4 < S_4 \leq 0.6$ and severe if $S_4 > 0.6$, and equivalently, phase scintillation is considered weak if $\sigma_\phi \leq 0.25$ rad, moderate if $0.25 < \sigma_\phi \leq 0.5$ rad, and severe if $\sigma_\phi > 0.5$ (VILÁ-VALLS et al., 2020).

In order to minimize multipath effects in the data analysis, a mask of 30° degrees of satellite elevation can be employed (JIAO; MORTON, 2015) to filter out satellites with elevation lower than 30° degrees. Also, carrier-to-noise density ratio C/N_0 mask can be employed to filter out satellite signals with less than 40 dB-Hz (CURRAN et al., 2015).

2.4   Generation of synthetic scintillation data for simulations

The Cornell Scintillation Model (CSM) is a statistical model adjusted with empirical data gathered from GPS receivers, including data gathered by the Brazilian Institute for Space Research (INPE) (HUMPHREYS et al., 2005), (HUMPHREYS et al., 2004), (CERRUTI et al., 2006), and from the WIDEBAND satellite project (KINTNER et al., 2009a). The complex samples of scintillation time series synthesized by the model are described by a Rice distribution characterizing the amplitude and by an auto-correlation function of a complex white noise with Gaussian distribution passing through a second order low pass Butterworth filter (HUMPHREYS et al., 2010).

The amplitude distribution is specified by the S_4 index, which is directly related to the Ricean parameter K, and the cutoff frequency of the Butterworth filter is related to the decorrelation time τ_0, which is the time taken to the auto-correlation function decay from its value at time 0 to e^{-1} (KINTNER et al., 2009a). The sampling time

of the model is 10 ms. The model parameters were adjusted in a software testbed, where the implemented carrier tracking loops were tested with the empirical data, comparing statistics produced by the model, such as the phase standard deviation, mean time to first cycle slip and number of cycle slips, with the statistics computed with the collected data. Additional validation was accomplished with hardware-in-the-loop test of a GNSS receiver implemented on a DSP (Digital Signal Processor) chip (KINTNER et al., 2009a), (HUMPHREYS et al., 2010).

Besides the CSM, there are other models available for synthetic scintillation data generation to assess the performance of GNSS receivers via simulation (VILÁ-VALLS et al., 2018), (VILÁ-VALLS et al., 2020). The most widely used are the WideBand Model (WBMOD) (SECAN et al., 1997), phase-screen models (PSIAKI et al., 2007), the Global Ionospheric Scintillation Model (GISM) (GIOVANNI; RADICELLA, 1990) and the GPS Scintillation Simulator from the University of Colorado (JIAO et al., 2018). The CSM is considered to have some limitations, since only time series representing equatorial scintillation can be generated, with a maximum value of S_4 equal to 1, and wideband UHF (Ultra High Frequency) observations were used in the model validation (MACABIAU et al., 2012), in addition to L1 observations. Despite of this, the CSM is a popular model, largely employed in the literature for generation of scintillation data (VILÁ-VALLS et al., 2020), and is more convenient for simulation (VILÁ-VALLS et al., 2018). Thus, the CSM is used throughout this work in the simulations with synthetic scintillation data.

3 STOCHASTIC PROCESSES AND BAYESIAN FILTERING

This chapter presents a review of the stochastic processes relevant for the modeling of the LOS dynamics and the induced ionospheric scintillation effects, the Itô stochastic differential equations, and the derivation of the Bayesian nonlinear filter, from which the Kalman filter is derived. The kinematic process model, employed for LOS dynamics modeling in the Kalman filters, and the AR process model, employed in the scintillation mitigation problem, are also presented. We present the more general autoregressive moving average (ARMA) model, from which the AR model can be derived.

3.1 Stochastic models for Bayesian estimation of LOS and scintillation dynamics

In this section, we present a review of the basic stochastic processes, the stochastic differential equations, and the AR as well as the kinematic process models.

3.1.1 Wiener process

The Wiener process $\mu(t)$ is a continuous-state process generated by taking the sum of independent steps $s \to 0$, equally probable in each direction, at time intervals $h \to 0$ such that $\frac{s}{\sqrt{h}} \to \sqrt{\alpha}$, where α is a constant. The probability density function of $\mu(t)$ is the normal (Gaussian) distribution $\mathcal{N}(0, \alpha t)$, with zero mean and variance αt (BAR-SHALOM et al., 2001), (PAPOULIS; PILLAI, 2002).

Requiring the limiting process with $s \to 0$ and $h \to 0$ to have variance σ^2 per unit time and zero mean allows to write in the limit $s = \sigma\sqrt{h}$, so the constant $\alpha = \sigma^2$ is the variance per unit time. The step s is proportional to the square root of the time interval $\sqrt{h}$. The increments in the Wiener process during the time interval are independent and normally distributed random variables (COX; MILLER, 1965). We can write for the Wiener process

$$\mu(t) = \int_0^t n(\tilde{t})d\tilde{t}, \tag{3.1}$$

or, otherwise

$$d\mu(t) = n(t)dt, \tag{3.2}$$

where $n(t)$ is Gaussian white noise, so the independent normal increments $d\mu(t)$ have variance $\sigma^2 dt$. The Wiener process is not stationary since its variance is a function of time, and therefore it does not have a power spectral density representation.

3.1.2 Markov process

In a Markov process, the conditional probability of the random variables does not have to be computed considering their past occurrences over the complete time interval, but can be computed considering only the latest time interval. The probabilities over long time intervals can be derived recursively from the probabilities over shorter time intervals. The Wiener process is a Markov process, since

$$
\begin{aligned}
\mu(t) &= \int_0^t n(\tilde{t})d\tilde{t} \\
&= \int_0^{t_k} n(\tilde{t})d\tilde{t} + \int_{t_k}^t n(\tilde{t})d\tilde{t} \\
&= \mu(t_k) + \int_{t_k}^t n(\tilde{t})d\tilde{t},
\end{aligned}
\tag{3.3}
$$

for $t_k < t$.

If we evaluate the Markov process in discrete time instants, the formed discrete sequence of random variables has the property that the conditional distribution depends only on the current state (COX; MILLER, 1965). We can obtain a discrete time (DT) Wiener process which is a Markov process. If we consider a finite time interval h, a variance per unit time σ^2 and an increasing sequence of time $0, ..., t_{k-1}, t_k$ on the index k such that $t_k - t_{k-1} = h$, we get

$$
\begin{aligned}
\mu(t_k) &= \mu(t_{k-1}) + \int_{t_{k-1}}^{t_k} n(\tilde{t})d\tilde{t} \\
&= \mu(t_{k-1}) + \int_{t_{k-1}}^{t_k} d\mu(\tilde{t}) \\
&= \mu(t_{k-1}) + \nu(t_{k-1}),
\end{aligned}
\tag{3.4}
$$

where $\nu(t_k)$ is a Gaussian white noise sequence with variance $\sigma^2 h$. Generalizing, we can obtain the following discrete representation of a linear dynamic system excited by Gaussian white noise

$$
\mathbf{x}(t_k) = \mathbf{F}(t_{k-1})\mathbf{x}(t_{k-1}) + \boldsymbol{\nu}(t_{k-1}),
\tag{3.5}
$$

for the state and noise vectors $\mathbf{x}(t_k) \in \mathbb{R}^{n_x \times 1}$ and $\boldsymbol{\nu}(t_k) \in \mathbb{R}^{n_x \times 1}$, respectively, and the state transition matrix $\mathbf{F}(t_k)$. Thus, we consider a Gauss-Markov sequence, which is Gaussian because of the linearity and Markov because of whiteness of the noise sequence (BAR-SHALOM et al., 2001).

3.1.3 Linear stochastic differential equations

The independent increment characteristics of the Wiener process makes it suitable to model unknown variables and define the stochastic differential equations to be employed in problems of state estimation. A continuous time (CT) linear state-space representation of a system of first order Itô (ITÔ, 1951) stochastic differential equations can be defined as

$$d\mathbf{x}(t) = \mathbf{F}_c\mathbf{x}(t)dt + \mathbf{G}_cd\boldsymbol{\mu}(t), \tag{3.6}$$

where $\mathbf{x}(t) \in \mathbb{R}^{n_x \times 1}$ is the system state vector, $\boldsymbol{\mu}(t) \in \mathbb{R}^{n_\mu \times 1}$ is a vector of Wiener processes modeling the process noise with incremental covariance $\mathbf{Q}_cdt \in \mathbb{R}^{n_\mu \times n_\mu}$, $\mathbf{F}_c \in \mathbb{R}^{n_x \times n_x}$ is the system matrix and $\mathbf{G}_c \in \mathbb{R}^{n_x \times n_\mu}$ is the process noise gain matrix. The solution of the state equation can be given as

$$\mathbf{x}(t) = \boldsymbol{\Phi}(t, t_0)\mathbf{x}_0 + \int_{t_0}^{t} \boldsymbol{\Phi}(t, s)\mathbf{G}_cd\boldsymbol{\mu}(s), \tag{3.7}$$

where $\boldsymbol{\Phi}(t, s)$ is the fundamental matrix, with the property $\frac{d\boldsymbol{\Phi}(t,t_0)}{dt} = \mathbf{F}_c\boldsymbol{\Phi}(t, t_0)$, and $\mathbf{x}_0 = \mathbf{x}(t_0)$. The computation of the state solution for one finite sampling interval $t_k - t_{k-1} = h$ leads to

$$\begin{aligned}
\mathbf{x}(t_k) &= \boldsymbol{\Phi}(t_k, t_{k-1})\mathbf{x}(t_{k-1}) + \int_{t_{k-1}}^{t_k} \boldsymbol{\Phi}(t_k, t)\mathbf{G}_cd\boldsymbol{\mu}(t) \\
&= \boldsymbol{\Phi}(t_k, t_{k-1})\mathbf{x}(t_{k-1}) + \boldsymbol{\nu}(t_{k-1}).
\end{aligned} \tag{3.8}$$

The covariance of the Gaussian white noise sequence $\boldsymbol{\nu}(t_{k-1})$ is

$$\begin{aligned}
E[\boldsymbol{\nu}(t_{k-1})\boldsymbol{\nu}^{\mathrm{T}}(t_{k-1})] &= E\left[\int_{t_{k-1}}^{t_k}\int_{t_{k-1}}^{t_k} \boldsymbol{\Phi}(t_k, t)\mathbf{G}_cd\boldsymbol{\mu}(t)d\boldsymbol{\mu}^{\mathrm{T}}(s)\mathbf{G}_c^{\mathrm{T}}\boldsymbol{\Phi}^{\mathrm{T}}(t_k, s)\right] \\
&= \int_{t_{k-1}}^{t_k}\int_{t_{k-1}}^{t_k} \boldsymbol{\Phi}(t_k, t)\mathbf{G}_cE[d\boldsymbol{\mu}(t)d\boldsymbol{\mu}^{\mathrm{T}}(s)]\mathbf{G}_c^{\mathrm{T}}\boldsymbol{\Phi}^{\mathrm{T}}(t_k, s) \\
&= \int_{t_{k-1}}^{t_k} \boldsymbol{\Phi}(t_k, t)\mathbf{G}_c\mathbf{Q}_c\mathbf{G}_c^{\mathrm{T}}\boldsymbol{\Phi}(t_k, t)dt \triangleq \mathbf{Q}
\end{aligned} \tag{3.9}$$

3.1.4 Autoregressive moving average process

The CT ARMA process $y(t)$ is generated by the time-invariant model

$$A_c(p)y(t) = B_c(p)e_c(t), \tag{3.10}$$

where $A_c(p) = p^n + a_1 p^{n-1} + ... + a_n$ and $B_c(p) = b_0 p^m + b_1 p^{m-1} + ... + b_m$ are polynomials on the differential operator p of order n and $m < n$, respectively. The ARMA model output is $y(t)$, and $e_c(t)$ is Gaussian white noise with spectral density σ^2, defined such that $d\mu(t) = e_c(t)dt$ is the increment of the Wiener process $\mu(t)$, with incremental variance $\sigma^2 dt$. Proper rational models ($m = n$) lead to unbounded variance of $y(t)$ (WAHLBERG et al.,). In order to have a stationary process, it is also required that the real parts of the roots of the polynomial $A_c(p)$ to be negative, resulting in a stable system (GARNIER; WANG, 2008).

The ARMA model is a general linear model representation that yields the stationary process $y(t)$, with rational power spectral density based on its autoregressive and noise terms. A pure AR model is obtained by making $B_c(p) = 1$. The CT ARMA model state-space representation is

$$\begin{cases} d\mathbf{x}(t) = \mathbf{F}_c \mathbf{x}(t)dt + \mathbf{G}_c d\mu(t) \\ y(t) = \mathbf{H}\mathbf{x}(t), \end{cases} \tag{3.11}$$

with $\mathbf{F}_c \in \mathbb{R}^{n \times n}$, $\mathbf{G}_c \in \mathbb{R}^{n \times 1}$ and $\mathbf{H} \in \mathbb{R}^{1 \times n}$. The relationship between the polynomial representation and the state-space representation is obtained via the CT spectrum $\Phi_c(s)$, in terms of the Laplace operator s (SÖDERSTRÖM, 2002)

$$\Phi_c(s) = \sigma^2 \frac{B(s)B(-s)}{A(s)A(-s)} = \mathbf{H}(s\mathbf{I} - \mathbf{F}_c)^{-1}\mathbf{G}_c \sigma^2 \mathbf{G}_c^{\mathrm{T}}(-s\mathbf{I} - \mathbf{F}_c^{\mathrm{T}})^{-1}\mathbf{H}^{\mathrm{T}}, \tag{3.12}$$

and the spectral density is obtained by evaluating $\Phi_c(j\omega)$. The evaluation of the ARMA process at discrete instants of time with time interval h, such that $t_k - t_{k-1} = h$, leads to the DT model

$$\begin{cases} \mathbf{x}(t_k) = \mathbf{F}\mathbf{x}(t_{k-1}) + \boldsymbol{\nu}(t_{k-1}) \\ y(t_k) = \mathbf{H}\mathbf{x}(t_k), \end{cases} \tag{3.13}$$

with the index $k = 0, 1, 2, \ldots, \in \mathbb{Z}^+$, $\mathbf{F} = e^{\mathbf{F}_c h}$, and

$$\boldsymbol{\nu}(t_k) = \int_{t_k}^{t_k+h} e^{\mathbf{F}_c(t_k+h-s)} \mathbf{G}_c d\mu(s) = \int_{t_k}^{t_k+h} e^{\mathbf{F}_c(t_k+h-s)} \mathbf{G}_c e_c(s) ds \tag{3.14}$$

is a vector-valued white-noise sequence with covariance matrix

$$\mathbf{Q} = E[\boldsymbol{\nu}(t_k)\boldsymbol{\nu}^{\mathrm{T}}(t_k)] = \int_0^h e^{\mathbf{F}_c s} \mathbf{G}_c \sigma^2 \mathbf{G}_c^{\mathrm{T}} e^{\mathbf{F}_c^{\mathrm{T}} s} ds. \tag{3.15}$$

The DT ARMA model can be obtained from the DT state-space representation, and can be written in the polynomial form as

$$D(q)y(t_{k-n}) = C(q)e_d(t_{k-m}), \tag{3.16}$$

where $D(q) = q^n + d_1 q^{n-1} + ... + d_n$ and $C(q) = q^m + c_1 q^{n-1} + ... + c_m$ are polynomials on the shift operator q, which is defined as $qs(t_k) = s(t_{k+1})$ or $q^{-1}s(t_k) = s(t_{k-1})$ for a signal $s(t_k)$ (LJUNG, 1987), (AGUIRRE, 2000), and $e_d(t_k)$ is a Gaussian white noise sequence with variance $E[e_d^2(t_k)] = \lambda^2$. The discrete spectrum $\Phi_d(z)$ in terms of the z-transform is (SÖDERSTRÖM, 2002)

$$\Phi_d(z) = \lambda^2 \frac{C(z)C(z^{-1})}{D(z)D(z^{-1})} = \mathbf{H}(z\mathbf{I} - \mathbf{F})^{-1}\mathbf{Q}(z^{-1}\mathbf{I} - \mathbf{F}^{\mathrm{T}})^{-1}\mathbf{H}^{\mathrm{T}}. \tag{3.17}$$

Note that, once we have $\mathbf{F}$ from $\mathbf{F}_c$ and $\mathbf{Q}$ from $\mathbf{F}_c$, $\mathbf{G}_c$ and σ^2, for the sampling interval h, the right side of the equation above will be defined. Then, the variance λ^2 of the white noise sequence and the polynomials $D(q)$, with $D(z) = \det(z\mathbf{I} - \mathbf{F})$, and $C(q)$ forming the polynomial representation of the DT ARMA model could be found by solving the spectral factorization problem defined by the equation above (SÖDERSTRÖM, 2002), where $\det(\cdot)$ is the determinant of a matrix.

The spectral density is obtained by evaluating $\Phi_d(e^{j\omega h})$. The DT stochastic model has the same covariance function $r_y(\tau)$ of the original CT stochastic model, evaluated at multiples of the time interval h, and the spectral density of the DT stochastic model tends to the spectral density of the original CT stochastic model as the sampling period h tends to zero, provided there is no aliasing effect (SÖDERSTRÖM, 2002).

The state covariance matrix $\mathbf{P}$ in the steady-state must satisfy the CT Lyapunov equation (SÖDERSTRÖM, 2002)

$$\mathbf{F}_c\mathbf{P} + \mathbf{P}\mathbf{F}_c^{\mathrm{T}} + \sigma^2\mathbf{G}_c\mathbf{G}_c^{\mathrm{T}} = \mathbf{0}, \tag{3.18}$$

and $\mathbf{P}$ also must satisfy the DT Lyapunov equation (SÖDERSTRÖM, 1991)

$$\mathbf{R} = \mathbf{P} - \mathbf{F}\mathbf{P}\mathbf{F}^{\mathrm{T}}. \tag{3.19}$$

The state covariance function $\mathbf{R}_x(\tau) = E[\mathbf{x}(t+\tau)\mathbf{x}^{\mathrm{T}}(t)]$ for the time lag τ is (SÖDERSTRÖM, 2002)

$$\mathbf{R}_x(\tau) = e^{\mathbf{F}_c\tau}\mathbf{P}, \tag{3.20}$$

and the output covariance function $r_y(\tau) = E[y(t+\tau)y(t)]$ is (SÖDERSTRÖM, 2002)

$$r_y(\tau) = \mathbf{H}e^{\mathbf{F}_c\tau}\mathbf{P}\mathbf{H}^{\mathrm{T}}. \tag{3.21}$$

The state and output DT covariance functions can be obtained by evaluating $\mathbf{R}_x(\tau)$ and $r_y(\tau)$ at times τ multiples of sampling period h, respectively.

Pure AR discrete time models derived from sampling of the continuous time stochastic models will occur with zero probability if the parameters in the continuous model are chosen at random (SÖDERSTRÖM, 1990). A continuous AR model of order n with $m < n$ zeros yields a discrete AR model with m intrinsic zeros and $n - m - 1$ sampling zeros (GARNIER; WANG, 2008), (ÅSTROM, 1970). Therefore, a discrete-time AR model of order greater than one cannot be generated from a continuous-time stochastic AR model. This model should have moving average terms, thus being an ARMA model. However, an AR model of any order can be defined directly in discrete time, thus not having a counterpart in continuous time. A continuous-time AR model is directly obtained by making $B_c(p) = 1$ in (3.10). A discrete-time AR model is directly obtained by making $C(q) = 1$ in (3.16).

3.1.5 Kinematic process model

A kinematic process model (BAR-SHALOM et al., 2001) is derived from the equations of motion of a rigid body, taking into account the kinematic relations between the states describing the motion, obtained by differentiation. The velocity is obtained by differentiation of the position, acceleration is obtained by differentiation of the velocity, jerk is obtained by differentiation of the acceleration, and so on. The model does not encompass the dynamics of the motion, but the kinematic relations obtained by the sequential differentiation of the position. Such models are widely used in target tracking problems (LI; JILKOV, 2003).

In the deterministic case, if we want to describe a constant velocity motion, we consider a null acceleration. In the stochastic case, we consider the acceleration to be a Gaussian process with zero mean and a determined variance, meaning that, in practice, the velocity undergoes some changes. If we consider changes in acceleration, the jerk is a zero mean Gaussian process, and, therefore, the acceleration is a Wiener process, leading to a third order state-space model.

Considering the case of acceleration as a Wiener process $\mu(t)$ with variance per unit time of $\sigma_{j_D}^2$, and with position, velocity and acceleration as the states x_1, x_2 and x_3,

respectively, we get the model

$$
\begin{bmatrix} dx_1 \\ dx_2 \\ dx_3 \end{bmatrix} = \mathbf{F}_c \begin{bmatrix} x_1 \\ x_2 \\ x_3 \end{bmatrix} dt + \mathbf{G}_c \begin{bmatrix} 0 \\ 0 \\ d\mu(t) \end{bmatrix}, \tag{3.22}
$$

with the matrices

$$
\mathbf{F}_c = \begin{bmatrix} 0 & 1 & 0 \\ 0 & 0 & 1 \\ 0 & 0 & 0 \end{bmatrix}, \tag{3.23}
$$

and

$$
\mathbf{G}_c = \begin{bmatrix} 1 & 0 & 0 \\ 0 & 1 & 0 \\ 0 & 0 & 1 \end{bmatrix}. \tag{3.24}
$$

Since only the acceleration is a stochastic process, the noise gain matrix $\mathbf{G}_c$ is the identity matrix for the noise vector $\begin{bmatrix} 0 & 0 & d\mu(t) \end{bmatrix}^{\mathrm{T}}$, which possesses a covariance per unit time

$$
\mathbf{Q}_c = \sigma_{j_D}^2 \begin{bmatrix} 0 & 0 & 0 \\ 0 & 0 & 0 \\ 0 & 0 & 1 \end{bmatrix}. \tag{3.25}
$$

The state transition matrix $\boldsymbol{\Phi}(u_2, u_1) = e^{\mathbf{F}_c(u_2 - u_1)}$ can be obtained by computation of the matrix exponential via the power series $e^{\mathbf{F}_c(u_2 - u_1)} = \mathbf{I} + \mathbf{F}_c(u_2 - u_1) + \frac{\mathbf{F}_c^2 (u_2 - u_1)^2}{2} +$ ..., where, truncating at the second order term, since $\mathbf{F}_c^n$ results in a matrix where all elements are equal to zero for $n \geq 3$, we get

$$
\begin{aligned}
\boldsymbol{\Phi}(u_2, u_1) &= \begin{bmatrix} 1 & 0 & 0 \\ 0 & 1 & 0 \\ 0 & 0 & 1 \end{bmatrix} + \begin{bmatrix} 0 & (u_2 - u_1) & 0 \\ 0 & 0 & (u_2 - u_1) \\ 0 & 0 & 0 \end{bmatrix} + \begin{bmatrix} 0 & 0 & (u_2 - u_1)^2/2 \\ 0 & 0 & 0 \\ 0 & 0 & 0 \end{bmatrix} \\
&= \begin{bmatrix} 1 & (u_2 - u_1) & (u_2 - u_1)^2/2 \\ 0 & 1 & (u_2 - u_1) \\ 0 & 0 & 1 \end{bmatrix}.
\end{aligned} \tag{3.26}
$$

The state transition matrix also could be obtained via the computation of the inverse Laplace transform of

$$
(s\mathbf{I} - \mathbf{F}_c)^{-1} = \begin{bmatrix} 1/s & 1/s^2 & 1/s^3 \\ 0 & 1/s & 1/s^2 \\ 0 & 0 & 1/s \end{bmatrix}, \tag{3.27}
$$

considering that the inverse transform of $1/s$ is 1 and the inverse transform of $n!/s^{n+1}$ is t^n, for $n = 1, 2, ...$, with t substituted by $u_2 - u_1$.

The product $\mathbf{\Phi}(u_2, u_1)\mathbf{G}_c\mathbf{Q}_c\mathbf{G}_c^{\mathrm{T}}\mathbf{\Phi}^{\mathrm{T}}(u_2, u_1)$ becomes

$$\mathbf{\Phi}(u_2, u_1)\mathbf{G}_c\mathbf{Q}_c\mathbf{G}_c^{\mathrm{T}}\mathbf{\Phi}^{\mathrm{T}}(u_2, u_1) = \tag{3.28}$$

$$\sigma_{j_D}^2 \begin{bmatrix} (u_2 - u_1)^4/4 & (u_2 - u_1)^3/2 & (u_2 - u_1)^2/2 \\ (u_2 - u_1)^3/2 & (u_2 - u_1)^2 & (u_2 - u_1) \\ (u_2 - u_1)^2/2 & (u_2 - u_1) & 1 \end{bmatrix}.$$

Substituting $u_2 = t_k$ and $u_1 = t_{k-1}$, such that $h = t_k - t_{k-1}$, in the integral (3.9), we get the discrete process noise covariance matrix for the kinematic model with acceleration as a Wiener process

$$\mathbf{Q} = \sigma_{j_D}^2 \begin{bmatrix} (t_k - t_{k-1})^5/20 & (t_k - t_{k-1})^4/8 & (t_k - t_{k-1})^3/6 \\ (t_k - t_{k-1})^4/8 & (t_k - t_{k-1})^3/3 & (t_k - t_{k-1})^2/2 \\ (t_k - t_{k-1})^3/6 & (t_k - t_{k-1})^2/2 & (t_k - t_{k-1}) \end{bmatrix}$$

$$= \sigma_{j_D}^2 \begin{bmatrix} h^5/20 & h^4/8 & h^3/6 \\ h^4/8 & h^3/3 & h^2/2 \\ h^3/6 & h^2/2 & h \end{bmatrix}. \tag{3.29}$$

The discrete process matrix $\mathbf{F}$ is the fundamental matrix (3.26) also evaluated at one time interval h, yielding

$$\mathbf{F} = \mathbf{\Phi}(t_k, t_{k-1}) = \begin{bmatrix} 1 & h & h^2/2 \\ 0 & 1 & h \\ 0 & 0 & 1 \end{bmatrix}. \tag{3.30}$$

3.2 Bayesian estimation and Kalman filtering

The problem of estimating quantities from a set of observations was introduced by Gauss (GAUSS, 1963), with his derivation of the least squares (LS) method to estimate the Keplerian elements of the orbit of celestial bodies from telescopic measurement data. Central for the development of the method was the concept that incorporation of more observations than the minimum required would reduce the influence of the measurement errors on the estimation of the parameters, as redundant data would confirm the results from estimation (SORENSON, 1970).

In the case of the estimation from a noisy set of observations, the probabilistic approach was first employed in the filtering problem by Kolmogorov (KOLMOGOROV, 1962) and Wiener (WIENER, 1949), assuming a linear system and stationary stochastic processes. Regarding Wiener filtering theory, it was restricted to scalar signals and noises and assumed an infinite amount of data. The stochastic processes involved were not modeled by stochastic differential equations and the filtering problem was reduced to the solution of the Wiener-Hopf integral equation in frequency domain using spectral factorization (JAZWINSKI, 1970).

The Kalman filter (KALMAN, 1960), (KALMAN; BUCY, 1961), (KALMAN, 1963) generalizes the Wiener filter to nonstationary stochastic processes, accommodating vector signals and noises, and using the state space representation of the system (KAY, 1993) with the probabilistic Bayesian approach in which the problem is modeled by a set of stochastic difference or differential equations (JAZWINSKI, 1970). The Kalman filter provides estimation of the states of a dynamical system excited by noise from noisy observations, being the optimal estimator in the minimum mean square error (MMSE) sense if signals and noises are jointly Gaussian, and the optimal linear MMSE if they are not jointly Gaussian (KAY, 1993).

A Bayesian estimator takes into account *a priori* information regarding the states, which are considered random variables, in the form of prior probability density function to obtain the maximum *a posteriori* (MAP) density via Bayes' rule

$$Pr\{A|B\} = \frac{Pr\{B|A\}Pr\{A\}}{Pr\{B\}},$$

(3.31)

where events A and B are subsets of the sample space Ω with elements ω, with probabilities assigned by the probability function $Pr\{\cdot\}$ defined on a Borel field B_F. $Pr\{A|B\}$ is the posterior probability of A given B, and $Pr\{B\} \neq 0$. Bayes' rule is derived from the definition of conditional probability

$$Pr\{A|B\} = \frac{Pr\{A \cap B\}}{Pr\{B\}},$$

(3.32)

where $Pr\{A \cap B\}$ is the joint probability of A and B, with $Pr\{B\} \neq 0$.

Taking $\mathbf{x} \in \mathbb{R}^{n \times 1}$ and $\mathbf{y} \in \mathbb{R}^{m \times 1}$ as jointly distributed random vectors with joint probability density function $p_{\mathbf{x},\mathbf{y}}(\boldsymbol{x}, \boldsymbol{y})$, equivalently we can write the Bayes' rule for $(\mathbf{x}, \mathbf{y})$

$$p_{\mathbf{x}|\mathbf{y}}(\boldsymbol{x}|\boldsymbol{y}) = \frac{p_{\mathbf{y}|\mathbf{x}}(\boldsymbol{y}|\boldsymbol{x})p_{\mathbf{x}}(\boldsymbol{x})}{p_{\mathbf{y}}(\boldsymbol{y})},$$

(3.33)

and the conditional probability

$$p_{\mathbf{x}|\mathbf{y}}(\boldsymbol{x}|\boldsymbol{y}) = \frac{p_{\mathbf{x},\mathbf{y}}(\boldsymbol{x}, \boldsymbol{y})}{p_{\mathbf{y}}(\boldsymbol{y})}, \tag{3.34}$$

where $p_{\mathbf{x}|\mathbf{y}}(\boldsymbol{x}|\boldsymbol{y})$ is the conditional density of $\mathbf{x}$ given $\{\mathbf{y}(\omega) = \boldsymbol{y}\}$ and $p_{\mathbf{y}}(\boldsymbol{y}) = \int p_{\mathbf{x},\mathbf{y}}(\boldsymbol{x}, \boldsymbol{y})d\boldsymbol{x}$ is the marginal density. In this vector notation, for the random vectors $\mathbf{x} = \begin{bmatrix} \mathrm{x}_1 & \cdots & \mathrm{x}_n \end{bmatrix}^{\mathrm{T}}$ and $\mathbf{y} = \begin{bmatrix} \mathrm{y}_1 & \cdots & \mathrm{y}_m \end{bmatrix}^{\mathrm{T}}$, the conditional and marginal densities can be written in detail, respectively, as

$$p_{\mathbf{x}|\mathbf{y}}(\boldsymbol{x}|\boldsymbol{y}) = p_{\mathrm{x}_1,\cdots,\mathrm{x}_n|\mathrm{y}_1,\cdots,\mathrm{y}_n}(x_1, \cdots, x_n|y_1, \cdots, y_m) \tag{3.35}$$

and

$$\begin{aligned} p_{\mathbf{y}}(\boldsymbol{y}) &= \int p_{\mathbf{x},\mathbf{y}}(\boldsymbol{x}, \boldsymbol{y})d\boldsymbol{x} \\ &= \int \cdots \int p_{\mathrm{x}_1,\cdots,\mathrm{x}_n,\mathrm{y}_1,\cdots,\mathrm{y}_n}(\xi_1, \cdots, \xi_n, y_1, \cdots, y_m)d\xi_1 \cdots d\xi_n. \end{aligned} \tag{3.36}$$

Considering the random vectors indexed by the time t, namely, vector stochastic processes, the prior information of the density function of $\mathbf{x}(t_0)$ at initial time t_0 can be incorporated in the Bayesian estimator, together with a realization of the sequence of observations of $\mathbf{y}(t)$, to obtain estimates $\hat{\boldsymbol{x}}(t)$ from the conditional density $p_{\mathbf{x}|\mathbf{y}}(\boldsymbol{x}(t)|\boldsymbol{y}(t))$. Given the sequence of observations $Y_{t_l} = \{\boldsymbol{y}(t_0), \cdots, \boldsymbol{y}(t_l)\}$ in discrete instants of time $t_0, \cdots, t_l$, the estimation of $\boldsymbol{x}(t_k)$ is a filtering problem if $k = l$, a prediction problem if $k > l$ and a smoothing problem if $k < l$. We consider the filtering problem, where the evolution in time of the conditional density $p_{\mathbf{x}|\mathbf{y}}(\boldsymbol{x}(t_k)|Y_{t_k})$ is to be found (JAZWINSKI, 1970), by first considering a general stochastic dynamic system represented by a set of Itô (ITÔ, 1951) stochastic differential equations, that can be written in vector form as

$$d\mathbf{x}(t) = \mathbf{f}_c(\mathbf{x}(t), t)dt + \mathbf{G}_c(\mathbf{x}(t), t)d\boldsymbol{\mu}(t), \tag{3.37}$$

where the process $\mathbf{x}(t) \in \mathbb{R}^{n \times 1}$ generated by the Itô's equation is a Markov process (JAZWINSKI, 1970), $\mathbf{f}_c(\mathbf{x}(t), t) \in \mathbb{R}^{n \times 1}$ is a nonlinear vector function of $\mathbf{x}(t)$, $\boldsymbol{\mu}(t) \in \mathbb{R}^{r \times 1}$ is a vector of Wiener processes exciting the system with incremental covariance $\mathbf{Q}_c(t)dt$ and a noise distribution matrix $\mathbf{G}_c(\mathbf{x}(t), t) \in \mathbb{R}^{n \times r}$ nonlinear in $\mathbf{x}(t)$.

We first present the derivation of the general nonlinear filter based on the Bayesian probabilistic approach for the continuous time random state vector $\mathbf{x}(t)$. Later, we specialize the Bayesian filter to the linear case in discrete time to obtain the

Kalman filter formulation. The derivation mainly follows (JAZWINSKI, 1970). In the following, we simplify our notation by removing the subscript random variables from the probability density function notation, so that, for example, $p_{\mathbf{x}}(\cdot)$ is written as $p(\cdot)$ henceforth. As we are considering GNSS receivers implemented in software, the measurements are available at discrete instants of time. Therefore, we consider the observation equation at discrete instants of time t_k

$$\mathbf{y}(t_k) = \mathbf{h}(\mathbf{x}(t_k), t_k) + \mathbf{n}(t_k), \tag{3.38}$$

where $\mathbf{y}(t_k) \in \mathbb{R}^{m \times 1}$ is the random observation vector, $\mathbf{h}(\mathbf{x}(t_k), t_k) \in \mathbb{R}^{m \times 1}$ is a vector function nonlinear in $\mathbf{x}(t)$, evaluated at t_k, and $\mathbf{n}(t_k) \in \mathbb{R}^{m \times 1}$ is a vector Gaussian sequence $\mathbf{n}(t_k) \sim \mathcal{N}(\mathbf{0}, \mathbf{R}(t_k))$.

The Kolmogorov's forward equation describes the evolution of the transition probability density of the Markov process $\boldsymbol{x}(t)$ generated by Itô's stochastic differential equation, and can be written as (JAZWINSKI, 1970)

$$dp = \mathcal{L}(p)dt, \tag{3.39}$$

for the forward diffusion operator $\mathcal{L}$ defined by

$$\mathcal{L}(\cdot) = -\sum_{i=1}^{n} \frac{\partial(\cdot f_{c_i})}{\partial x_i} + \frac{1}{2} \sum_{i=1}^{n} \sum_{j=1}^{n} \frac{\partial^2 [\cdot (\mathbf{G}_c \mathbf{Q}_c \mathbf{G}_c^{\mathrm{T}})_{ij}]}{\partial x_i \partial x_j}, \tag{3.40}$$

using the simplified notations $p = p(\boldsymbol{x}(t)|\boldsymbol{x}(\tau))$, with $\tau < t$, $\mathbf{G}_c = \mathbf{G}_c(\mathbf{x}(t), t)$, $\mathbf{Q}_c = \mathbf{Q}_c(t)$, f_{c_i} are the elements of $\mathbf{f}_c(\mathbf{x}(t), t)$, and x_i are the elements of $\mathbf{x}(t)$.

Between observations, $t_{k-1} \leq t < t_k$, having $\mathbf{y}(t_{k-1})$ available, the Kolmogorov's forward equation can be used to compute $p(\boldsymbol{x}(t)|Y_{t_{k-1}})$ with initial condition $p(\boldsymbol{x}(t_{k-1})|Y_{t_{k-1}})$, as (JAZWINSKI, 1970)

$$dp(\boldsymbol{x}(t)|Y_{t_{k-1}}) = \mathcal{L}(p(\boldsymbol{x}(t)|Y_{t_{k-1}}))dt. \tag{3.41}$$

At t_k, with the observation $\mathbf{y}(t_k)$ available, we get from Bayes' rule

$$\begin{aligned} p(\boldsymbol{x}(t_k)|Y_{t_k}) &= \frac{p(Y_{t_k}|\boldsymbol{x}(t_k))p(\boldsymbol{x}(t_k))}{p(Y_{t_k})} \\ &= \frac{p(\boldsymbol{y}(t_k), Y_{t_{k-1}}|\boldsymbol{x}(t_k))p(\boldsymbol{x}(t_k))}{p(\boldsymbol{y}(t_k), Y_{t_{k-1}})}. \end{aligned} \tag{3.42}$$

Sequential application of the conditional probability definition on the term $p(\boldsymbol{y}(t_k), Y_{t_{k-1}}|\boldsymbol{x}(t_k))$ leads to

$$
\begin{aligned}
p(\boldsymbol{y}(t_k), Y_{t_{k-1}}|\boldsymbol{x}(t_k)) &= \frac{p(\boldsymbol{y}(t_k), Y_{t_{k-1}}, \boldsymbol{x}(t_k))}{p(\boldsymbol{x}(t_k))} \\
&= \frac{p(\boldsymbol{y}(t_k)|Y_{t_{k-1}}, \boldsymbol{x}(t_k))p(Y_{t_{k-1}}, \boldsymbol{x}(t_k))}{p(\boldsymbol{x}(t_k))} \\
&= \frac{p(\boldsymbol{y}(t_k)|Y_{t_{k-1}}, \boldsymbol{x}(t_k))p(Y_{t_{k-1}}|\boldsymbol{x}(t_k))p(\boldsymbol{x}(t_k))}{p(\boldsymbol{x}(t_k))} \\
&= p(\boldsymbol{y}(t_k)|Y_{t_{k-1}}, \boldsymbol{x}(t_k))p(Y_{t_{k-1}}|\boldsymbol{x}(t_k)).
\end{aligned}
\tag{3.43}
$$

Equivalently, application of the conditional probability definition to the denominator term yields $p(\boldsymbol{y}(t_k), Y_{t_{k-1}}) = p(\boldsymbol{y}(t_k)|Y_{t_{k-1}})p(Y_{t_{k-1}})$. Returning to the Bayes' rule, we get

$$
\begin{aligned}
p(\boldsymbol{x}(t_k)|Y_{t_k}) &= \frac{p(\boldsymbol{y}(t_k)|Y_{t_{k-1}}, \boldsymbol{x}(t_k))p(Y_{t_{k-1}}|\boldsymbol{x}(t_k))p(\boldsymbol{x}(t_k))}{p(\boldsymbol{y}(t_k)|Y_{t_{k-1}})p(Y_{t_{k-1}})} \\
&= \frac{p(\boldsymbol{y}(t_k)|Y_{t_{k-1}}, \boldsymbol{x}(t_k))p(\boldsymbol{x}(t_k)|Y_{t_{k-1}})p(Y_{t_{k-1}})p(\boldsymbol{x}(t_k))}{p(\boldsymbol{y}(t_k)|Y_{t_{k-1}})p(Y_{t_{k-1}})p(\boldsymbol{x}(t_k))} \\
&= \frac{p(\boldsymbol{y}(t_k)|Y_{t_{k-1}}, \boldsymbol{x}(t_k))p(\boldsymbol{x}(t_k)|Y_{t_{k-1}})}{p(\boldsymbol{y}(t_k)|Y_{t_{k-1}})},
\end{aligned}
\tag{3.44}
$$

where, from the first to the second line, the Bayes' rule was applied to obtain $p(Y_{t_{k-1}}|\boldsymbol{x}(t_k)) = \frac{p(\boldsymbol{x}(t_k)|Y_{t_{k-1}})p(Y_{t_{k-1}})}{p(\boldsymbol{x}(t_k))}$. Since the sequence $\mathbf{n}(t_k)$ is white, $p(\boldsymbol{y}(t_k)|Y_{t_{k-1}}, \boldsymbol{x}(t_k)) = p(\boldsymbol{y}(t_k)|\boldsymbol{x}(t_k))$. Similarly, we can also substitute the marginal density in the denominator, resulting in

$$
\begin{aligned}
p(\boldsymbol{x}(t_k)|Y_{t_k}) &= \frac{p(\boldsymbol{y}(t_k)|\boldsymbol{x}(t_k))p(\boldsymbol{x}(t_k)|Y_{t_{k-1}})}{p(\boldsymbol{y}(t_k)|Y_{t_{k-1}})} \\
&= \frac{p(\boldsymbol{y}(t_k)|\boldsymbol{x}(t_k))p(\boldsymbol{x}(t_k)|Y_{t_{k-1}})}{\int p(\boldsymbol{y}(t_k)|\boldsymbol{x}(t_k))p(\boldsymbol{x}(t_k)|Y_{t_{k-1}})d\boldsymbol{x}(t_k)}.
\end{aligned}
\tag{3.45}
$$

The posterior density $p(\boldsymbol{x}(t_k)|Y_{t_k})$ is decomposed in three general terms: the prior density $p(\boldsymbol{x}(t_k)|Y_{t_{k-1}})$, which defines the knowledge of the model; the likelihood $p(\boldsymbol{y}(t_k)|\boldsymbol{x}(t_k))$, which determines the observation model; and the evidence $p(\boldsymbol{y}(t_k)|Y_{t_{k-1}}) = \int p(\boldsymbol{y}(t_k)|\boldsymbol{x}(t_k))p(\boldsymbol{x}(t_k)|Y_{t_{k-1}})d\boldsymbol{x}(t_k)$. These terms are the essence of Bayesian filtering (CHEN, 2003). Once $p(\boldsymbol{y}(t_k)|\boldsymbol{x}(t_k))$ is determined, the equation above will provide the difference equation for the conditional density at an observation. Since $p(\boldsymbol{y}(t_k)|\boldsymbol{x}(t_k)) = p(\boldsymbol{y}(t_k) - \mathbf{h}(\mathbf{x}(t_k), t_k))$ and $\mathbf{n}(t_k) \sim \mathcal{N}(\mathbf{0}, \mathbf{R}(t_k))$, we get

for the likelihood (JAZWINSKI, 1970)

$$p(\boldsymbol{y}(t_k)|\boldsymbol{x}(t_k)) = \frac{1}{(2\pi)^{m/2}\det(\mathbf{R}(t_k))^{1/2}}$$
$$e^{-\frac{1}{2}[\boldsymbol{y}(t_k)-\mathbf{h}(\mathbf{x}(t_k),t_k)]^{\mathrm{T}}\mathbf{R}(t_k)^{-1}[\boldsymbol{y}(t_k)-\mathbf{h}(\mathbf{x}(t_k),t_k)]}. \quad (3.46)$$

For the scalar function $\gamma(\boldsymbol{x}(t))$, twice continuously differentiable, we can define the expectation

$$\hat{\gamma}_\tau(\boldsymbol{x}(t)) \triangleq E[\gamma(\boldsymbol{x}(t))|Y_\tau] = \int \gamma(\boldsymbol{x}(t))p(\boldsymbol{x}(t)|Y_\tau)d\boldsymbol{x}(t), \quad (3.47)$$

where $E[\cdot]$ is the expectation operator, and $t \geq \tau$. Since $p(\boldsymbol{x}(t)|Y_\tau)$ satisfy the Kolmogorov's forward equation, the evolution of $\hat{\gamma}_\tau(\boldsymbol{x}(t))$ can be obtained between observations, at $t_{k-1} \leq t < t_k$, by (JAZWINSKI, 1970)

$$d\hat{\gamma}_{t_{k-1}}(\boldsymbol{x}(t)) = E[\gamma_{\boldsymbol{x}}^{\mathrm{T}}\mathbf{f}_c(\mathbf{x}(t),t)|Y_{t_{k-1}}]dt + \frac{1}{2}\mathrm{Tr}(E[\mathbf{G}_c\mathbf{Q}_c\mathbf{G}_c^{\mathrm{T}}\gamma_{\boldsymbol{x}\boldsymbol{x}}|Y_{t_{k-1}}])dt, \quad (3.48)$$

where $\mathrm{Tr}(\cdot)$ is the trace of a matrix, $\mathbf{G}_c = \mathbf{G}_c(\mathbf{x}(t),t)$, $\mathbf{Q}_c = \mathbf{Q}_c(t)$, $\gamma_{\boldsymbol{x}}$ is the gradient of the function and $\gamma_{\boldsymbol{x}\boldsymbol{x}}$ is the Hessian matrix. At observations, using (3.45), we get (JAZWINSKI, 1970)

$$\hat{\gamma}_{t_k}(\boldsymbol{x}(t_k)) = \int \gamma(\boldsymbol{x}(t))p(\boldsymbol{x}(t)|Y_{t_k})d\boldsymbol{x}(t)$$
$$= \frac{E[\gamma(\boldsymbol{x}(t_k))p(\boldsymbol{y}(t_k)|\boldsymbol{x}(t_k))|Y_{t_{k-1}}]}{E[p(\boldsymbol{y}(t_k)|\boldsymbol{x}(t_k))|Y_{t_{k-1}}]}, \quad (3.49)$$

with $\boldsymbol{y}(t_k)$ fixed, so the right-hand side is a function of $\boldsymbol{y}(t_k)$. Equations (3.48) and (3.49) allow the determination of the evolution of all the moments of the conditional density. The conditional mean can be obtained by

$$\hat{\boldsymbol{x}}_\tau(t) = E[\boldsymbol{x}(t)|Y_\tau], \quad (3.50)$$

and the conditional covariance matrix by

$$\mathbf{P}_\tau(t) = E[(\boldsymbol{x}(t) - \hat{\boldsymbol{x}}_\tau(t))(\boldsymbol{x}(t) - \hat{\boldsymbol{x}}_\tau(t))^{\mathrm{T}}|Y_\tau]$$
$$= E[\boldsymbol{x}(t)\boldsymbol{x}^{\mathrm{T}}(t)|Y_\tau] - \hat{\boldsymbol{x}}_\tau(t)\hat{\boldsymbol{x}}_\tau^{\mathrm{T}}(t), \quad (3.51)$$

by setting, respectively, $\gamma(\boldsymbol{x}(t)) = x_i$ and $\gamma(\boldsymbol{x}(t)) = x_i x_j$, since $\gamma(\cdot)$ was defined as a scalar function. The generalization to vectors and matrices can be obtained, therefore, by the composition with the application to their elements. Thus, between

observations, at $t_{k-1} \leq t < t_k$, we get for the conditional mean and covariance (JAZWINSKI, 1970)

$$
\begin{aligned}
\frac{d\hat{\boldsymbol{x}}_{t_{k-1}}(t)}{dt} &= \hat{\mathbf{f}}_{c_{t_{k-1}}}(\mathbf{x}(t), t) \\
\frac{d\mathbf{P}_{t_{k-1}}(t)}{dt} &= (E[\boldsymbol{x}(t)\mathbf{f}_c^{\mathrm{T}}(\mathbf{x}(t), t)|Y_{t_{k-1}}] - \hat{\boldsymbol{x}}_{t_{k-1}}(t)\hat{\mathbf{f}}_{c_{t_{k-1}}}^{\mathrm{T}}(\mathbf{x}(t), t)) \\
&\quad + (E[\mathbf{f}_c(\mathbf{x}(t), t)\boldsymbol{x}^{\mathrm{T}}(t)|Y_{t_{k-1}}] - \hat{\mathbf{f}}_{c_{t_{k-1}}}(\mathbf{x}(t), t)\hat{\boldsymbol{x}}_{t_{k-1}}^{\mathrm{T}}(t)) \\
&\quad + E[\mathbf{G}_c(\mathbf{x}(t), t)\mathbf{Q}_c(t)\mathbf{G}_c^{\mathrm{T}}(\mathbf{x}(t), t)|Y_{t_{k-1}}],
\end{aligned}
\tag{3.52}
$$

and at observation at t_k we get (JAZWINSKI, 1970)

$$
\begin{aligned}
\hat{\boldsymbol{x}}_{t_k}(t_k) &= \frac{E[\boldsymbol{x}(t_k)p(\boldsymbol{y}(t_k)|\boldsymbol{x}(t_k))|Y_{t_{k-1}}]}{E[p(\boldsymbol{y}(t_k)|\boldsymbol{x}(t_k))|Y_{t_{k-1}}]} \\
\mathbf{P}_{t_k}(t_k) &= \frac{E[\boldsymbol{x}(t_k)\boldsymbol{x}^{\mathrm{T}}(t_k)p(\boldsymbol{y}(t_k)|\boldsymbol{x}(t_k))|Y_{t_{k-1}}]}{E[p(\boldsymbol{y}(t_k)|\boldsymbol{x}(t_k))|Y_{t_{k-1}}]} - \hat{\boldsymbol{x}}_{t_k}(t_k)\hat{\boldsymbol{x}}_{t_k}^{\mathrm{T}}(t_k).
\end{aligned}
\tag{3.53}
$$

The computation of the first two moments of the conditional density, by the two equations above, depends on higher order moments in the general nonlinear Bayesian filter, so approximations are necessary to obtain a realizable filter. In the case of the linear Bayesian filter, the conditional density is Gaussian, and thus moments of higher order are null and closed forms can be obtained.

Specializing to the system linear in relation to the state vector $\mathbf{x}(t)$, we consider the set of Itô linear differential equations

$$
d\mathbf{x}(t) = \mathbf{F}_c(t)\mathbf{x}(t)dt + \mathbf{G}_c(t)d\boldsymbol{\mu}(t),
\tag{3.54}
$$

with $\mathbf{x}(t) \in \mathbb{R}^{n \times 1}$, $\boldsymbol{\mu}(t) \in \mathbb{R}^{r \times 1}$ is a vector Wiener process with incremental covariance $\mathbf{Q}_c(t)dt$, $\mathbf{F}_c(t) \in \mathbb{R}^{n \times n}$ and $\mathbf{G}_c(t) \in \mathbb{R}^{n \times r}$. And the discrete time observation equation, linear in relation to $\mathbf{x}(t)$

$$
\mathbf{y}(t_k) = \mathbf{H}(t_k)\mathbf{x}(t_k) + \mathbf{n}(t_k),
\tag{3.55}
$$

with $\mathbf{y}(t_k) \in \mathbb{R}^{m \times 1}$, $\mathbf{n}(t_k) \in \mathbb{R}^{m \times 1}$ is a vector Gaussian sequence $\mathbf{n}(t_k) \sim \mathcal{N}(\mathbf{0}, \mathbf{R}(t_k))$ and $\mathbf{H}(t_k) \in \mathbb{R}^{m \times n}$. The initial condition distribution is assumed to be $\mathbf{x}(t_0) \sim \mathcal{N}(\hat{\boldsymbol{x}}(t_0), \mathbf{P}(t_0))$, and $\mathbf{x}(t_0)$, $\boldsymbol{\mu}(t)$ and $\mathbf{n}(t_k)$ are assumed independent.

Between observations, at $t_{k-1} \leq t < t_k$, the Kolmogorov's forward equation (3.41)

for the conditional density becomes (Jazwinski, 1970)

$$\frac{\partial p(\boldsymbol{x}(t)|Y_{t_{k-1}})}{\partial t} = -p(\boldsymbol{x}(t)|Y_{t_{k-1}})\text{Tr}(\mathbf{F}_c(t)) - p_{\boldsymbol{x}}^{\text{T}}\mathbf{F}_c(t)\boldsymbol{x}(t) \tag{3.56}$$
$$+ \frac{1}{2}\text{Tr}(\mathbf{G}_c(t)\mathbf{Q}_c(t)\mathbf{G}_c^{\text{T}}(t)p_{\boldsymbol{xx}}),$$

where $p_{\mathbf{x}}$ and $p_{\mathbf{xx}}$ are, respectively, the gradient and the Hessian of $p(\boldsymbol{x}(t)|Y_{t_{k-1}})$. To obtain the evolution of the conditional mean $\hat{\boldsymbol{x}}_{t_{k-1}}(t)$ and covariance $\mathbf{P}_{t_{k-1}}(t)$ between observations from (3.52), we notice that $\hat{\mathbf{f}}_{c_{t_{k-1}}}(\mathbf{x}(t), t) = \mathbf{F}(t)\hat{\boldsymbol{x}}_{t_{k-1}}(t)$, $E[\mathbf{G}_c(t)\mathbf{Q}_c(t)\mathbf{G}_c^{\text{T}}(t)|Y_{t_{k-1}}] = \mathbf{G}_c(t)\mathbf{Q}_c(t)\mathbf{G}_c^{\text{T}}(t)$, and

$$E[\boldsymbol{x}(t)\mathbf{f}_{c_{t_{k-1}}}^{\text{T}}(\mathbf{x}(t), t)|Y_{t_{k-1}}] - \hat{\boldsymbol{x}}_{t_{k-1}}(t)\hat{\mathbf{f}}_{c_{t_{k-1}}}^{\text{T}}(\mathbf{x}(t), t)$$
$$= E[\boldsymbol{x}(t)\boldsymbol{x}^{\text{T}}(t)\mathbf{F}_c^{\text{T}}(t)|Y_{t_{k-1}}] - \hat{\boldsymbol{x}}_{t_{k-1}}(t)\hat{\boldsymbol{x}}_{t_{k-1}}^{\text{T}}(t)\mathbf{F}_c^{\text{T}}(t)$$
$$= (E[\boldsymbol{x}(t)\boldsymbol{x}^{\text{T}}(t)|Y_{t_{k-1}}] - \hat{\boldsymbol{x}}_{t_{k-1}}(t)\hat{\boldsymbol{x}}_{t_{k-1}}^{\text{T}}(t))\mathbf{F}_c^{\text{T}}(t) \tag{3.57}$$
$$= \mathbf{P}_{t_{k-1}}(t)\mathbf{F}_c^{\text{T}}(t),$$

so that the evolution of the conditional mean and covariance between observations are

$$\frac{d\hat{\boldsymbol{x}}_{t_{k-1}}(t)}{dt} = \mathbf{F}_c(t)\hat{\boldsymbol{x}}_{t_{k-1}}(t)$$
$$\frac{d\mathbf{P}_{t_{k-1}}(t)}{dt} = \mathbf{F}_c(t)\mathbf{P}_{t_{k-1}}(t) + \mathbf{P}_{t_{k-1}}(t)\mathbf{F}_c^{\text{T}}(t) + \mathbf{G}_c(t)\mathbf{Q}_c(t)\mathbf{G}_c^{\text{T}}(t). \tag{3.58}$$

The evolution of the conditional mean and covariance at observations, at t_k, can be computed via (3.45), noticing that

$$p(\boldsymbol{x}(t_k)|Y_{t_{k-1}}) \sim \mathcal{N}(\hat{\boldsymbol{x}}_{t_{k-1}}(t_k), \mathbf{P}_{t_{k-1}}(t_k)), \tag{3.59}$$

$$E[\boldsymbol{y}(t_k)|Y(t_{k-1})] = \mathbf{H}(t_k)\hat{\boldsymbol{x}}_{t_{k-1}}(t_k), \tag{3.60}$$

and

$$E[(\boldsymbol{y}(t_k) - E[\boldsymbol{y}(t_k)|Y(t_{k-1})])(\boldsymbol{y}(t_k) - E[\boldsymbol{y}(t_k)|Y(t_{k-1})])^{\text{T}}|Y(t_{k-1})] =$$
$$\mathbf{H}(t_k)\mathbf{P}_{t_{k-1}}(t_k)\mathbf{H}^{\text{T}}(t_k) + \mathbf{R}(t_k), \tag{3.61}$$

so that $p(\boldsymbol{y}(t_k)|Y(t_{k-1})) \sim \mathcal{N}(\mathbf{H}(t_k)\hat{\boldsymbol{x}}_{t_{k-1}}(t_k), \mathbf{H}(t_k)\mathbf{P}_{t_{k-1}}(t_k)\mathbf{H}^{\text{T}}(t_k) + \mathbf{R}(t_k))$, and

from (3.46), that

$$p(\boldsymbol{y}(t_k)|\boldsymbol{x}(t_k)) = \frac{1}{(2\pi)^{m/2} \det(\mathbf{R}(t_k))^{1/2}}$$
$$e^{-(1/2)[\boldsymbol{y}(t_k)-\mathbf{H}(t_k)\boldsymbol{x}(t_k)]^{\mathrm{T}}\mathbf{R}(t_k)^{-1}[\boldsymbol{y}(t_k)-\mathbf{H}(t_k)\boldsymbol{x}(t_k)]}, \quad (3.62)$$

after substitution in (3.45), considering also that

$$p(\boldsymbol{x}(t_k)|Y_{t_k}) \sim \mathcal{N}(\hat{\boldsymbol{x}}_{t_k}(t_k), \mathbf{P}_{t_k}(t_k)), \quad (3.63)$$

and performing the matrix algebra involved (JAZWINSKI, 1970), we obtain the desired relations

$$\hat{\boldsymbol{x}}_{t_k}(t_k) = \hat{\boldsymbol{x}}_{t_{k-1}}(t_k) + \mathbf{K}(t_k)(\boldsymbol{y}(t_k) - \mathbf{H}(t_k)\hat{\boldsymbol{x}}_{t_{k-1}}(t_k))$$
$$\mathbf{P}_{t_k}(t_k) = \mathbf{P}_{t_{k-1}}(t_k) - \mathbf{K}(t_k)\mathbf{H}(t_k)\mathbf{P}_{t_{k-1}}(t_k), \quad (3.64)$$

where

$$\mathbf{K}(t_k) \triangleq \mathbf{P}_{t_{k-1}}(t_k)\mathbf{H}^{\mathrm{T}}(t_k)[\mathbf{H}(t_k)\mathbf{P}_{t_{k-1}}(t_k)\mathbf{H}^{\mathrm{T}}(t_k) + \mathbf{R}(t_k)]^{-1} \quad (3.65)$$

is the Kalman gain. The set of Equations (3.58), (3.64) and (3.65), with the initial conditions $\hat{\boldsymbol{x}}(t_0)$ and $\mathbf{P}(t_0)$ semi-positive definite, form the minimum variance Kalman-Bucy filter (KALMAN; BUCY, 1961), for the continuous-discrete system.

To obtain the minimum variance linear filter for the discrete-discrete system, we use the results presented in Section 3.1.3 to obtain difference equations for the conditional mean and covariance between observations. Notice that, in Section 3.1.3, in the discretization process, we preferred to incorporate the noise distribution matrix in the the noise process vector in the resulting difference equation for the process dynamics, resulting in a Gaussian process noise vector $\boldsymbol{\nu}(t_k) \in \mathbb{R}^{n \times 1}$ with covariance $E[\boldsymbol{\nu}(t_k)\boldsymbol{\nu}^{\mathrm{T}}(t_k)] = \mathbf{Q}(t_k)$. The difference equation for the process dynamics is re-written below

$$\mathbf{x}(t_k) = \boldsymbol{\Phi}(t_k, t_{k-1})\mathbf{x}(t_{k-1}) + \boldsymbol{\nu}(t_{k-1}). \quad (3.66)$$

The conditional mean between observations is, therefore

$$\hat{\boldsymbol{x}}_{t_{k-1}}(t_k) = E[\boldsymbol{x}(t_k)|Y_{t_{k-1}}] = \boldsymbol{\Phi}(t_k, t_{k-1})\hat{\boldsymbol{x}}_{t_{k-1}}(t_{k-1}), \quad (3.67)$$

and the conditional covariance between observations is

$$
\begin{aligned}
\mathbf{P}_{t_{k-1}}(t_k) =& E[(\boldsymbol{x}(t_k) - \hat{\boldsymbol{x}}_{t_{k-1}}(t_k))(\boldsymbol{x}(t_k) - \hat{\boldsymbol{x}}_{t_{k-1}}(t_k))^{\mathrm{T}}|Y_{t_{k-1}}] \\
=& E[(\boldsymbol{\Phi}(t_k, t_{k-1})\boldsymbol{x}(t_{k-1}) + \boldsymbol{\nu}(t_{k-1}) - \boldsymbol{\Phi}(t_k, t_{k-1})\hat{\boldsymbol{x}}_{t_{k-1}}(t_{k-1})) \\
& (\boldsymbol{\Phi}(t_k, t_{k-1})\boldsymbol{x}(t_{k-1}) + \boldsymbol{\nu}(t_{k-1}) - \boldsymbol{\Phi}(t_k, t_{k-1})\hat{\boldsymbol{x}}_{t_{k-1}}(t_{k-1}))^{\mathrm{T}}|Y_{t_{k-1}}] \\
=& E[\boldsymbol{\Phi}(t_k, t_{k-1})(\boldsymbol{x}(t_{k-1}) - \hat{\boldsymbol{x}}_{t_{k-1}}(t_{k-1}))(\boldsymbol{x}(t_{k-1}) - \hat{\boldsymbol{x}}_{t_{k-1}}(t_{k-1}))^{\mathrm{T}}\boldsymbol{\Phi}(t_k, t_{k-1})^{\mathrm{T}} \\
& + \boldsymbol{\nu}(t_{k-1})\boldsymbol{\nu}^{\mathrm{T}}(t_{k-1})|Y_{t_{k-1}}] \\
=& \boldsymbol{\Phi}(t_k, t_{k-1})\mathbf{P}_{t_{k-1}}(t_{k-1})\boldsymbol{\Phi}^{\mathrm{T}}(t_k, t_{k-1}) + \mathbf{Q}(t_{k-1}).
\end{aligned}
\tag{3.68}
$$

The set of Equations (3.67), (3.68), (3.64) and (3.65), with the initial conditions $\hat{\boldsymbol{x}}(t_0)$ and $\mathbf{P}(t_0)$ semi-positive definite, form the minimum variance Kalman filter (KALMAN, 1960).

The Kalman filter can be modified to be employed to systems with nonlinear process and/or observation equations, providing a suboptimal solution. This is the case of the extended Kalman filter, resulting from a linearization procedure of the nonlinear equations of the system. In the more general case of the extended Kalman filter, the state evolution and the measurement equations are formed by nonlinear functions according to the discrete system equations

$$
\begin{aligned}
\mathbf{x}[k] &= \mathbf{f}(\mathbf{x}[k-1]) + \boldsymbol{\nu}[k-1] \\
\mathbf{y}[k] &= \mathbf{h}(\mathbf{x}[k]) + \mathbf{n}[k],
\end{aligned}
\tag{3.69}
$$

where $\mathbf{f}(\cdot) \in \mathbb{R}^{n\times 1}$ and $\mathbf{h}(\cdot) \in \mathbb{R}^{m\times 1}$ are nonlinear functions of the state vector $\mathbf{x}[k] \in \mathbb{R}^{n\times 1}$, $\mathbf{y}[k] \in \mathbb{R}^{m\times 1}$ is the measurement vector, $\boldsymbol{\nu}[k] \in \mathbb{R}^{n\times 1}$ and $\mathbf{n}[k] \in \mathbb{R}^{m\times 1}$ are independent Gaussian process and measurement noises whose covariance matrices are $\mathbf{Q}[k] \in \mathbb{R}^{n\times n}$ and $\mathbf{R}[k] \in \mathbb{R}^{m\times m}$, respectively. The propagation step and the update step of the Kalman filter can be given as

$$
\begin{aligned}
\hat{\mathbf{x}}[k|k-1] &= \mathbf{f}(\hat{\mathbf{x}}[k-1]) \\
\mathbf{P}[k|k-1] &= \mathbf{F}[k-1]\mathbf{P}[k-1]\mathbf{F}^{\mathrm{T}}[k-1] + \mathbf{Q}[k-1]
\end{aligned}
\tag{3.70}
$$

and

$$
\begin{aligned}
\mathbf{K}[k] &= \mathbf{P}[k|k-1]\mathbf{H}^{\mathrm{T}}[k](\mathbf{H}[k]\mathbf{P}[k|k-1]\mathbf{H}^{\mathrm{T}}[k] + \mathbf{R}[k])^{-1} \\
\mathbf{P}[k] &= (\mathbf{I} - \mathbf{K}[k]\mathbf{H}[k])\mathbf{P}[k|k-1] \\
\hat{\mathbf{x}}[k] &= \hat{\mathbf{x}}[k|k-1] + \mathbf{K}[k]\{\mathbf{y}[k] - \mathbf{h}(\hat{\mathbf{x}}[k|k-1])\}.
\end{aligned}
\tag{3.71}
$$

The measurement residual or innovation is $\boldsymbol{\varepsilon}[k] = \mathbf{y}[k] - \mathbf{h}(\hat{\mathbf{x}}[k|k-1])$, $\mathbf{P}[k] \in \mathbb{R}^{n\times n}$ is the state covariance matrix and $\mathbf{K}[k] \in \mathbb{R}^{n\times m}$ is the Kalman gain. In the case

of the Kalman filter, the process and measurement equations are linear functions of the state vector, so that $\mathbf{f}(\mathbf{x}[k-1]) = \mathbf{F}[k-1]\mathbf{x}[k-1]$ with $\mathbf{F}[k-1] \in \mathbb{R}^{n \times n}$ and $\mathbf{h}(\mathbf{x}[k]) = \mathbf{H}[k]\mathbf{x}[k]$ with $\mathbf{H}[k] \in \mathbb{R}^{m \times n}$, respectively. In the case of the extended Kalman filter, $\mathbf{f}(\mathbf{x}[k-1])$ and/or $\mathbf{h}(\mathbf{x}[k])$ are nonlinear functions of the states, whose Jacobians

$$\mathbf{F}[k-1] = \left.\frac{\partial \mathbf{f}}{\partial \mathbf{x}}\right|_{\mathbf{x}=\hat{\mathbf{x}}[k-1]}, \ \mathbf{H}[k] = \left.\frac{\partial \mathbf{h}}{\partial \mathbf{x}}\right|_{\mathbf{x}=\hat{\mathbf{x}}[k|k-1]} \tag{3.72}$$

are employed in the prediction and update equations of the extended Kalman filter.

4 REAL-TIME SCINTILLATION MONITORING EXPLOITING LOS-ONLY TRACKING LOOPS

Ionospheric scintillation monitoring contributes to the scientific research of the ionosphere, where networks of spatially distributed monitoring stations provide data to support the study of the dynamics of the related physical processes. Monitoring stations are deployed for other purposes also, such as for space weather research in general (XU et al., 2015a), or as part of the infrastructure for aircraft instrument landing systems (MAYER et al., 2009). They perform tasks such as forecast, broadcast, and correction of information related to ionospheric scintillation. Usually, in a monitoring station, a static receiver with a known position and precise reference oscillator provides estimates of the dynamics of the LOS to the tracked satellites with additional accurate information, such as the clock biases and ephemerides of the tracked satellites (LEE et al., 2017), (DIERENDONCK et al., 1993). Although other factors such as multipath, related to the surrounding environment, can also affect scintillation estimation, it is essential to have highly reliable receivers to isolate the scintillation induced effects from the LOS dynamics tracked by the receivers. Also, the occurrence of cycle slips, for example, impair scintillation amplitude and phase estimation (BANVILLE; LANGLEY, 2013).

Originally, the traditional tracking loop structures implemented in monitoring receivers are composed of PLLs and/or FLLs, which are not directly providing estimates of amplitude or phase scintillation. Their design parameters are fixed and adjusted for LOS-only tracking. Robustness to ionospheric scintillation in such structures can be improved via the tuning of parameters such as the noise bandwidth (LEGRAND et al., 2000) of PLLs or employing an FLL-assisted PLL structure (XU et al., 2015a), for example. The typical approach to obtain scintillation estimates based on those structures consists of the analysis of stored receiver data, where batch post-processing algorithms are employed to the I/Q outputs of the prompt correlator and the tracked carrier phase. After detrending, filtering with Butterworth filters, compensation of oscillator effects common to all processing receiver channels, LOS dynamics and any possible multipath effect can be separated from scintillation amplitude and phase, from which scintillation metrics such as the S4 index and phase standard deviation can be computed (DIERENDONCK et al., 1993), (FREMOUW et al., 1978), (ZHANG et al., 2010), (FORTE, 2007), (O'HANLON et al., 2011),(NIU et al., 2012).

In this chapter, we explore the linear approximation of the traditional FLL designed to track the LOS dynamics, recovering complementary information in the frequency

47

domain present in its sensitivity and complementary sensitivity transfer functions, to design a real-time scintillation monitoring algorithm based on LTI filtering of available internal observables of the traditional FLL. The algorithm provides estimates of the scintillation phase, from which the scintillation phase metrics can be computed also in real-time. It can be either added to an already implemented tracking loop in a receiver for real-time estimation or can be employed in data post-processing if the observables are stored. We emphasize its real-time application, which can be important for different applications that require ionospheric monitoring, for example differential GNSS (D-GNSS). The parameters of the filters can be adjusted to delimit the frequency band of interest, as is typically done in the batch post-processing with Butterworth filters (NIU et al., 2012), (ZHANG et al., 2010). The approach is extended to LOS-only Kalman FLLs by analogy of the Kalman filter gains with the parameters of the linear approximation of the traditional FLL. Similarly, a simple modification can be introduced in the algorithm to allow it to be employed to LOS-only traditional and Kalman PLLs.

The performance of the algorithm is evaluated with numerical simulations using synthetic scintillation data generated by the CSM (HUMPHREYS et al., 2010) and real collected data by a COTS professional GNSS receiver, where we show that the monitoring performance of the scintillation phase estimation for subsequent computation of its standard deviation is similar to the batch post-processing procedure performance, with the advantage of its real-time capability and reduced complexity, since it is based on LTI filtering, avoiding some operations of the batch post-processing, such as the polynomial fitting in the phase detrending.

Initially, the structure of a FLL with a noncoherent DLL traditionally implemented in GNSS receivers is presented. From this structure, we obtain a linear approximation of the traditional FLL, which is compared to the nonlinear implementation via numeric simulations, in test cases representing slight errors in the initial conditions provided by the acquisition stage of a satellite and sinusoidal phase disturbances added to the input signals. The complementary frequency content of the sensitivity and the complementary sensitivity transfer functions is highlighted, and the internal observables presenting such complementary characteristic are defined. Then, we show how to derive the observables from the Kalman FLL by analogy with the linear approximation of the traditional FLL. After that, we present the real-time monitoring algorithm implementation for the traditional and Kalman FLLs and how the algorithm can be adapted to traditional and Kalman PLLs. Finally, we present the results of the performance evaluation with synthetic and real scintillation data.

4.1 Linear analysis of traditional carrier tracking loops

Traditionally, code and carrier synchronization in a GNSS receiver are performed by, respectively, a DLL and a PLL or FLL. In the most general case, the code and carrier loops are implemented as separate loops, although the synchronization of one loop influences the synchronization of the other. In order to improve some characteristics of the tracking loops, such as noise reduction, one loop can be aided by observables from other loops or by augmentation signals, hence mixing code loop with carrier loop or mixing phase and frequency loops in a carrier tracking loop, and thus creating an additional coupling between them (KAPLAN; HEGARTY, 2017).

We consider a receiver composed of a traditional FLL with a noncoherent DLL, without any augmentation signals. The traditional FLL is composed of elements such as a linear loop filter, a numerically controlled oscillator (NCO), a carrier generator and signal mixer, a prompt correlator, and a frequency discriminator. The tracking loops not considered as "traditional" in this work are the ones based on the Kalman filter, to be presented later. A traditional FLL with a noncoherent DLL receiver is shown in Figure 4.1, where $\mathbf{e}[k] \in \mathbb{R}^{N \times 1}$, $\mathbf{l}[k] \in \mathbb{R}^{N \times 1}$, and $\mathbf{p}[k] \in \mathbb{R}^{N \times 1}$ are vectors formed by N samples of the kth integration period of the sampled early, late, and prompt code replicas, respectively. Similarly, $\mathbf{s}[k] \in \mathbb{C}^{N \times 1}$ is the vector of the baseband GNSS input signal samples, as defined in (2.14), and the superscript $^{\mathrm{H}}$ denotes Hermitian (conjugate transpose).

Figure 4.1 - Traditional FLL/DLL receiver.
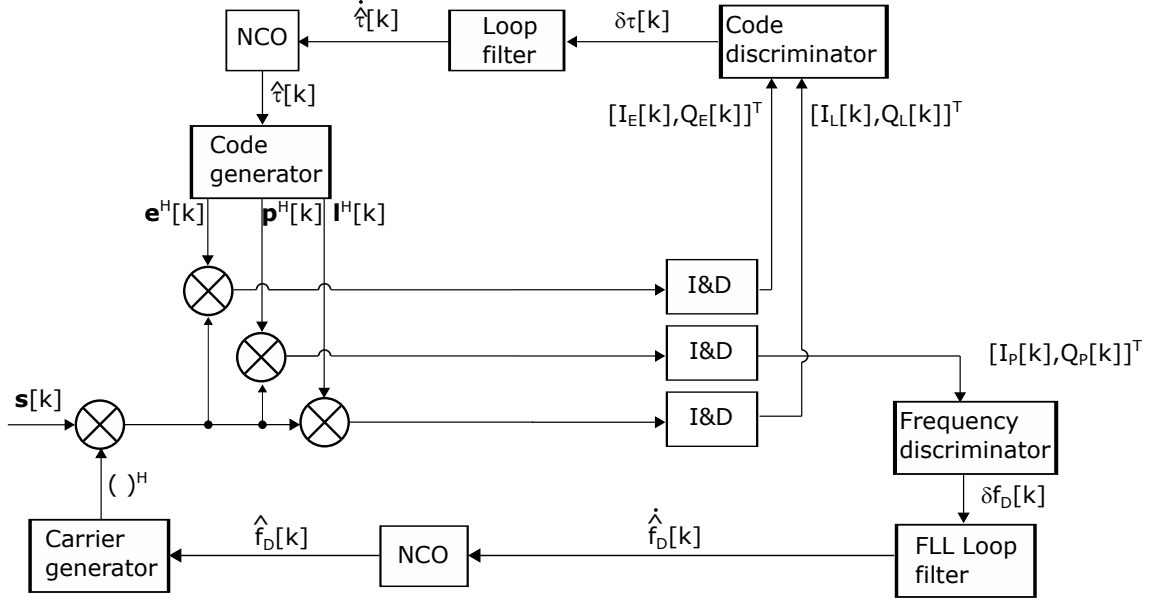
SOURCE: Author's production.

Each correlator branch includes an integrate and dump (I&D) block, and $[I_e[k], Q_e[k]]^{\mathrm{T}}$, $[I_l[k], Q_l[k]]^{\mathrm{T}}$, and $[I_p[k], Q_p[k]]^{\mathrm{T}}$ are, respectively, the early, late, and prompt output I/Q samples. Frequency and code delay errors computed by frequency and code discriminators are represented by $\delta f_D[k]$ and $\delta \tau[k]$, respectively. The code and carrier replicas are generated with the estimated code delay $\hat{\tau}[k]$ and the estimated Doppler shift $\hat{f}_D[k]$ from the code and carrier NCOs, respectively. The code delay rate $\dot{\hat{\tau}}[k]$ and the Doppler drift $\dot{\hat{f}}_D[k]$ are estimated by the DLL and FLL loop filters, respectively.

Therefore, throughout this work, we consider that a "traditional" FLL, is the FLL composed of elements such as loop filter, NCO, carrier generation, and the frequency discriminator. Equivalently, we consider that a "traditional" PLL is composed of the same elements, with the exception of the discriminator, where an arc-tangent phase discriminator is employed in the PLLs.

Neglecting the coupling between the code and carrier loops, a linear approximation for the FLL in the discrete-time domain can be obtained by considering the NCO block as an integrator, and the operations of mixing the input signal with the

generated carrier replica, correlation, and frequency discriminator computation as the difference $f_D[k] - \hat{f}_D[k] = \delta f_D[k]$. This is valid when synchronization errors in code and carrier loops are relatively small. With these assumptions, we can establish the block diagram as shown in Figure 4.2 for the linear approximation of the FLL in the z-domain. We prefer to present the analysis in discrete time, with the z-transforms, to emphasize the real-time application of the monitoring algorithm to GNSS hardware and software receivers. The detailed block diagram is presented in Figure 4.2(a). The frequency discriminator provides the Doppler shift error signal $\delta f_D(z)$, which, according to (2.28), is the derivative of the phase error $\delta\phi(z)$, and $G_{FLL}(z)$ encompasses the loop filter and the NCO. The remaining integrator represents the replica carrier generation from the Doppler frequency shift estimate, as the loop is presented in terms of the phase. A simplified block diagram in terms of Doppler frequency shift only can be obtained by removing the derivative and integration blocks, as shown in Figure 4.2(b). Integration is approximated by Euler's method (EULER, 1768), so that $\frac{1}{s} = \frac{T_I}{1-z^{-1}}$, for the coherent integration period T_I. Euler's method is chosen due to its simplicity, when compared to the bilinear transform, and it provides a good approximation for the coherent integration period and the dynamics considered.

Figure 4.2 - FLL linear approximation.
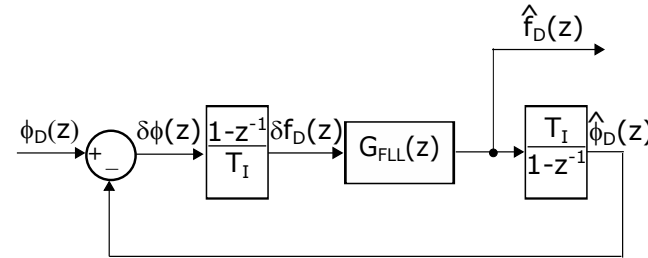
(a) Complete.
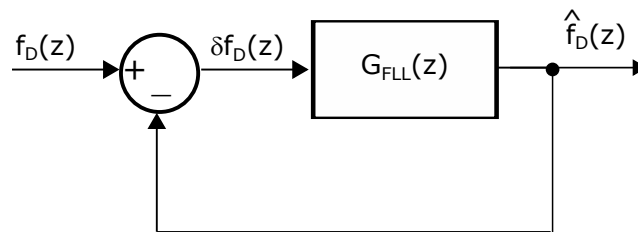
(b) Simplified.

SOURCE: Author's production.

51

The loop filter transfer function, including the NCO integrator, is typically of second or third order (KAPLAN; HEGARTY, 2017), (BORRE et al., 2007). A second order loop filter has the following z-transform

$$G_{FLL}(z) = \frac{(T_I^2\omega_n^2 + 2\xi\omega_n T_I) - 2\xi\omega_n T_I z^{-1}}{1 - 2z^{-1} + z^{-2}}, \tag{4.1}$$

with damping ratio ξ and natural frequency ω_n. Typically, $\xi = 1/\sqrt{2}$, and ω_n is the design parameter. A third order loop filter has the following z-transform

$$G_{FLL}(z) = \frac{\begin{array}{c}(T_I^3\omega_0^3 + a_3 T_I^2\omega_0^2 + b_3 T_I\omega_0) \\ + (-a_3 T_I^2\omega_0^2 - 2b_3 T_I\omega_0)z^{-1} + T_I b_3\omega_0 z^{-2}\end{array}}{1 - 3z^{-1} + 3z^{-2} - z^{-3}}, \tag{4.2}$$

where typically $a_3 = 1.1$ and $b_3 = 2.4$, and ω_0 is the design parameter (KAPLAN; HEGARTY, 2017). Working with a second order loop filter, the closed loop has the following z-transform for the Doppler frequency shift from the total input phase $\phi_T(z) = \phi_D(z) + \phi(z)$

$$\frac{\hat{f}_D(z)}{\phi_T(z)} = \frac{(T_I\omega_n^2 + 2\xi\omega_n) + (-T_I\omega_n^2 - 4\xi\omega_n)z^{-1} + 2\xi\omega_n z^{-2}}{(T_I^2\omega_n^2 + 2\xi\omega_n T_I + 1) + (-2\xi\omega_n T_I - 2)z^{-1} + z^{-2}}. \tag{4.3}$$

The expanded block diagram of Figure 4.2(b) is shown in Figure 4.3, where the internal states of the closed loop are depicted explicitly. The output of the upstream integrator, the state $\hat{f}_{D_1}(z)$, is an estimate of the Doppler frequency drift, but the zeros of its transfer function are different from the zeros of the transfer function to $\hat{\hat{f}}_D(z)$, which is given by the integral of $\hat{f}_D(z)$.

Figure 4.3 - Simplified FLL linear approximation expanded.
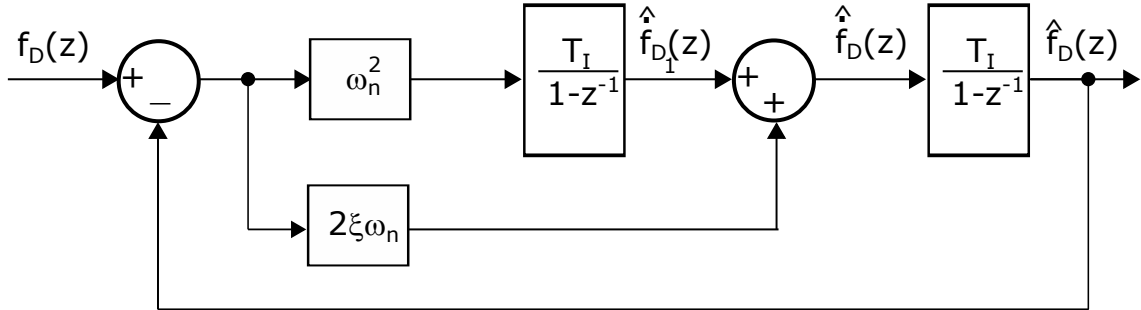
SOURCE: Author's production.

Considering that $\hat{\phi}_D[k]$ can be obtained from the integration of $\hat{f}_D[k]$, the error signal in terms of phase in Figure 4.2(a) is

$$\delta\phi(z) = \phi_T(z) - \hat{\phi}_D(z) \tag{4.4}$$

$$= \phi_T(z) - \frac{T_I}{1 - z^{-1}}\hat{f}_D(z) \tag{4.5}$$

$$= \left(1 - \frac{T_I}{1 - z^{-1}}\frac{\hat{f}_D(z)}{\phi_T(z)}\right)\phi_T(z). \tag{4.6}$$

Therefore, for the second order loop filter, the transfer function for $\delta\phi(z)$ is

$$\frac{\delta\phi(z)}{\phi_T(z)} = \left(1 - \frac{T_I}{1 - z^{-1}}\frac{\hat{f}_D(z)}{\phi_T(z)}\right)$$
$$= \frac{1 - 2z^{-1} + z^{-2}}{(T_I^2\omega_n^2 + 2\xi\omega_n T_I + 1) + (-2\xi\omega_n T_I - 2)z^{-1} + z^{-2}}. \tag{4.7}$$

This phase error has information content in the frequency domain that is complementary to the integral of the Doppler frequency shift estimate $\hat{f}_D(z)$. This can be verified by adding the integral of (4.3) to (4.7), yielding

$$\frac{\hat{f}_D(z)T_I/(1 - z^{-1}) + \delta\phi(z)}{\phi_T(z)} = 1. \tag{4.8}$$

This property also holds for the double integral of $\hat{f}_D(z)$

$$\frac{\hat{f}_D(z)T_I^2/(1 - z^{-1})^2 + \delta\phi(z)}{\phi_T(z)} = 1, \tag{4.9}$$

but not for the double integral of $\hat{f}_{D_1}(z)$.

4.1.1 Numerical evaluations of the linear approximation of the traditional FLL

The frequency domain characteristic of (4.8) can be graphically displayed in a Bode plot. For this, we consider the Laplace transform of (4.3) and (4.7) with the integrator in discrete time represented by $\frac{1}{s} \Leftrightarrow \frac{T_I}{1-z^{-1}}$, yielding

$$\frac{\hat{f}_D(s)}{\phi_T(s)} = \frac{2\xi\omega_n s^2 + \omega_n^2 s}{s^2 + 2\xi\omega_n s + \omega_n^2}, \tag{4.10}$$

and

$$\frac{\delta\phi(s)}{\phi_T(s)} = \frac{s^2}{s^2 + 2\xi\omega_n s + \omega_n^2}.$$ (4.11)

Accordingly, $\frac{1}{s}\frac{\hat{f}_D(s)}{\phi_T(s)} + \frac{\delta\phi(s)}{\phi_T(s)} = 1$. The frequency responses of $\frac{1}{s}\frac{\hat{f}_D(s)}{\phi_T(s)}$ and $\frac{\delta\phi(s)}{\phi_T(s)}$ are shown in the Bode plots of Figure 4.4, for $\xi = 1/\sqrt{2}$ and noise bandwidth $B_n = 10$ Hz, illustrating the low frequency content of $\frac{1}{s}\frac{\hat{f}_D(s)}{\phi_T(s)}$ and the complementary high frequency content of $\frac{\delta\phi(s)}{\phi_T(s)}$. The complementary characteristic can be verified by the Bode plot of the sum of the transfer functions, as shown in 4.5, with zero dB magnitude and zero degree phase at all frequencies, as expected.

Figure 4.4 - Bode plot of $\frac{1}{s}\frac{\hat{f}_D(s)}{\phi_T(s)}$ and $\frac{\delta\phi(s)}{\phi_T(s)}$, for $\xi = 1/\sqrt{2}$ and noise bandwidth $B_n = 10$ Hz.
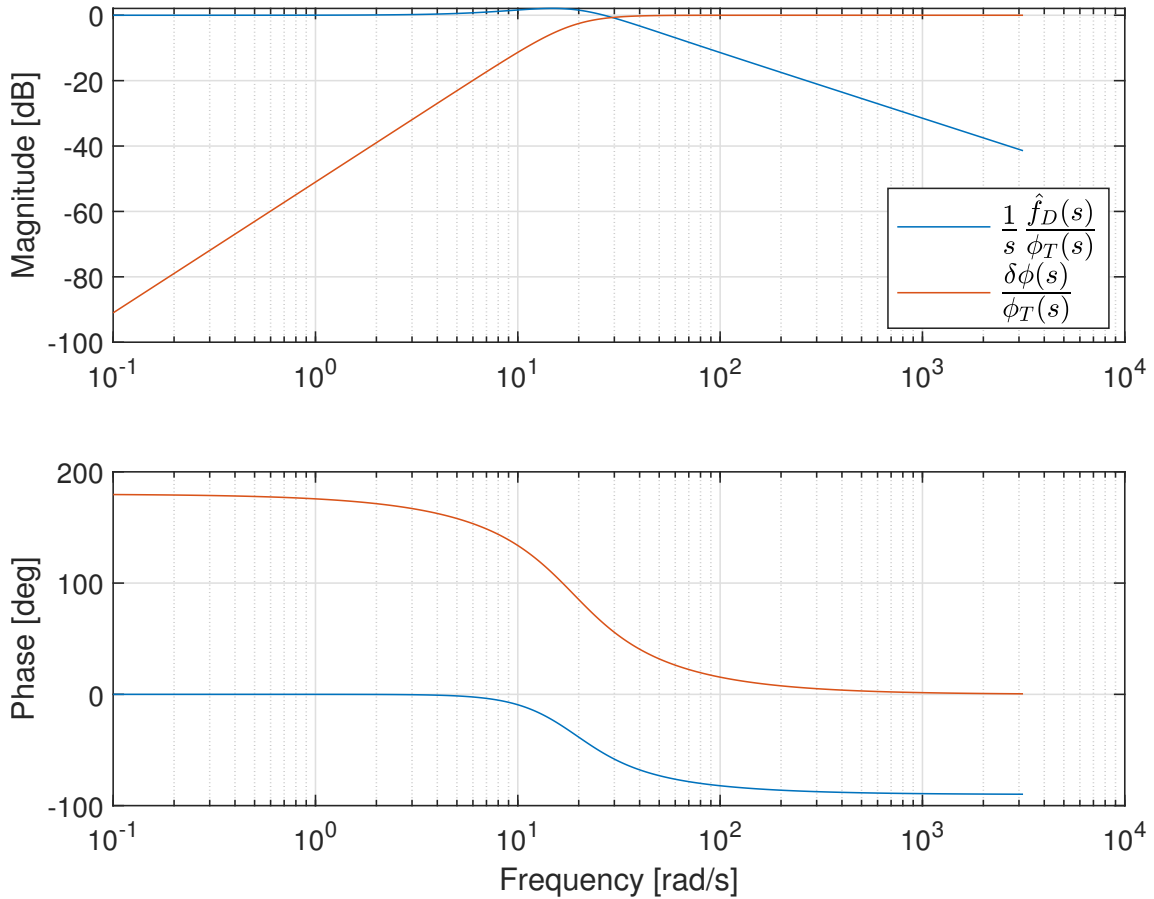
SOURCE: Author's production.

Figure 4.5 - Bode plot of $\frac{\hat{f}_D(s)/s + \delta\phi(s)}{\phi_T(s)}$, for $\xi = 1/\sqrt{2}$ and noise bandwidth $B_n = 10$ Hz.
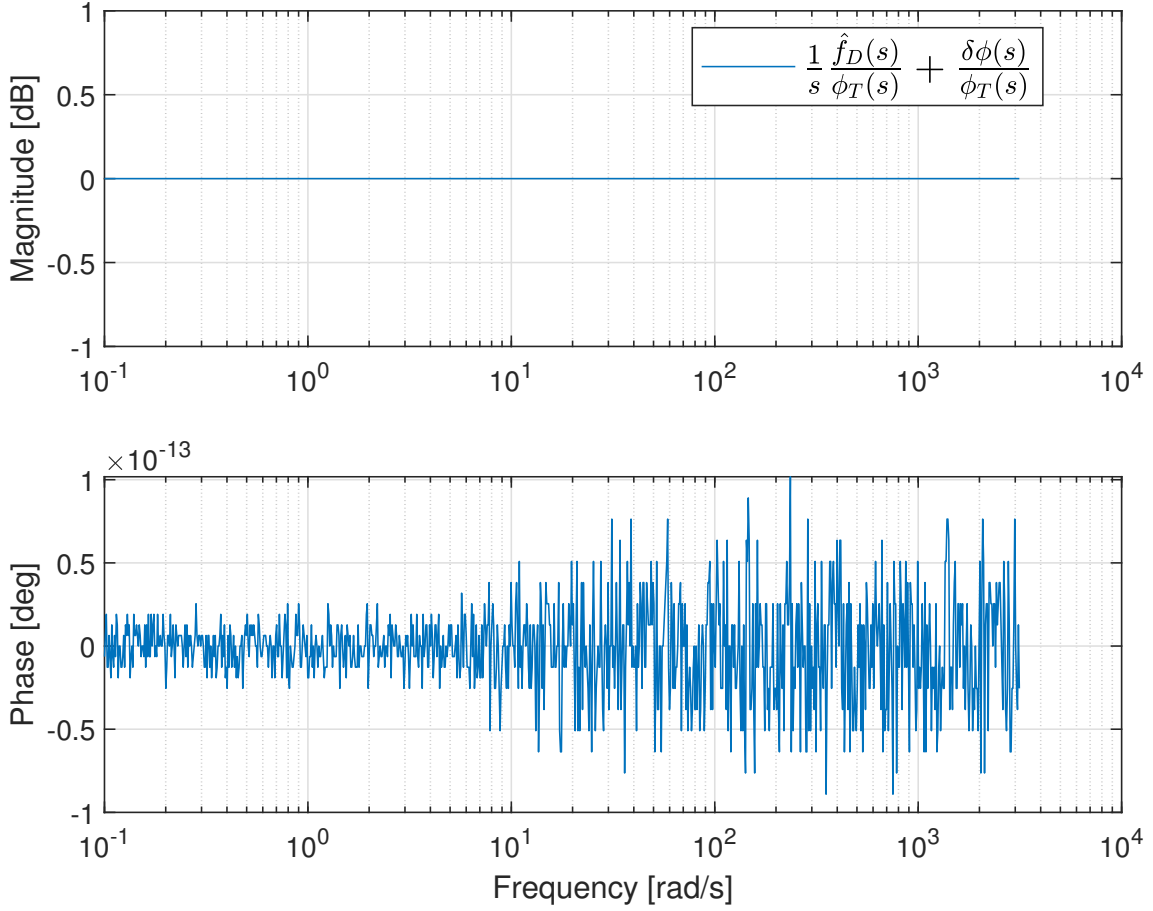
SOURCE: Author's production.

The quality of the linear approximation of the traditional FLL is evaluated by simulations of the nonlinear receiver tracking loop with FLL/DLL with baseband GPS L1 C/A code input signal, introducing disturbances in this input signal, and comparing the dynamic response of the receiver to the dynamic response of the linear approximation of the FLL. The intent is to reinforce via numerical simulations that the linear approximation can represent the nonlinear receiver for the analysis and design of the monitoring algorithm, which is one contribution of this work. The linear approximation itself is not considered a contribution. Therefore, we present the graphs of the dynamic responses to the disturbances for a qualitative evaluation, showing that the response of the linear approximation is close to the nonlinear receiver for the same disturbances applied, and thus the linear approximation is

a good representation of the dynamics of the receiver carrier tracking loop. Initial condition error and sinusoidal disturbances are considered.

The baseband input signal is composed of an initial Doppler shift of 1000 Hz, zero initial phase, an initial code delay of 0.25 Tc, a Doppler drift of 0.94 Hz/s and PRN 1 code sequence with true code delay of 0.25 Tc. The second order FLL damping ratio and noise bandwidth in all simulations regarding the evaluation of the linear approximation are, respectively, $\xi_{FLL} = 1/\sqrt{2}$ and $B_{n_{FLL}} = 10$ Hz (for 2nd order loop filters with $\xi = 1/\sqrt{2}$, ω_n in radians is equal to $1.8856B_n$, with B_n in Hertz (KAPLAN; HEGARTY, 2017)). The code loop employed is a traditional second order DLL with $\xi_{DLL} = 1/\sqrt{2}$ and $B_{n_{DLL}} = 2$ Hz.

The receiver processes baseband input signals composed of a carrier signal defined by the carrier phase and Doppler frequency shift modulating the code sequence of one of the GPS L1 C/A codes. A unitary amplitude is considered. The parameters of the simulated receiver implementing a traditional FLL with a noncoherent DLL are presented in Table 4.1. It integrates 4092 samples at each dump cycle. The receiver bandwidth is twice the sampling frequency.

Table 4.1 - Parameters of the simulated receiver.

Sampling frequency (f_S)	4.092 MHz
Pseudorandom noise (PRN) sequence	1
Early-late correlator spacing (ΔTc)	0.5 chip
Coherent integration time	1 ms

For the initial condition responses evaluation, a slight error in the initial condition of the Doppler shift provided by the acquisition is introduced. For the the evaluation of the responses to sinusoidal disturbances, sine waves of different amplitudes and frequencies are added to the Doppler phase in the baseband input signal. Such disturbances are phase variations of the form

$$\phi(t) = A_\phi \sin[2\pi f_\phi \max\{(t - t_0), 0\}], \tag{4.12}$$

for the amplitude A_ϕ, frequency f_ϕ in Hertz, and applied at time t_0. Thus, the total phase is

$$\phi_T(t) = \phi_D(t) + \phi(t). \tag{4.13}$$

Four combinations of amplitudes and frequencies for the phase variations are con-

sidered:

a) low frequency and low amplitude: $f_\phi = 1$ Hz and $A_\phi = 5\frac{\pi}{180}$;

b) high frequency and low amplitude: $f_\phi = 70$ Hz and $A_\phi = 5\frac{\pi}{180}$;

c) low frequency and high amplitude: $f_\phi = 1$ Hz and $A_\phi = 175\frac{\pi}{180}$;

d) high frequency and high amplitude: $f_\phi = 70$ Hz and $A_\phi = 175\frac{\pi}{180}$.

The amplitude values are in terms of radians of phase variations, equivalent to 5 degrees and 175 degrees for, respectively, low amplitude and high amplitude. In all cases the sinusoidal phase variations are applied at $t_0 = 0.5$ s, and the initial conditions of the linear model integrators and the receiver NCOs are set to the acquisition values $\phi_{D_{acq}} = 0$ rad, $f_{D_{acq}} = 1000$ Hz and $\tau_{acq} = 0.25$ Tc, observing that the code delay τ_{acq} is not applicable to the FLL linear approximation.

4.1.1.1 Initial condition error

A slight error in the Doppler shift initial condition is introduced in the receiver and in the integrator relative to $\hat{f}_D$ in the linear approximation, which is the last integrator of $G_{FLL}(z)$ in Figure 4.2(a), simulating their responses to an error of 10 Hz in the Doppler shift from acquisition, so that $f_{D_{acq}} = 990$ Hz. The baseband input signal is applied to the receiver and the equivalent total carrier frequency $\phi_T(t)$ is applied to the linear model of Figure 4.2(a). The comparison of the Doppler shift estimated by the receiver and by the linear approximation is presented in Figure 4.6, and the comparison of the arc tangent applied to the I/Q prompt correlator in the receiver and the $\delta\phi(t)$ from the linear approximation is presented in Figure 4.7. In Figure 4.6, we also show the true value of the Doppler shift. The linear response is practically superimposed to the nonlinear response, and they track the Doppler shift after the transient due to the initial condition error. Figure 4.7 shows the phase errors practically superimposed as well. Therefore, this simulation shows a good agreement between the receiver and its linear approximation, thus confirming the validity of the linear approximation.

Figure 4.6 - Comparison of $\hat{f}_D(t)$ from the receiver and the FLL linear approximation, in simulation of Doppler shift initial condition error.
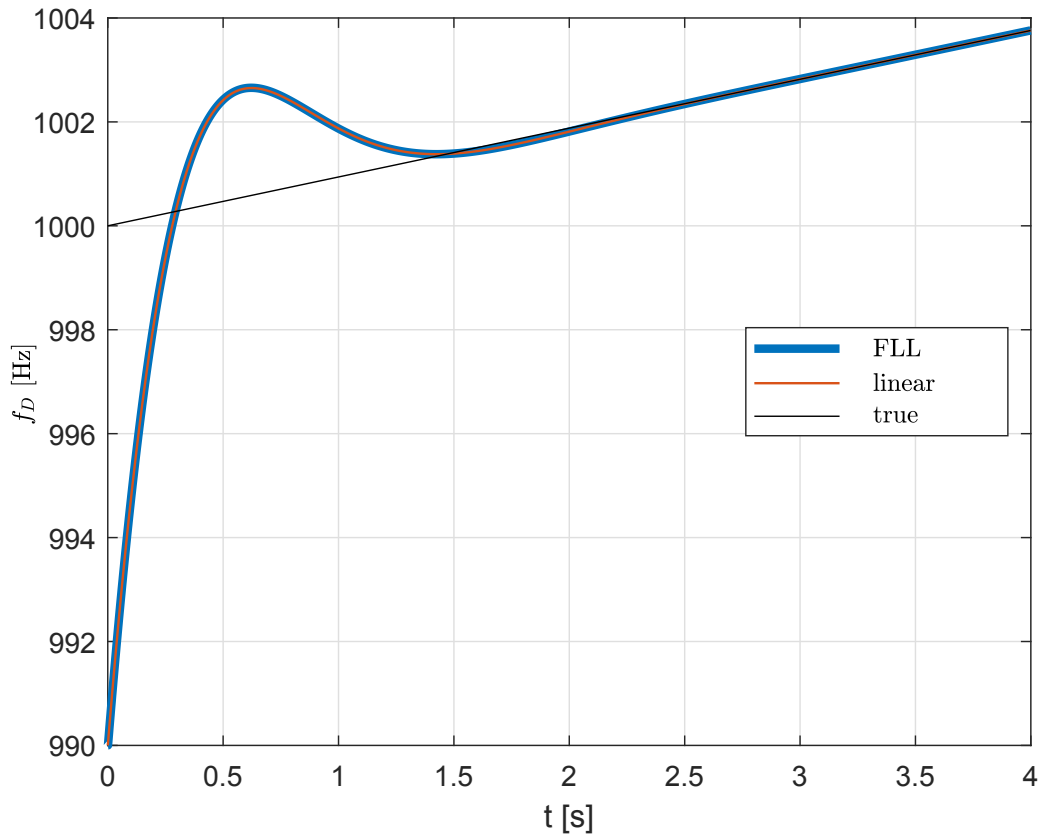
SOURCE: Author's production.

Figure 4.7 - Comparison of $\delta\phi(t)$ from the receiver and the FLL linear approximation, in simulation of Doppler shift initial condition error.
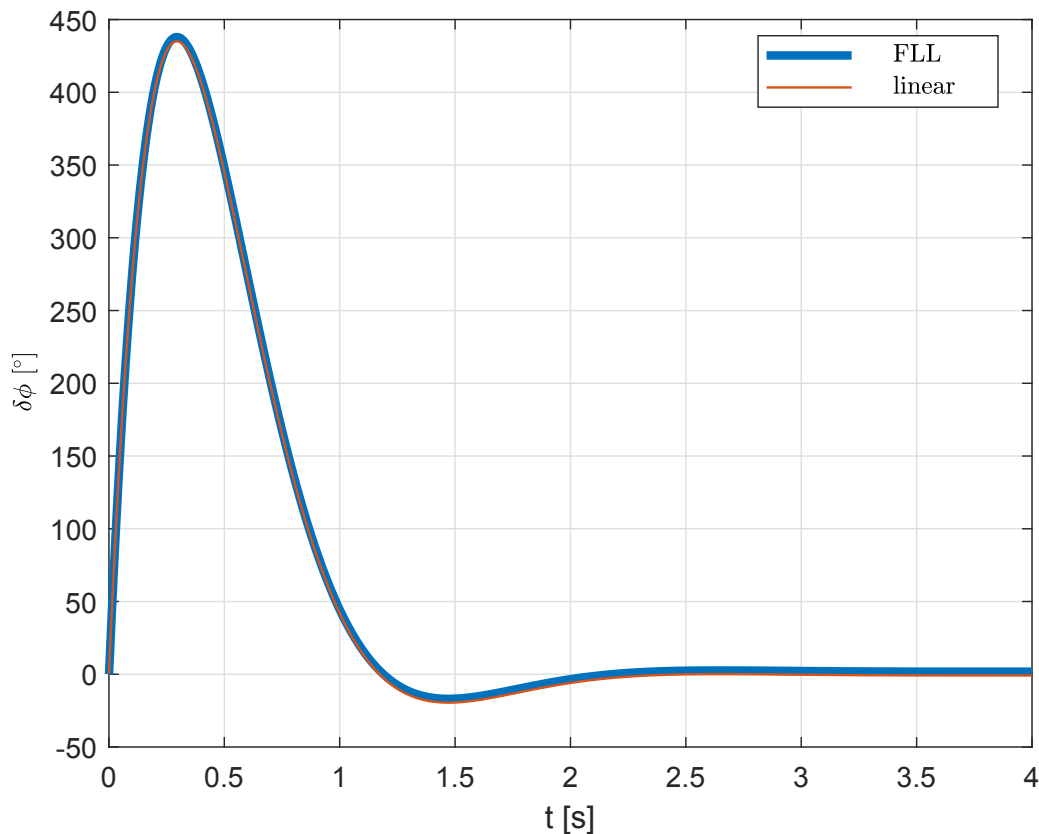
4.1.1.2 Low frequency and low amplitude disturbances in phase

A low frequency and low amplitude sinusoidal disturbance is added to the Doppler phase, with $f_\phi = 1$ Hz and $A_\phi = 5\frac{\pi}{180}$. The comparison of the Doppler shift estimated by the receiver and by the linear approximation is presented in Figure 4.8, and the comparison of the arc tangent applied to the I/Q prompt correlator in the receiver and the $\delta\phi(t)$ from the linear approximation is presented in Figure 4.9, showing a good agreement between the receiver and its linear approximation for phase variations with low frequency and low amplitude, thus confirming the validity of the linear approximation.

Figure 4.8 - Comparison of $\hat{f}_D(t)$ from the receiver and the FLL linear approximation, in simulation of sinusoidal phase variations added to the baseband input signal with low frequency and low amplitude.

SOURCE: Author's production.

Figure 4.9 - Comparison of $\delta\phi(t)$ from the receiver and the FLL linear approximation, in simulation of sinusoidal phase variations added to the baseband input signal with low frequency and low amplitude.

SOURCE: Author's production.

4.1.1.3 High frequency and low amplitude disturbances in phase

A high frequency and low amplitude sinusoidal disturbance is added to the Doppler phase, with $f_\phi = 70$ Hz and $A_\phi = 5\frac{\pi}{180}$. The comparison of the Doppler shift estimated by the receiver and by the linear approximation is presented in Figure 4.10, and the comparison of the arc tangent applied to the I/Q prompt correlator in the receiver and the $\delta\phi(t)$ from the linear approximation is presented in Figure 4.11, showing a good agreement between the receiver and its linear approximation for phase variations with high frequency and low amplitude, thus confirming the validity of the linear approximation.

61

Figure 4.10 - Comparison of $\hat{f}_D(t)$ from the receiver and the FLL linear approximation, in simulation of sinusoidal phase variations added to the baseband input signal with high frequency and low amplitude.

SOURCE: Author's production.

Figure 4.11 - Comparison of $\delta\phi(t)$ from the receiver and the FLL linear approximation, in simulation of sinusoidal phase variations added to the baseband input signal with high frequency and low amplitude.
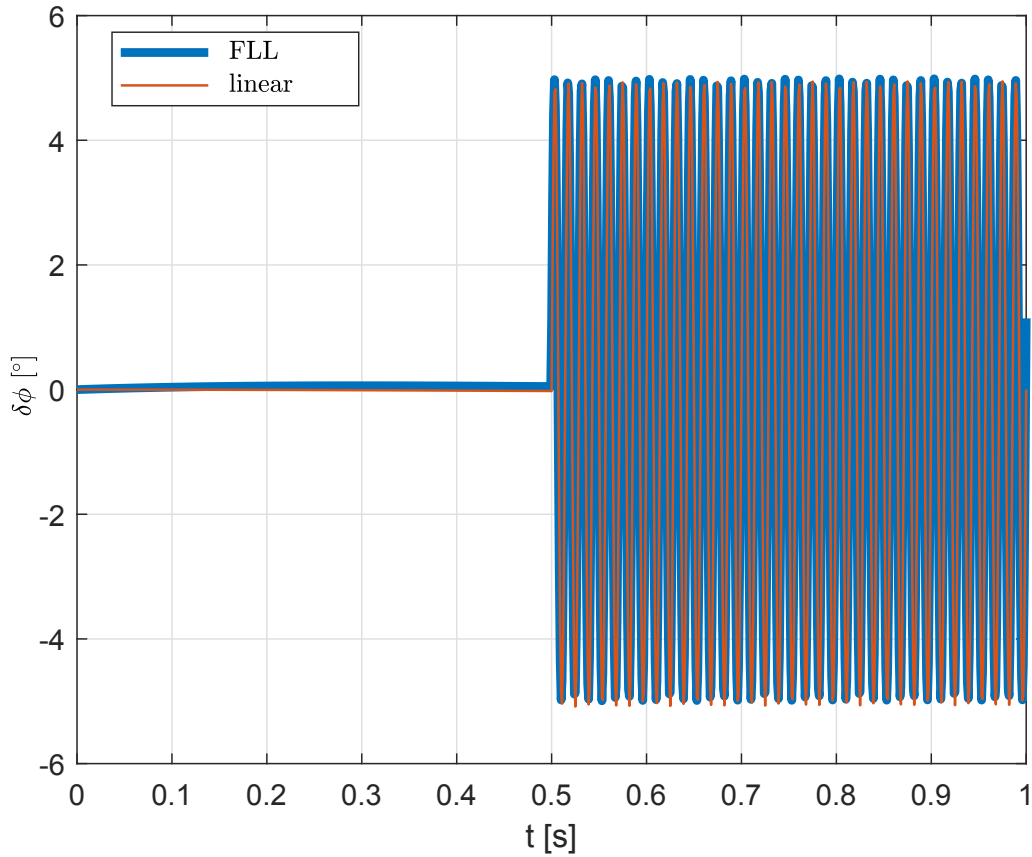
4.1.1.4 Low frequency and high amplitude disturbances in phase

A low frequency and high amplitude sinusoidal disturbance is added to the Doppler phase, with $f_\phi = 1$ Hz and $A_\phi = 175\frac{\pi}{180}$. The comparison of the Doppler shift estimated by the receiver and by the linear approximation is presented in Figure 4.12, and the comparison of the arc tangent applied to the I/Q prompt correlator in the receiver and the $\delta\phi(t)$ from the linear approximation is presented in Figure 4.13, showing a good agreement between the receiver and its linear approximation for phase variations with low frequency and high amplitude, thus confirming the validity of the linear approximation.

Figure 4.12 - Comparison of $\hat{f}_D(t)$ from the receiver and the FLL linear approximation, in simulation of sinusoidal phase variations added to the baseband input signal with low frequency and high amplitude.
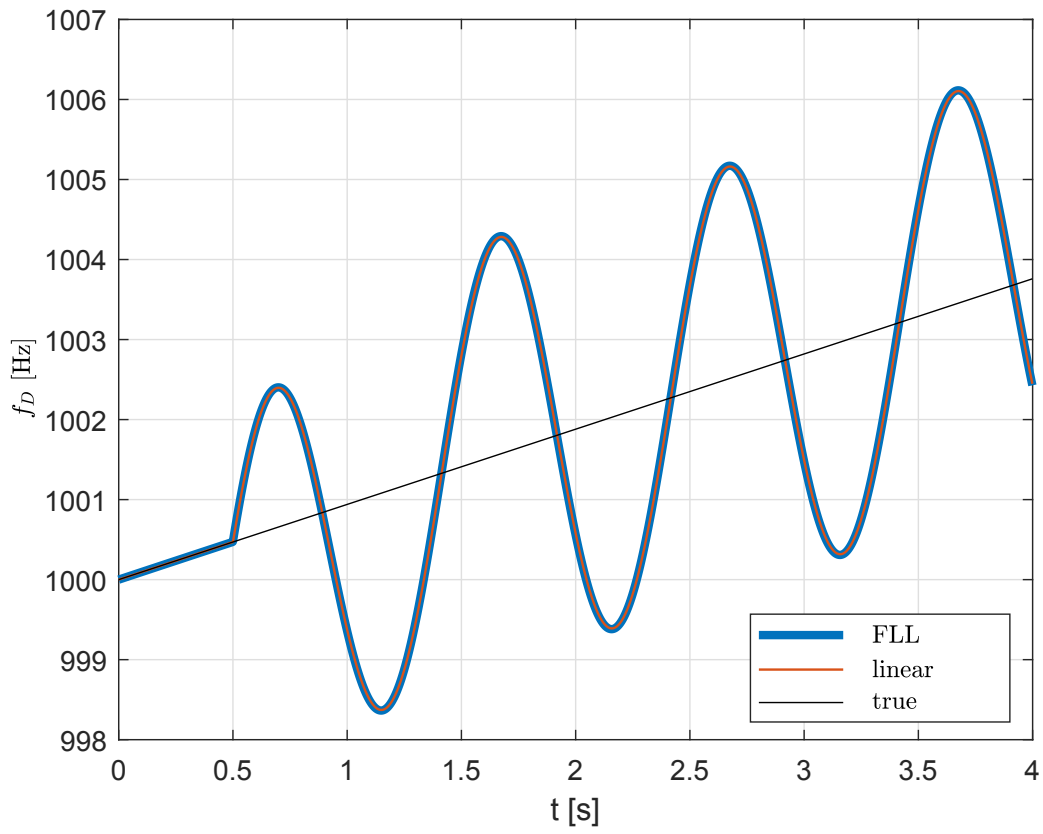
SOURCE: Author's production.

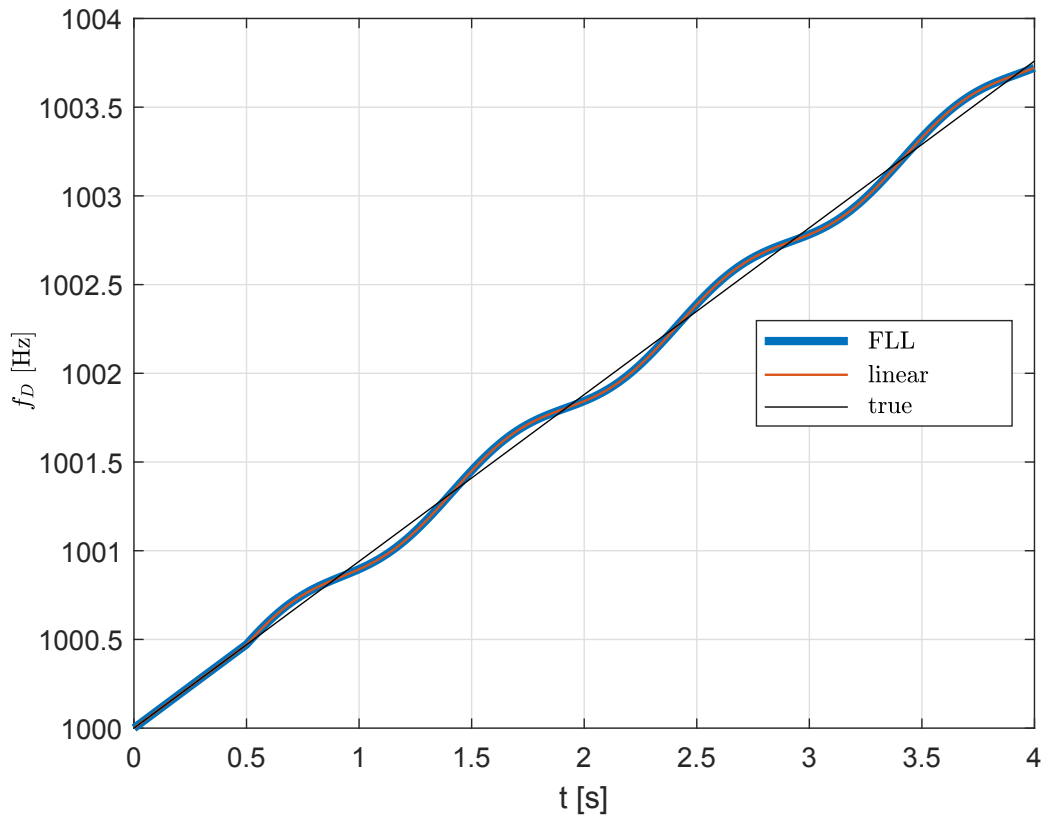Figure 4.13 - Comparison of $\delta\phi(t)$ from the receiver and the FLL linear approximation, in simulation of sinusoidal phase variations added to the baseband input signal with low frequency and high amplitude.
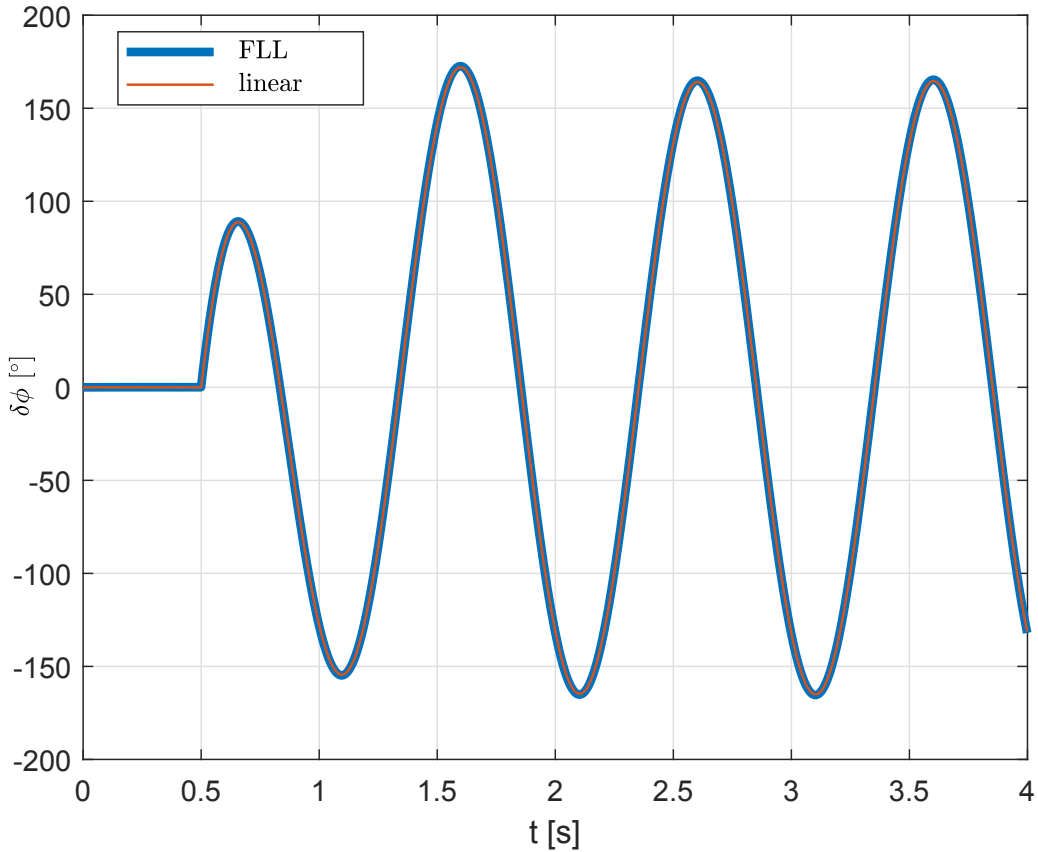
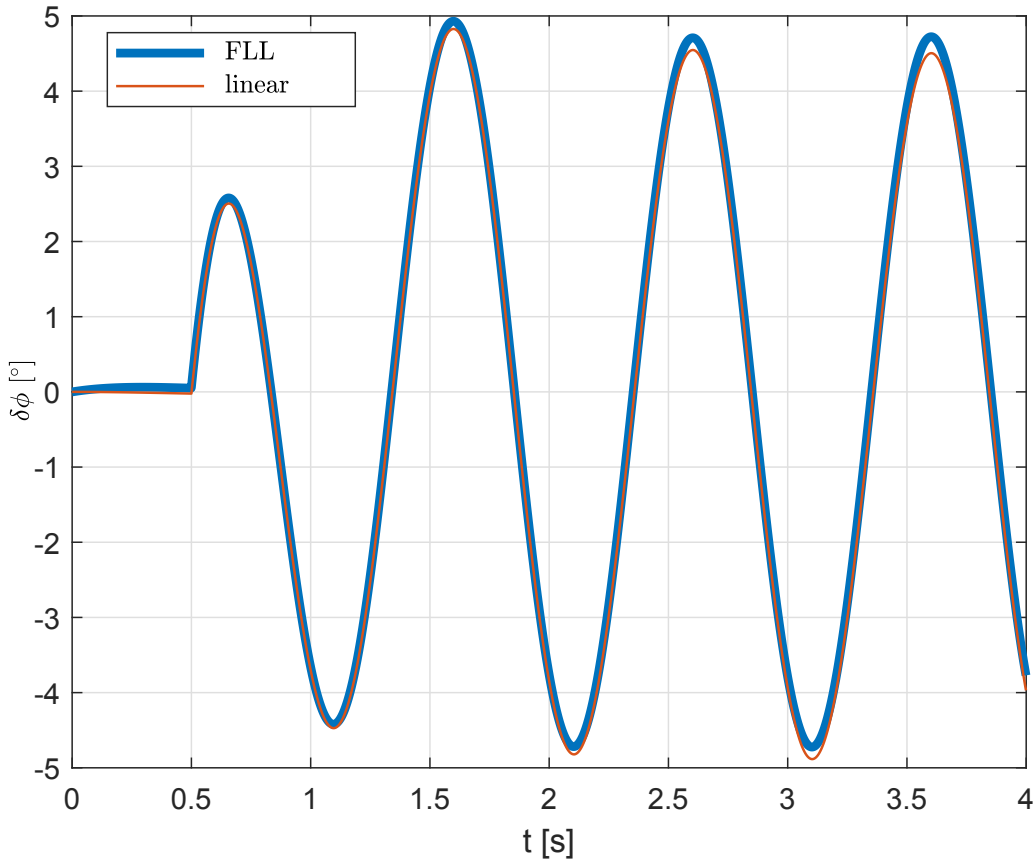#### 4.1.1.5 High frequency and high amplitude disturbances in phase

A high frequency and high amplitude sinusoidal disturbance is added to the Doppler phase, with $f_\phi = 70$ Hz and $A_\phi = 175\frac{\pi}{180}$. The comparison of the Doppler shift estimated by the receiver and by the linear approximation is presented in Figure 4.14, and the comparison of the arc tangent applied to the I/Q prompt correlator in the receiver and the $\delta\phi(t)$ from the linear approximation is presented in Figure 4.15, showing a good agreement between the receiver and its linear approximation for phase variations with high frequency and high amplitude, thus confirming the validity of the linear approximation.

Figure 4.14 - Comparison of $\hat{f}_D(t)$ from the receiver and the FLL linear approximation, in simulation of sinusoidal phase variations added to the baseband input signal with high frequency and high amplitude.
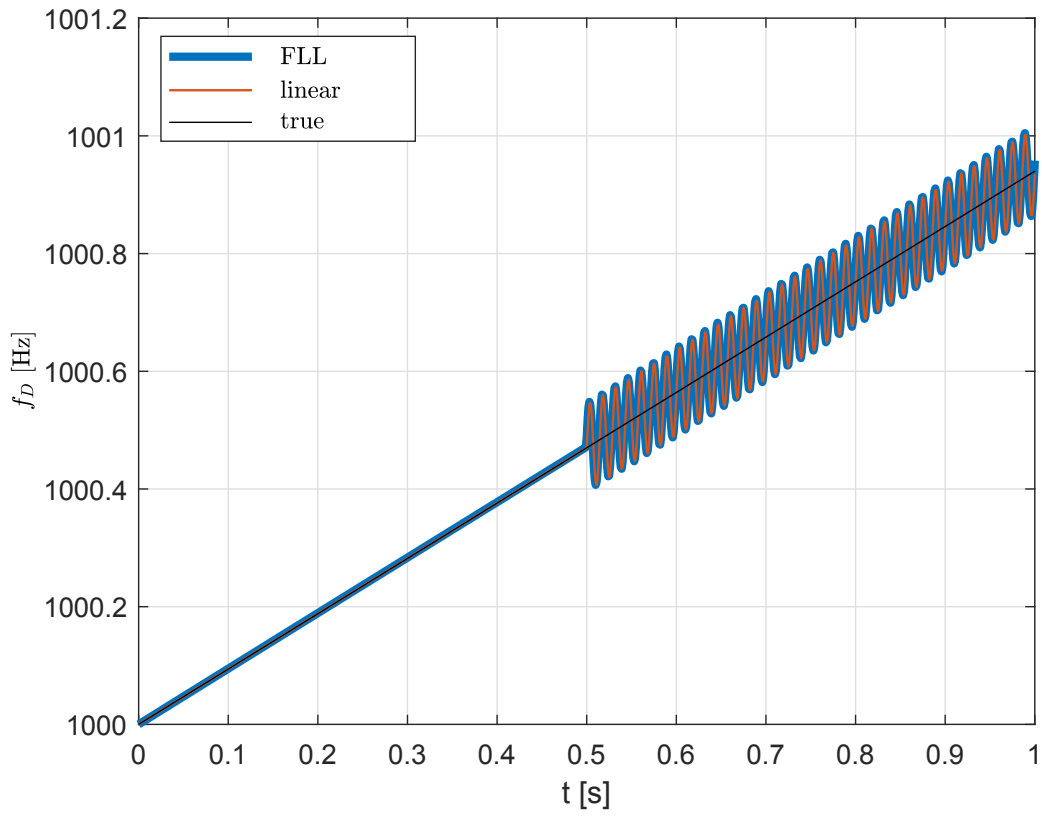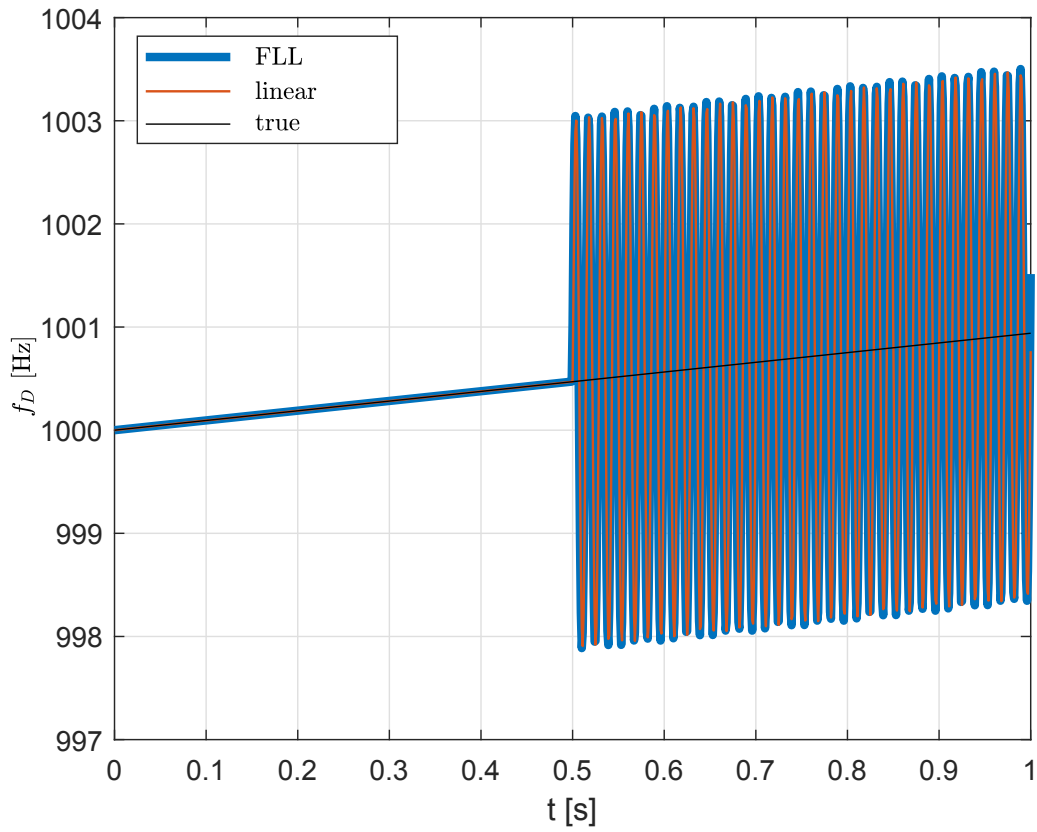
Figure 4.15 - Comparison of $\delta\phi(t)$ from the receiver and the FLL linear approximation, in simulation of sinusoidal phase variations added to the baseband input signal with high frequency and high amplitude.
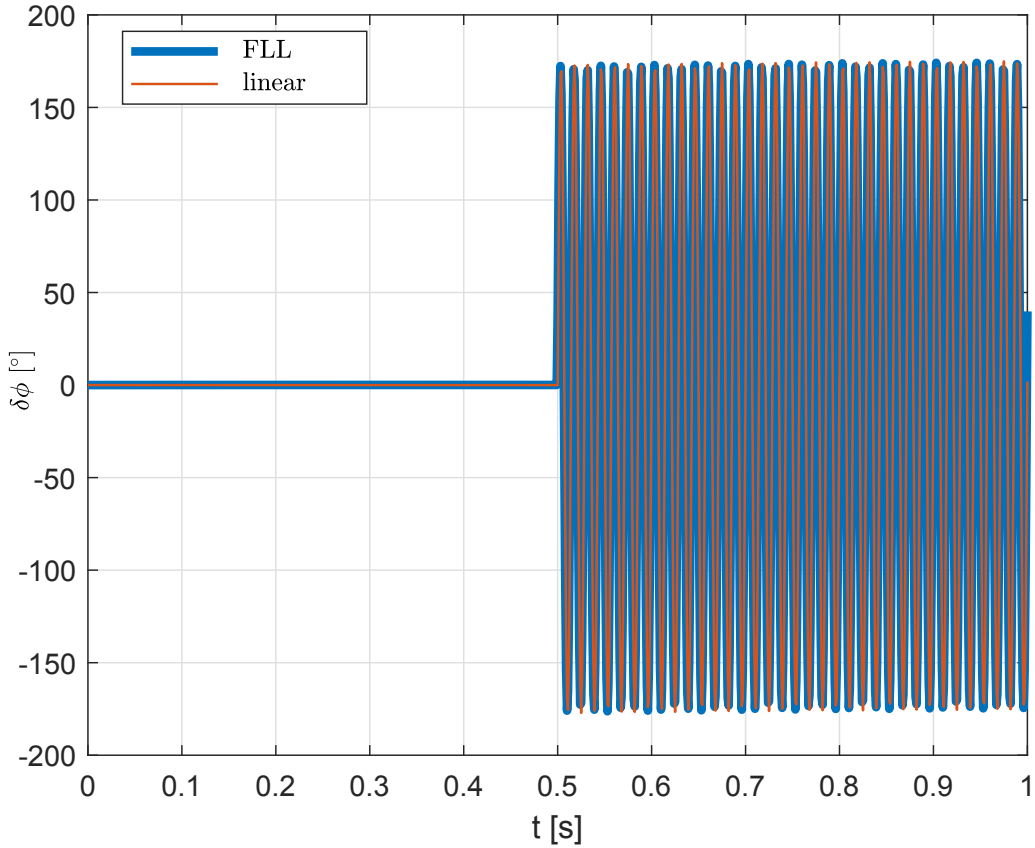
4.2 Kalman FLL for LOS-only tracking

The proposed scintillation monitoring algorithm exploits the linear approximation of FLLs, which is also applicable to the Kalman filter based FLL tracking only the LOS dynamics. In this section, we present the modeling of a discriminator-based Kalman FLL, the block diagram of this Kalman FLL with traditional noncoherent DLL, and then we obtain the correspondence of the Kalman FLL with the linear approximation of the traditional FLL. The linear approximation of the Kalman FLL enables the application of the proposed monitoring algorithm to receivers employing a Kalman FLL.

In a discriminator-based Kalman filter working as the carrier tracking loop in a receiver, the LOS dynamics is modeled by the kinematic process model (BAR-SHALOM et al., 2001) presented in Chapter 3. The carrier replica is generated based on Kalman filter state estimates, and the residuals, or innovations, of the filter are taken from the discriminator output (VILÁ-VALLS et al., 2017).

The Kalman FLL for LOS dynamics tracking is defined by the state vector

$$\mathbf{x}_D[k] = \begin{bmatrix} f_D[k] & a_D[k] \end{bmatrix}^{\mathrm{T}}, \tag{4.14}$$

and the process equations are defined by the state transition and process noise covariance matrices

$$\mathbf{F}_D = \begin{bmatrix} 1 & T_I \\ 0 & 1 \end{bmatrix}, \mathbf{Q}_D = \sigma_{j_D}^2 \begin{bmatrix} T_I^3/3 & T_I^2/2 \\ T_I^2/2 & T_I \end{bmatrix}, \tag{4.15}$$

after truncation of (2.11) at the second order term and excluding the state relative to Doppler phase, with Gaussian Doppler drift rate variance $\sigma_{j_D}^2$, which is the control parameter of the process model.

The innovation sequence is formed by the outputs of the frequency discriminator (2.28). Since the frequency discriminator provides a Doppler shift error, we can write the matrix of observations for the LOS-only FLL as

$$\mathbf{H}_D = \begin{bmatrix} 1 & 0 \end{bmatrix}. \tag{4.16}$$

The block diagram of a receiver with a discriminator-based Kalman filter FLL and a traditional noncoherent DLL is shown in Figure 4.16.

Figure 4.16 - Kalman FLL/traditional DLL receiver.
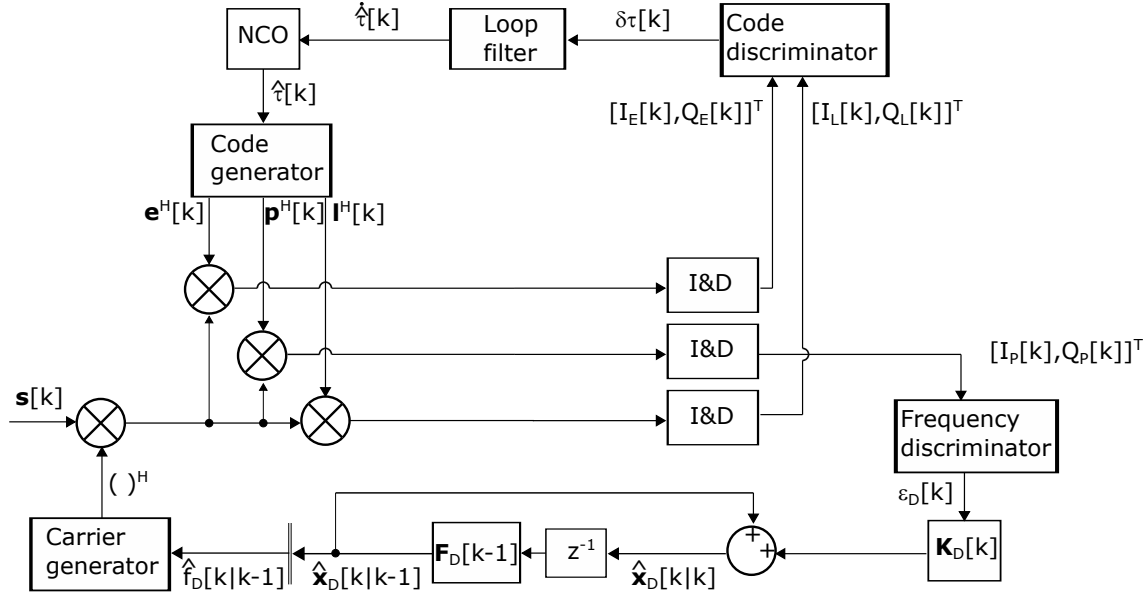
SOURCE: Author's production.

A linear approximation for the Kalman FLL depicted in Figure 4.16 with the Kalman gain

$$\mathbf{K}_D[k] = \begin{bmatrix} K_{D,1}[k] & K_{D,2}[k] \end{bmatrix}^{\mathrm{T}}, \tag{4.17}$$

can be obtained in the same manner as for the traditional FLL, where $K_{D,1}[k]$ and $K_{D,2}[k]$ are, respectively, the first and second elements of the Kalman gain vector $\mathbf{K}_D[k] \in \mathbb{R}^{2 \times 1}$. If we consider the continuous time representation of the traditional FLL, with the corresponding Laplace transform of the second order loop filter (4.1), the continuous time Kalman FLL would have the same block diagram as shown in Figure 4.3, substituting $2\xi\omega_n$ by $K_{D,1}[k]$ and ω_n^2 by $K_{D,2}[k]$. The difference between both second order filters is that the traditional FLL filter has fixed parameters while the parameters of the Kalman FLL are time-varying and computed according to the optimality premises of the Kalman filter. Equivalence of the Kalman filter with a LTI filter of the same order, in continuous time representation, can be found in (BROWN; HWANG, 1996) and (KALMAN; BUCY, 1961). The state estimates $\hat{f}_D[k] = \hat{f}_D(kT_I)$ and $\hat{a}_D[k] = \hat{a}_D(kT_I)$ of the Kalman FLL are equivalent to $\hat{f}_D(kT_I)$ and $\hat{\dot{f}}_{D_1}(kT_I)$ of the linear approximation, respectively. These variables are shown in the block diagram of Figure 4.3. There is a slight dynamic difference between $\hat{a}_D[k]$ and $\hat{\dot{f}}_D[k]$,

for which the property (4.9) is valid.

Taking into account the continuous/discrete equivalence (BROWN; HWANG, 1996) and correcting for the update rate T_I, the estimate

$$\hat{\dot{f}}_D[k] = \hat{a}_D[k] + K_{D,1}[k]\varepsilon_D[k]/T_I \tag{4.18}$$

can be given, dependent on the Doppler drift $\hat{a}_D[k]$ estimated by the Kalman FLL and the Kalman filter residual $\varepsilon_D[k]$, which is equivalent to the frequency discriminator output $\delta f_D[k]$.

4.3 Real-time ionospheric scintillation monitoring

Our proposed monitoring algorithm exploits the carrier tracking loops designed for the LOS dynamics tracking, which do not include terms to directly address the estimation of amplitude and phase scintillation. This is the case for many receivers employed in monitoring stations. Thus, the algorithm can be implemented as an additional piece of code in a software receiver or the software part of a hardware receiver, using internal observables computed by its carrier tracking loop to provide scintillation phase estimates. Based on these estimates, and amplitude estimates obtained as the norm of the phasor formed by I/Q prompt correlator outputs, scintillation metrics such as the phase standard deviation σ_ϕ and the S$_4$ index (DIEREN-DONCK et al., 1993) can be also computed in real-time. The algorithm can also be used as alternative to standard post-processing methods if the needed receiver data is stored.

From the linear approximations of the traditional and Kalman FLLs, we employ the property (4.9) to observables that can be obtained from the FLLs, with complementary frequency content, to retrieve low and high frequency contents of the scintillation phase by a low and a high frequency LTI filtering branches and provide a scintillation phase estimate. Initially, we develop the proposed algorithm for traditional and Kalman FLLs, once the needed observables are directly available in the FLL structure. The signal processing of the proposed algorithm for scintillation monitoring is based on the LOS-only tracking loops presented in Figures 4.1 and 4.16 for the traditional and Kalman FLL, respectively. Afterwards, we present a simple modification to adapt the algorithm to traditional and Kalman PLLs.

4.3.1 Traditional and Kalman FLLs for LOS-only tracking

The traditional FLL is tracking the Doppler shift, so that the linear approximation (4.3) is a low pass filter with bandwidth defined by the noise bandwidth of the loop, considering a second order loop filter with a fixed damping ratio $\xi = 1/\sqrt{2}$. The linear approximation for the phase error (4.7) is a high pass filter, with frequency content complementary to the integral of (4.3), according to (4.8). The raw total phase could be recovered via the sum of the phase error, which is the integral of the frequency error computed by the frequency discriminator, and the integral of the Doppler shift computed by the FLL NCO. However, the raw total phase is the sum of the Doppler phase, which is the integral of Doppler shift, and the scintillation phase. To separate them, it is necessary to remove the secular low frequency component related to the LOS dynamics from the raw total phase.

For a static receiver positioned on ground, the LOS acceleration is almost constant, so that the Doppler drift $\dot{f}_D[k]$ varies slowly in relation to the scintillation dynamics. Therefore, high pass filtering with a low cutoff frequency can remove this bias related to the LOS acceleration from the output of the loop filter $\hat{f}_D[k]$ in the traditional FLL, just prior the NCO, or can be derived according to (4.18) for the Kalman FLL. In this case it is necessary to combine the bias removal with a double integration to obtain a component in terms of phase.

Application of a phase discriminator on $[I_P[k], Q_P[k]]^{\mathrm{T}}$ provides a signal whose linear approximation is $\delta\phi[k]$ in Figure 4.2(a), which is the integral of the frequency error $\delta f_D[k]$ computed by the frequency discriminator of the FLL, as shown in Figure 4.2(a). Our proposed scintillation monitor takes the complementary frequency information from $\delta\phi[k]$ and $\hat{f}_D[k]$ by adding the high frequency content in $\delta\phi[k]$ to the low frequency content in the double integral approximation of $\hat{f}_D[k]$, handling the biases built up and possible divergence in the double integration due to small errors related to nonlinearities, noise, or other sources, by defining a lower frequency limit. Therefore, for the low frequency content, the algorithm removes the Doppler drift bias and approximates the double integration down to a lower frequency limit to obtain the low frequency component in terms of the phase. This component is combined with the high frequency component, where any initial constant phase error is removed from $\delta\phi[k]$ with a wash-out filter and an upper frequency limit is defined by a downstream low pass filter.

The scintillation phase monitor combined with a traditional FLL is illustrated in Figure 4.17. In Figure 4.17, the blocks with solid lines describe the traditional FLL

from Figure 4.1 while the blocks with dashed lines describe the scintillation monitor, which uses $[I_P[k], Q_P[k]]^\mathrm{T}$ from the prompt correlator and $\hat{f}_D[k]$ from the loop filter. The filters in the dashed blocks are presented in their z-transform.

Figure 4.17 - Traditional FLL/DLL receiver with scintillation phase estimation.
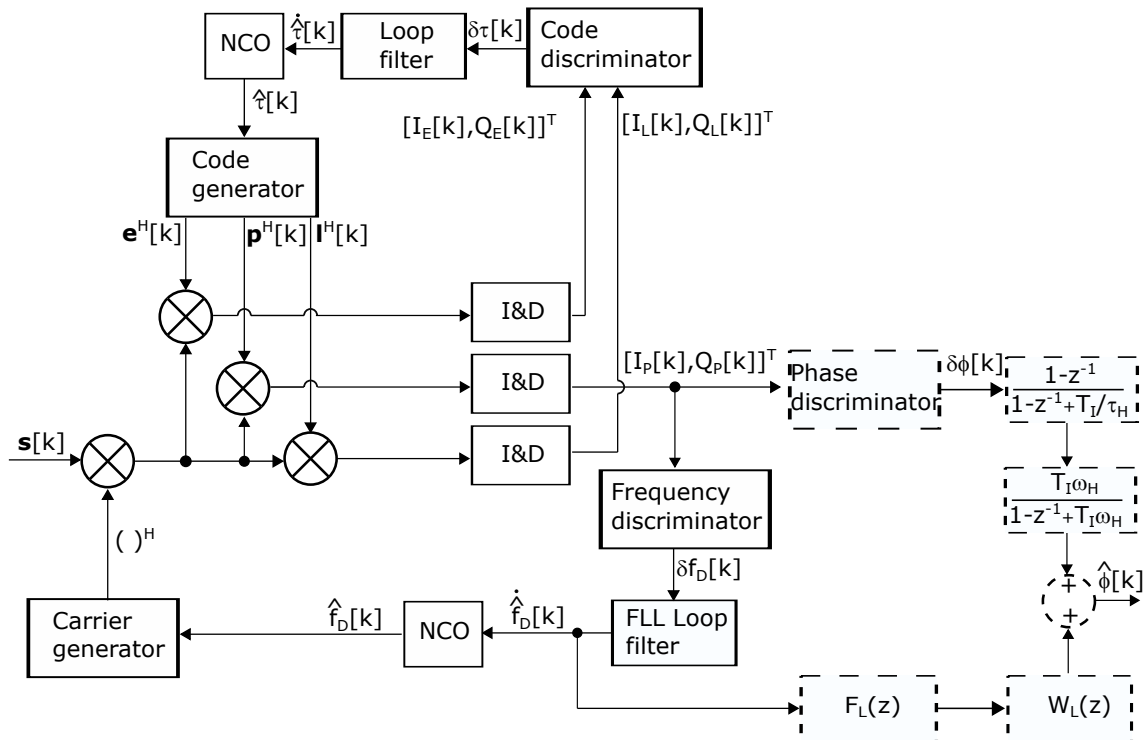
SOURCE: Author's production.

The FLL tracks the input signal up to its bandwidth, so $\delta\phi[k]$ coming from the phase discriminator has frequency content above the FLL bandwidth, added to a possible bias resulting from initial FLL transient. The task of the first filter applied to $\delta\phi[k]$ in the high frequency branch is to wash-out the bias. The cutoff frequency of this first order high pass filter is defined by $1/\tau_H$, such that the higher the time constant τ_H, the lower the cutoff frequency for the bias removal. The second filter in the high frequency branch is a roll-off filter with the task of limiting the higher frequency content, by setting the cutoff frequency ω_H of this first order low pass filter. Thus, ω_H defines the upper frequency of interest limit of the monitoring algorithm. A Bode plot representative of the high frequency branch is shown in Figure 4.18, for $\tau_H = 10$

s and $\omega_H = 2\pi \times 25$ rad/s, to illustrate its overall band pass characteristic, delimited by $1/\tau_H$ and ω_H.

Figure 4.18 - Bode plots of the Laplace transforms relative to the wash-out and low pass filters from the high frequency branch.
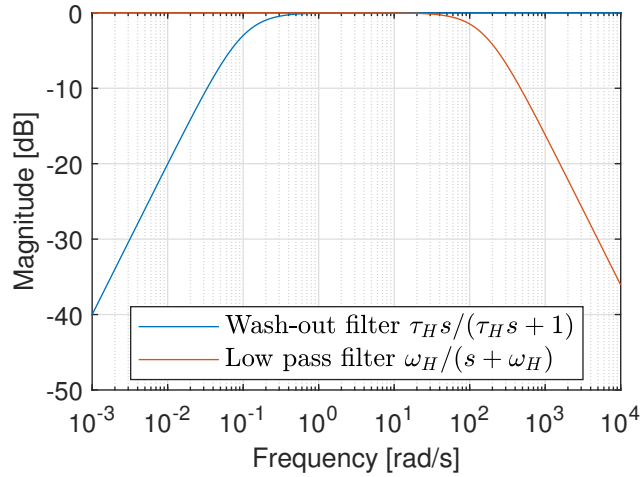
(a) Magnitude.
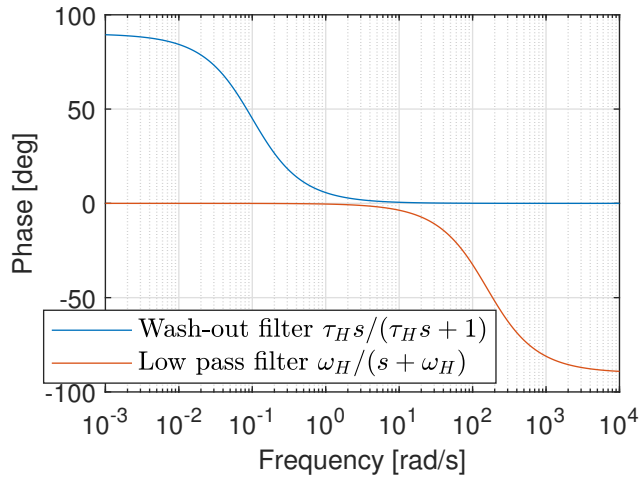
(b) Phase.

SOURCE: Author's production.

In the low frequency branch, the purpose of the filter $F_L(z)$ is to approximate the second integral while filtering out the slowly varying bias caused by nonlinearities and other sources. The filter $F_L(z)$ is a third order high pass filter in $u(z)$ to $y(z)$. Its block diagram is presented in Figure 4.19. We can set $a_3 = 1.1$ and $b_3 = 2.4$, and

ω_L is the design parameter of the filter.

Figure 4.19 - Filter $F_L(z)$.
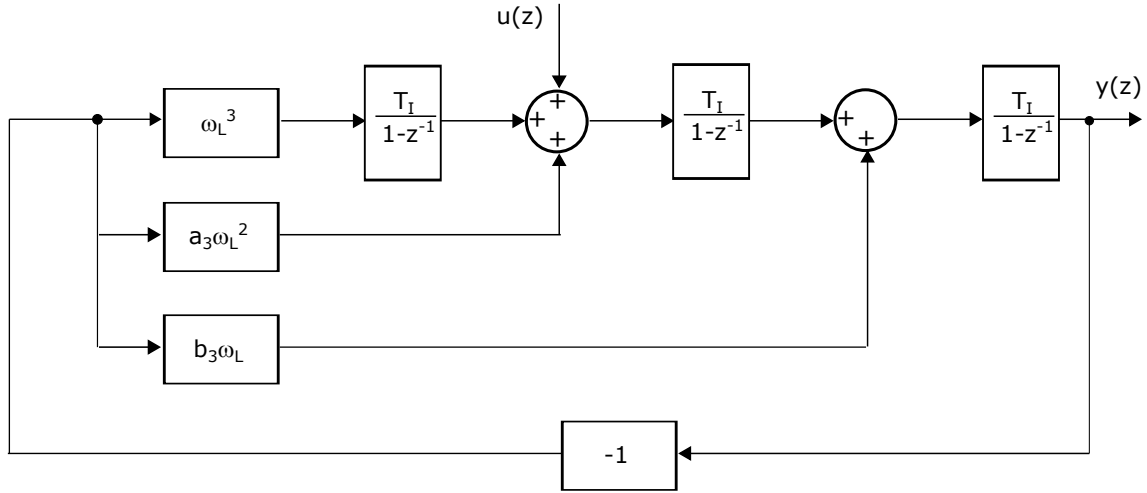
The purpose of the filter $W_L(z)$, downstream of $F_L(z)$, is to further reduce the gain below the frequency of interest defined by ω_L in $F_L(z)$. $W_L(z)$ is a high pass second order filter with cutoff frequency ω_W that should be equal to ω_L or tuned around its value. Typically, the lower limit of the scintillation frequency content is in the range 0.01-0.1 Hz (FREMOUW et al., 1978), (FORTE, 2007). The filter structure of $W_L(z)$ is presented in Figure 4.20. The desired effect of this filter is presented in the Bode plot of the respective continuous representations in Figure 4.21, for $\omega_L = \omega_W = 4 \times 10^{-6}$ rad/s, showing that $F_L(z)$ approximates a double integrator down to ω_L, and the application of $W_L(z)$ downstream $F_L(z)$ further reduce the gain below this frequency.

Figure 4.20 - Filter $W_L(z)$.
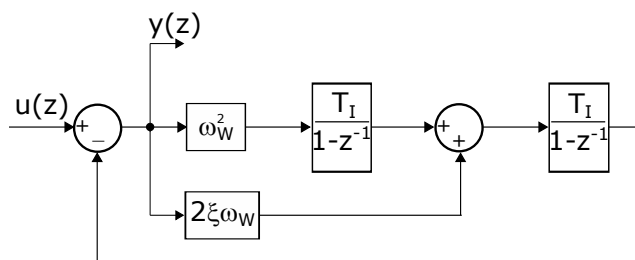
SOURCE: Author's production.

Figure 4.21 - Bode plots of a double integrator compared to the Laplace transforms relative to $F_L(z)$ and $F_L(z) \cdot W_L(z)$.

(a) Magnitude.

(b) Phase.

SOURCE: Author's production.

75
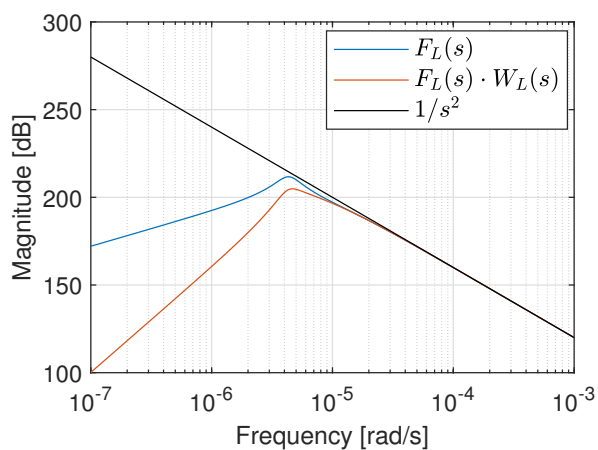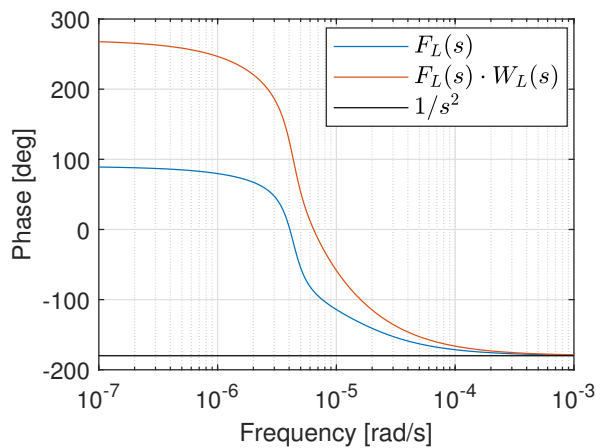
The monitoring algorithm control parameters are, therefore, τ_H, ω_H, ω_L and ω_W. Their values depend on the particular receiver, and should be adjusted after an initial analysis of stored data, setting ω_L and ω_W to remove the integration bias, possible low frequency nonlinearities and define a lower limit in frequency of interest, τ_H to remove any phase error bias, and ω_H to define an upper frequency limit. The filters employed in the scintillation monitor with a Kalman FLL are the same filters employed in the scintillation monitor with a traditional FLL. Naturally, the tuning parameters may be adjusted to different values. The only difference in the signal processing is that $\hat{f}_D[k]$ must be derived by (4.18) in the Kalman FLL, so that its frequency content is complementary to the frequency content in $\delta\phi[k]$, since $\hat{a}_D[k]$ is not dynamically equivalent to $\hat{f}_D[k]$. The Kalman FLL with the scintillation monitoring signal processing is shown in Figure 4.22.

Figure 4.22 - Kalman FLL/traditional DLL receiver with scintillation phase estimation.
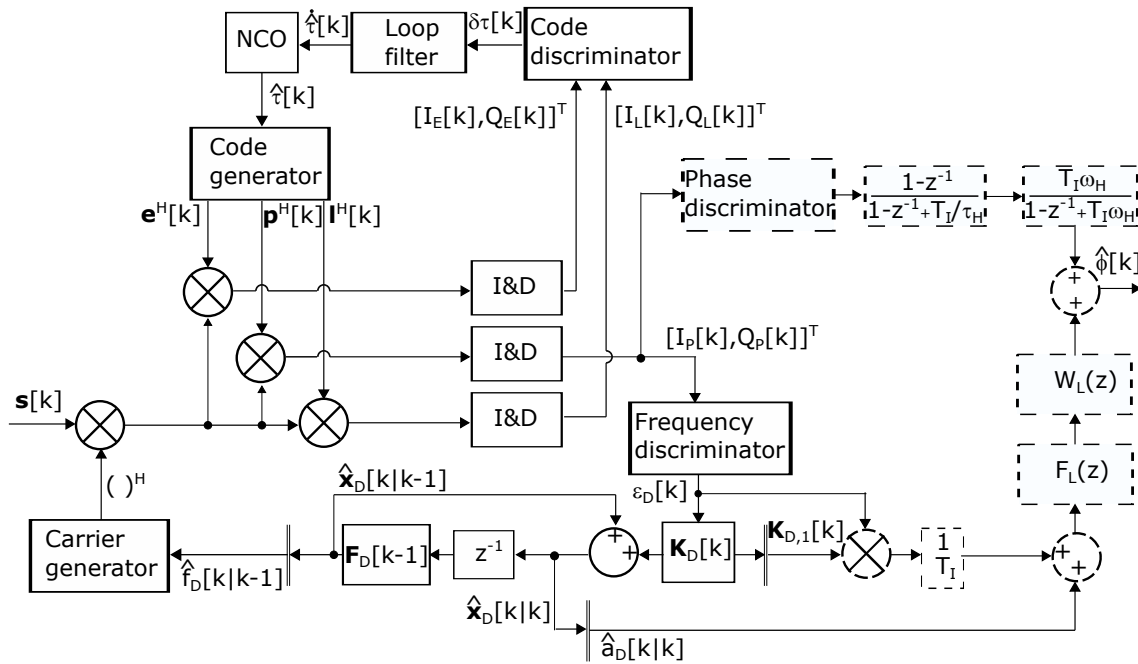
Typically, the phase discriminator employed in phase tracking loops of the monitoring stations is the two-quadrant arc tangent (Costas loop), that would generate $\delta\phi[k] = \arctan(Q_P[k]/I_P[k])$ in the interval $[-\pi/2, \pi/2]$. Instead, in our monitoring

algorithm, we consider the total scintillation phase in the full circle $[-\pi, \pi]$, by employing the four quadrant phase discriminator $\delta\phi[k] = \arctan2(Q_P[k], I_P[k])$, which is sensitive to navigation bit transitions. Therefore, we consider the existence of a navigation bit transition detector (KAPLAN; HEGARTY, 2017) in our monitoring algorithm to avoid half cycle spurious transitions in $\delta\phi[k]$, whenever we apply a phase discriminator. The advantage of using the $\arctan2(\cdot)$ phase discriminator is that we can cope with higher levels of rapid scintillation phase excursions, in the full interval $[-\pi, \pi]$, that can be present in severe scintillation events. However, the monitoring algorithm can also be applied to receivers with Costas PLL, limited to the rapid scintillation phase excursions in the interval $[-\pi/2, \pi/2]$.

The proposed scintillation monitoring algorithm does not interfere in the existing traditional FLL or Kalman FLL designed for LOS tracking in a receiver, regardless of their design parameters. Surely, there are differences between traditional and Kalman filter tracking loops in terms of robustness to scintillation (HUMPHREYS et al., 2005), (ZHANG; MORTON, 2009), but regardless of these differences, our proposed algorithm for scintillation monitoring exploits both loops equivalently to provide estimates of the scintillation phase.

4.3.2 Adaptation to the traditional PLL and Kalman PLL for LOS-only tracking

The monitoring algorithm can be adapted to second order traditional PLLs and to Kalman PLLs tracking LOS-only dynamics. It is inspired by the traditional FLL structure, where the estimate of Doppler drift $\hat{f}_D[k]$, used in the low frequency branch of the monitoring algorithm, is naturally provided to the NCO by the loop filter despite the loop filter order. In the case of the traditional PLL, the loop filter provides the estimate of Doppler shift $\hat{f}_D[k]$ to the NCO, and then the estimate $\hat{f}_D[k]$ used by the monitoring algorithm must be derived from the PLL loop filter. This would be only advisable for second order loop filters, because for third order loop filters the computation would involve an open loop integration, which can lead to divergence even in the case of small errors being integrated. The block diagram of the linear approximation of a second order PLL, with the loop filter expanded, is shown in Figure 4.23.

Figure 4.23 - Linear approximation of a second order PLL.
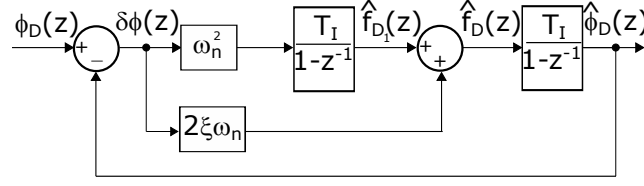
SOURCE: Author's production.

The linear approximation of the second order PLL can be represented analogously to the second order FLL, substituting $f_D(z)$ by $\phi_D(z)$, $\hat{f}_D(z)$ by $\hat{\phi}_D(z)$, $\hat{\dot{f}}_D(z)$ by $\hat{\dot{f}}_D(z)$, and $\hat{f}_{D_1}(z)$ by $\hat{f}_{D_1}(z)$. Also, the error signal in the PLL is $\delta\phi(z)$, instead of $\delta f_D(z)$ as for the FLL. Thus, taking the time derivative of $\hat{\phi}_D[k]$ in the second order PLL, we get

$$\hat{\dot{\phi}}[k] = \hat{f}_D[k] = \hat{f}_{D_1}[k] + 2\xi\omega_n\delta\phi[k], \tag{4.19}$$

and taking the time derivative of the expression above leads to

$$\hat{\ddot{\phi}}[k] = \hat{\dot{f}}_D[k] = \hat{\dot{f}}_{D_1}[k] + 2\xi\omega_n\dot{\delta\phi}[k] = \omega_n^2\delta\phi[k] + 2\xi\omega_n\delta f_D[k], \tag{4.20}$$

which provides the estimate $\hat{\dot{f}}_D[k]$, necessary in the monitoring algorithm. As the PLL does not have a frequency discriminator, it is also required to add a frequency discriminator to compute $\delta f_D[k]$ based on $I_P[k]$ and $Q_P[k]$ in order to employ the monitoring algorithm to traditional PLLs. It is interesting to note that in the case of a third order loop filter, the third integrator of the loop would appear in the expression above, requiring an extra term with integration to obtain $\hat{\dot{f}}_D[k]$.

In the case of the Kalman PLL, the Doppler phase is introduced to the state vector, which reads

$$\mathbf{x}_D[k] = \begin{bmatrix} \phi_D[k] & f_D[k] & a_D[k] \end{bmatrix}^{\mathrm{T}}, \tag{4.21}$$

with state transition matrix

$$\mathbf{F}_D = \begin{bmatrix} 1 & T_I & T_I^2/2 \\ 0 & 1 & T_I \\ 0 & 0 & 1 \end{bmatrix}, \tag{4.22}$$

78

process noise covariance matrix

$$\mathbf{Q}_D = \sigma_{j_D}^2 \begin{bmatrix} T_I^5/20 & T_I^4/8 & T_I^3/6 \\ T_I^4/8 & T_I^3/3 & T_I^2/2 \\ T_I^3/6 & T_I^2/2 & T_I \end{bmatrix}, \tag{4.23}$$

and matrix of observations

$$\mathbf{H}_D = \begin{bmatrix} 1 & 0 & 0 \end{bmatrix}. \tag{4.24}$$

Similarly to the Kalman FLL, the state $\hat{a}_D[k]$ estimated by the Kalman PLL is not dynamically equivalent to the double derivative of $\hat{\phi}_D[k]$. The equivalent continuous time block diagram for the Kalman PLL in Figure 4.24 shows the dynamic relations between the variables. From this block diagram, we get for the derivative of $\hat{\phi}_D$

$$\dot{\hat{\phi}}_D = \hat{f}_{D_1} + K_{D,1}\delta\phi. \tag{4.25}$$

Taking the double derivative, we get

$$\ddot{\hat{\phi}}_D = \dot{\hat{f}}_D = \dot{\hat{f}}_{D_1} + K_{D,1}\delta\dot{\phi} = \dot{\hat{f}}_{D_1} + K_{D,1}\delta f_D, \tag{4.26}$$

with $\dot{\hat{f}}_{D_1} = \hat{a}_D + K_{D,2}\delta\phi$. Substituting into the expression above leads to the expression for $\dot{\hat{f}}_D$ in continuous time

$$\dot{\hat{f}}_D = \hat{a}_D + K_{D,1}\delta f_D + K_{D,2}\delta\phi, \tag{4.27}$$

and, in analogy with the $\hat{f}_D[k]$ derivation for the Kalman FLL, correcting for the update rate T_I in continuous/discrete equivalence, we get for the Kalman PLL

$$\dot{\hat{f}}_D[k] = \hat{a}_D[k] + K_{D,1}[k]\varepsilon_D[k]/T_I + K_{D,2}[k]\varepsilon_P[k]/T_I, \tag{4.28}$$

where now the Kalman filter residual is $\varepsilon_P[k]$, which is equivalent to the arctan2($\cdot$) phase discriminator output $\delta\phi[k]$, and $\varepsilon_D[k]$ can be obtained by a frequency discriminator applied to $I_P[k]$ and $Q_P[k]$, which is equivalent to $\delta f_D[k]$. It should be noticed that, if we would not have $\hat{a}_D[k]$ available from the Kalman PLL, we would need to integrate $\delta\phi[k]$, which is the case of a third order PLL, as mentioned above.

Figure 4.24 - Equivalent continuous time block diagram for the Kalman PLL.
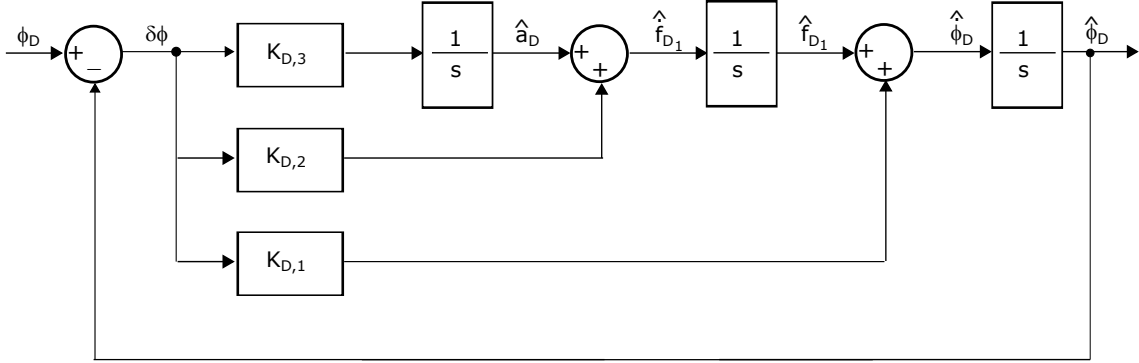
SOURCE: Author's production.

4.4 Performance evaluation of the monitoring algorithm

The proposed monitoring algorithm is firstly evaluated by numerical simulations considering synthetic scintillation input data generated by the CSM (HUMPHREYS et al., 2010) in severe scintillation scenarios defined by amplitude strength index $S_4 = 0.8$ and decorrelation time $\tau_0 = 0.1$ s. Rapidity of scintillation is inversely proportional to decorrelation time. The performance of the monitoring algorithm applied to traditional and Kalman FLLs is evaluated with 300 Monte Carlo simulations with 150 s time window of severe scintillation realizations generated by CSM and receiver thermal noise realizations. Then, the algorithm is evaluated with real data collected by a COTS professional GNSS receiver, where the phase standard deviation is computed with the scintillation phase estimated by the algorithm and compared to the phase standard deviation computed by the standard post-processing procedure.

4.4.1 Synthetic scintillation data

We consider the simplified signal model (2.25) of synthetic GPS L1 C/A code baseband input signals, with carrier generated with a Doppler shift of 1000 Hz and Doppler drift of 0.94 Hz/s, which is approximately the maximum value that an on-ground static receiver would experience based on the orbital dynamics of the GPS satellites, added to the CSM scintillation data. No navigation bit transitions are considered and the carrier amplitude is unitary. Gaussian receiver noise is added to the sampled I/Q signal components in all simulations, generated with variance such that the nominal carrier-to-noise density ratio C/N_0 is 45 dB-Hz. The samples of the

scintillation data are generated by CSM each 10 ms, and the coherent integration time is $T_I = 10$ ms.

In the Monte Carlo simulations, the severe scintillation realizations generated by CSM are added to the input signal carrier, and applied to traditional and Kalman FLLs with the monitoring algorithm added, as presented in Figures 4.17 and 4.22, respectively. The traditional FLL is configured with a second order loop filter with $\xi = 1/\sqrt{2}$ and noise bandwidth $B_n = 1$ Hz. The Kalman FLL process noise covariance matrix is defined by $\sigma_{j_D}^2 = 0.2$, as typically employed in the LOS dynamics tracking (FOHLMEISTER et al., 2018b). The approximate expression (2.29) gives the frequency discriminator noise variance as a function of C/N_0 (LUO et al., 2017), which fluctuates according to the scintillation excursions, since the receiver noise variance is fixed for the nominal C/N_0. We define the measurement noise covariance of the Kalman filter with the value computed by this expression for a conservative value of $C/N_0 = 35$ dB-Hz. The monitoring algorithm parameters are tuned to $\tau_H = 10$ s, $\omega_H = 2\pi \times 25$ rad/s, and $\omega_L = \omega_W = 2\pi \times 10^{-2}$ rad/s with $a_3 = 1.1$ and $b_3 = 2.4$, for both traditional and Kalman FLLs.

The results are presented in terms of the root mean square error

$$\text{RMSE}_x[k] = \sqrt{\frac{1}{M} \sum_{m=1}^{M} \frac{1}{k} \sum_{i=1}^{k} \left(x_m[i] - \hat{x}_m[i] \right)^2}, \tag{4.29}$$

with x being substituted by the variable of interest, for the time index k, the Monte Carlo iteration index m and the number of Monte Carlo simulations M. In the following, we label the monitoring algorithm applied to traditional FLLs as TFLL-REC and the monitoring algorithm applied to Kalman FLLs as KFLL-REC. From the 300 runs, 45 presented cycle slips for the traditional FLL, while no cycle slip was observed for the Kalman FLL. The Kalman filter in general is more robust to cycle slips and loss of lock (VILÁ-VALLS et al., 2018).

Considering all Monte Carlo runs, the performance of the monitoring algorithm and the Doppler tracking using a traditional FLL is significantly worse than using a Kalman FLL, due to the greater number of cycle slips occurrences. The cycle slips contribute to a significant increase in the Doppler phase errors, and, as a consequence, to a significant increase in the scintillation phase estimated by the monitoring algorithm due to the induced disturbance. Figure 4.25 presents the RMSE of the scintillation phase ϕ estimated by the algorithm applied to the FLLs, and Figure 4.26 presents the RMSE of the Doppler phase ϕ_D resulting from the FLLs, which is

not influenced by the monitoring algorithm. Occurring cycle slips are discarded in the results presented in Figures 4.25 and 4.26.

Figure 4.25 - Scintillation phase estimation RMSE$_\phi$, considering only the Monte-Carlo runs not presenting cycle slips in the traditional FLL computation.
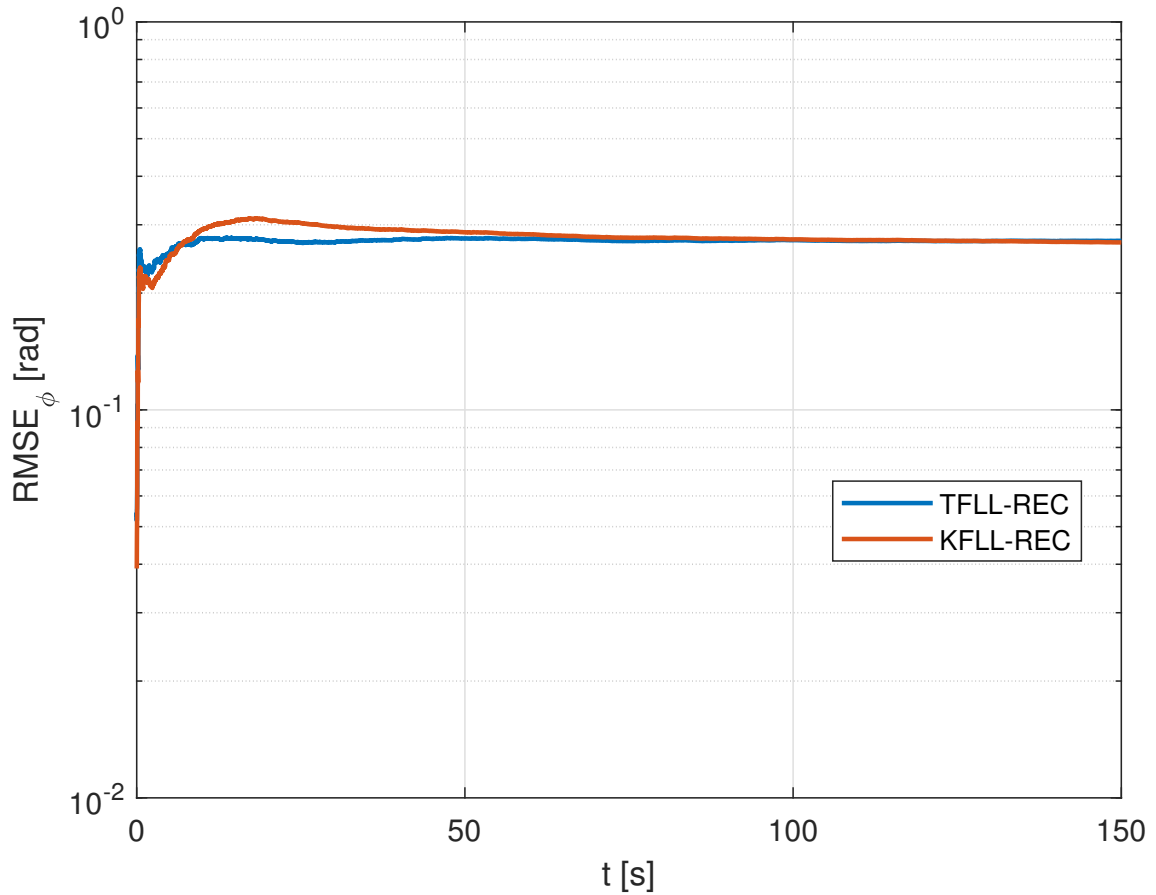
SOURCE: Author's production.

Figure 4.26 - Doppler phase estimation RMSE_{ϕ_D}, considering only the Monte-Carlo runs not presenting cycle slips in the traditional FLL computation.
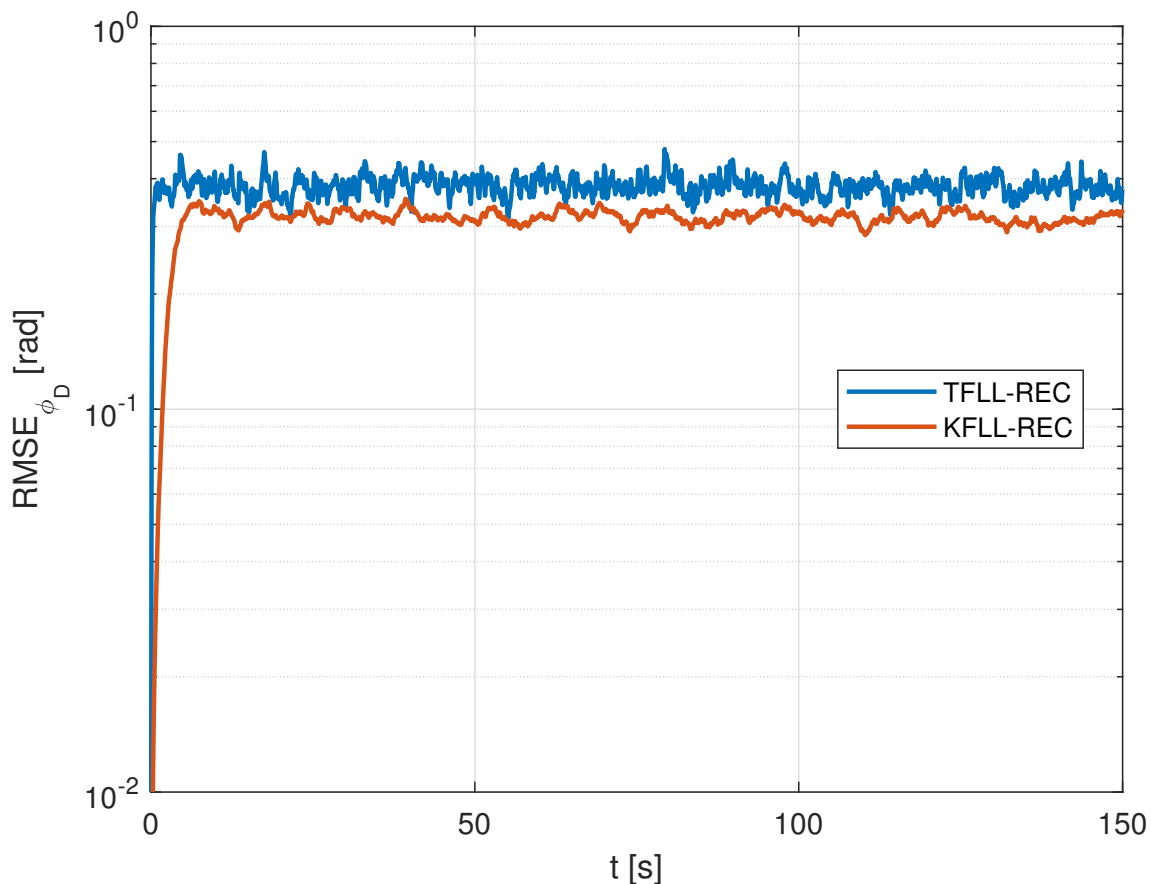
SOURCE: Author's production.

Discarding the traditional FLL runs with cycle slips, the scintillation phase estimation performance is similar, comparing the results of the monitoring algorithm using the traditional (TFLL-REC) and the Kalman (KFLL-REC) FLL. This is consistent with the algorithm design, since the monitoring algorithm for the Kalman FLL was derived from the algorithm for the traditional FLL. Regarding the Doppler tracking, the Kalman FLL presents superior performance. It is interesting to note that the difference in Doppler tracking performance did not imply significant differences in the monitoring algorithm performance, in the absence of cycle slips. This indicates a good robustness of the monitoring algorithm with respect to FLL structure and parameters.

One sample time-series from the Monte Carlo runs with cycle slip occurring with the traditional FLL is presented in Figure 4.27 to illustrate the level of disturbance induced by severe scintillation. In the top graph, after the occurrence of the cycle slip at around 50 s, the Doppler phase error departs from a stable equilibrium point around zero to a next equilibrium point around -2π. In the bottom graph, the estimated scintillation phase starts to diverge from the true scintillation phase due to the cycle slip disturbance, slowly returning to track the true phase following the transient of the monitoring filters. Figure 4.28 shows the respective increase in the RMSEs after the cycle slip. The RMSE of the Doppler phase estimate $\hat{\phi}_D$ stabilizes at a higher level, while the RMSE of the scintillation phase decreases as the transient of the filters vanishes, after the initial increase due to the cycle slip.

Figure 4.27 - One sample time-series presenting a cycle slip, occurring at around 50 s.
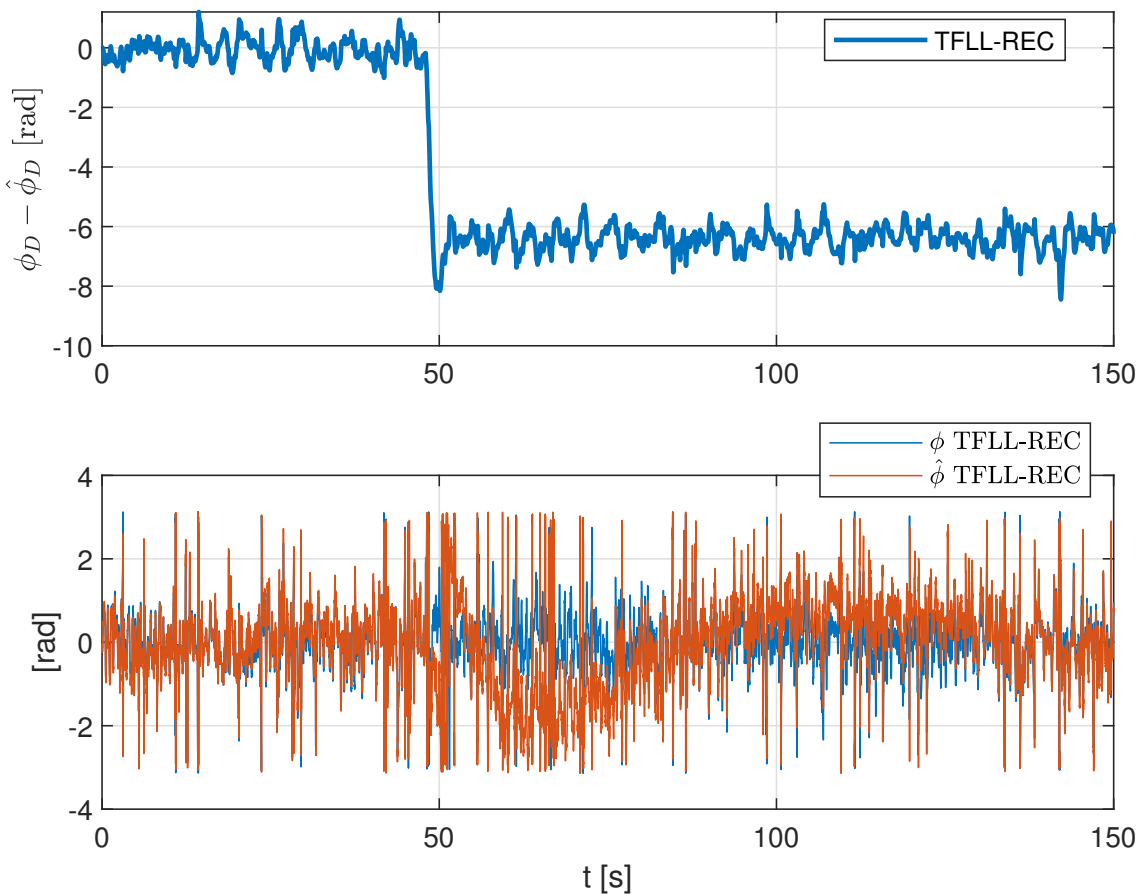
SOURCE: Author's production.

Figure 4.28 - Scintillation phase and Doppler phase RMSEs for the sample time-series presenting a cycle slip.
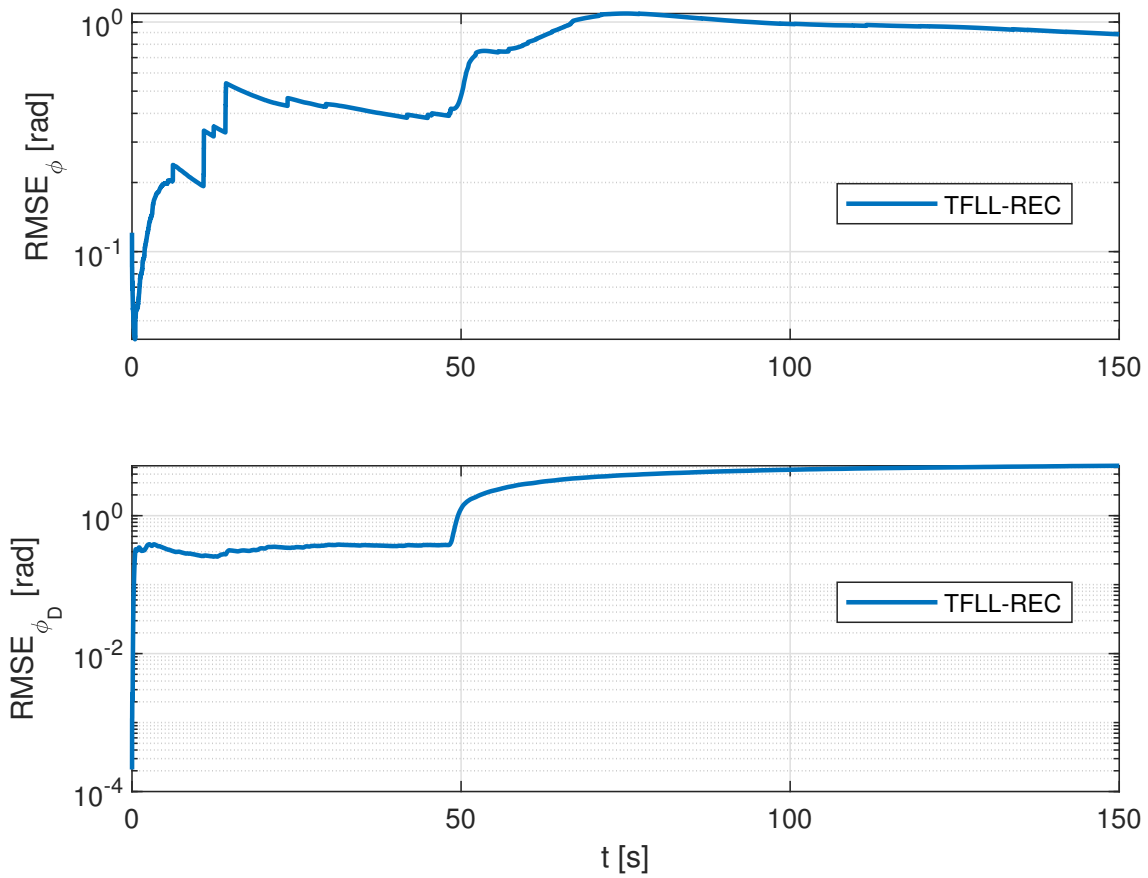
SOURCE: Author's production.

4.4.2 Real scintillation data

The performance of the monitoring algorithm is also assessed with real data collected by a JAVAD Delta 3 receiver connected to a Leica AR25 choke-ring antenna (GNSS, 2018), installed at the rooftop of the building of the Department of Teleinformatics Engineering of the Federal University of Ceará (UFC) in Fortaleza, Brazil, which is part of a scintillation monitoring station operated by the German Aerospace Center (DLR) and UFC. The data presenting ionospheric scintillation was recorded on April 7, 2016, just after the sunset, from 19:00 to 20:00 local time, corresponding to 22:00 UTC to 23:00 UTC (FOHLMEISTER et al., 2018a), on October 27, 2017, from 22:00 UTC to 23:00 UTC and from 23:00 UTC to 00:00 UTC, and on November 16, 2017, from 22:00 UTC to 23:00 UTC. In the following, we label the data recorded

on April 7, 2016, as dataset 1, the data recorded on October 27, 2017, from 22:00 UTC to 23:00 UTC and from 23:00 UTC to 00:00 UTC, as dataset 2 and dataset 3, respectively, and the data recorded on November 16, 2017, as dataset 4.

The JAVAD receiver can provide I/Q, Doppler shift, and Doppler phase samples among other GPS and Galileo signals at L1/E1 and L5/E5a frequency bands. The samples are provided at a rate of 50 Hz, and the coherent integration time used for the receiver tracking loops is $T_I = 20$ ms. We consider the GPS L1 C/A signals from satellites PRN 04 of dataset 1, PRN 24 of dataset 2, PRN 15 of dataset 3, and PRN 21 of dataset 4, for the analysis of the monitoring algorithm. The S_4 indices computed for these satellites are shown in Figure 4.29, with minute 0 corresponding to the beginning of the hourly time windows used in the analysis. Amplitude scintillation activity is considered weak if $S_4 \leq 0.4$, moderate if $0.4 < S_4 \leq 0.6$ and severe if $S_4 > 0.6$, following (HUMPHREYS et al., 2009).

Figure 4.29 - S$_4$ index for scintillating channels.
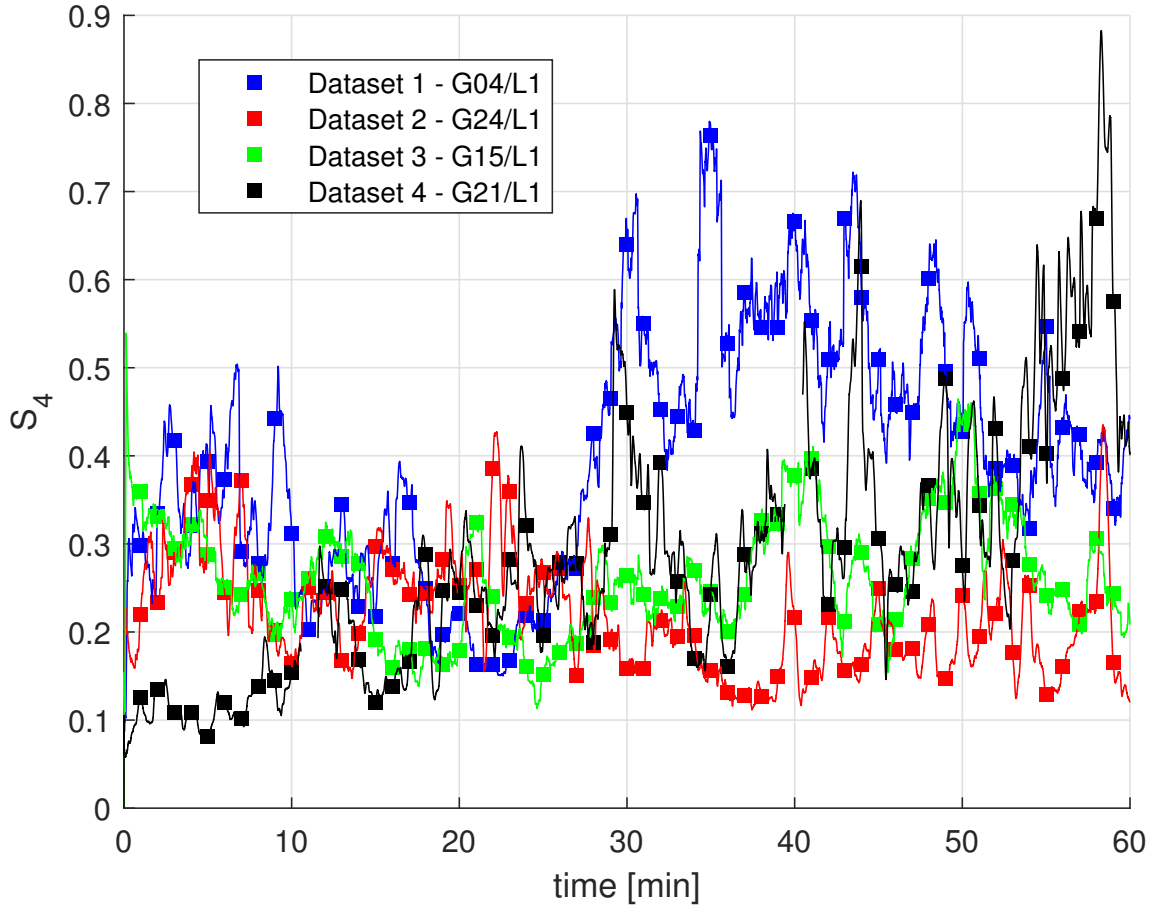
SOURCE: Author's production.

The receiver is configured to the default settings. The L1 C/A carrier tracking loop is composed of a third order PLL with noise bandwidth of 25 Hz, according to the receiver documentation. Implementation details are not provided by the manufacturer, once it is a COTS receiver. Therefore, there is some degree of uncertainty regarding any kind of correction, augmentation, performed in the receiver tracking loops. As the monitoring algorithm is dependent on the receiver tracking loop structure and parameters, we tentatively evaluate the monitoring algorithm with the information available.

We use the monitoring algorithm version adapted to a PLL. As the receiver carrier tracking loop is a third order PLL, we avoid to estimate $\hat{\hat{f}}_D[k]$ from the I/Q samples since it would involve a term with open loop integration, according to Section 4.3.2.

Instead, we obtain this estimate by simple differencing of the recorded Doppler shift estimate $\hat{f}_D[k]$, so $\hat{\dot{f}}_D[k] = (\hat{f}_D[k] - \hat{f}_D[k-1])/T_I$. The phase discriminator is applied to the I/Q samples to obtain $\delta\phi[k]$, used in the complementary high frequency branch of the algorithm.

The monitoring algorithm computes the residual phase estimates of scintillating channels, including scintillation and clock induced phase variations common to all processing channels. To remove the receiver clock phase effect, we selected a non-scintillating channel from each dataset to be used as the reference channel, and then we subtracted the residual phase estimate computed by the monitoring algorithm for this channel from the residual phase estimates of the scintillating channels. The C/N_0 of the channels considered are above the level of 40 dB-Hz, which is typically employed as a mask for scintillation analysis (CURRAN et al., 2015). Surely, due to the deep signal fades, the C/N_0 dropped below 40 dB-Hz in the scintillating channels during the scintillation activity. We did not consider an elevation mask in the analysis.

The σ_ϕ is computed recursively for a sliding time window of 60 s. The σ_ϕ computed with the estimates from the monitoring algorithm was compared to the σ_ϕ computed by the standard procedure employed in post-processing data analysis, as described in (DIERENDONCK et al., 1993), (ZHANG et al., 2010), where a fourth order polynomial is fitted to the Doppler phase with least squares in batch processing using a sliding time window of 100 s to detrend the phase (ZHANG et al., 2010). The common phase variation induced by the receiver clock is removed from the resulting detrended phase by subtracting the detrended phase from the reference channel, and the result is filtered by three high pass Butterworth filters, which have the same lower limit frequency defined by ω_L and ω_W, as defined for the monitoring algorithm.

Rather than investigating the specific effects on the phase due to equatorial scintillation activity present in the datasets, we explore the characteristics of the real-time monitoring algorithm to provide phase estimates for the computation of σ_ϕ consistent with the batch standard post-processing procedure. The parameters of the filters are adjusted based on the analysis of the data. Two cases are evaluated, for two different lower limit frequencies defined by the cutoff frequency ω_{BF} of the three high pass Butterworth filters in the standard post-processing procedure and by ω_L and ω_W in our monitoring algorithm. In case 1, $\omega_{BF} = \omega_L = \omega_W = 2\pi \times 0.0175$ rad/s and, in case 2, $\omega_{BF} = \omega_L = \omega_W = 2\pi \times 0.05$ rad/s. In both cases, the remaining parameters of the monitoring algorithm are $\tau_H = 200$ s, $\omega_H = 2\pi \times 5$ rad/s, $a_3 = 1.1$,

$b_3 = 2.4$ and $\xi = 1/\sqrt{2}$. The Butterworth filtering in the standard post-processing procedure introduces phase changes in the filtered signal, according to its frequency response. This reflects in a time mismatch between the scintillation phase estimated by this procedure and the scintillation phase estimated by our monitoring algorithm. Thus, the detrended scintillation phase from the post-processing algorithm is compensated by a time shift computed from the mean time shift introduced by the Butterworth filter prior to the σ_ϕ computation, to achieve a better comparison with our monitoring algorithm.

The comparison between the proposed monitoring algorithm and the post-processing algorithm described in (DIERENDONCK et al., 1993), (ZHANG et al., 2010) is illustrated in Figures 4.30, 4.31, 4.32, and 4.33, for datasets 1, 2, 3, and 4, respectively, for the first case, and in Figures 4.34, 4.35, 4.36, and 4.37, for datasets 1, 2, 3, and 4, respectively, for the second case.

Figure 4.30 - Phase standard deviation comparison for GPS PRN 04 (G04), dataset 1, and case 1.
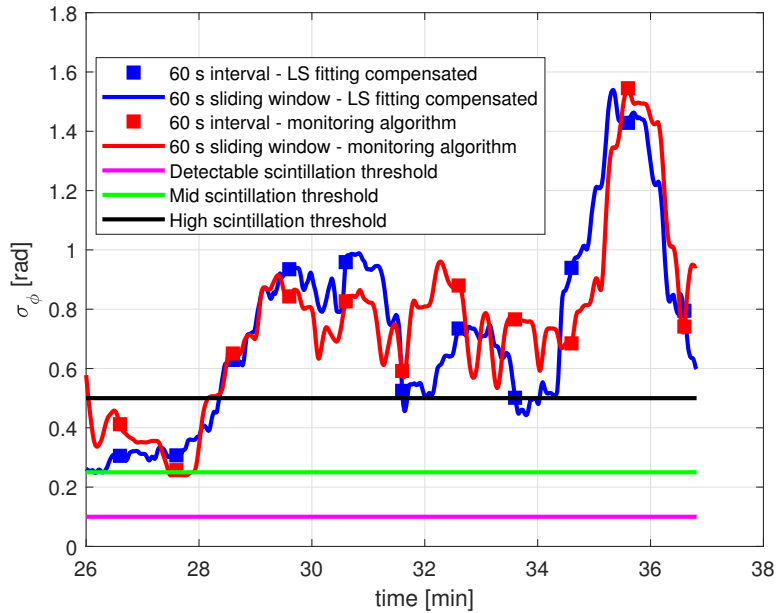
SOURCE: Author's production.

Figure 4.31 - Phase standard deviation comparison for GPS PRN 24 (G24), dataset 2, and case 1.
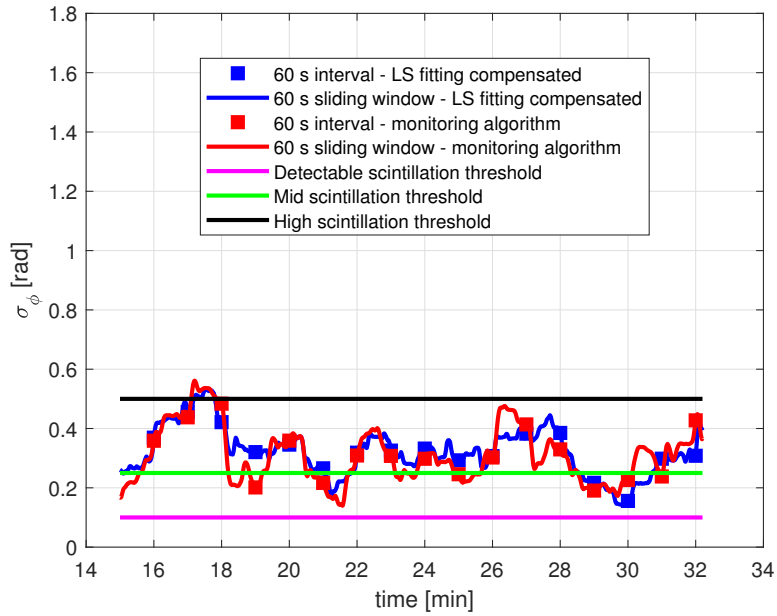
SOURCE: Author's production.

Figure 4.32 - Phase standard deviation comparison for GPS PRN 15 (G15), dataset 3, and case 1.
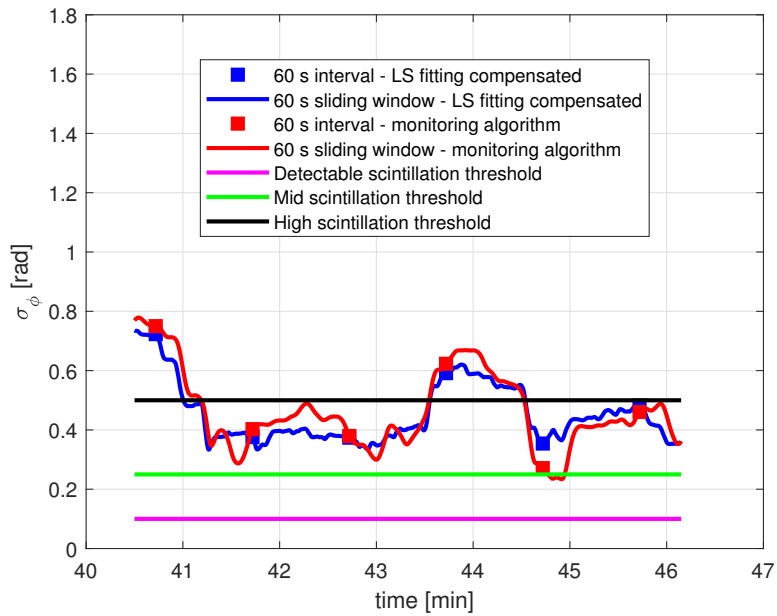
SOURCE: Author's production.

Figure 4.33 - Phase standard deviation comparison for GPS PRN 21 (G21), dataset 4, and case 1.
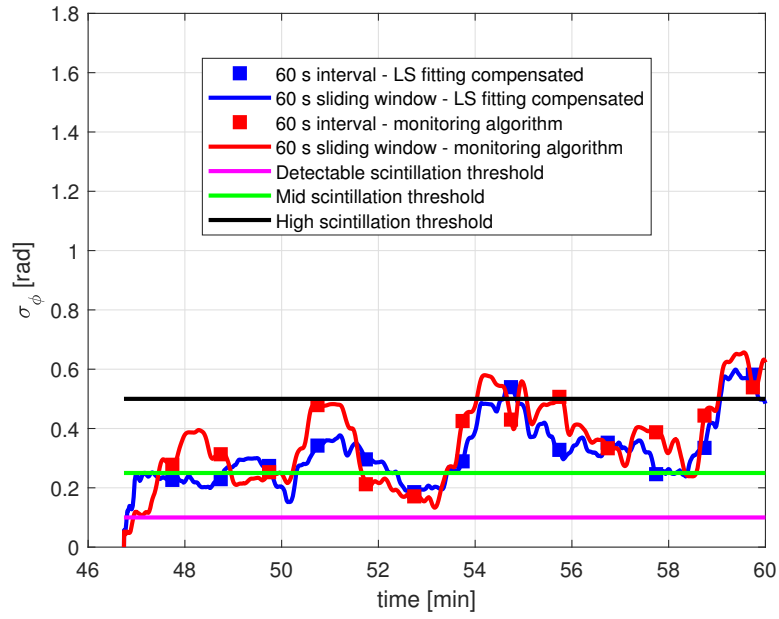
SOURCE: Author's production.

Figure 4.34 - Phase standard deviation comparison for GPS PRN 04 (G04), dataset 1, and case 2.

SOURCE: Author's production.

91
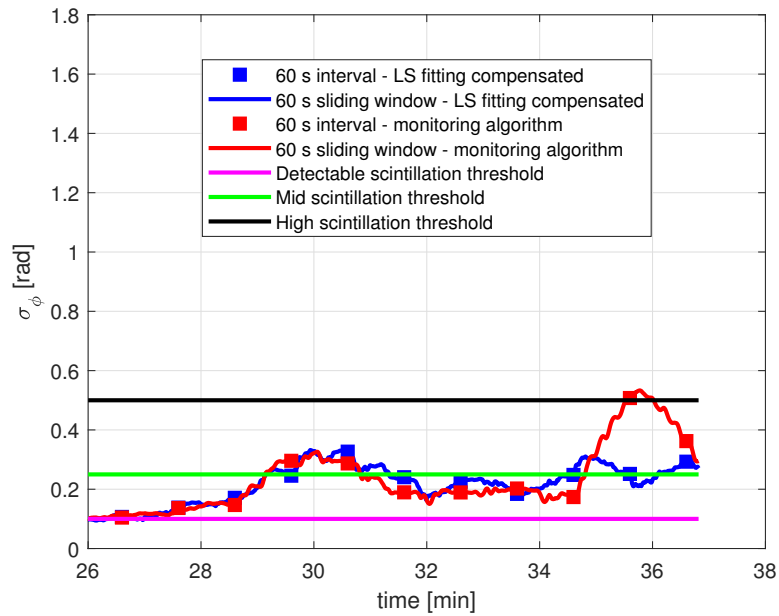
Figure 4.35 - Phase standard deviation comparison for GPS PRN 24 (G24), dataset 2, and case 2.
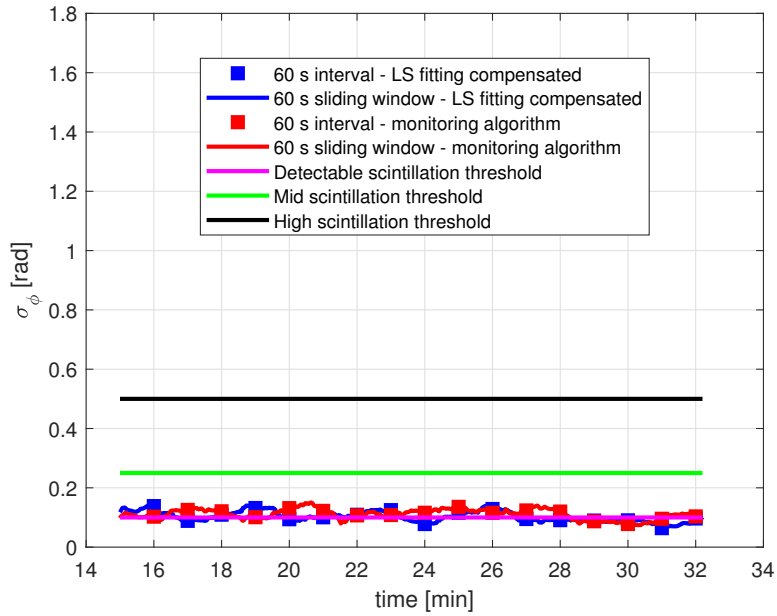
SOURCE: Author's production.

Figure 4.36 - Phase standard deviation comparison for GPS PRN 15 (G15), dataset 3, and case 2.
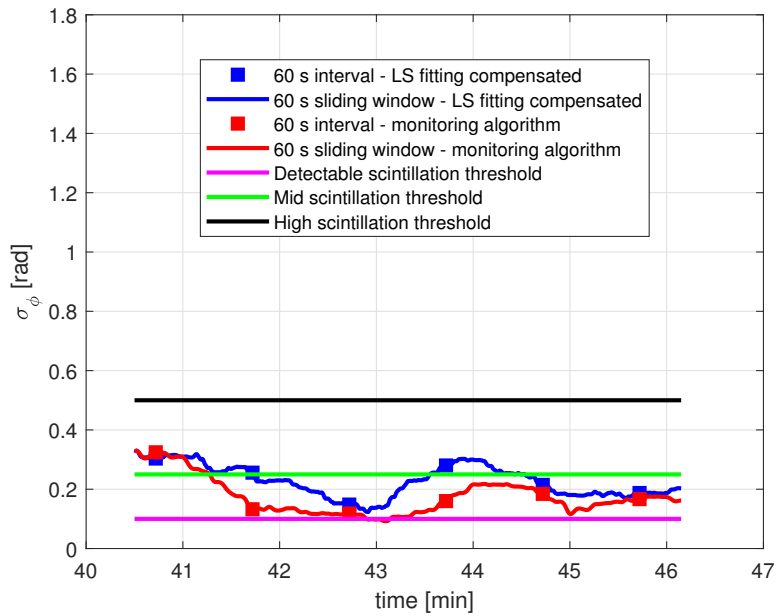
SOURCE: Author's production.

Figure 4.37 - Phase standard deviation comparison for GPS PRN 21 (G21), dataset 4, and case 2.
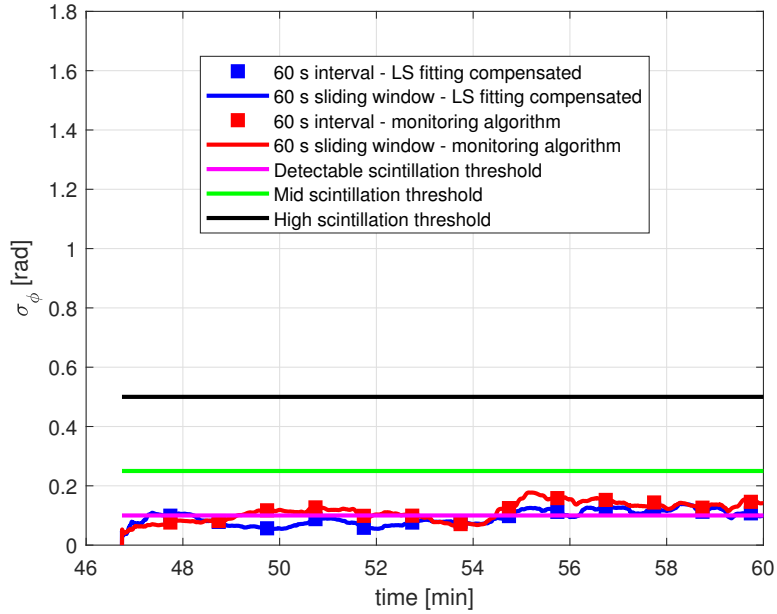
SOURCE: Author's production.

In general, the phase standard deviation computed based on the phase estimates from the monitoring algorithm is consistent with the phase standard deviation computed by the post-processing procedure. The only exception is the more significant difference observed in the last 2 minutes of dataset 1, for 0.05 Hz, as shown in Figure 4.34, but returning to show good agreement after the transient. We consider the thresholds of 0.1 rad for detectable scintillation activity in phase, 0.25 rad for moderate scintillation activity, and 0.5 rad for severe scintillation activity, following (VILÁ-VALLS et al., 2020). The purpose of the lower frequency limit is to filter out spurious low frequency content induced by other sources, e.g., multipath. A more detailed investigation is necessary to define the suitable lower limit to be used when studying scintillation effects, taking into account factors such as the specific receiver tracking loop structure, the receiver mounting and surrounding area, complementary information related to the physics of the ionosphere and the scintillation effects for the time period and location where the data was collected. As we increase the lower limit frequency from 0.0175 Hz to 0.05 Hz, more frequency content is removed, thus decreasing the phase standard deviation, as can be observed comparing Figures 4.30 - 4.33 to Figures 4.34 - 4.37. In this work, our objective is to show that the real-time monitoring algorithm can be adjusted accordingly, after a comprehensive analysis,

93

and it can provide results in real-time consistent with the post-processing procedure. Even though the receiver manufacturer provides a lot of information about the implemented signal processing of the COTS receiver, we do not have all necessary information on its exact PLL structure, which directly affects the monitoring algorithm. However, despite of this, the phases estimated by the monitoring algorithm are displaying standard deviation in a level close to the post-processing algorithm. Typically, in the post-processing data analysis, the phase standard deviation is computed at multiples of a predefined time internal, where the most common is the 60 s time interval. Hence, we present the results also in a sliding time window of 60 s to show the possibility of having a real-time phase scintillation metric computation downstream the real-time phase estimation in our monitoring algorithm.

5 SCINTILLATION MITIGATION WITH KALMAN PLLS

The signal processing channels in a GNSS receiver perform carrier and code delay tracking of GNSS satellite signals. Regarding the received signal carrier, ionospheric irregularities are one source of amplitude and phase scintillation adding up to the LOS dynamics, introducing disturbances to GNSS tracking algorithms in the receiver that in many cases cause a reduction of precision in the positioning and eventually the loss of lock of GNSS signals. Scintillation is more frequently observed at equatorial and high-latitude regions, with most critical effects induced by severe scintillation activity at the equatorial region, resulting in rapid amplitude and phase scintillation with deep amplitude fades for short periods. The mitigation of the scintillation effects, in addition to the detection and monitoring, is challenging from the signal processing perspective (VILÁ-VALLS et al., 2020).

High accuracy carrier tracking is vital for positioning accuracy improvement in modern receivers applying carrier-based positioning such as RTK and PPP (JACOBSEN; ANDALSVIK, 2016), (BANVILLE; LANGLEY, 2013). Once the scintillation effects are more pronounced in the carrier tracking, robust carrier synchronization structures contemplating the induced phase and amplitude scintillation can significantly improve carrier tracking. Originally, the traditional tracking loop structures implemented with PLLs and/or FLLs are not directly taking into account amplitude or phase scintillation. Their parameters are fixed and adjusted for LOS-only tracking. Robustness can be improved via the tuning of parameters such as noise bandwidth (LEGRAND et al., 2000) in PLLs or employing an FLL-assisted PLL structure (XU et al., 2015b), for example.

The Kalman filter has been successfully employed in GNSS carrier tracking loops with this intent. Early applications involved suboptimal computation of the Kalman gains by solving only the steady-state Riccati equation, as in (STATMAN; HURD, 1990). Typically, a constant gain Kalman filter structure is chosen in the case the simplicity of the suboptimal solution is more suitable for the application than introducing the computational load to perform the real-time update of the gains. A Kalman filter PLL was employed in (HUMPHREYS et al., 2005) with LOS and clock error state variables, and measurement noise adjusted as a function of the carrier-to-noise density ratio C/N_0, allowing better phase tracking during the power fades and phase dynamics induced by scintillation when compared to a constant bandwidth loop.

The introduction of models representing the scintillation dynamics in the received

signal into the Kalman filter formulation enabled decoupling both scintillation and LOS contributions to overcome the limitations of techniques that only adjust the level of uncertainty in models accounting for states related to the LOS dynamics, e.g., based on an estimate of C/N_0 (VILÁ-VALLS et al., 2020). Ionospheric scintillation is typically modeled as an autoregressive process. In (VILÁ-VALLS et al., 2015), the parameters of the AR model are identified *a priori* in an offline procedure, the measurement noise covariance is online adapted based on an C/N_0 estimator and a discriminator-based Kalman filter PLL structure estimating the scintillation phase is employed. In (VILÁ-VALLS et al., 2018), an extended Kalman filter PLL structure using the prompt correlator in-phase/quadrature outputs as measurements is used for scintillation mitigation, providing estimates of both scintillation amplitude and phase, with the parameters of their AR models identified offline and adaptive measurement noise covariance update. This concept is generalized in (VILÁ-VALLS et al., 2018) with an extended Kalman filter with increased complexity including an online batch identification of the AR models parameters and online updating of the process noise covariance matrix based on the identification statistics. Other techniques also consider adaptive Kalman filtering with online adaptive estimation of the AR scintillation model parameters, as in (FOHLMEISTER et al., 2018b), where a dual Kalman filter was applied. In this approach the scintillation phase and amplitude are estimated by a first Kalman filter. They are then used as measurements in the second Kalman filter to estimate the parameters of the respective AR process. Afterwards, the LOS and scintillation phase error estimates are then fed back into the carrier signal replica generator by a linear quadratic Gaussian control approach.

In this chapter, we present two Kalman PLL structures for ionospheric scintillation mitigation employing radial basis function networks instead of the AR models representing scintillation phase and amplitude dynamics. In the first structure, the innovations of the Kalman filter are taken from the phase discriminator output and the carrier replica is generated in the NCO with the Kalman filter estimates, such as the discriminator-based Kalman PLL structure of (VILÁ-VALLS et al., 2015). In the second structure, the Kalman filter takes the prompt correlator I/Q outputs as measurements, such as in (VILÁ-VALLS et al., 2018). In this case, a state feedback controller operating on the error states estimated by the Kalman filter is designed to provide a control signal to the NCO for the carrier replica generation, following a pole placement procedure to compute the gain matrix to drive the closed loop error dynamics to zero. In both structures we have nonlinear process equations due to the RBF networks, so that both Kalman PLL structures implement the extended Kalman filter. We propose to employ the RBF networks to model scintillation due to

the capability of their nonlinear radial basis functions to capture eventual nonlinear dynamics, possibly evolving with time, induced by the ionospheric scintillation in the receiver, unlike the AR models. The RBF networks allow greater flexibility in scintillation induced effects modeling, and we can include pure AR terms in their structure, in addition to the nonlinear radial basis functions. Also, we can use recursive least squares to estimate the weights of the networks, since they have a linear structure with respect to their weights. The results of the least squares identification are used to update the process equations and process noise covariance matrices of the Kalman filters, as in (VILÁ-VALLS et al., 2018). The measurement noise covariance matrices are also adaptively computed, as in (VILÁ-VALLS et al., 2018), based on an C/N_0 estimator.

Next, we present both adaptive Kalman PLL structures using AR models representing scintillation phase and amplitude dynamics. Then, we replace the AR scintillation models by the RBF networks to present the proposed Kalman PLL structures employing the RBF networks. Finally, we asses the performances of the proposed adaptive Kalman PLLs employing the RBF networks for scintillation mitigation via numerical simulations by adding synthetic severe scintillation data generated by the CSM (HUMPHREYS et al., 2010) to simulated baseband GPS L1 C/A code signal input data, comparing their results regarding robust LOS tracking and estimation of scintillation induced effects to the results of the corresponding state-of-the-art adaptive Kalman PLLs employing pure AR scintillation models (VILÁ-VALLS et al., 2018). The performance of the proposed Kalman PLLs employing the RBF networks is also assessed with real scintillation data collected by a commercial receiver, and compared to the structures employing the AR models.

5.1 Kalman PLLs with AR scintillation models

Let the LOS dynamics and the scintillation phase and amplitude be considered independent processes. Then, the scintillation process model can be added to the LOS process model, so that LOS robust tracking and scintillation phase and amplitude estimation are accomplished by a Kalman PLL. Substituting h in the equations presented in Section 3.1.5 by the coherent integration period T_I, the LOS dynamics is represented by the kinematic process model (BAR-SHALOM et al., 2001)

$$
\underbrace{\begin{bmatrix} \phi_D[k] \\ f_D[k] \\ a_D[k] \end{bmatrix}}_{=\mathbf{x}_D[k]} = \underbrace{\begin{bmatrix} 1 & T_I & T_I^2/2 \\ 0 & 1 & T_I \\ 0 & 0 & 1 \end{bmatrix}}_{=\mathbf{F}_D} \underbrace{\begin{bmatrix} \phi_D[k-1] \\ f_D[k-1] \\ a_D[k-1] \end{bmatrix}}_{=\mathbf{x}_D[k-1]} + \boldsymbol{\nu}_D[k-1], \qquad (5.1)
$$

97

after truncation of (2.11) at the second order term. The LOS state vector $\mathbf{x}_D[k]$ consists of the Doppler phase $\phi_D[k]$, frequency shift $f_D[k]$, and frequency drift $a_D[k]$. The kinematic model truncated at the second order term represents the LOS dynamics with zero-mean Gaussian jerk with power $\sigma_{j_D}^2$, so the process noise $\boldsymbol{\nu}_D[k]$ is defined by the covariance matrix

$$\mathbf{Q}_D = \sigma_{j_D}^2 \begin{bmatrix} T_I^5/20 & T_I^4/8 & T_I^3/6 \\ T_I^4/8 & T_I^3/3 & T_I^2/2 \\ T_I^3/6 & T_I^2/2 & T_I \end{bmatrix}. \tag{5.2}$$

Scintillation phase and amplitude are typically modeled by AR processes in Kalman PLLs for scintillation mitigation (VILÁ-VALLS et al., 2015), (VILÁ-VALLS et al., 2018), (VILÁ-VALLS et al., 2018), (LOCUBICHE-SERRA et al., 2016). The AR model for the scintillation phase can be written as

$$\phi[k] = \sum_{i=1}^{n_\phi} \theta_{\phi_i} \phi[k-i] + \eta_\phi[k-1] = \boldsymbol{\theta}_\phi^{\mathrm{T}} \mathbf{x}_\phi[k-1] + \eta_\phi[k-1], \tag{5.3}$$

and the AR model for the scintillation amplitude as

$$\rho[k] = \theta_{\rho 0} + \sum_{i=1}^{n_\rho} \theta_{\rho_i} \rho[k-i] + \eta_\rho[k-1] = \theta_{\rho 0} + \boldsymbol{\theta}_\rho^{\mathrm{T}} \mathbf{x}_\rho[k-1] + \eta_\rho[k-1], \tag{5.4}$$

where n_ϕ and n_ρ are the orders of the phase and amplitude models, respectively, θ_{ϕ_i} and θ_{ρ_i} are the parameters of the phase and amplitude models, respectively, and $\eta_\phi[k]$ with variance $\sigma_{\eta_\phi}^2$ and $\eta_\rho[k]$ with variance $\sigma_{\eta_\rho}^2$ are the errors of the phase and amplitude models, respectively. The bias term $\theta_{\rho 0}$ is introduced in the amplitude model due to the nonzero mean of the amplitude variations. From the AR models, we can write the process equations for the scintillation phase as

$$\mathbf{x}_\phi[k] = \underbrace{\begin{bmatrix} \boldsymbol{\theta}_\phi^{\mathrm{T}} \\ \begin{bmatrix} \mathbf{I}_{n_\phi-1} & \mathbf{0}_{n_\phi-1} \end{bmatrix} \end{bmatrix}}_{=\mathbf{F}_{\phi_{\mathrm{AR}}}} \mathbf{x}_\phi[k-1] + \boldsymbol{\nu}_\phi[k-1], \tag{5.5}$$

and for the scintillation amplitude as

$$\mathbf{x}_\rho[k] = \underbrace{\begin{bmatrix} \boldsymbol{\theta}_\rho^{\mathrm{T}} \\ \begin{bmatrix} \mathbf{I}_{n_\rho-1} & \mathbf{0}_{n_\rho-1} \end{bmatrix} \end{bmatrix}}_{=\mathbf{F}_{\rho_{\mathrm{AR}}}} \mathbf{x}_\rho[k-1] + \underbrace{\begin{bmatrix} \theta_{\rho 0} \\ \mathbf{0}_{n_\rho-1} \end{bmatrix}}_{=\mathbf{b}_{\rho_{\mathrm{AR}}}} + \boldsymbol{\nu}_\rho[k-1], \tag{5.6}$$

with the scintillation phase state vector

$$\mathbf{x}_\phi[k] = \begin{bmatrix} \phi[k] & \cdots & \phi[k - n_\phi + 1] \end{bmatrix}^\mathrm{T}, \tag{5.7}$$

and the scintillation amplitude state vector

$$\mathbf{x}_\rho[k] = \begin{bmatrix} \rho[k] & \cdots & \rho[k - n_\phi + 1] \end{bmatrix}^\mathrm{T}. \tag{5.8}$$

The scintillation phase process noise vector is

$$\boldsymbol{\nu}_\phi[k] = \begin{bmatrix} \eta_\phi[k] \\ \mathbf{0}_{n_\phi - 1} \end{bmatrix}, \tag{5.9}$$

and the scintillation amplitude process noise vector is

$$\boldsymbol{\nu}_\rho[k] = \begin{bmatrix} \eta_\rho[k] \\ \mathbf{0}_{n_\rho - 1} \end{bmatrix}, \tag{5.10}$$

where $\mathbf{I}_z$ and $\mathbf{0}_z$ are the identity matrix of size z and a vector including only zeroes of size z, respectively. The process noise covariance matrix of the scintillation phase is

$$\mathbf{Q}_{\phi_\mathrm{AR}} = \mathrm{diag}\left(\begin{bmatrix} \sigma_{\eta_\phi}^2, \mathbf{0}_{n_\phi - 1}^\mathrm{T} \end{bmatrix}^\mathrm{T} \right) \tag{5.11}$$

and the process noise covariance matrix of the scintillation amplitude is

$$\mathbf{Q}_{\rho_\mathrm{AR}} = \mathrm{diag}\left(\begin{bmatrix} \sigma_{\eta_\rho}^2, \mathbf{0}_{n_\rho - 1}^\mathrm{T} \end{bmatrix}^\mathrm{T} \right), \tag{5.12}$$

where $\mathrm{diag}(\mathbf{v})$ denotes a diagonal matrix formed by the elements of the vector $\mathbf{v}$.

Different Kalman PLL structures can be implemented for carrier synchronization, working either with direct states or with error states (WON et al., 2010), (YANG et al., 2017). In the first case, the Kalman filter provides estimates of LOS and scintillation states, the carrier replica is directly generated with the Kalman filter estimates in the NCO, and the phase discriminator outputs are taken as the filter innovations. In the second case, in general, the Kalman filter provides estimates of the error in LOS and scintillation phase states, used in the carrier synchronization feedback. The filter observations can be taken from the phase discriminator outputs or from the prompt correlator I/Q outputs. Additionally, a controller taking the phase error state as input is necessary to provide a control signal to the NCO for the replica generation. Other Kalman PLLs employing direct or error states are possible, e.g.,

as shown in (WON et al., 2010).

In this work, we propose a Kalman PLL structure for scintillation mitigation henceforth called discriminator-based Kalman PLL, which includes the scintillation phase dynamics in the Kalman filter model with discriminator outputs taken as filter innovations, and a Kalman PLL structure with prompt correlator I/Q outputs taken as observations including both scintillation phase and amplitude estimation, henceforth called correlator-based Kalman PLL. Next, we describe the Kalman PLL formulation for both structures using the AR scintillation models.

5.1.1 Discriminator-based Kalman PLL

In the direct state discriminator-based Kalman PLL, the scintillation amplitude is not part of the state vector, which is formed by the LOS states and the scintillation phase states. The state vector $\mathbf{x}_1[k]$ of the discriminator-based Kalman PLL is defined as

$$\mathbf{x}_1[k] = \begin{bmatrix} \mathbf{x}_D^{\mathrm{T}}[k] & \mathbf{x}_\phi^{\mathrm{T}}[k] \end{bmatrix}^{\mathrm{T}}. \tag{5.13}$$

When using the AR model for the scintillation phase, the process equations are linear with respect to $\mathbf{x}_1[k]$, and the state transition matrix is

$$\mathbf{F}_1 = \mathrm{blkdiag}\left(\mathbf{F}_D, \mathbf{F}_{\phi_{\mathrm{AR}}}\right), \tag{5.14}$$

where $\mathrm{blkdiag}(\mathbf{M}_1, \cdots, \mathbf{M}_o)$ denotes a block-diagonal matrix formed by the matrices $\mathbf{M}_1, \cdots, \mathbf{M}_o$ on its main diagonal. The process noise covariance matrix is

$$\mathbf{Q}_1 = \mathrm{blkdiag}\left(\mathbf{Q}_D, \mathbf{Q}_{\phi_{\mathrm{AR}}}\right). \tag{5.15}$$

The process equations, then, are

$$\mathbf{x}_1[k] = \mathbf{F}_1 \mathbf{x}_1[k-1] + \boldsymbol{\nu}_1[k-1], \tag{5.16}$$

where $\boldsymbol{\nu}_1[k] = \begin{bmatrix} \boldsymbol{\nu}_D^{\mathrm{T}}[k] & \boldsymbol{\nu}_\phi^{\mathrm{T}}[k] \end{bmatrix}^{\mathrm{T}}$.

The carrier replica is generated in the NCO directly with the states estimated by the Kalman filter, but now including the scintillation phase estimate. The signal model for the carrier replica is obtained from the carrier phase model (2.18), including the scintillation phase estimate along the Doppler phase and frequency shift estimates.

Thus, the carrier replica is

$$\mathbf{d}_1[k; \hat{f}_D[k]; \hat{\phi}[k]] = \left[e^{j(\hat{\phi}_D[k] + \hat{\phi}[k])}, \ldots, e^{j(\hat{f}_D[k](N-1)T_s + \hat{\phi}_D[k] + \hat{\phi}[k])} \right]^{\mathrm{T}}, \qquad (5.17)$$

and now, accordingly, the phase discriminator (2.26) is

$$\varepsilon_P[k] = \delta\phi[k] + \delta\phi_D[k] + \eta_A[k], \qquad (5.18)$$

with $\delta\phi[k] = \phi[k] - \hat{\phi}[k]$. The Kalman filter innovations sequence is directly formed by the outputs of the phase discriminator above (5.18). The innovation is the sum of the Doppler and the scintillation phase errors. Hence, the matrix of observations is

$$\mathbf{H}_1 = \begin{bmatrix} 1 & 0 & 0 & 1 & \mathbf{0}_{n_\phi - 1}^{\mathrm{T}} \end{bmatrix}, \qquad (5.19)$$

with measurement noise covariance defined by the arctangent discriminator noise approximation (2.27)

$$\mathbf{R}_1 = \frac{1}{2c/n_0 T_I} \left(1 + \frac{1}{2c/n_0 T_I} \right). \qquad (5.20)$$

The parameters of the scintillation phase AR model can be estimated by recursive least squares (SÖDERSTRÖM; STOICA, 1989). We implement the recursive least squares algorithm with rectangular sliding window as proposed in (YOUNG, 2011) to estimate the AR model parameters and the model error variance in real-time. Then, we adaptively update $\mathbf{F}_\phi$ and $\mathbf{Q}_\phi$ in the Kalman filter with $\hat{\boldsymbol{\theta}}_\phi[k-1]$ and $\hat{\sigma}_\phi^2[k-1]$, respectively. In addition, we also adaptively update $\mathbf{R}_1$ using $\widehat{c/n_0}[k-1]$ at each iteration. There are many algorithms available for c/n_0 estimation (FALLETTI et al., 2011).

5.1.2 Correlator-based Kalman PLL

In the correlator-based Kalman PLL structure employing the AR scintillation models, the Kalman filter estimates the scintillation amplitude in addition to the phase error state vector including LOS and scintillation phase states which is used in the carrier synchronization feedback loop. We can write the phase error state vector as

$$\delta\mathbf{x}_1[k] = \mathbf{x}_1[k] - \begin{bmatrix} \mathbf{x}_{D_{\mathrm{NCO}}}[k] \\ \mathbf{x}_{\phi_{\mathrm{NCO}}}[k] \end{bmatrix} = \mathbf{x}_1[k] - \mathbf{x}_{\mathrm{NCO}}[k], \qquad (5.21)$$

with $\mathbf{x}_1[k]$ defined by (5.13), and $\mathbf{x}_{D_{\mathrm{NCO}}}[k] \in \mathbb{R}^{3 \times 1}$ and $\mathbf{x}_{\phi_{\mathrm{NCO}}}[k] \in \mathbb{R}^{n_\phi \times 1}$ are the LOS and the scintillation phase state vectors of the NCO state vector $\mathbf{x}_{\mathrm{NCO}}[k] =$

$\begin{bmatrix} \mathbf{x}_{D_{\mathrm{NCO}}}^{\mathrm{T}}[k] & \mathbf{x}_{\phi_{\mathrm{NCO}}}^{\mathrm{T}}[k] \end{bmatrix}^{\mathrm{T}}$, with

$$\mathbf{x}_{D_{\mathrm{NCO}}}[k] = \begin{bmatrix} \phi_{D_{\mathrm{NCO}}}[k] & f_{D_{\mathrm{NCO}}}[k] & a_{D_{\mathrm{NCO}}}[k] \end{bmatrix}^{\mathrm{T}}, \tag{5.22}$$

and

$$\mathbf{x}_{\phi_{\mathrm{NCO}}}[k] = \begin{bmatrix} \phi_{\mathrm{NCO}}[k] & \dots & \phi_{\mathrm{NCO}}[k - n_\phi + 1] \end{bmatrix}^{\mathrm{T}}. \tag{5.23}$$

Then, Kalman filter state vector is

$$\mathbf{x}_2[k] = \begin{bmatrix} \delta\mathbf{x}_1[k] \\ \mathbf{x}_\rho[k] \end{bmatrix}, \tag{5.24}$$

and the state transition matrix is

$$\mathbf{F}_2 = \mathrm{blkdiag}\left(\mathbf{F}_1, \mathbf{F}_{\rho_{\mathrm{AR}}}\right), \tag{5.25}$$

with process noise covariance matrix

$$\mathbf{Q}_2 = \mathrm{blkdiag}\left(\mathbf{Q}_1, \mathbf{Q}_{\rho_{\mathrm{AR}}}\right). \tag{5.26}$$

The NCO process equations are

$$\mathbf{x}_{\mathrm{NCO}}[k] = \mathbf{F}_{\mathrm{NCO}}\mathbf{x}_{\mathrm{NCO}}[k-1] + \mathbf{G}_{\mathrm{NCO}}\mathbf{u}_{\mathrm{NCO}}[k-1], \tag{5.27}$$

with $\mathbf{F}_{\mathrm{NCO}} = \mathbf{F}_1$ and $\mathbf{G}_{\mathrm{NCO}} = \mathbf{I}_{3+n_\phi}$.

From (5.16), (5.21), (5.24) and (5.27), and considering $\mathbf{F}_{\mathrm{NCO}} = \mathbf{F}_1$, we get the Kalman filter process equations

$$\begin{aligned} \mathbf{x}_2[k] &= \begin{bmatrix} \mathbf{x}_1[k] - \mathbf{x}_{\mathrm{NCO}}[k] \\ \mathbf{x}_\rho[k] \end{bmatrix} \\ &= \begin{bmatrix} \mathbf{F}_1\mathbf{x}_1[k-1] + \boldsymbol{\nu}_1[k-1] - \mathbf{F}_{\mathrm{NCO}}\mathbf{x}_{\mathrm{NCO}}[k-1] - \mathbf{G}_{\mathrm{NCO}}\mathbf{u}_{\mathrm{NCO}}[k-1] \\ \mathbf{F}_{\rho_{\mathrm{AR}}}\mathbf{x}_\rho[k-1] + \mathbf{b}_{\rho_{\mathrm{AR}}} + \boldsymbol{\nu}_\rho[k-1] \end{bmatrix} \\ &= \begin{bmatrix} \mathbf{F}_1\delta\mathbf{x}_1[k-1] - \mathbf{G}_{\mathrm{NCO}}\mathbf{u}_{\mathrm{NCO}}[k-1] + \boldsymbol{\nu}_1[k-1] \\ \mathbf{F}_{\rho_{\mathrm{AR}}}\mathbf{x}_\rho[k-1] + \mathbf{b}_{\rho_{\mathrm{AR}}} + \boldsymbol{\nu}_\rho[k-1] \end{bmatrix} \\ &= \mathbf{F}_2\mathbf{x}_2[k-1] + \mathbf{G}_2 \begin{bmatrix} \mathbf{u}_{\mathrm{NCO}}[k-1] \\ \mathbf{b}_{\rho_{\mathrm{AR}}} \end{bmatrix} + \boldsymbol{\nu}_2[k-1], \end{aligned} \tag{5.28}$$

where $\mathbf{G}_2 = \mathrm{blkdiag}(-\mathbf{G}_{\mathrm{NCO}}, \mathbf{I}_{n_\rho}) = \mathrm{blkdiag}(-\mathbf{I}_{3+n_\phi}, \mathbf{I}_{n_\rho})$ and $\boldsymbol{\nu}_2[k] = [\boldsymbol{\nu}_1^{\mathrm{T}}[k] \ \boldsymbol{\nu}_\rho^{\mathrm{T}}[k]]^{\mathrm{T}}$.

The Kalman filter provides estimates $\hat{\mathbf{x}}_2[k] = \begin{bmatrix} \delta\hat{\mathbf{x}}_1^{\mathrm{T}}[k] & \hat{\mathbf{x}}_\rho^{\mathrm{T}}[k] \end{bmatrix}^{\mathrm{T}}$ using the prompt correlator outputs as observations. In (2.25), the scintillation phase was not considered in the carrier replica generation. For scintillation mitigation, the NCO uses its scintillation phase estimate along with its LOS estimates to generate the carrier replica. The carrier replica generated by the NCO is

$$\mathbf{d}_2[k; f_{D_{\mathrm{NCO}}}[k]; \phi_{\mathrm{NCO}}[k]] = \left[e^{j(\phi_{D_{\mathrm{NCO}}}[k] + \phi_{\mathrm{NCO}}[k])}, \right.$$
$$\left. \dots, e^{j(f_{D_{\mathrm{NCO}}}[k](N-1)T_s + \phi_{D_{\mathrm{NCO}}}[k] + \phi_{\mathrm{NCO}}[k])} \right]^{\mathrm{T}}. \tag{5.29}$$

Calling $\phi_T[k] = \phi_D[k] + \phi[k]$ and $\phi_{T_{\mathrm{NCO}}}[k] = \phi_{D_{\mathrm{NCO}}}[k] + \phi_{\mathrm{NCO}}[k]$, so that $\delta\phi_T[k] = \phi_T[k] - \phi_{T_{\mathrm{NCO}}}[k]$, we can modify (2.25) to obtain the observation equations of the correlator-based Kalman filter from the I/Q prompt correlators outputs, as

$$\mathbf{y}_2[k] = \begin{bmatrix} \rho[k]\cos(\phi_T[k] - \phi_{T_{\mathrm{NCO}}}[k]) \\ \rho[k]\sin(\phi_T[k] - \phi_{T_{\mathrm{NCO}}}[k]) \end{bmatrix} + \begin{bmatrix} \eta_{D_I}[k] \\ \eta_{D_Q}[k] \end{bmatrix} = \begin{bmatrix} \rho[k]\cos(\delta\phi_T[k]) \\ \rho[k]\sin(\delta\phi_T[k]) \end{bmatrix} + \begin{bmatrix} \eta_{D_I}[k] \\ \eta_{D_Q}[k] \end{bmatrix}, \tag{5.30}$$

whose noise covariance matrix is

$$\mathbf{R}_2 = (\sigma_{\eta_D}^2/2)\mathbf{I}_2, \tag{5.31}$$

with $\sigma_{\eta_{D_I}}^2 = \sigma_{\eta_{D_Q}}^2 = \sigma_{\eta_D}^2/2$, as described in Section 2.1. The matrix of observations employed in the extended Kalman filter equations is obtained by linearization of the observation equations, leading to

$$\mathbf{H}_2 = \begin{bmatrix} \overline{\rho}\sin\delta\overline{\phi}_T & \mathbf{0}_2^{\mathrm{T}} & \overline{\rho}\sin\delta\overline{\phi}_T & \mathbf{0}_{n_\phi-1}^{\mathrm{T}} & \cos\delta\overline{\phi}_T & \mathbf{0}_{n_\rho-1}^{\mathrm{T}} \\ \text{-}\overline{\rho}\cos\delta\overline{\phi}_T & \mathbf{0}_2^{\mathrm{T}} & \text{-}\overline{\rho}\cos\delta\overline{\phi}_T & \mathbf{0}_{n_\phi-1}^{\mathrm{T}} & \sin\delta\overline{\phi}_T & \mathbf{0}_{n_\rho-1}^{\mathrm{T}} \end{bmatrix}, \tag{5.32}$$

where $\overline{\rho} = \hat{\rho}[k|k-1]$ and $\delta\overline{\phi}_T = \delta\hat{\phi}_D[k|k-1] + \delta\hat{\phi}[k|k-1]$, from the prediction step of the Kalman filter.

We use a state feedback control law to provide the control signal $\mathbf{u}_{\mathrm{NCO}}[k]$ to the NCO, such that

$$\mathbf{u}_{\mathrm{NCO}}[k] = \mathbf{L}\delta\hat{\mathbf{x}}_1[k], \tag{5.33}$$

where $\mathbf{L} \in \mathbb{R}^{(3+n_\phi)\times(3+n_\phi)}$ is a fixed feedback gain matrix, which is computed to drive the phase error dynamics to zero fast. Assuming that the Kalman filter provides accurate estimation of $\delta\mathbf{x}_1[k]$, relying on the separation principle (CURRY, 1969),

103

the error dynamics are

$$
\begin{aligned}
\delta\mathbf{x}_1[k] = \mathbf{x}_1[k] - \mathbf{x}_{\mathrm{NCO}}[k] &= \mathbf{F}_1\delta\mathbf{x}_1[k-1] - \mathbf{G}_{\mathrm{NCO}}\mathbf{u}_{\mathrm{NCO}}[k-1] + \boldsymbol{\nu}_1[k-1] \\
&= \mathbf{F}_1\delta\mathbf{x}_1[k-1] - \mathbf{G}_{\mathrm{NCO}}\mathbf{L}\delta\hat{\mathbf{x}}_1[k-1] + \boldsymbol{\nu}_1[k-1] \\
&\approx \left(\mathbf{F}_1 - \mathbf{L}\right)\delta\mathbf{x}_1[k-1] + \boldsymbol{\nu}_1[k-1],
\end{aligned}
\tag{5.34}
$$

and we can compute the gain matrix $\mathbf{L}$ to place the eigenvalues of $(\mathbf{F}_1 - \mathbf{L})$ at the chosen target poles $\mathbf{p}_1$.

Doppler phase, Doppler shift, and scintillation phase estimates can be obtained by $\hat{\phi}_D[k] = \phi_{D_{\mathrm{NCO}}}[k] + \delta\hat{\phi}_D[k]$, $\hat{f}_D[k] = f_{D_{\mathrm{NCO}}}[k] + \delta\hat{f}_D[k]$ and $\hat{\phi}[k] = \phi_{\mathrm{NCO}}[k] + \delta\hat{\phi}[k]$, respectively.

Similarly to the discriminator-based Kalman PLL, we adaptively update $\mathbf{F}_{\phi_{\mathrm{AR}}}$, $\mathbf{F}_{\rho_{\mathrm{AR}}}$, $\mathbf{b}_{\rho_{\mathrm{AR}}}$, $\mathbf{Q}_{\phi_{\mathrm{AR}}}$, and $\mathbf{Q}_{\rho_{\mathrm{AR}}}$ in the Kalman filter with, respectively, $\hat{\boldsymbol{\theta}}_\phi[k-1]$, $\hat{\boldsymbol{\theta}}_\rho[k-1]$, $\hat{\theta}_{\rho 0}[k-1]$, $\hat{\sigma}_\phi^2[k-1]$, and $\hat{\sigma}_\rho^2[k-1]$ from the recursive sliding window least squares parameter estimation. We also adaptively update $\mathbf{R}_2$ with $\hat{\sigma}_{\eta_D}^2[k-1] = 1/(T_I\widehat{c/n_0}[k-1])$.

5.2 Kalman PLLs for scintillation mitigation with RBF networks modeling scintillation

RBFs have been firstly employed in multidimensional interpolation problems (POW-ELL, 1985), (HARDY, 1971). They are typically associated with neural networks due to their interpolation structure, which can be considered as a special case of a neural network with one hidden layer formed by the nonlinear RBFs taking the role of the activation functions and one output layer formed by the weighted sum of the output of the functions, with guaranteed learning rule (BROOMHEAD; LOWE, 1988).

The radial basis function $\psi(\cdot)$ is a nonlinear mapping $\psi(\cdot) : \mathbb{R}^+ \to \mathbb{R}$ on a d-dimensional space. The RBF network takes the form (AGUIRRE et al., 2004)

$$
g(\mathbf{x}) = \omega_0 + \sum_{i=1}^{n_r} \omega_i \psi(\|\mathbf{x} - \mathbf{c}_i\|_2),
\tag{5.35}
$$

where $\mathbf{x} \in \mathbb{R}^{d \times 1}$ is the input, $\|\cdot\|_2$ is the Euclidean norm, $\mathbf{c}_i \in \mathbb{R}^{d \times 1}$ are fixed points called centers, n_r is the number of centers, and ω_i, $i = 0, \ldots, n_r$ are the weights. The function arguments are the distances in the d-dimensional space from $\mathbf{x}$ to the centers, which can be chosen in several ways. They can be chosen randomly from the dataset, or can be uniformly distributed in the region of the space covered by

the data (SMITH, 1992). Once the centers are defined, the network structure is linear with respect to the weights, and thus we can use standard least squares to estimate the weights (AGUIRRE, 2000), with regressors formed by the nonlinear RBFs.

Considering the RBF network in the modeling of autonomous dynamic systems, $\mathbf{x}$ is composed of autoregressive terms, and linear AR terms can be added to the network (AGUIRRE et al., 2004), taking the form

$$
\begin{aligned}
\alpha[k] = & \omega_0 + \sum_{i=1}^{n_r} \omega_i \psi(\|\boldsymbol{\alpha}[k-1] - \mathbf{c}_{\alpha_i}\|_2) + \\
& \sum_{i=1}^{n_\alpha} \omega_{n_r+i} \alpha[k-i] + \eta_\alpha[k-1],
\end{aligned}
\tag{5.36}
$$

where $\boldsymbol{\alpha}[k-1] \in \mathbb{R}^{n_\alpha \times 1}$ is composed of the n_α AR terms of the variable of interest $\alpha[k]$, so that $\boldsymbol{\alpha}[k-1] = \begin{bmatrix} \alpha[k-1] & \dots & \alpha[k-n_\alpha] \end{bmatrix}^{\mathrm{T}}$, and $\eta_\alpha[k]$ is the RBF network error with variance $\sigma_{\eta_\alpha}^2$. We have additional n_α weights relative to the linear terms, and $n_r + n_\alpha + 1$ weights in total. The centers $\mathbf{c}_{\alpha_i}$ can be similarly formed by AR terms taken from the modeling dataset, or can be distributed in a region of the phase space covered by the modeling dataset, for example. The choice to include the linear AR terms and the bias ω_0 depends on the dynamics to be modeled.

The RBFs can be divided into global (SCHAGEN, 1979) and local functions (WENDLAND, 2006). In this work we consider the Thin Plate Spline, which is a global function of the form

$$
\psi(r_i) = r_i^2 \ln(r_i),
\tag{5.37}
$$

where $r_i = \|\boldsymbol{\alpha}[k-1] - \mathbf{c}_i\|_2$. For the scintillation phase, $\alpha[k]$ is substituted by $\phi[k]$, and for the scintillation amplitude, $\alpha[k]$ is substituted by $\rho[k]$ in the RBF model (5.36). Also, $\boldsymbol{\alpha}[k-1]$ is substituted by $\mathbf{x}_\phi[k-1] \in \mathbb{R}^{n_\phi \times 1}$ for the scintillation phase, and by $\mathbf{x}_\rho[k-1] \in \mathbb{R}^{n_\rho \times 1}$ for the scintillation amplitude, so that we have $\mathbf{x}_\phi[k-1] = [\phi[k-1], \dots, \phi[k-n_\phi]]^{\mathrm{T}}$ and $\mathbf{x}_\rho[k-1] = [\rho[k-1], \dots, \rho[k-n_\rho]]^{\mathrm{T}}$. Using the RBF network as process model for both scintillation phase and amplitude in the Kalman PLLs requires the computation of the gradient of $\alpha[k]$ with respect to $\boldsymbol{\alpha}[k-1]$ to form the first line of the Jacobian matrix of the process equations employed in the extended Kalman filter. The gradient can be written as

$$
\begin{aligned}
\boldsymbol{\nabla}\alpha[k] &= \left[\frac{\partial \alpha[k]}{\partial \alpha[k-1]}, \dots, \frac{\partial \alpha[k]}{\partial \alpha[k-n_\alpha]} \right]^{\mathrm{T}} \\
&= \sum_{i=1}^{n_r} \omega_i \frac{\partial \psi}{\partial r_i} \boldsymbol{\nabla} r_i + [\omega_{n_r+1}, \dots, \omega_{n_r+n_\alpha}]^{\mathrm{T}},
\end{aligned}
\tag{5.38}
$$

with

$$\frac{\partial \psi}{\partial r_i} = r_i(1 + 2\ln(r_i)),$$ (5.39)

and

$$\boldsymbol{\nabla} r_i = \frac{1}{r_i}(\boldsymbol{\alpha}[k-1] - \mathbf{c}_{\alpha_i}).$$ (5.40)

Substituting (5.39) and (5.40) into (5.38), we get the expression for the gradient of $\alpha[k]$

$$\boldsymbol{\nabla}\alpha[k] = \sum_{i=1}^{n_r} \frac{\omega_i \partial\psi/\partial r_i}{r_i}(\boldsymbol{\alpha}[k-1] - \mathbf{c}_{\alpha_i})$$
$$+ [\omega_{n_r+1}, \ldots, \omega_{n_r+n_\alpha}]^{\mathrm{T}}.$$ (5.41)

Therefore, we can write the Jacobian matrix $\mathbf{F}_\alpha[k-1]$ for the process equations of the RBF network $\boldsymbol{\alpha}[k] = \mathbf{f}_\alpha(\boldsymbol{\alpha}[k-1])$ as

$$\mathbf{F}_\alpha[k-1] = \left.\frac{\partial \mathbf{f}_\alpha}{\partial \boldsymbol{\alpha}}\right|_{\boldsymbol{\alpha}=\hat{\boldsymbol{\alpha}}[k-1]} = \begin{bmatrix} \boldsymbol{\nabla}^{\mathrm{T}}\alpha[k] \\ \begin{bmatrix} \mathbf{I}_{n_\alpha-1} & \mathbf{0}_{n_\alpha-1} \end{bmatrix} \end{bmatrix}.$$ (5.42)

Substituting α by ϕ and ρ, we get the Jacobians of the process equations for the scintillation phase and amplitude dynamics, respectively. The scintillation phase varies around 0, while the scintillation amplitude varies around 1, according to the signal model normalized by the undisturbed amplitude, presented in Section 2.1. Therefore, we drop the bias term from the scintillation phase RBF network, and we keep the linear AR terms in both phase and amplitude RBF networks for now, for the sake of generality. The scintillation phase RBF network, already discarding the bias term, can be compactly written as

$$\phi[k] = \boldsymbol{\omega}_{\phi_{\mathrm{RBF}}}^{\mathrm{T}}\boldsymbol{\psi}(\mathbf{x}_\phi[k-1]) + \boldsymbol{\omega}_{\phi_{\mathrm{LIN}}}^{\mathrm{T}}\mathbf{x}_\phi[k-1] + \eta_\phi[k-1],$$ (5.43)

and the scintillation amplitude RBF network as

$$\rho[k] = \omega_{0_\rho} + \boldsymbol{\omega}_{\rho_{\mathrm{RBF}}}^{\mathrm{T}}\boldsymbol{\psi}(\mathbf{x}_\rho[k-1]) + \boldsymbol{\omega}_{\rho_{\mathrm{LIN}}}^{\mathrm{T}}\mathbf{x}_\rho[k-1] + \eta_\rho[k-1],$$ (5.44)

where $\boldsymbol{\omega}_{\phi_{\mathrm{RBF}}} = [\omega_{\phi_1}, \ldots, \omega_{\phi_{n_r}}]^{\mathrm{T}}$, $\boldsymbol{\psi}(\mathbf{x}_\phi[k-1]) = [\psi(\|\mathbf{x}_\phi[k-1]-\mathbf{c}_{\phi_1}\|_2), \ldots, \psi(\|\mathbf{x}_\phi[k-1] - \mathbf{c}_{\phi_{n_r}}\|_2)]^{\mathrm{T}}$, $\boldsymbol{\omega}_{\phi_{\mathrm{LIN}}} = [\omega_{\phi_{n_r+1}}, \ldots, \omega_{\phi_{n_r+n_\phi}}]^{\mathrm{T}}$, $\boldsymbol{\omega}_{\rho_{\mathrm{RBF}}} = [\omega_{\rho_1}, \ldots, \omega_{\rho_{n_r}}]^{\mathrm{T}}$, $\boldsymbol{\psi}(\mathbf{x}_\rho[k-1]) = [\psi(\|\mathbf{x}_\rho[k-1] - \mathbf{c}_{\rho_1}\|_2), \ldots, \psi(\|\mathbf{x}_\rho[k-1] - \mathbf{c}_{\rho_{n_r}}\|_2)]^{\mathrm{T}}$ and $\boldsymbol{\omega}_{\rho_{\mathrm{LIN}}} = [\omega_{\rho_{n_r+1}}, \ldots, \omega_{\rho_{n_r+n_\rho}}]^{\mathrm{T}}$.

Unlike the scintillation phase and amplitude process models using the pure AR

models, the process models using the RBF networks are nonlinear with respect to scintillation phase and amplitude state vectors. For the scintillation phase RBF network, the process equations can be written as

$$\mathbf{x}_\phi[k] = \underbrace{\begin{bmatrix} \boldsymbol{\omega}_{\phi_{\text{RBF}}}^{\text{T}} \boldsymbol{\psi}(\mathbf{x}_\phi[k-1]) + \boldsymbol{\omega}_{\phi_{\text{LIN}}}^{\text{T}} \mathbf{x}_\phi[k-1] \\ \begin{bmatrix} \mathbf{I}_{n_\phi-1} & \mathbf{0}_{n_\phi-1} \end{bmatrix} \mathbf{x}_\phi[k-1] \end{bmatrix}}_{=\mathbf{f}_{\phi_{\text{RBF}}}(\mathbf{x}_\phi[k-1])} + \boldsymbol{\nu}_\phi[k-1], \qquad (5.45)$$

and for the scintillation amplitude, as

$$\mathbf{x}_\rho[k] = \underbrace{\begin{bmatrix} \boldsymbol{\omega}_{\rho_{\text{RBF}}}^{\text{T}} \boldsymbol{\psi}(\mathbf{x}_\rho[k-1]) + \boldsymbol{\omega}_{\rho_{\text{LIN}}}^{\text{T}} \mathbf{x}_\rho[k-1] \\ \begin{bmatrix} \mathbf{I}_{n_\rho-1} & \mathbf{0}_{n_\rho-1} \end{bmatrix} \mathbf{x}_\rho[k-1] \end{bmatrix}}_{=\mathbf{f}_{\rho_{\text{RBF}}}(\mathbf{x}_\rho[k-1])} + \underbrace{\begin{bmatrix} \omega_{\rho_0} \\ \mathbf{0}_{n_\rho-1} \end{bmatrix}}_{=\mathbf{b}_{\rho_{\text{RBF}}}} + \boldsymbol{\nu}_\rho[k-1], \qquad (5.46)$$

with the RBF process noise vectors

$$\boldsymbol{\nu}_\phi[k] = \begin{bmatrix} \eta_\phi[k] & \mathbf{0}_{n_\phi-1}^{\text{T}} \end{bmatrix}^{\text{T}} \qquad (5.47)$$

and

$$\boldsymbol{\nu}_\rho[k] = \begin{bmatrix} \eta_\rho[k] & \mathbf{0}_{n_\rho-1}^{\text{T}} \end{bmatrix}^{\text{T}}, \qquad (5.48)$$

whose covariance matrices are

$$\mathbf{Q}_{\phi_{\text{RBF}}} = \text{diag}\left(\begin{bmatrix} \sigma_{\eta_\phi}^2, \mathbf{0}_{n_\phi-1}^{\text{T}} \end{bmatrix}^{\text{T}} \right) \qquad (5.49)$$

and

$$\mathbf{Q}_{\rho_{\text{RBF}}} = \text{diag}\left(\begin{bmatrix} \sigma_{\eta_\rho}^2, \mathbf{0}_{n_\rho-1}^{\text{T}} \end{bmatrix}^{\text{T}} \right), \qquad (5.50)$$

respectively.

The Jacobian matrix of the scintillation phase process equations is

$$\begin{aligned} \mathbf{F}_{\phi_{\text{RBF}}}[k-1] &= \left. \frac{\partial \mathbf{f}_{\phi_{\text{RBF}}}}{\partial \mathbf{x}_\phi} \right|_{\mathbf{x}_\phi = \hat{\mathbf{x}}_\phi[k-1]} \\ &= \begin{bmatrix} \sum_{i=1}^{n_{r_\phi}} \frac{\omega_{\phi_i} \partial \psi / \partial r_{\phi_i}}{r_{\phi_i}} (\hat{\mathbf{x}}_\phi[k-1] - \mathbf{c}_{\phi_i})^{\text{T}} + \boldsymbol{\omega}_{\phi_{\text{LIN}}}^{\text{T}} \\ \begin{bmatrix} \mathbf{I}_{n_\phi-1} & \mathbf{0}_{n_\phi-1} \end{bmatrix} \end{bmatrix}, \end{aligned} \qquad (5.51)$$

and the Jacobian matrix of the scintillation amplitude process equations is

$$
\begin{aligned}
\mathbf{F}_{\rho_{\mathrm{RBF}}}[k-1] &= \left.\frac{\partial \mathbf{f}_{\rho_{\mathrm{RBF}}}}{\partial \mathbf{x}_\rho}\right|_{\mathbf{x}_\rho=\hat{\mathbf{x}}_\rho[k-1]} \\
&= \begin{bmatrix} \sum_{i=1}^{n_{r_\rho}} \frac{\omega_{\rho_i} \partial \psi / \partial r_{\rho_i}}{r_{\rho_i}} (\hat{\mathbf{x}}_\rho[k-1] - \mathbf{c}_{\rho_i})^{\mathrm{T}} + \boldsymbol{\omega}_{\rho_{\mathrm{LIN}}}^{\mathrm{T}} \\ \begin{bmatrix} \mathbf{I}_{n_\rho-1} & \mathbf{0}_{n_\rho-1} \end{bmatrix} \end{bmatrix}.
\end{aligned}
\tag{5.52}
$$

The proposed discriminator-based and correlator-based Kalman PLLs with the RBF networks modeling scintillation phase and amplitude dynamics are based on the formulation of the Kalman PLLs employing the AR scintillation models presented in the previous section, with some modifications to adjust the Kalman PLLs to the inclusion of the RBF networks as process models of the scintillation dynamics.

5.2.1 Discriminator-based Kalman PLL with RBF networks

In the discriminator-based Kalman PLL, now we have nonlinear process equations with respect to the state vector $\mathbf{x}_1[k] = \begin{bmatrix} \mathbf{x}_D^{\mathrm{T}}[k] & \mathbf{x}_\phi^{\mathrm{T}}[k] \end{bmatrix}^{\mathrm{T}}$. The process equations, used for the state propagation in the Kalman filter, can be written as

$$
\mathbf{x}_1[k] = \begin{bmatrix} \mathbf{F}_D \mathbf{x}_D[k-1] \\ \mathbf{f}_{\phi_{\mathrm{RBF}}}(\mathbf{x}_\phi[k-1]) \end{bmatrix} + \boldsymbol{\nu}_1[k-1],
\tag{5.53}
$$

with $\mathbf{f}_{\phi_{\mathrm{RBF}}}(\mathbf{x}_\phi[k-1])$ defined in (5.45) and with $\boldsymbol{\nu}_1[k] = \begin{bmatrix} \boldsymbol{\nu}_D^{\mathrm{T}}[k] & \boldsymbol{\nu}_\phi^{\mathrm{T}}[k] \end{bmatrix}^{\mathrm{T}}$, where now $\boldsymbol{\nu}_\phi[k]$ is formed by the RBF network error, as defined in (5.47). The Jacobian matrix of the process equations, used in the state covariance propagation in the Kalman filter, is

$$
\mathbf{F}_1 = \mathrm{blkdiag}(\mathbf{F}_D, \mathbf{F}_{\phi_{\mathrm{RBF}}}[k-1]),
\tag{5.54}
$$

the process noise covariance matrix is

$$
\mathbf{Q}_1 = \mathrm{blkdiag}(\mathbf{Q}_D, \mathbf{Q}_{\phi_{\mathrm{RBF}}}),
\tag{5.55}
$$

and the matrix of observations is

$$
\mathbf{H}_1 = \begin{bmatrix} 1 & 0 & 0 & 1 & \mathbf{0}_{n_\phi-1}^{\mathrm{T}} \end{bmatrix}.
\tag{5.56}
$$

Due to the nature of the scintillation phase dynamics in severe scintillation, that may present rapid variations and discontinuities with half cycle jumps, the Jacobian computation near such discontinuities may lead to filter divergence. We compute

the Jacobian around zero for the scintillation phase, which is a point of symmetry of the phase variations. Thus, the Jacobian is computed as

$$\overline{\mathbf{F}}_{\phi\text{RBF}} = \left.\frac{\partial \mathbf{f}_{\phi\text{RBF}}}{\partial \mathbf{x}_\phi}\right|_{\mathbf{x}_\phi=\overline{\mathbf{x}}_\phi}, \tag{5.57}$$

with $\overline{\mathbf{x}}_\phi = \mathbf{0}_{n_\phi}^{\mathrm{T}}$, and we substitute $\mathbf{F}_{\phi\text{RBF}}[k-1]$ by $\overline{\mathbf{F}}_{\phi\text{RBF}}$ in the above expression for $\mathbf{F}_1$ computation.

The RBF network weights and the network error variance are also estimated by the recursive sliding window least squares algorithm from (YOUNG, 2011), since the network structure is linear with respect to the weights, and the filter adaptation with the least squares results is performed in the same way. We adaptively update $\mathbf{f}_{\phi\text{RBF}}(\mathbf{x}_\phi[k-1])$ and $\overline{\mathbf{F}}_{\phi\text{RBF}}$ with $\hat{\boldsymbol{\omega}}_{\phi\text{RBF}}[k-1]$ and $\hat{\boldsymbol{\omega}}_{\phi\text{LIN}}[k-1]$, and $\mathbf{Q}_{\phi\text{RBF}}$ with $\hat{\sigma}_\phi^2[k-1]$ in the Kalman filter. The measurement noise covariance $\mathbf{R}_1$ is defined in the same way as in the discriminator-based structure using the AR models, and is adaptively updated with $\widehat{c/n_0}[k-1]$.

5.2.2 Correlator-based Kalman PLL with RBF networks

In the correlator-based structure, we cannot work with the phase error states in the Kalman filter, since we have nonlinear process equations. Instead, the Kalman filter estimates the direct phase states, and then we compute the difference between the estimated phase states and the NCO phase states from the previous iteration to obtain the phase error state vector estimate used by the state feedback controller of the phase loop. The carrier replica is generated with the NCO states in the same way as in the correlator-based structure using the AR models. The model is the same. The Jacobian of the scintillation phase dynamics, used for the NCO state feedback gain computation via pole placement and for the state covariance propagation in the Kalman filter is computed according to (5.57).

The state vector of the Kalman filter is now

$$\mathbf{x}_2[k] = \begin{bmatrix} \mathbf{x}_1[k] \\ \mathbf{x}_\rho[k] \end{bmatrix}, \tag{5.58}$$

with $\mathbf{x}_1[k] = \begin{bmatrix} \mathbf{x}_D^{\mathrm{T}}[k] & \mathbf{x}_\phi^{\mathrm{T}}[k] \end{bmatrix}^{\mathrm{T}}$. The control signal to the NCO is computed by

$$u_{\text{NCO}}[k] = \mathbf{L}\delta\hat{\mathbf{x}}_1[k], \tag{5.59}$$

with $\delta\hat{\mathbf{x}}_1[k] = \hat{\mathbf{x}}_1[k] - \mathbf{x}_{\mathrm{NCO}}[k-1]$. The process equations, used for the state propagation in the Kalman filter, can be written as

$$\mathbf{x}_2[k] = \begin{bmatrix} \mathbf{F}_D\mathbf{x}_D[k-1] \\ \mathbf{f}_{\phi_{\mathrm{RBF}}}(\mathbf{x}_\phi[k-1]) \\ \mathbf{f}_{\rho_{\mathrm{RBF}}}(\mathbf{x}_\rho[k-1]) \end{bmatrix} + \begin{bmatrix} \mathbf{0}_{3+n_\phi} \\ \mathbf{b}_{\rho_{\mathrm{RBF}}} \end{bmatrix} + \boldsymbol{\nu}_2[k-1], \qquad (5.60)$$

with $\mathbf{f}_{\phi_{\mathrm{RBF}}}(\mathbf{x}_\phi[k-1])$ defined in (5.45), $\mathbf{f}_{\rho_{\mathrm{RBF}}}(\mathbf{x}_\rho[k-1])$ defined in (5.46) and with $\boldsymbol{\nu}_2[k] = \begin{bmatrix} \boldsymbol{\nu}_D^{\mathrm{T}}[k] & \boldsymbol{\nu}_\phi^{\mathrm{T}}[k] & \boldsymbol{\nu}_\rho^{\mathrm{T}}[k] \end{bmatrix}^{\mathrm{T}}$, where now $\boldsymbol{\nu}_\phi[k]$ and $\boldsymbol{\nu}_\rho[k]$ are formed by the RBF network error, as defined in (5.47) and (5.48). The Jacobian matrix of the process equations, used in the state covariance propagation in the Kalman filter, is

$$\mathbf{F}_2 = \mathrm{blkdiag}(\mathbf{F}_D, \mathbf{F}_{\phi_{\mathrm{RBF}}}[k-1], \mathbf{F}_{\rho_{\mathrm{RBF}}}[k-1]), \qquad (5.61)$$

the process noise covariance matrix is

$$\mathbf{Q}_2 = \mathrm{blkdiag}(\mathbf{Q}_D, \mathbf{Q}_{\phi_{\mathrm{RBF}}}, \mathbf{Q}_{\rho_{\mathrm{RBF}}}), \qquad (5.62)$$

and the matrix of observations is

$$\mathbf{H}_2 = \begin{bmatrix} \overline{\rho}\sin\delta\overline{\phi}_T & \mathbf{0}_2^{\mathrm{T}} & \overline{\rho}\sin\delta\overline{\phi}_T & \mathbf{0}_{n_\phi-1}^{\mathrm{T}} & \cos\delta\overline{\phi}_T & \mathbf{0}_{n_\rho-1}^{\mathrm{T}} \\ -\overline{\rho}\cos\delta\overline{\phi}_T & \mathbf{0}_2^{\mathrm{T}} & -\overline{\rho}\cos\delta\overline{\phi}_T & \mathbf{0}_{n_\phi-1}^{\mathrm{T}} & \sin\delta\overline{\phi}_T & \mathbf{0}_{n_\rho-1}^{\mathrm{T}} \end{bmatrix}, \qquad (5.63)$$

where, now, as the Kalman filter is estimating the direct states instead of the error states, we have $\delta\overline{\phi}_T = \hat{\phi}_D[k|k-1] + \hat{\phi}[k|k-1] - \phi_{D_{\mathrm{NCO}}}[k-1] - \phi_{\mathrm{NCO}}[k-1]$. For the amplitude, we have $\overline{\rho} = \hat{\rho}[k|k-1]$.

The Jacobian of the scintillation phase dynamics is computed according to (5.57), so $\mathbf{F}_{\phi_{\mathrm{RBF}}}[k-1] = \overline{\mathbf{F}}_{\phi_{\mathrm{RBF}}}$, and the Jacobian of the scintillation amplitude dynamics is

$$\mathbf{F}_{\rho_{\mathrm{RBF}}}[k-1] = \left.\frac{\partial\mathbf{f}_{\rho_{\mathrm{RBF}}}}{\partial\mathbf{x}_\rho}\right|_{\mathbf{x}_\rho=\hat{\mathbf{x}}_\rho[k-1]}. \qquad (5.64)$$

The RBF network weights and the network error variance are also estimated by the recursive sliding window least squares algorithm from (YOUNG, 2011). Similarly, we adaptively update $\mathbf{f}_{\phi_{\mathrm{RBF}}}(\mathbf{x}_\phi[k-1])$, $\overline{\mathbf{F}}_{\phi_{\mathrm{RBF}}}$, $\mathbf{f}_{\rho_{\mathrm{RBF}}}(\mathbf{x}_\rho[k-1])$, $\mathbf{F}_{\rho_{\mathrm{RBF}}}[k-1]$, $\mathbf{b}_{\rho_{\mathrm{RBF}}}$, $\mathbf{Q}_{\phi_{\mathrm{RBF}}}$ and $\mathbf{Q}_{\rho_{\mathrm{RBF}}}$ in the Kalman filter with $\hat{\boldsymbol{\omega}}_{\phi_{\mathrm{RBF}}}[k-1]$ and $\hat{\boldsymbol{\omega}}_{\phi_{\mathrm{LIN}}}[k-1]$, $\hat{\boldsymbol{\omega}}_{\rho_{\mathrm{RBF}}}[k-1]$, $\hat{\boldsymbol{\omega}}_{\rho_{\mathrm{LIN}}}[k-1]$ and $\omega_{\rho_0}[k-1]$, $\hat{\sigma}_\phi^2[k-1]$ and $\hat{\sigma}_\rho^2[k-1]$, from the recursive least squares estimation. We also adaptively update $\mathbf{R}_2$ with $\hat{\sigma}_{\eta_D}^2[k-1] = 1/(T_I\widehat{c/n_0}[k-1])$.

5.3 Evaluation of the proposed Kalman PLLs with RBF networks modeling scintillation

The proposed Kalman PLL structures for scintillation mitigation employing RBF networks to model scintillation are firstly evaluated by Monte Carlo simulations considering synthetic scintillation input data generated by the CSM (HUMPHREYS et al., 2010) in severe scintillation scenarios. Then, the Kalman PLLs are evaluated with real data collected by a COTS GNSS receiver.

5.3.1 Synthetic scintillation data

The proposed adaptive Kalman PLL algorithms for scintillation mitigation employing the RBF networks to model scintillation phase and amplitude dynamics are evaluated by numerical simulations considering synthetic scintillation realizations generated by the CSM (HUMPHREYS et al., 2010) in severe scintillation scenarios defined by amplitude strength index $S_4 = 0.8$ and decorrelation time $\tau_0 = 0.1$ s. The carrier input signal has the same configuration of the previous chapter, with a Doppler frequency shift of 1000 Hz and a Doppler frequency drift of 0.94 Hz/s. The carrier signal is added to the scintillation data generated by the CSM to form the complete input signal. Perfect code delay synchronization is assumed in the BB GNSS input signals, no navigation bit transitions are considered and the carrier amplitude is unitary. Gaussian receiver thermal noise is added to the sampled I/Q signal components in all simulations, generated with variance such that the nominal C/N_0 is 45 dB-Hz. The samples of the scintillation data are generated by CSM each 10 ms, and the coherent integration period T_I is 10 ms. The overall parameters of the Monte Carlo simulations are the same as those used to evaluate the monitoring algorithm in the previous chapter.

The performance of the proposed Kalman PLLs employing the RBF networks is evaluated with 300 Monte Carlo simulations with the severe scintillation and receiver noise realizations, each with a 150 s time window, and compared to the performance of the Kalman PLLs employing the pure AR models. The performance measure is the root mean square error

$$\text{RMSE}_x[k] = \sqrt{\frac{1}{M} \sum_{m=1}^{M} \frac{1}{k} \sum_{i=1}^{k} \left(x_m[i] - \hat{x}_m[i] \right)^2}, \tag{5.65}$$

with x being substituted by the variable of interest, for the time index k, the Monte Carlo iteration index m and the number of Monte Carlo simulations M. We also

compute the root mean of the trace of the state covariance matrix $\mathbf{P}[k]$ from the Kalman filter, as an indicator of the reliability of the Kalman filters. Since the diagonal elements represent variances of the components of the state vector, if their sum converges, no single element is diverging, then it is an indicator of convergence of the filter (GAMSE et al., 2010). Thus, we define

$$\text{RMSS}_{\text{Tr}(\mathbf{P})}[k] = \sqrt{\frac{1}{M} \sum_{m=1}^{M} \frac{1}{k} \sum_{i=1}^{k} \text{Tr}(\mathbf{P}_m[i])}, \qquad (5.66)$$

where $\text{Tr}(\cdot)$ represents the trace of a matrix, and we call the index RMSS by root mean of sum of squares, since the variances are squares of standard deviations, so the index is defined in terms of standard deviations, as the RMSE. In the following, we label the adaptive discriminator-based and correlator-based Kalman PLLs employing the RBF networks as DKPLL-RBF and CKPLL-RBF, respectively, and the adaptive discriminator-based and correlator-based Kalman PLLs employing pure AR models as DKPLL-AR and CKPLL-AR, respectively.

The block of the process noise covariance matrix related to the LOS dynamics is defined by $\sigma_{j_D}^2$, which is the control parameter to adjust the expected level of jerk, or the Doppler drift rate in our case. We consider the maximum Doppler drift rate observed by a static receiver positioned on ground of $2\pi \times 1.35 \times 10^{-4}$ rad/s^3, according to the results from Section 2.2, so that any absolute value below the maximum Doppler drift rate $j_{D_{\max}} = 2\pi \times 1.35 \times 10^{-4}$ rad/s^3 is considered equally probable, to obtain an approximate value for $\sigma_{j_D}^2$. [1]

Similar argument is used to define the initial state covariance matrix of the Kalman filters in all simulations. We consider the maximum initial errors of Doppler phase $\phi_{D_{\max}}[0] = \pi$ rad, Doppler shift $f_{D_{\max}}[0] = 2\pi \times 10$ rad/s, Doppler drift $a_{D_{\max}}[0] = 2\pi \times 0.45$ rad/s^2, scintillation phase $\phi_{\max}[0] = \pi$ rad and scintillation amplitude $\rho_{\max}[0] = 0.5$, to approximate the respective variances by the uniform distribution variance computed for each maximum initial error, and define the initial state covariance matrix. Regarding the state vector initialization, we consider that the tracking loops receive a correct Doppler shift initial value of $2\pi \times 1000$ rad/s from the acquisition, and we consider unitary initial scintillation amplitude. The initial value of all the other state vector elements is 0.

There are many methods available for C/N$_0$ estimation in GNSS receivers (FALLETTI

---

[1]The uniform distribution variance is $\sigma_{\text{UD}}^2 = (2l_{\max})^2/12$, where $l_{\max}$ is the maximum absolute value.

et al., 2011), (MUTHURAMAN; BORIO, 2010) that can be employed to adaptively update the measurement noise covariance matrices $\mathbf{R}_1$ and $\mathbf{R}_2$ in the discriminator-based and correlator-based Kalman PLLs, respectively. Here, we estimate the C/N_0 according to

$$\widehat{c/n_0}[k] = (\hat{\rho}[k])^2 \overline{c/n_0}, \qquad (5.67)$$

for $\widehat{c/n_0}[k]$ in Hz, and $\overline{c/n_0} = 10^{45/10}$ Hz, which is the nominal c/n_0 equivalent to 45 dB-Hz. In the case of the correlator-based Kalman PLLs, $\hat{\rho}[k]$ is the scintillation amplitude estimated by the Kalman filters, and, in the case of the discriminator-based Kalman PLLs, we use $\hat{\rho}[k] = \sqrt{I_P^2[k] + Q_P^2[k]}$, where $I_P[k]$ and $Q_P[k]$ are the I/Q prompt correlator outputs, respectively.

We used one severe scintillation realization to perform the system identification of the AR models and the RBF networks representing scintillation phase and amplitude dynamics, thus obtaining the AR models parameters θ_{ϕ_i} and θ_{ρ_i}, and the AR model error variances, the weights of the RBF networks ω_{ϕ_i} and ω_{ρ_i}, and the network error variances, to define a nominal set of parameters/weights employed as initial conditions for the recursive least squares and to define the initial covariance matrices related to the scintillation processes.

The order of the models can be defined using an information criterion, such as the Akaike Information Criterion (AIC) or the Bayesian Information Criterion (BIC), applied to candidate regressors, that can be ordered according to the Error Reduction Ratio (ERR) criterion, for example (AGUIRRE, 2000). In this work, we use the partial autocorrelation function (PAF) to define the order of the models, as typically found in the literature (VILÁ-VALLS et al., 2018), (VILÁ-VALLS et al., 2015), (VILÁ-VALLS et al., 2018), (FOHLMEISTER et al., 2018b), including the regressors in the ascending order of the lags until the PAF value falls within the confidence interval. From this procedure, performed offline, the AR and RBF models order for the scintillation phase is $n_\phi = 2$ and for the scintillation amplitude is $n_\rho = 5$, according to the partial autocorrelation functions of the phase and amplitude samples presented in Figures 5.1 and 5.2, respectively.

Figure 5.1 - Scintillation phase models order.
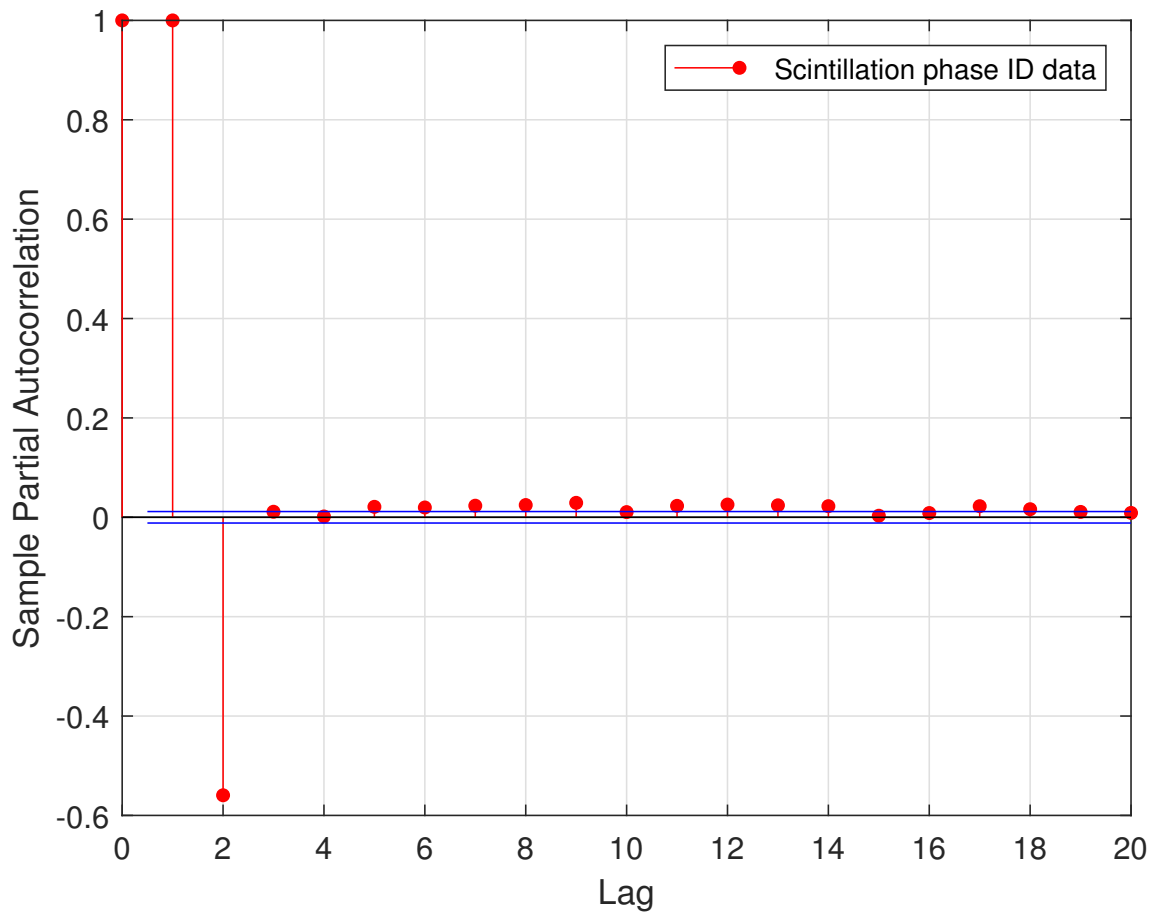
SOURCE: Author's production.

Figure 5.2 - Scintillation amplitude models order.
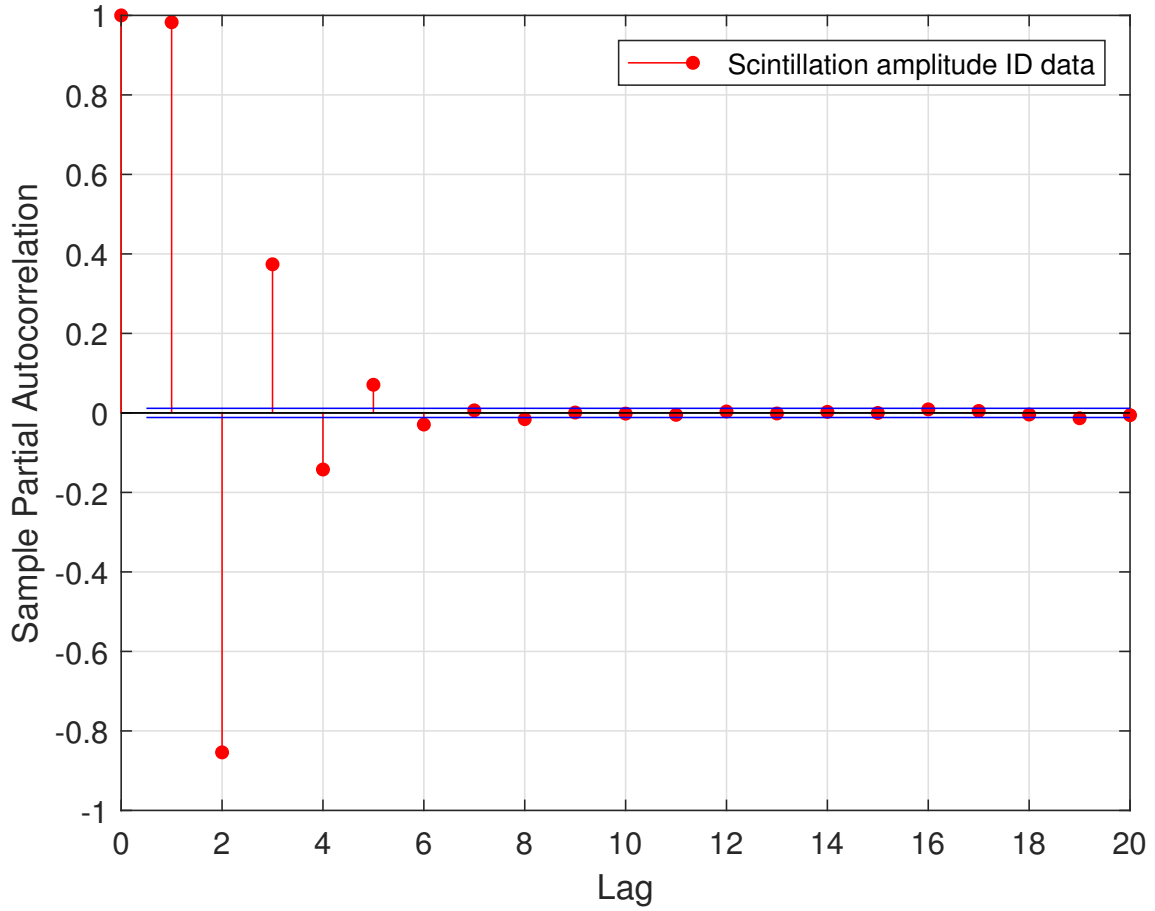
SOURCE: Author's production.

In the system identification of the RBF networks, the centers are taken from the identification data, equally spaced in time. The number of centers is $n_{r_\phi} = 38$ for the scintillation phase network and $n_{r_\rho} = 20$ for the scintillation amplitude network. In the amplitude network we included the linear autoregressive terms.

The online parameter estimation in the simulations employed the recursive least squares algorithm of (YOUNG, 2011), for 1500 points rectangular sliding window. This approach significantly reduces the parameter estimation complexity, when compared to the approach of (VILÁ-VALLS et al., 2018) employing batch least squares in the sliding window. The controller gains for CKPLL-AR and CKPLL-RBF were computed to place the respective phase error closed loop dynamics at the same target eigenvalues. The results of the Monte Carlo simulations comparing DKPLL-AR

and DKPLL-RBF, discarding the cases presenting cycle slips from the RMSE computation, are presented in Figures 5.3 and 5.4, for, respectively, Doppler phase $\phi_D[k]$ and scintillation phase $\phi[k]$, and in Figure 5.5 for the RMSS of the trace of the state covariance matrix $\text{Tr}(\mathbf{P}[k])$.

Figure 5.3 - Doppler phase estimation RMSE_{ϕ_D} for DKPLL-AR and DKPLL-RBF.
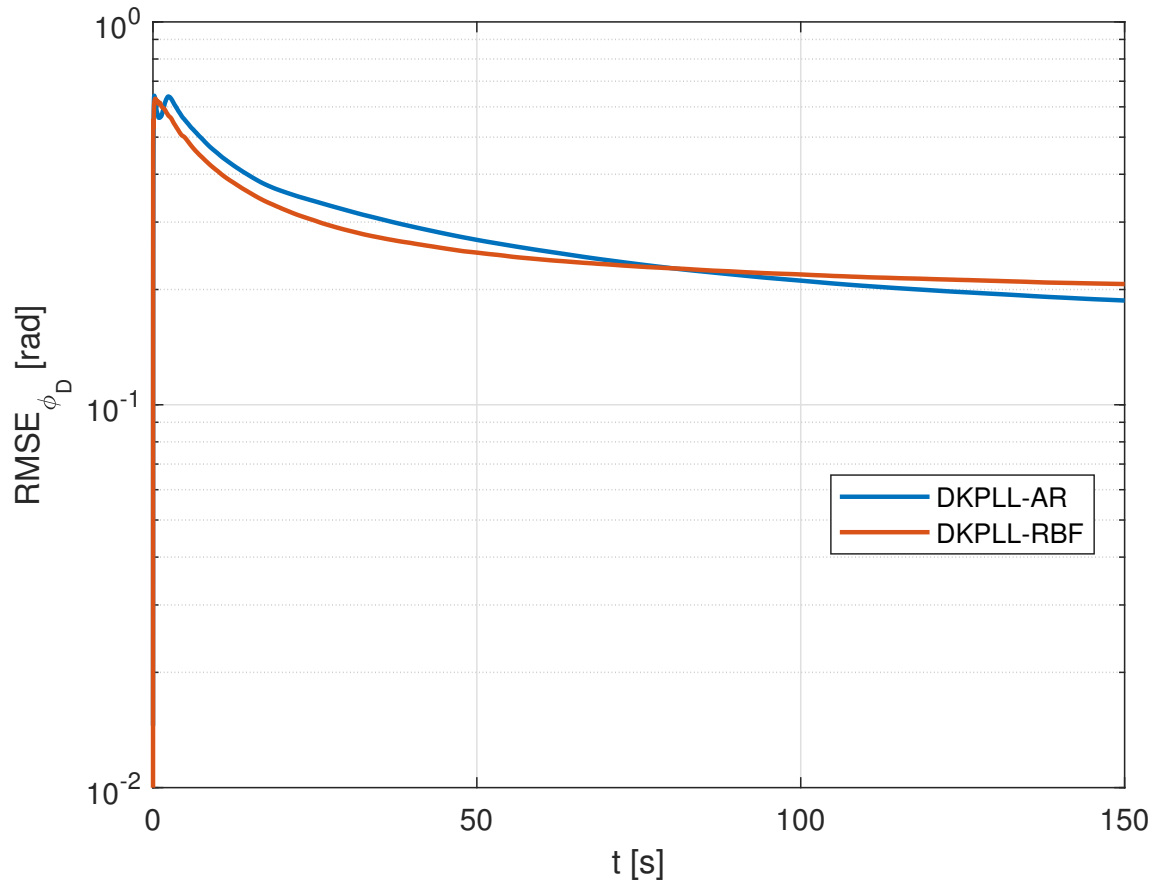
SOURCE: Author's production.

Figure 5.4 - Scintillation phase estimation RMSE_ϕ for DKPLL-AR and DKPLL-RBF.

SOURCE: Author's production.

Figure 5.5 - State covariance $\mathrm{RMSS}_{\mathrm{Tr}(\mathbf{P})}$ for DKPLL-AR and DKPLL-RBF.

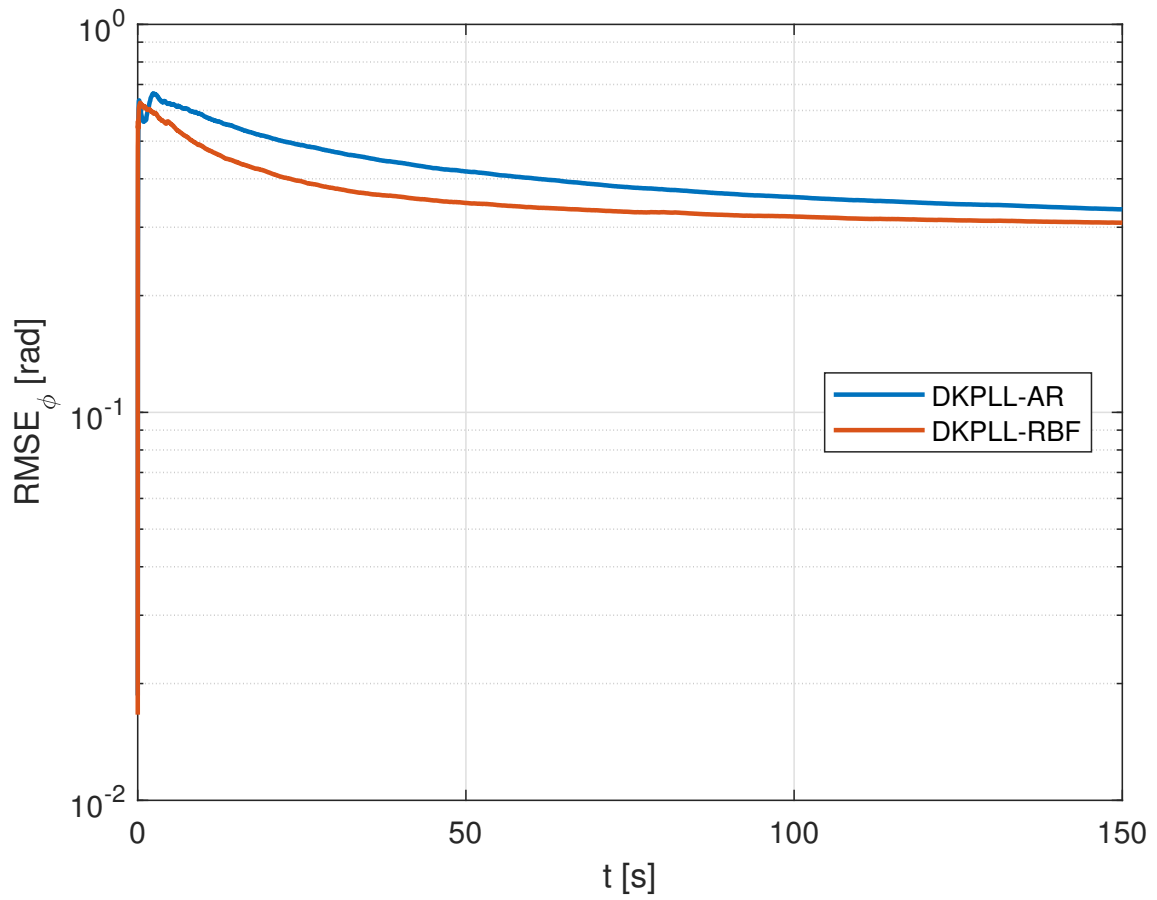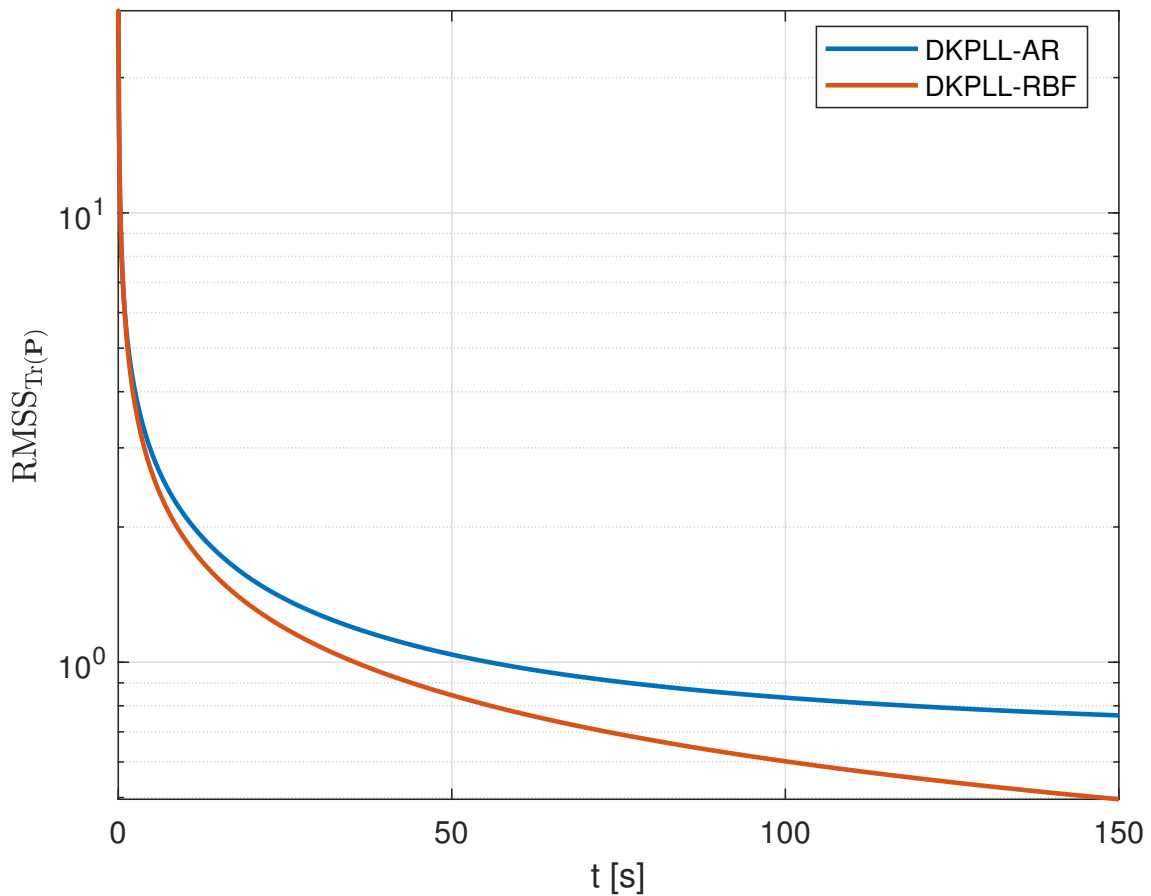The results of the Monte Carlo simulations comparing CKPLL-AR and CKPLL-RBF, discarding the cases presenting cycle slips from the RMSE computation, are presented in Figures 5.6, 5.7, and 5.8, for, respectively, Doppler phase $\phi_D[k]$, scintillation phase $\phi[k]$, scintillation amplitude $\rho[k]$, for, respectively, Doppler phase $\phi_D[k]$, scintillation phase $\phi[k]$, scintillation amplitude $\rho[k]$, and in Figure 5.9 for the RMSS of the trace of the state covariance matrix $\mathrm{Tr}(\mathbf{P}[k])$.

Figure 5.6 - Doppler phase estimation RMSE$_{\phi_D}$ for CKPLL-AR and CKPLL-RBF.

SOURCE: Author's production.

Figure 5.7 - Scintillation phase estimation $RMSE_\phi$ for CKPLL-AR and CKPLL-RBF.

Figure 5.8 - Scintillation amplitude estimation $RMSE_\rho$ for CKPLL-AR and CKPLL-RBF.

SOURCE: Author's production.

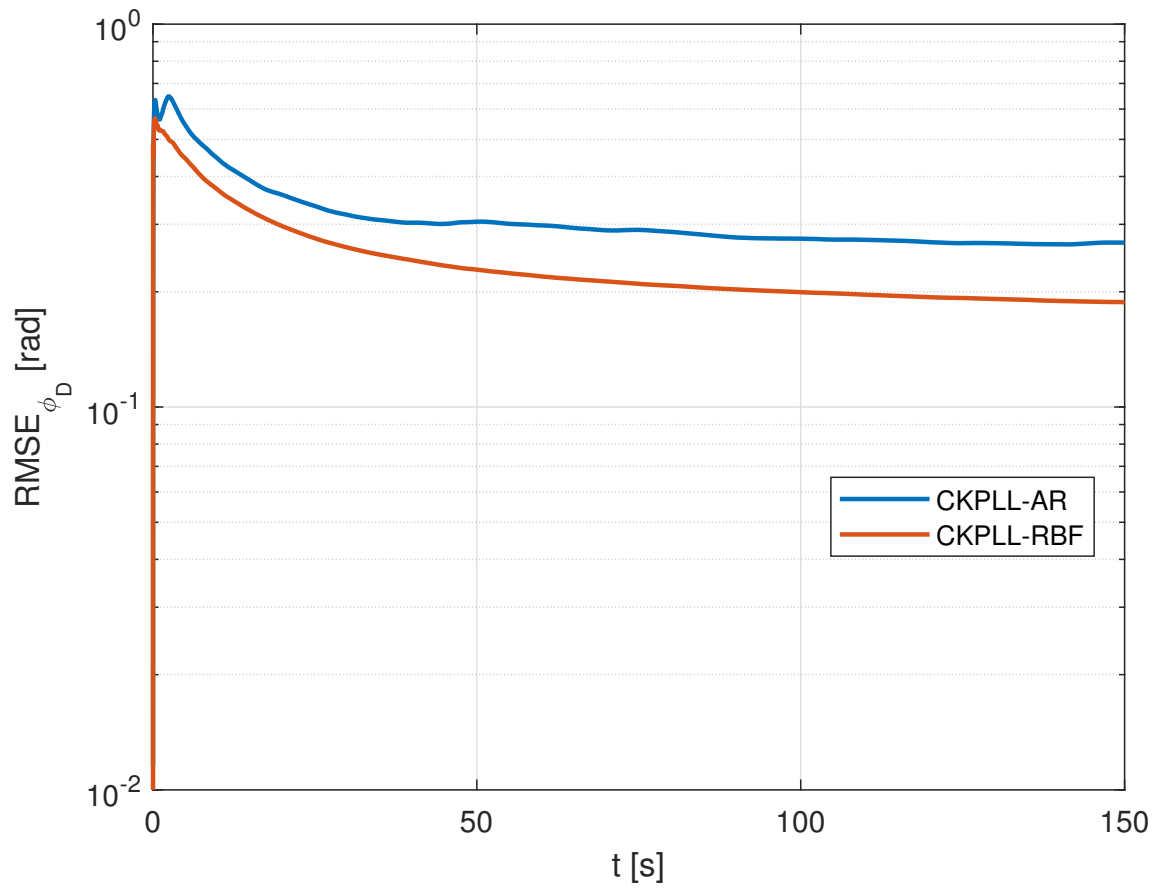Figure 5.9 - State covariance $\mathrm{RMSS}_{\mathrm{Tr}(\mathbf{P})}$ for CKPLL-AR and CKPLL-RBF.
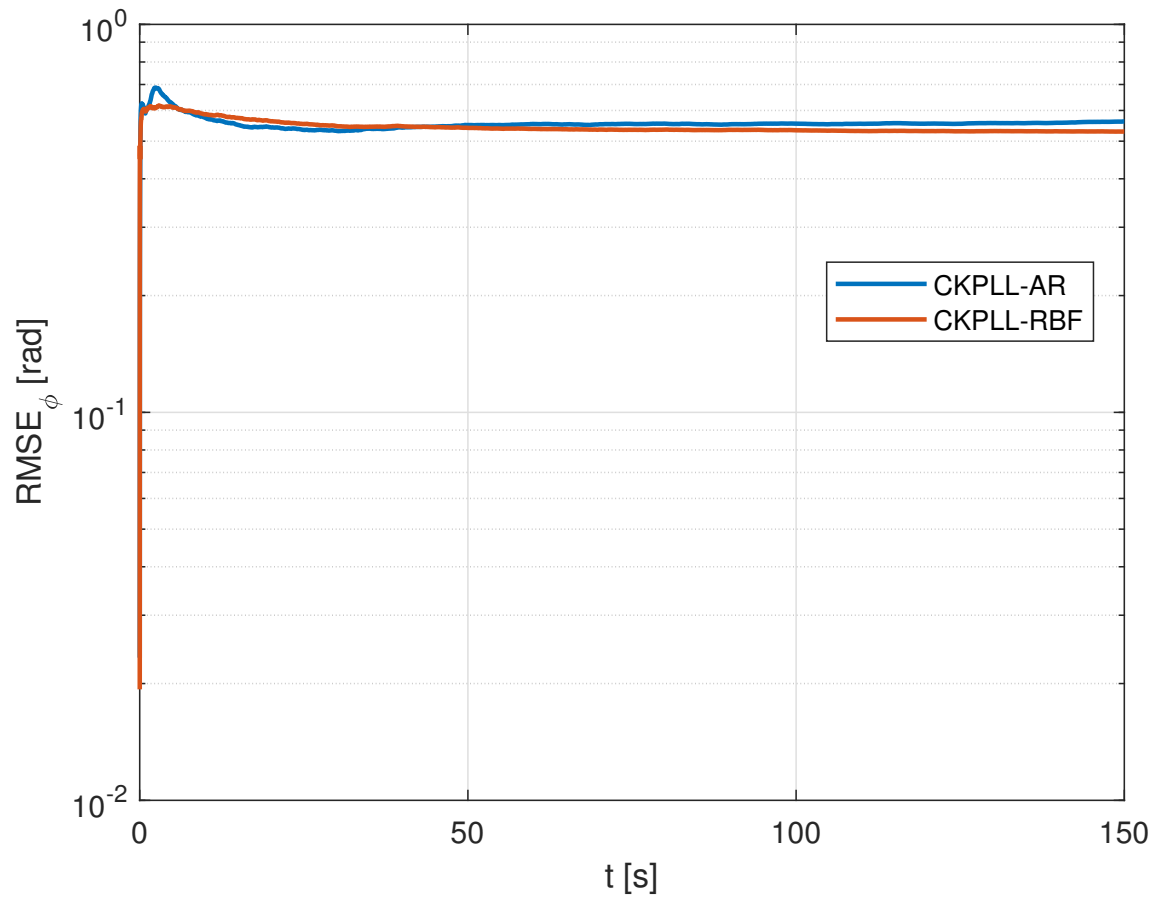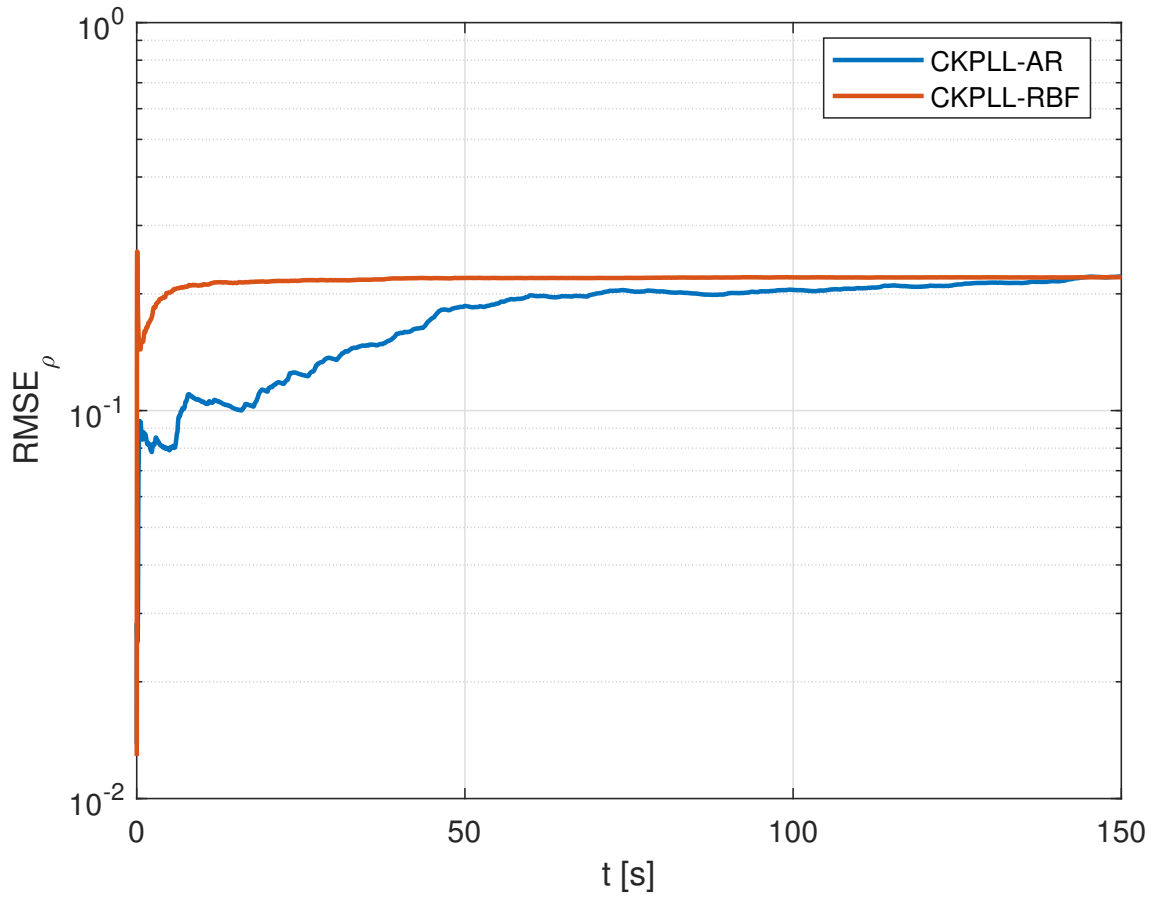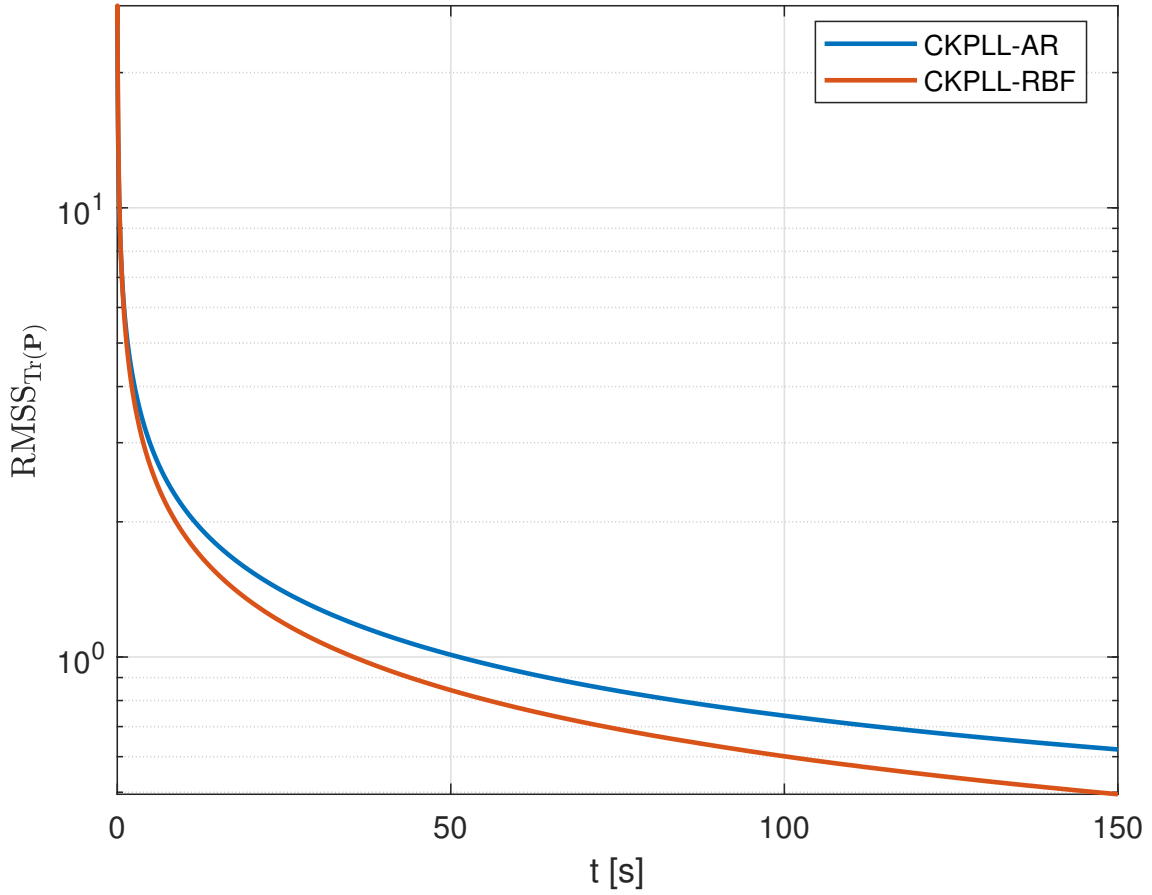

SOURCE: Author's production.

All the Kalman PLLs present good convergence characteristics. We can note that, in general, the results of the proposed adaptive Kalman PLL structures with RBF networks modeling the scintillation dynamics are comparable to those of the corresponding structures with the AR scintillation models, with a slight advantage to the RBF in the case of the correlator-based structures. Comparing the discriminator-based structures, DKPLL-RBF and DKPLL-AR, we can observe in Figure 5.3 that DKPLL-AR presented a slightly smaller carrier synchronization error, but almost equivalent, while DKPLL-RBF presented a smaller scintillation phase estimation error, according to Figure 5.4. The scintillation amplitude is not estimated in the discriminator-based Kalman PLLs.

Regarding the correlator-based structures, CKPLL-RBF and CKPLL-AR, we can

observe a bigger difference in the carrier synchronization error, with advantage to the RBF, as shown in Figure 5.6. We credit this to a higher sensitivity of the CKPLL-AR to errors in the initial conditions. The results of CKPLL-RBF are comparable to the results presented in Figure 5.3. The scintillation estimation errors of both CKPLL-RBF and CKPLL-AR are very close, as shown in Figures 5.7 and 5.8, for the scintillation phase and the scintillation amplitude, respectively. The larger errors observed in scintillation phase estimation of the correlator-based structures, when compared to the errors presented in Figure 5.4 of the discriminator-based structures, are related to the dynamics introduced in the loop by the NCO controller. This is highlighted by the half-cycle phase discontinuities induced by severe scintillation, where the correlator-based structures are less responsive to follow such discontinuities, resulting in the increase of the RMSE values. Despite of this, they are able to improve robustness to the scintillation effects in the carrier synchronization. In the absence of half-cycle phase discontinuities, the scintillation phase estimation in the carrier-based structures is equivalent to the estimation in the discriminator-based structures, as presented next in the results with real scintillation data. However, according to (VILÁ-VALLS et al., 2018), the discriminator-based approach is considered to be a less robust architecture, with the nonlinearities of the discriminator and possible saturation at low C/N_0.

The results of the Monte Carlo simulations suggest that the proposed Kalman PLLs employing the RBF networks are capable to provide similar performance, with a slight advantage, when compared to the state-of-the-art Kalman PLL structures employing AR models (VILÁ-VALLS et al., 2018). In general, the RBF networks will allow more flexibility in scintillation induced effects modeling due to the nonlinear radial basis functions, at the expense of a more complex structure when compared to the AR models. Possibly, the degree of nonlinearity present in the scintillation data generated by the CSM was not able to clearly highlight the advantage of using the RBF networks, but they may be useful to capture possible nonlinear dynamics present in real scintillation induced effects, helping to improve the robustness of GNSS receivers to such effects.

5.3.2 Real scintillation data

The performances of the Kalman PLLs are also assessed with real data collected by the JAVAD Delta 3 receiver. The receiver configuration and the data presenting scintillation were described in the previous chapter. Part of GPS L1 C/A signal from satellite PRN 24, recorded on October 27, 2017, from 22:00 UTC to 23:00

UTC, is used to the evaluation of the Kalman PLLs. Scintillation phase, scintillation amplitude and carrier time series are obtained from the data using a standard post-processing procedure, as described in (DIERENDONCK et al., 1993), (ZHANG et al., 2010). A fourth order polynomial is fitted to the carrier phase estimate of the scintillating channel tracking GPS PRN 24 with least squares using a 100 s sliding window to obtain the carrier phase (ZHANG et al., 2010). The scintillation phase is obtained from the least squares residual, after removing the common phase induced by the receiver clock, taken from the residual of the least squares fitting of a reference channel tracking a non-scintillating satellite signal, and filtering by 3 cascaded high pass Butterworth filters with cutoff frequency of 0.0175 Hz to remove possible low frequency effects, such as multipath. The scintillation amplitude is taken from the norm of prompt I/Q, and normalized by its filtered value from 0.01 Hz low pass cascaded Butterworth filters, so that we have unitary amplitude when no scintillation effect is present.

We adjusted both AR and RBF network models to the scintillation phase and amplitude samples obtained from the real data. In general, the AR model order is chosen from 1 to 3, depending on the observed scintillation characteristics (VILÁ-VALLS et al., 2018). The chosen model order, or the number of lags, was the minimum value that provided the best fitting to the data, for both the AR and RBF network models. Despite the detrending employed in the the data post-processing procedure, residual effects can be expected to still be present in the samples. Also, the scintillation characteristics can evolve along the relatively large selected time-window of approximately 1400 s, changing its pattern, or even presenting nonlinear behavior. This is especially observed in the scintillation phase samples of the recorded data, so that the resulting model order of the AR model was 10, while the model order of the RBF network was 1, for the scintillation phase. The model order of both the AR and RBF models was 1, for the scintillation amplitude. The number of centers of the RBF networks was 40 for the scintillation phase and 20 for the scintillation amplitude. No linear AR terms were added to both networks.

The parameters of the kinematic process model of the LOS dynamics employed in the Kalman PLLs were defined with the same values used in the Monte Carlo simulations with the synthetic scintillation data. In the first simulation with the real data, we compare the results of the proposed Kalman PLLs with the results of the Kalman PLLs with the AR scintillation models with the online parameter estimation disabled in both structures. The comparison of the RMSE of $\phi_D[k]$ and $\phi[k]$ is presented, respectively, in Figures 5.10 and 5.11, for DKPLL-AR, DKPLL-

RBF, CKPLL-AR, and CKPLL-RBF. The RMSE of $\rho[k]$ is presented in Figure 5.12, for CKPLL-AR, and CKPLL-RBF.

Figure 5.10 - RMSE_{ϕ_D}, with online parameter estimation disabled.
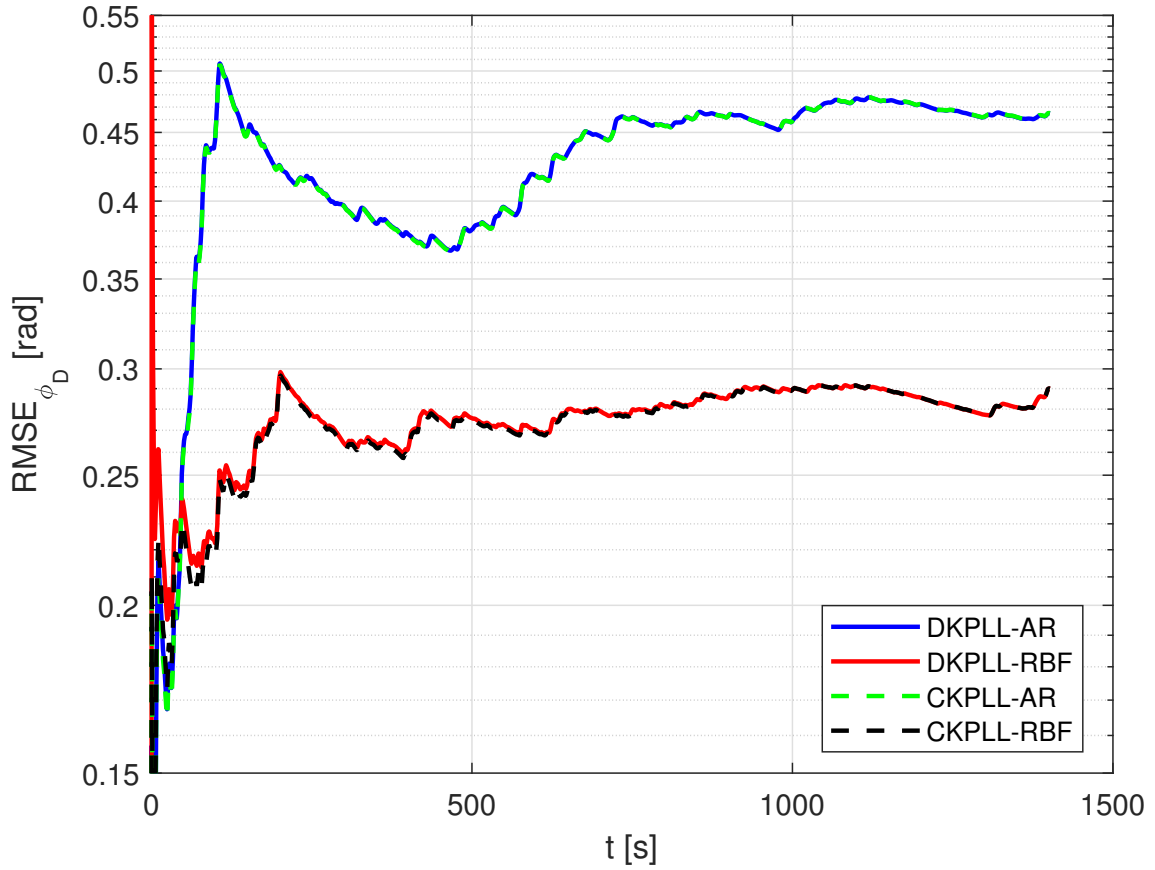
SOURCE: Author's production.

Figure 5.11 - RMSE$_\phi$, with online parameter estimation disabled.

SOURCE: Author's production.

Figure 5.12 - RMSE$_\rho$, with online parameter estimation disabled.

SOURCE: Author's production.

In the second simulation, we compare the results of the proposed Kalman PLLs with the results of the Kalman PLLs with the AR scintillation models with the online parameter estimation enabled in both structures, with 1500 points sliding window. The comparison of the RMSE of $\phi_D[k]$ and $\phi[k]$ is presented, respectively, in Figures 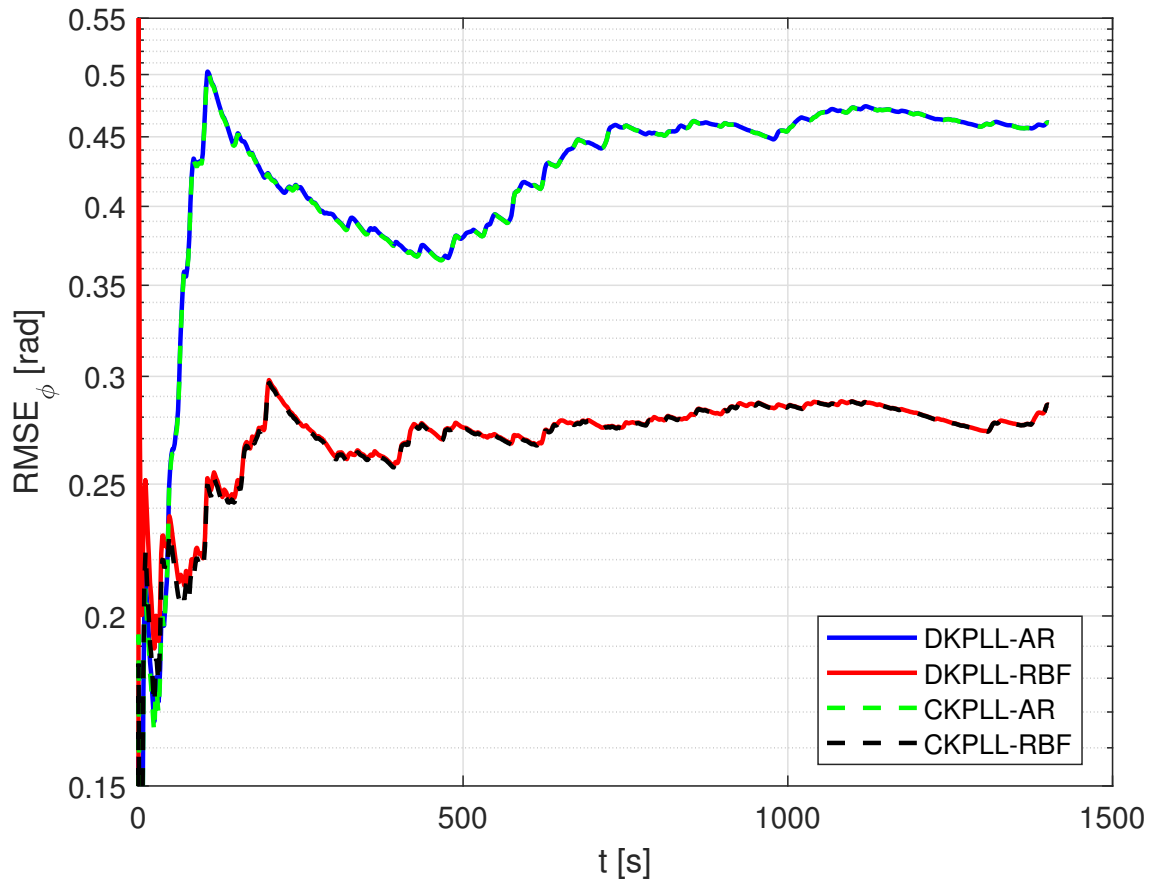5.13 and 5.14, for DKPLL-AR, DKPLL-RBF, CKPLL-AR, and CKPLL-RBF. The RMSE of $\rho[k]$ is presented in Figure 5.15, for CKPLL-AR, and CKPLL-RBF.

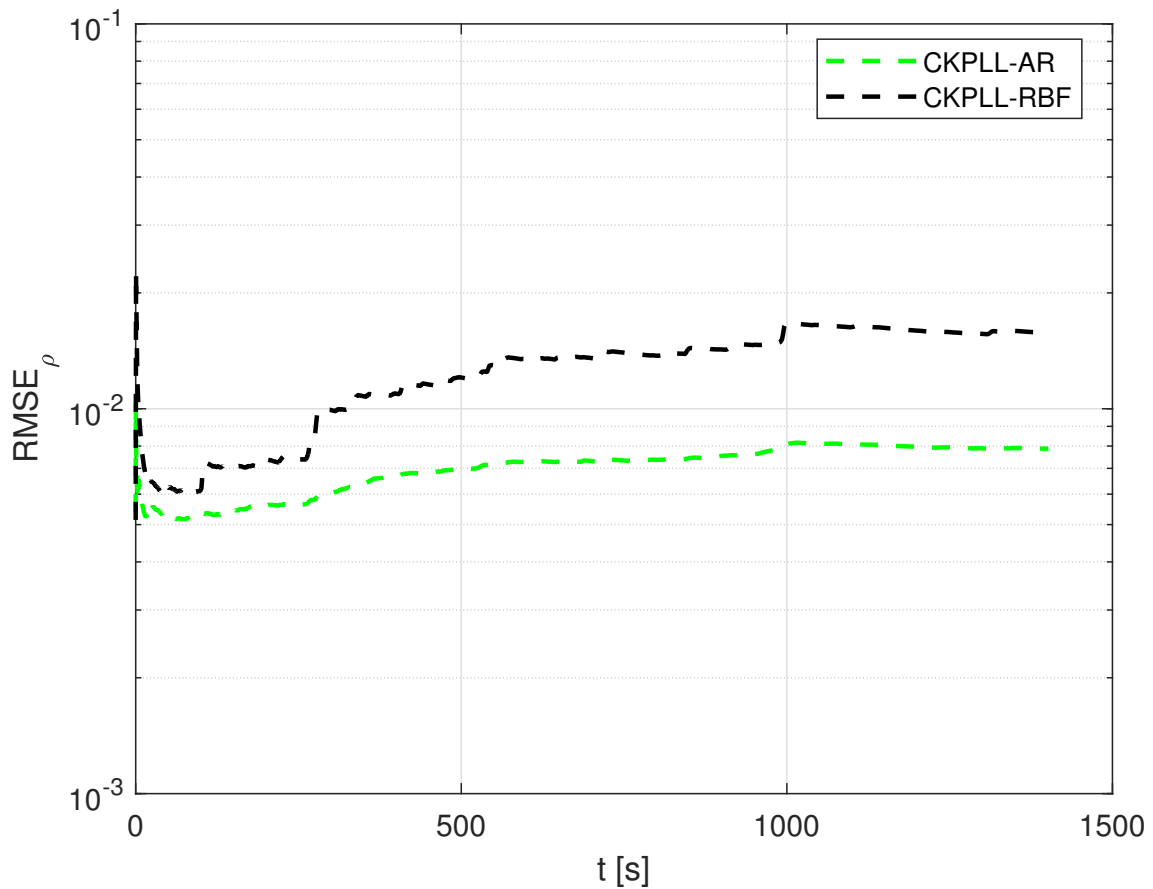Figure 5.13 - RMSE$_{\phi_D}$, with online parameter estimation enabled.

SOURCE: Author's production.

Figure 5.14 - RMSE$_\phi$, with online parameter estimation enabled.
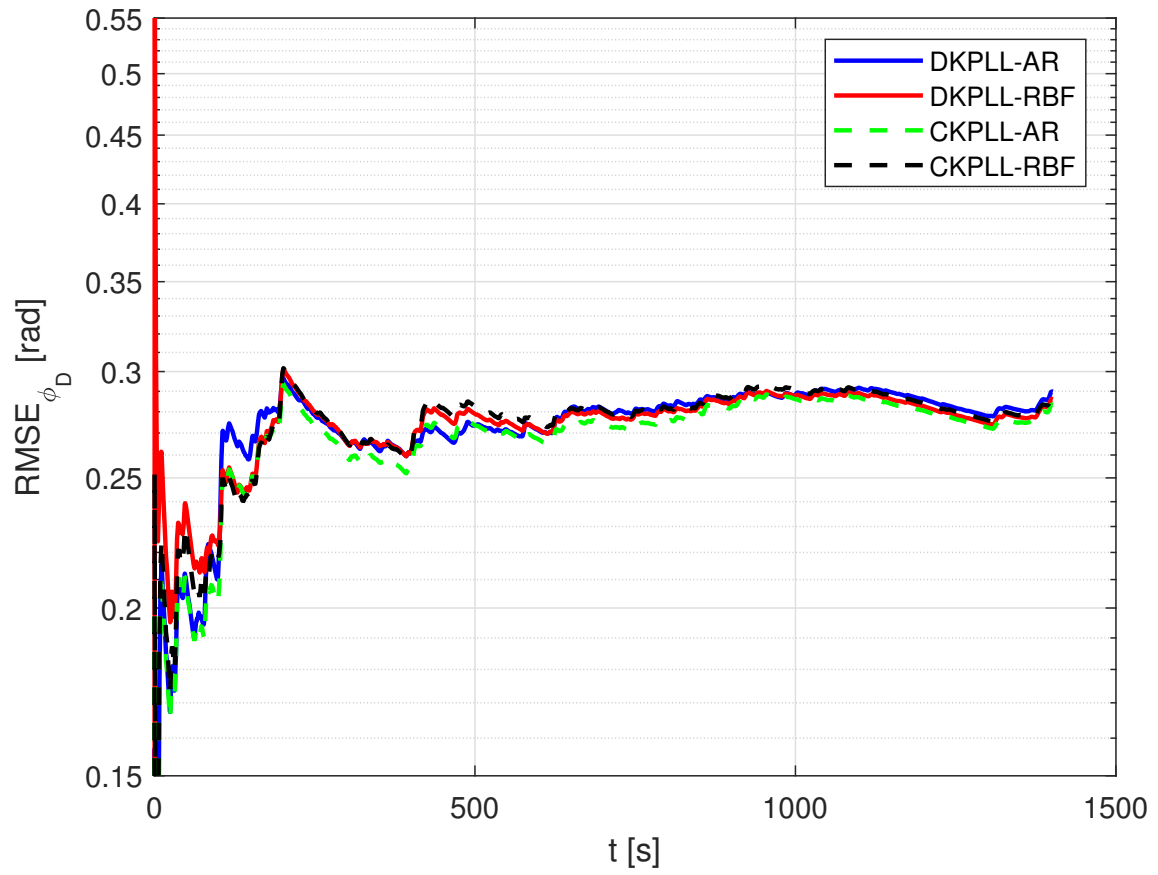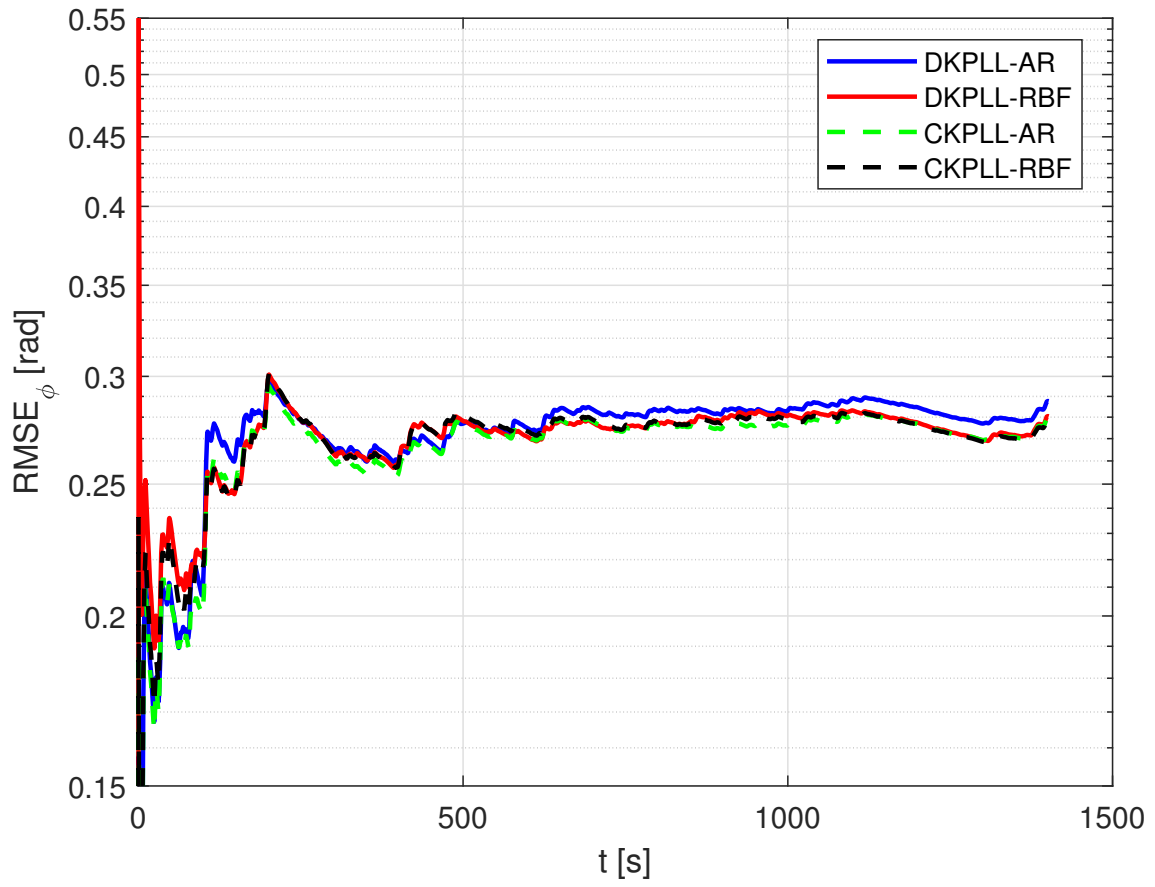

SOURCE: Author's production.

Figure 5.15 - RMSE$_\rho$, with online parameter estimation enabled.
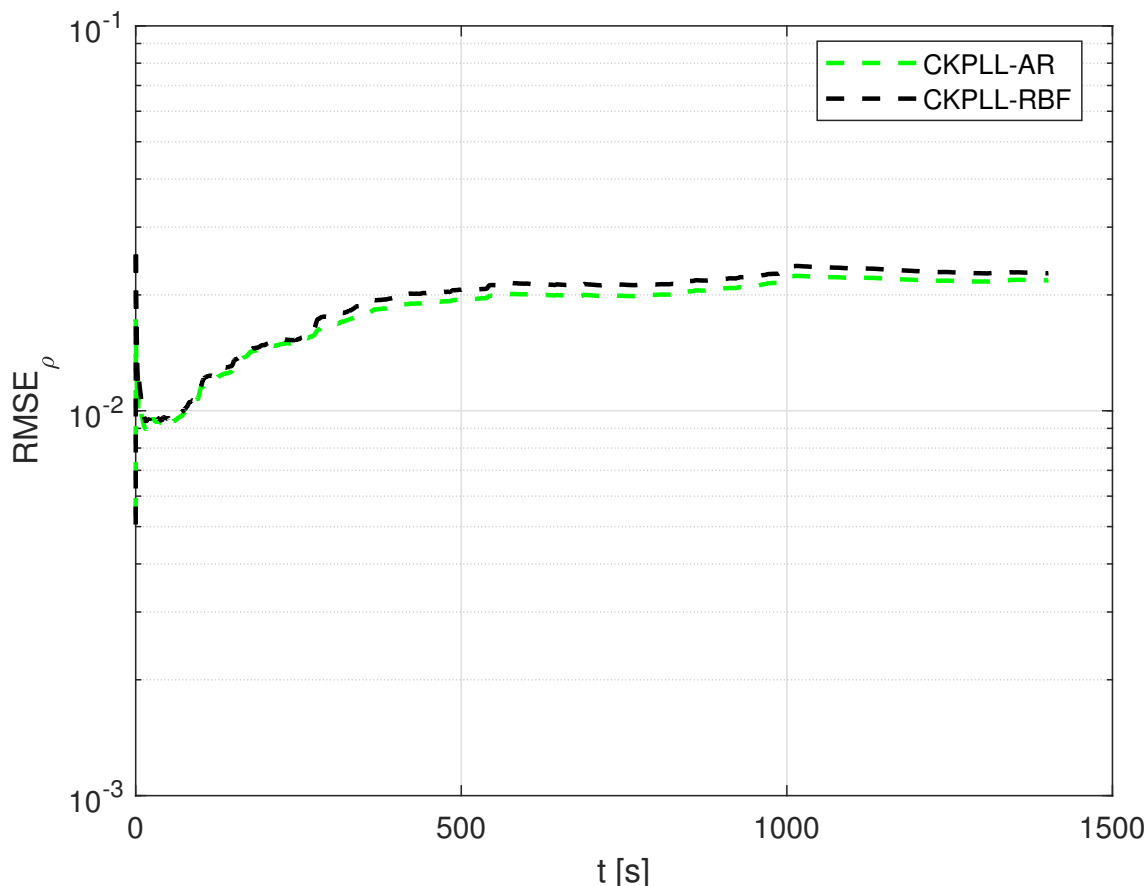
The results of the two simulations highlight the approximation capability of the RBFs in the learning process, which is performed by least squares estimation of the weights of the RBF network, since the network has a linear structure with respect to its weights. The simulations also highlight the generalization capability of the network to different scintillation patterns. Regarding scintillation phase and carrier phase estimation, the RMSE values of the Kalman PLLs employing the RBF network of order 1 is approximately the same in both simulations. The RBF was able to capture the scintillation phase dynamics in the learning process, and thus the online parameter estimation did not improve the results. Otherwise, the results of the Kalman PLLs employing the AR model of order 10 improved significantly when the online parameter estimation was enabled, with both scintillation and carrier phases presenting RMSE values close to the RMSE values of the Kalman PLLs

employing the RBF network. An overparameterized linear AR model was required to fit to the data, and online parameter estimation was required to adjust this model to the evolving scintillation effects. Regarding the scintillation amplitude, both the AR and RBF models of order 1 were able to provide reduced RMSE values in the Kalman PLL structures, with or without the online parameter estimation.

6 CONCLUSION

This work focused on two problems related to the ionospheric scintillation of the radio waves emitted by the GNSS satellites: the monitoring and the mitigation of scintillation induced effects on GNSS receivers. In the monitoring problem, the interest is to obtain estimations of phase and amplitude scintillation on the carrier tracking loops designed for LOS-only tracking, to compute the scintillation indices S_4 and σ_ϕ, respectively. And, in the mitigation problem, the interest is to increase the carrier tracking loops robustness to those scintillation induced effects in order to keep tracking of the GNSS satellites.

The approach to the monitoring problem involved the study of the linearization of a traditional FLL, where the linear approximation showed good agreement with the original nonlinear FLL. This linear approximation is valid once the tracking error is small so the arctangent function employed in the discriminators is approximately linear. From the sensitivity and complementary sensitivity functions of the loop, we could extract information to retrieve the scintillation phase. The approach to the mitigation problem involved the study of the Bayesian approach to estimation, the study of relevant stochastic processes and the study of the RBF networks, to propose the so called discriminator-based and correlator-based Kalman PLLs using RBF networks to model the scintillation dynamics.

The monitoring problem was addressed in Chapter 4, where we proposed a scintillation phase estimation algorithm based on linear filtering of observables from the traditional and Kalman FLLs presenting complementary frequency content, that can be implemented to run in real-time exploiting the LOS-only tracking loops to compute the σ_ϕ for monitoring purposes. The algorithm was evaluated by numeric computer simulations with synthetic ionospheric scintillation data representing severe scintillation. The results of 300 Monte Carlo simulations for both traditional and Kalman FLLs, with different scintillation and receiver noise realizations, showed the capability of the monitoring algorithm to provide scintillation phase estimates with low RMSEs, allowing a statistical meaningful evaluation of the performance of the monitoring algorithm. Despite the different carrier synchronization capabilities of traditional and Kalman FLLs, the scintillation phase estimation performance, discarding cycle slips, of the monitoring algorithm applied to both loops are significantly close, indicating that the algorithm is robust concerning the carrier tracking loop structure and parameters. Once there is a loss-of-lock in the tracking loop or a major disturbance such as cycle slips, induced by ionospheric scintillation, the

algorithm produces permanent or temporary spurious results, respectively, since it is composed of stable linear filters running in an open-loop structure.

The monitoring algorithm was also adapted to run with traditional and Kalman PLLs tracking LOS-only dynamics, since it was originally developed for FLLs. With this adaptation, we could also test the monitoring algorithm with real data presenting scintillation, collected by a JAVAD receiver installed in a monitoring station. The standard deviation was computed for the scintillation phase estimates for both the proposed real-time algorithm and the standard post-processing procedure described in (DIERENDONCK et al., 1993), (ZHANG et al., 2010), showing good agreement between them despite some uncertainty related to the PLL structure of the receiver, which directly affects the monitoring algorithm. We presented the standard deviation computation for a sliding window of 60 s to highlight the possibility of having a real-time phase scintillation metric computation downstream of the real-time phase estimation based on our monitoring algorithm. Its performance is similar to the post-processing procedure, with the additional advantage of avoiding some intricate operations of the batch procedure, such as phase detrending, since the monitoring algorithm is composed of reduced order LTI filtering.

The mitigation problem was addressed in Chapter 5. We proposed two adaptive Kalman PLL structures for mitigation of ionospheric scintillation induced effects on GNSS receivers, where such effects are modeled by RBF networks. In the first structure, the innovations of the Kalman filter are computed by the arctangent phase discriminator. In the second structure, the Kalman filter measurements are taken form the I/Q prompt correlator outputs, and the scintillation amplitude is also estimated. The error state feedback controller provides the control signal for carrier replica generation in the NCO. In both structures, the weights of the RBF networks are estimated by recursive sliding window least squares.

The proposed algorithms were evaluated via Monte Carlo simulations with synthetic ionospheric scintillation data and real ionospheric scintillation data collected by the JAVAD receiver. Regarding the synthetic scintillation data, the results showed the capability of the Kalman PLL structures employing the RBF networks to perform robust carrier synchronization with performance similar to the corresponding state-of-the-art structures employing AR scintillation phase and amplitude models, with a slight advantage to the structures with the RBF networks. The RBF networks allow to capture eventual nonlinear dynamics induced in the receiver by the ionospheric scintillation, an advantage in relation to the linear AR models, at the expense

of a more complex structure. However, possibly the synthetic data considered did not present significant nonlinearities to clearly highlight this advantage of the RBF networks.

Regarding the real ionospheric scintillation data, other residual effects and evolving scintillation characteristics, possibly nonlinear, are present in the data, unlike the simulations with synthetic scintillation data generated by a specific model, the CSM, with fixed characteristics, added to the carrier to form the input signals. This highlighted the learning and generalization capabilities of the RBF networks to cope with such effects, where the Kalman PLL structures employing the RBF networks presented reduced errors with regard to the scintillation and carrier phases estimation when compared to the Kalman PLL structures employing the AR scintillation models, when the online parameter estimation was disabled. It was necessary to enable the online parameter estimation so that the AR model could be adjusted to the evolving receiver and scintillation characteristics over time to present errors close to the structures employing the RBF networks.

The Kalman PLL structures employing the AR scintillation models and the RBF networks were not compared in terms of computational complexity metrics. However, in principle, we expect the algorithm employing the RBF networks with online parameter estimation performed by recursive sliding window least squares to be less complex when compared to the algorithm employing the AR models with online parameter estimation performed by batch sliding window least squares, since there is no matrix inversions in the recursive implementation. Otherwise, in the case of online parameter estimation disabled in both cases or performed by recursive least squares in the algorithm employing the AR models, the algorithm employing the RBF network will be more complex due to the RBFs.

Therefore, there is a trade-off to be taken into account, depending on the size of the RBF network, which is a relatively simple neural network whose learning can be performed by recursive least squares, to provide the required approximation capability, and the computational power available to implement the algorithm in real-time. The evaluation of the computational performance of the proposed algorithms for scintillation mitigation is suggested as a future work, as well as the implementation of the algorithms in a software GNSS receiver. The implementation of the monitoring algorithm in a software GNSS receiver is also suggested as future work. In addition, we also suggest the exploration of other Kalman filter structures for the scintillation mitigation problem that avoid the direct evaluation of the Jacobians,

as the variants of sigma-point Kalman filters, such as the unscented and the central difference Kalman filters.

REFERENCES

AGUIRRE, L. A. **Introdução à identificação de sistemas: técnicas lineares e não-lineares aplicadas a sistemas reais**. Belo Horizonte: Editora UFMG, 2000. 33, 105, 113

AGUIRRE, L. A.; LOPES, R. A. M.; AMARAL, G. F. V.; LETELLIER, C. Constraining the topology of neural networks to ensure dynamics with symmetry properties. **Physical Review E (Statistical, Nonlinear, and Soft Matter Physics)**, v. 69, p. 026701–11, 2004. 104, 105

ALFONSI, L.; FRANCESCHI, G. D.; ROMANO, V.; BOURDILLON, A.; HUY, M. L. GPS scintillations and TEC gradients at equatorial latitudes on April 2006. **Advances in Space Research**, v. 47, n. 10, p. 1750–1757, 2011. 2, 21

ÅSTROM, K. J. **Introduction to stochastic control theory**. New York; London: Academic Press, 1970. 34

BALANIS, C. A. **Antenna theory: analysis and design**. 2. ed. New York, NY, USA: John Wiley & Sons, 1996. 10

BANVILLE, S.; LANGLEY, R. B. Mitigating the impact of ionospheric cycle slips in GNSS observations. **Journal of Geodesy**, v. 87, n. 2, p. 179–193, 2013. 3, 47, 95

BAR-SHALOM, Y.; LI, X. R.; KIRUBARAJAN, T. **Estimation with Applications to Tracking and Navigation**. [S.l.]: John Wiley and Sons, USA, 2001. 29, 30, 34, 68, 97

BASU, S.; MACKENZIE, E.; BASU, S. Ionospheric constraints on VHF/UHF communication links during solar maximum and minimum period. **Radio Science**, v. 23, n. 3, p. 363–378, 1988. 21

BETZ, J. W. Binary offset carrier modulations for radio navigation. **Navigation**, v. 48, n. 4, p. 227–246, 2002. 9

BORRE, K.; AKOS, D. M.; BERTELSEN, N.; RINDER, P.; JENSEN, S. H. **A software-defined GPS and Galileo receiver: a single-frequency approach**. Boston: Springer Science & Business Media, 2007. 11, 52

BROOMHEAD, D. S.; LOWE, D. Multivariable functional interpolation and adaptive networks. **Complex Systems**, v. 2, p. 321–355, 1988. 4, 104

BROWN, R. G.; HWANG, P. Y. C. **Introduction to random signals and applied Kalman filtering**. 3. ed. New York: John Wiley & Sons, 1996. 69, 70

BUTMAN, S.; TIMOR, U. Interplex - an efficient multichannel PSK/PM telemetry system. **IEEE Transactions on Communications**, v. 20, n. 8, p. 415–419, 1972. 9

CERRUTI, A. P.; LEDVINA, B. M.; KINTNER, P. M. Scattering height estimation using scintillating wide area augmentation system/satellite based augmentation system and GPS satellite signals. **Radio Science**, v. 41, p. 1–8, 2006. 26

CHEN, Z. Bayesian filtering: from Kalman filters to particle filters, and beyond. **Statistics**, v. 182, n. 1, p. 1–69, 2003. 40

COX, D. R.; MILLER, H. D. **The theory of stochastic processes**. London: Methuen, 1965. 29, 30

CURRAN, J. T.; BAVARO, M.; MORRISON, A.; FORTUNY, J. Event identication & recording for scintillation monitoring stations. In: INTERNATIONAL TECHNICAL MEETING OF THE INSTITUTE OF NAVIGATION, 2015, Dana Point, CA, USA. **Proceedings...** [S.l.], 2015. p. 114–122. 26, 88

CURRY, R. Separation theorem for nonlinear measurements. **IEEE Transactions on Automatic Control**, v. 14, n. 5, p. 561–564, 1969. 103

DAFESH, P. A.; LAZAR, S.; NGUYEN, T. Coherent adaptive subcarrier modulation (CASM) for GPS modernization. In: ION NTM, 1999, San Diego, USA. **Proceedings...** [S.l.], 1999. p. 649–660. 9

DIERENDONCK, J. V.; KLOBUCHAR, A. J.; HUA, Q. Ionospheric scintillation monitoring using commercial single frequency C/A code receivers. In: INTERNATIONAL TECHNICAL MEETING OF THE SATELLITE DIVISION OF THE INSTITUTE OF NAVIGATION, 6., 1993, Salt Lake City, UT. **Proceedings...** [S.l.], 1993. v. 93, p. 1333–1342. 3, 22, 23, 24, 47, 70, 88, 89, 124, 134

DUBEI, S.; WAHI, R.; MINGKHWAN, E.; GWAL, A. K. Study of amplitude and phase scintillation at GPS frequency. **Indian Journal of Radio & Space Physics**, v. 34, p. 402–407, 2005. 26

DUBEY, S.; WAHI, R.; GWAL, A. K. Ionospheric effects on GPS positioning. **Advances in Space Research**, v. 38, n. 11, p. 2478–2484, 2006. 26

EULER, L. Institutionum calculi integralis. 1768. 51

FALLETTI, E.; PINI, M.; PRESTI, L. L. Low complexity carrier-to-noise ratio estimators for GNSS digital receivers. **IEEE Transactions on Aerospace and Electronic Systems**, v. 47, n. 1, p. 420–437, 2011. 101, 113

FOHLMEISTER, F.; ANTREICH, F.; NOSSEK, J. A. Dual Kalman filtering based analysis of GNSS data from low latitudes. In: ASILOMAR CONFERENCE ON SIGNALS, SYSTEMS, AND COMPUTERS, 52., 2018. **Proceedings...** [S.l.], 2018. p. 532–536. 85

_____. Dual Kalman filtering based GNSS phase tracking for scintillation mitigation. In: IEEE/ION POSITION, LOCATION AND NAVIGATION SYMPOSIUM, 2018, Monterey, CA, USA. **Proceedings...** [S.l.], 2018. p. 1151–1158. 81, 96, 113

FORTE, B. On the relationship between the geometrical control of scintillation indices and the data detrending problems observed at high latitudes. **Annals of Geophysics**, v. 50, n. 6, p. 699–706, dez. 2007. 3, 23, 47, 74

FREMOUW, E. J.; LEADABRAND, R. L.; LIVINGSTON, R. C.; COUSINS, M. D.; RINO, C. L.; FAIR, B. C.; LONG, R. A. Early results from the DNA wideband satellite experiment - complex-signal scintillation. **Radio Science**, v. 13, n. 1, p. 167–187, jan. 1978. 3, 23, 47, 74

GAMSE, S.; WUNDERLICH, T. A.; WASMEIER, P.; KOGOJ, D. The use of Kalman filtering in combination with an electronic tacheometer. In: INTERNATIONAL CONFERENCE ON INDOOR POSITIONING AND NAVIGATION, 2010, Zurich, Switzerland. **Proceedings...** [S.l.], 2010. 112

GARNIER, H.; WANG, L. (Ed.). **Identification of continuous-time models from sampled data**. London: Springer-Verlag, 2008. 32, 34

GAUSS, K. G. **Theory of motion of heavenly bodies**. New York: Dover, 1963. 36

GIOVANNI, G. D.; RADICELLA, S. M. An analytical model ofthe electron density profile in the ionosphere. **Advances in Space Research**, v. 10, n. 11, p. 27–30, 1990. 27

GNSS, J. **JAVAD Delta 3**. Rev 1.5. [S.l.: s.n.], jan. 2018. Online. 85

GOLD, R. Optimal binary sequences for spread spectrum multiplexing. **IEEE Transactionson Information Technology**, v. 33, n. 3, out. 1967. 8

HARDY, R. L. Multiquadratic equations of topography and other irregular surfaces. **Journal of Geophysical Research**, v. 76, p. 1905–1915, 1971. 4, 104

HAYKIN, S. **Digital communication systems**. [S.l.]: Wiley, 2014. 8

HEGARTY, C.; BETZ, J.; SAIDI, A. Binary coded symbol modulations for GNSS. In: INSTITUTE OF NAVIGATION ANNUAL MEETING, 2004, Dayton, OH, USA. **Proceedings...** [S.l.], 2004. 9

HUMPHREYS, T. E.; LEDVINA, B. M.; PSIAKI, M. L.; KINTNER, P. M. Analysis of ionospheric scintillations using wideband GPS L1 C/A signal data. In: ION GNSS, 2004, Long Beach, California, US. **Proceedings...** [S.l.], 2004. p. 399–407. 26

HUMPHREYS, T. E.; PSIAKI, M. L.; HINKS, J. C.; O'HANLON, B.; KINTNER, P. M. Simulating ionosphere-induced scintillation for testing GPS receiver phase tracking loops. **IEEE Journal of Selected Topics in Signal Processing**, v. 3, n. 4, p. 707–715, 2009. 26, 86

HUMPHREYS, T. E.; PSIAKI, M. L.; KINTNER, P. M. GPS carrier tracking loop performance in the presence of ionospheric scintillations. In: INTERNATIONAL TECHNICAL MEETING OF THE SATELLITE DIVISION OF THE INSTITUTE OF NAVIGATION, 2005, Long Beach, CA, USA. **Proceedings...** [S.l.], 2005. p. 156–167. 26, 77, 95

_____. Modeling the effects of ionospheric scintillation on GPS carrier phase tracking. **IEEE Transactions on Aerospace and Electronic Systems**, v. 46, n. 4, p. 1624–1637, 2010. 26, 27, 48, 80, 97, 111

ITÔ, K. On stochastic differential equations. **Memoirs of the American Mathematical Society**, n. 4, 1951. 31, 38

JACOBSEN, K. S.; ANDALSVIK, Y. L. Overview of the 2015 St. Patrick's day storm and its consequences for RTK and PPP positioning in Norway. **Journal of Space Weather and Space Climate**, v. 6, n. A9, p. 1–12, 2016. 3, 95

JAZWINSKI, A. H. **Stochastic processes and filtering theory**. [S.l.]: Academic Press, 1970. 37, 38, 39, 41, 42, 43, 44

JIAO, Y. **High latitude ionosphere scintillation characterization**. Dissertação (Mestrado) — Miami University, Oxford, Ohio, USA, 2013. 26

JIAO, Y.; MORTON, Y.; TAYLOR, S.; PELGRUM, W. High latitude ionosphere scintillation characterization. In: INTERNATIONAL TECHNICAL MEETING OF THE INSTITUTE OF NAVIGATION, 2013b, San Diego, CA, USA. **Proceedings...** [S.l.], 2013b. p. 579–584. 26

JIAO, Y.; MORTON, Y. T. Comparison of the effect of high latitude and equatorial ionospheric scintillation on GPS signals during the maximum of solar cycle 24. **Radio Science**, v. 50, n. 9, p. 886–903, 2015. 26

JIAO, Y.; MORTON, Y. T.; TAYLOR, S.; PELGRUM, W. Characterization of high-latitude ionospheric scintillation of GPS signals. **Radio Science**, v. 48, n. 6, p. 698–708, 2013a. 2, 21, 26

JIAO, Y.; XU, D.; RINO, C. L.; MORTON, Y. T.; CARRANO, C. S. A multi-frequency GPS signal strong equatorial ionospheric scintillation simulator: algorithm, performance, and characterization. **IEEE Transactions on Aerospace and Electronic Systems**, v. 54, n. 4, p. 1947–1965, 2018. 27

KALMAN, R. E. A new approach to linear filtering and prediction problems. **Transactions of the ASME - Journal of Basic Engineering**, v. 82, p. 35–45, 1960. Series D. 37, 45

_____. New methods in Wiener filtering theory. In: BOGDANOFF, J. L.; KOZIN, F. (Ed.). **1st. Symp. Appl. Random Function Theory and Probability**. New York: Wiley, 1963. 37

KALMAN, R. E.; BUCY, R. S. New results in linear filtering and prediction theory. **Transactions of the ASME - Journal of Basic Engineering**, v. 83, p. 95–108, 1961. Series D. 37, 44, 69

KAPLAN, E. D.; HEGARTY, C. J. **Understanding GPS/GNSS: principles and applications**. 3. ed. Boston; London: Artech House, 2017. 1, 8, 13, 49, 52, 56, 77

KAY, S. M. **Fundamentals of statistical signal processing: estimation theory**. [S.l.]: Prentice Hall, 1993. 37

KINTNER, P.; HUMPHREYS, T.; HINKS, J. GNSS and ionospheric scintillation: how to survive the next solar maximum. **Inside GNSS**, p. 22–30, jul. 2009. 26, 27

KINTNER, P. M.; HUMPHREYS, T. E.; HINKS, J. GNSS and ionospheric scintillation: how to survive the next solar maximum. **Inside GNSS**, v. 4, n. 4, p. 22–33, 2009. 22

KOLMOGOROV, A. N. **Interpolation and extrapolation of stationary random sequences**. Santa Monica, California: [s.n.], 1962. Translated by W. Doyle and J. Selin. 37

LEE, J.; MORTON, J.; MOON, H.; SEO, J. Monitoring and mitigation of ionospheric anomalies for GNSS-based safety critical systems: a review of up-to-date signal processing techniques. **IEEE Signal Processing Magazine**, v. 34, n. 5, p. 96–110, 2017. 3, 47

LEE, J. S.; MILLER, L. E. **CDMA systems engineering handbook**. Norwood: Artech House, 1998. 8

LEGRAND, F.; MACABIAU, C.; ISSLER, J.-L.; LESTARQUIT, L.; MEHLEN, C. Improvement of pseudorange measurements accuracy by using fast adaptive bandwidth lock loops. In: ION GPS, 2000, Salt Lake City, USA. **Proceedings...** [S.l.], 2000. p. 2346–2356. 3, 47, 95

LI, X. R.; JILKOV, V. P. Survey of maneuvering target tracking. part I: dynamic models. **IEEE Transactions on Aerospace and Electronic Systems**, v. 39, n. 4, p. 1333–1364, 2003. 34

LINTY, N.; DOVIS, F.; ALFONSI, L. Software-defined radio technology for gnss scintillation analysis: bring antarctica to the lab. **GPS Solutions**, v. 22, n. 96, 2018. 26

LJUNG, L. **System identification: theory for the user**. New Jersey: Prentice Hall, 1987. 33

LOCUBICHE-SERRA, S.; SECO-GRANADOS, G.; LÓPEZ-SALCEDO, J. A. Doubly-adaptive autoregressive Kalman filter for GNSS carrier tracking under scintillation conditions. In: INTERNATIONAL CONFERENCE ON LOCALIZATION AND GNSS, 2016, Barcelona, Spain. **Proceedings...** [S.l.], 2016. p. 1–6. 98

LUO, Z.; DING, J.; ZHAO, L.; WU, M. An enhanced non-coherent pre-filter design for tracking error estimation in GNSS receivers. **Sensors (Basel)**, v. 17, n. 11, p. 1–23, 2017. 14, 15, 81

MACABIAU, C.; DEAMBROGIO, L.; BARREAU, V.; VIGNEAU, W.; VALETTE, J. J.; ARTAUD, G.; THEVENON, P.; RIES, L. Kalman filter based robust GNSS signal tracking algorithm in presence of ionospheric scintillations. In: INTERNATIONAL TECHNICAL MEETING OF THE SATELLITE DIVISION OF THE INSTITUTE OF NAVIGATION, 2012, Nashville, U.S. **Proceedings...** [S.l.], 2012. p. 3420–3434. 27

MAYER, C.; BELABBAS, B.; JAKOWSKI, N.; MEURER, M.; DUNKEL, W. Ionosphere threat space model assessment for GBAS. In: ION GNSS, 2009, Savannah, GA, USA. **Proceedings...** [S.l.], 2009. p. 22–25. 2, 47

MORAES, A. O.; RODRIGUES, F. S.; PERRELLA, W. J.; PAULA, E. R. de. Analysis of the characteristics of low-latitude GPS amplitude scintillation measured during solar maximum conditions and implications for receiver performance. **Surveys in Geophysics**, v. 33, n. 5, p. 1107–1131, 2012. 2, 21

MUTHURAMAN, K.; BORIO, D. C/N0 estimation for modernized GNSS signals: theoretical bounds and a novel iterative estimator. **Navigation: Journal of The Institute of Navigation**, v. 57, n. 4, 2010. 113

MYER, G.; MORTON, Y.; SCHIPPER, B. Ionospheric scintillation effects on GPS pseudorange and carrier phase measurements and an adaptive algorithm to limit position errors during scintillation. In: INTERNATIONAL TECHNICAL MEETING OF THE INSTITUTEOF NAVIGATION, 2017, Monterey, CA, USA. **Proceedings...** [S.l.], 2017. 21

NISHIOKA, M.; SAITO, A.; TSUGAWA, T. Occurrence characteristics of plasma bubble derived from global ground-based GPS receiver networks. **Journal of Geophysical Research**, v. 113, n. A05301, p. 1–12, 2008. 21

NIU, F.; MORTON, Y.; TAYLOR, S.; PELGRUM, W.; DIERENDONCK, A. J. V. Performances of GPS signal observables detrending methods for ionosphere scintillation studies. In: INTERNATIONAL TECHNICAL MEETING OF THE SATELLITE DIVISION OF THE INSTITUTE OF NAVIGATION, 2012, Nashville, TN, USA. **Proceedings...** [S.l.], 2012. p. 3435–3443. 3, 23, 25, 47, 48

O'HANLON, B.; PSIAKI, M.; POWELL, S.; BHATTI, J.; HUMPHREYS, T. E.; CROWLEY, G.; BUST, G. Cases: a smart, compact gps software receiver for space weather monitoring. In: ION GNSS, 2011. **Proceedings...** [S.l.], 2011. p. 2745–2753. 3, 25, 47

PAPOULIS, A.; PILLAI, S. U. **Probability, random variables and stochastic processes**. 4. ed. USA: McGraw-Hill, 2002. 8, 29

PARKINSON, B. W.; SPILKER JR., J. J. (Ed.). **Global positioning systems: theory and applications**. Washington DC: AIAA, 1996. 14, 15

POWELL, M. J. D. Radial basis functions for multivariate interpolation: a review. In: IMA CONFERENCE ON ALGORITHMS FOR THE APPROXIMATION OF FUNCTIONS AND DATA, 1985, Shrivenham, UK. **Proceedings...** [S.l.], 1985. p. 143–167. 4, 104

PSIAKI, M. L.; HUMPHREYS, T. E.; CERRUTI, A.; POWELL, S.; KINTNER, P. M. Tracking L1 C/A and L2C signals through ionospheric scitillations. In: INTERNATIONAL TECHNICAL MEETING OF THE SATELLITE DIVISION OF THE INSTITUTE OF NAVIGATION, 2007, FortWorth, TX, USA. **Proceedings...** [S.l.], 2007. 27

REBEYROL, E. **Galileo signals and payload optimization**. Tese (Doutorado) — l'Ecole Superieure des Telecommunications de Paris, Paris, 2007. 9

SCHAGEN, I. Interpolation in two dimensions - a new technique. **IMA Journal of Applied Mathematics**, v. 23, n. 1, p. 53–59, 1979. 105

SECAN, J. A.; BUSSEY, R. M.; FREMOUW, E. J. High-latitude upgrade to the wideband ionospheric scintillation. **Radio Science**, v. 32, n. 4, p. 1567–1574, 1997. 27

SIMON, M. K.; OMURA, J. K.; SCHOLTZ, R. A.; LEVITT, B. K. **Spread spectrum communications handbook**. New York: McGraw-Hill, 1994. 8, 9

SMITH, A. M.; MITCHELL, C. N.; WATSON, R. J.; MEGGS, R. W.; KINTNER, P. M.; KAURISTIE, K.; HONARY, F. GPS scintillation in the high arctic associated with an auroral arc. **Space Weather**, v. 6, n. S03D01, p. 1–7, 2008. 21

SMITH, L. A. Identification and prediction of low dimensional dynamics. **Physica D**, v. 58, p. 50–76, 1992. 105

SÖDERSTRÖM, T. On zero locations for sampled stochastic systems. **IEEE Transactions on Automatic Control**, v. 35, n. 11, p. 1249–1253, 1990. 34

_____. Computing stochastic continuous-time models from ARMA models. **International Journal of Control**, v. 53, n. 6, p. 1311–1326, 1991. 33

_____. **Discrete-time stochastic systems: estimation and control**. London: Springer-Verlag, 2002. 32, 33, 34

SÖDERSTRÖM, T.; STOICA, P. **System identification**. Hemel Hempstead, UK: Prentice-Hall International, 1989. 101

SORENSON, H. W. Least-squares estimation: from Gauss to Kalman. **IEEE Spectrum**, v. 7, n. 7, p. 63–68, 1970. 36

SPILKER JUNIOR, J. J. **Digital communications by satellite**. Englewood Cliffs, NJ, USA: Prentice-Hall, 1977. 9

STATMAN, J. I.; HURD, W. J. An estimator-predictor approach to PLL loop filter design. **IEEE Transactions on Communications**, v. 38, n. 10, p. 1667–1669, 1990. 3, 95

STRAW, R. D. (Ed.). **The ARRL antenna book: the ultimate reference for amateur radio antennas, transmission lines and propagation**. Newington, CT, USA: American Radio Relay League, 2003. 10

TAYLOR, S.; MORTON, Y.; JIAO, Y.; TRIPLETT, J.; PELGRUM, W. An improved ionosphere scintillation event detection and automatic trigger for GNSS data collection systems. In: INTERNATIONAL TECHNICAL MEETING OF THE INSTITUTE OF NAVIGATION, 2012, Newport Beach, CA, USA. **Proceedings...** [S.l.], 2012. p. 1563–1569. 26

TEUNISSEN, P. J. G.; MONTENBRUCK, O. (Ed.). **Springer handbook of global navigation satellite systems**. Switzerland: Springer International, 2017. 2, 9, 15, 20, 21

TIMOR, U. Equivalence of time-multiplexed and frequency-multiplexed signals in digital communications. **IEEE Transactions on Communications**, v. 20, n. 8, p. 435–438, 1972. 9

TSUI, J. **Fundamentals of global positioning system receivers: a software approach**. New York, NY, USA: John Wiley & Sons, 2000. 10

VILÁ-VALLS, J.; CLOSAS, P.; FERNANDEZ-PRADES, C.; CURRAN, J. T. On the ionospheric scintillation mitigation in advanced GNSS receivers. **IEEE Transactions on Aerospace and Electronic Systems**, v. 54, n. 4, p. 1692–1708, 2018. 27, 96, 98, 113, 123, 124

VILÁ-VALLS, J.; CLOSAS, P.; NAVARRO, M.; FERNANDEZ-PRADES, C. Are PLLs dead? a tutorial on kalman filter-based techniques for digital carrier synchronization. **IEEE Aerospace and Electronic Systems Magazine**, v. 32, n. 7, p. 28–45, 2017. 68

VILÁ-VALLS, J.; FERNANDEZ-PRADES, C.; ARRIBAS, J.; CURRAN, J. T.; CLOSAS, P. On-line model learning for adaptive GNSS ionospheric scintillation estimation and mitigation. In: IEEE/ION POSITION, LOCATION AND NAVIGATION SYMPOSIUM, 2018, Monterey, CA, USA. **Proceedings...** [S.l.], 2018. p. 1167–1172. 3, 81, 96, 97, 98, 113, 115, 123

VILÁ-VALLS, J.; FERNANDEZ-PRADES, C.; LÓPEZ-SALCEDO, J.; SECO-GRANADOS, G. Adaptive GNSS carrier tracking under ionospheric scintillation: estimation vs. mitigation. **IEEE Communications Letters**, v. 19, n. 6, p. 961–964, 2015. 96, 98, 113

VILÁ-VALLS, J.; LINTY, N.; CLOSAS, P.; DOVIS, F.; CURRAN, J. T. Survey on signal processing for GNSS under ionospheric scintillation: detection, monitoring, and mitigation. **Navigation**, v. 67, n. 3, p. 511–536, 2020. 2, 26, 27, 93, 95, 96

WAHLBERG, B.; LJUNG, L.; SÖDERSTRÖM, T. On sampling and reconstruction of continuous time stochastic systems. In: **IFAC Proceedings**. [S.l.: s.n.]. v. 25, n. 15, p. 281–285. 32

WENDLAND, H. Computational aspects of radial basis function approximation. **Studies in Computational Mathematics**, v. 12, p. 231–256, 2006. 105

WIENER, N. **The extrapolation, interpolation and smoothing of stationary time series**. New York: Wiley, 1949. 37

WON, J.; DÖTTERBÖCK, D.; EISSEFELLER, B. Performance comparison of different forms of Kalman filter approaches for a vector-based GNSS signal tracking loop. **Navigation**, v. 57, n. 3, p. 185–199, 2010. 99, 100

XU, D.; MORTON, Y.; AKOS, D.; WALTER, T. GPS multifrequency carrier phase characterization during strong equatorial ionospheric scintillation. In: INTERNATIONAL TECHNICAL MEETING OF THE SATELLITE DIVISION OF THE INSTITUTE OF NAVIGATION, 2015, Tampa, FL, USA. **Proceedings...** [S.l.], 2015. 2, 47

XU, R.; LIU, Z.; CHEN, W. Improved FLL-assisted PLL with in-phase pre-filtering to mitigate amplitude scintillation effects. **GPS Solutions**, v. 19, p. 263–276, 2015. 3, 95

YANG, R.; LING, K. V.; POH, E.-K.; MORTON, Y. Generalized GNSS signal carrier tracking: part I - modeling and analysis. **IEEE Transactions on Aerospace and Electronic Systems**, v. 53, n. 4, p. 1781–1797, 2017. 99

YOUNG, P. C. **Recursive estimation and time-series analysis**. 2. ed. Germany: Springer-Verlag, 2011. 101, 109, 110, 115

ZHANG, L.; MORTON, Y.; GRAAS, F. van; BEACH, T. Characterization of GNSS signal parameters under ionosphere scintillation conditions using software-based tracking algorithms. In: IEEE/ION POSITION, LOCATION AND NAVIGATION SYMPOSIUM, 2010, Indian Wells, CA, USA. **Proceedings...** [S.l.], 2010. p. 264–275. 3, 23, 25, 47, 48, 88, 89, 124, 134

ZHANG, L.; MORTON, Y. T. Tracking GPS signals under ionospheric scintillation conditions. In: ION GNSS, 2009, Savannah, GA, USA. **Proceedings...** [S.l.], 2009. p. 227–234. 77

PUBLICAÇÕES TÉCNICO-CIENTÍFICAS EDITADAS PELO INPE

Teses e Dissertações (TDI)

Teses e Dissertações apresentadas nos Cursos de Pós-Graduação do INPE.

Notas Técnico-Científicas (NTC)

Incluem resultados preliminares de pesquisa, descrição de equipamentos, descrição e ou documentação de programas de computador, descrição de sistemas e experimentos, apresentação de testes, dados, atlas, e documentação de projetos de engenharia.

Propostas e Relatórios de Projetos (PRP)

São propostas de projetos técnico-científicos e relatórios de acompanhamento de projetos, atividades e convênios.

Publicações Seriadas

São os seriados técnico-científicos: boletins, periódicos, anuários e anais de eventos (simpósios e congressos). Constam destas publicações o Internacional Standard Serial Number (ISSN), que é um código único e definitivo para identificação de títulos de seriados.

Pré-publicações (PRE)

Todos os artigos publicados em periódicos, anais e como capítulos de livros.

Manuais Técnicos (MAN)

São publicações de caráter técnico que incluem normas, procedimentos, instruções e orientações.

Relatórios de Pesquisa (RPQ)

Reportam resultados ou progressos de pesquisas tanto de natureza técnica quanto científica, cujo nível seja compatível com o de uma publicação em periódico nacional ou internacional.

Publicações Didáticas (PUD)

Incluem apostilas, notas de aula e manuais didáticos.

Programas de Computador (PDC)

São a seqüência de instruções ou códigos, expressos em uma linguagem de programação compilada ou interpretada, a ser executada por um computador para alcançar um determinado objetivo. Aceitam-se tanto programas fonte quanto os executáveis.